DOPPLER FLUCTUATION SPECTROSCOPY IN LIVING TISSUES

by

Zhe Li

A Dissertation

Submitted to the Faculty of Purdue University

In Partial Fulfillment of the Requirements for the degree of

Doctor of Philosophy

Department of Physics and Astronomy

West Lafayette, Indiana

May 2020

THE PURDUE UNIVERSITY GRADUATE SCHOOL

STATEMENT OF COMMITTEE APPROVAL

Dr. David Nolte, Chair

Department of Physics and Astronomy

Dr. Andrew Mugler

Department of Physics and Astronomy

Dr. Sri Iyer-Biswas

Department of Physics and Astronomy

Dr. Oana Malis

Department of Physics and Astronomy

Approved by:

Dr. John P. Finley

ACKNOWLEDGMENTS

This work was not possible without the guidance and assistance from many people. First and foremost, I would like to thank my advisor Professor Nolte, who provided invaluable advice on my research and communication. He guided me to understand what it means to be a real scientist. I would also like to thank Prof. Turek and Prof. Machaty who are knowledgeable and supportive collaborators in the projects. Thanks to my lab mates Honggu Choi and Zhen Hua whom I have had many fruitful discussions with. I want to thank my colleagues Natalie Ehmke and Ilka M Lorenzo-Lorenzo, who worked countless hours on the IVF project with me. Thanks to my thesis committee (Prof. Mugler, Prof. Iyer-Biswas, and Prof Malis) who provided valuable feedback for my research. Finally, I want to say thanks to my family and friends who have been very supportive and encouraging during my Ph.D. study.

TABLE OF CONTENTS

LIST OF TABLES

LIST OF FIGURES

ABSTRACT

Intracellular motions are important signatures of living tissues, and intracellular dynamics reflect overall cell function and health. Traditional microscopy methods can track 2D cellular motions but do not provide an ensemble evaluation of intracellular activity. Biodynamic imaging (BDI) is a unique 3D imaging technique based on the phase shifts of dynamic light scattering and is highly sensitive to intracellular dynamics in living cells and their changes. This makes BDI a versatile tool to evaluate many different types of samples under various scenarios, and BDI has the potential to improve patient diagnosis and to provide valuable information for health care research. This may include evaluating sample activity, profiling patient chemotherapy response, and studying drug mechanisms. This thesis discusses the theory and modeling of BDI, the construction of BDI systems, sample heterogeneity analysis (TDSI), and the use of BDI to study cytoskeletal drug mechanisms, improve embryo selection and select therapies in pre-clinical trials.

CHAPTER 1. INTRODUCTION

Biodynamic imaging is an optical imaging technology related to *en face* OCT [1], with enhanced partially-coherent speckle generated by broad-area illumination with coherence detection using digital holography [2-4]. Biodynamic imaging penetrates up to 1 mm into living tissue and returns high-content information in the form of dynamic light scattering across a broad spectral range [5, 6]. The fluctuation frequencies relate to Doppler frequency shifts caused by light scattering from subcellular constituents that are in motion, creating beats among all of the multiple partial waves. The speeds of intracellular dynamics range across four orders of magnitude from tens of nanometers per second (cell membrane) [7-10] to tens of microns per second (organelles, vesicles) [11-14]. This chapter gives an overview of the basic principles and the data analysis method of biodynamic imaging.

1.1 Imaging Techniques for Scattering Medium and Biomedical Targets

1.1.1 Imaging Through Opaque Scattering Layers

Biological tissues induce light scattering, having a diffusive effect on light beams and create speckle patterns, which reduces image resolution. Advances in imaging through scattering layers include introducing adaptive optics [15], using speckle memory effect and correlation analysis (correlography) with ensemble averages and ergodic-like properties of speckle [16-19], retrieving complex fields with holography [20], and phase-space measurement using the Wigner distribution function and iterative reconstruction [21, 22].

1.1.2 Diffuse Correlation Spectroscopy (DCS), Diffuse Reflectance Spectroscopy (DRS) and Diffuse Optical Tomography (DOT)

Diffuse correlation spectroscopy (DCS) is widely used for cerebral blood flow monitoring. Temporal autocorrelation functions of speckle or light electric fields are measured, analyzed, and then compared against certain types of motion, e.g. Brownian motion. Autocorrelation functions for molecular Brownian motion are usually measured in the time range of 10^{-5} to 10^{-2} seconds [23].

Diffuse reflectance spectroscopy (DRS) uses a spectrometer to analyze the diffuse reflectance of a tissue illuminated by a broadband light source, and is therefore useful for quantifying optical and physiological properties of tissues [24].

Intracellular, extracellular fluids, subcellular components and tissue density variances have different refractive indexes, which leads to differences in scattering coefficient μ_s' and g-factors that can be determined from optical measurements. This is the basic principle of diffuse optical tomography (DOT). The technique emits picosecond diode laser pulses, analyses the broadened and attenuated signal from tissue layers and constructs images of tissues [25].

1.1.3 Optical Coherence Tomography (OCT)

Optical Coherence Tomography uses coherent light to capture 2D or 3D micrometer-resolution images from scattering media. Since the development of OCT in 1990s, it has found wide applications in medicine, including ophthalmology, dermatology and dentistry etc. OCT has the advantage of being safe, inexpensive and having high depth and transverse resolution. Two basic types of OCT are time-domain OCT in Figure 1-1a) and Fourier-domain OCT in Figure 1-1b).

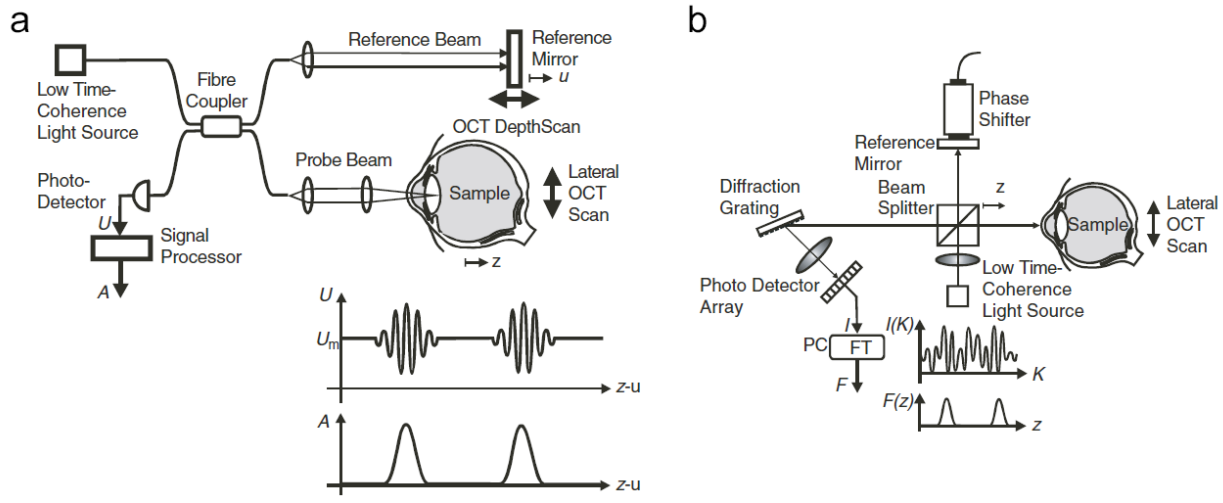

Figure 1-1. a) Time-domain reflectometer b) Fourier domain OCT [26]

Many extensions and improvements to OCT systems have been developed in the last two decades. Notable ones include polarization-sensitive OCT (PS-OCT), Doppler OCT (D-OCT) and full-field OCT (FF-OCT). PS-OCT utilizes the polarization properties of light and the fact that some biological structures alter the polarization state of the light, which gives contrast and quantitative

information in images [27, 28]. D-OCT combines OCT and the Doppler effect and is sensitive to blood flow [29]. FFOCT eliminates scanning and records 2D slices from a combination of interferometric images [30].

1.2 Fundamentals of Biodynamic Imaging

1.2.1 Optical Coherence

Two sources are perfectly coherent if they keep a constant phase difference. Temporal coherence describes a strong correlation of light at one location between two different times, while spatial coherence describes a strong correlation of light at the same time between two locations. In interferometry, a certain level of optical coherence is desired, and coherence length is especially important in coherence gated imaging systems.

1.2.2 Speckle Phenomenon

Speckle is a result of spatial coherence, when waves with amplitudes and phases are added together to create a randomly varying intensity pattern. The creation of speckles is a random-walk process in phase space. Speckle degrades image quality, and various methods have been proposed to reduce speckle [31-33], while in other applications autocorrelation information can be extracted from speckle and used to reconstruct object information [18, 20]. Speckle size is a second-order statistical property and is calculated as

$$a_{sp} = \frac{\lambda f}{D} \tag{1.2}$$

where λ is the wavelength of the light, f the distance of free space propagation and D is the smaller of aperture size or object size [34].

1.2.3 Coherence Length

The coherence length of a Gaussian light source is described by equation [26]

$$L = \frac{2\ln 2}{\pi n}\frac{\lambda^2}{\Delta\lambda} \tag{1.3}$$

where λ is the central wavelength of the source, $\Delta\lambda$ is the FWHM bandwidth of the source, and n is the refractive index of the medium. A desired coherence length can be achieved by selecting proper λ and $\Delta\lambda$ values. In a backscattering configuration, only the part of the backscattered light that has an optical path length (OPL) that matches the OPL of the reference arm within the coherence length will interfere. Therefore, different depths of a sample can be imaged as the OPL of the reference arm changes, achieving coherence gating. This is the fundamental of "flythroughs", i.e. depth scans of a sample.

1.2.4 Holography

The first hologram was recorded by Dennis Gabor in 1948. A hologram is an interference pattern constructed by an illumination beam and a reference beam. With the development of coherent sources like lasers, this imaging technique quickly improved, and in 1971 Gabor was awarded the Nobel Prize for his invention [35].

The two steps of holography are recording and reconstructing both the amplitude and phase of an optical wave arriving from a coherently illuminated object. If the field of the signal arm which is to be reconstructed is

$$u(x,y) = |u(x,y)| \exp\left[-i\phi(x,y)\right] \tag{1.4}$$

and a plane wave reference arm is

$$v(x,y) = A \exp\left[-i\left(k_1 x + k_2 y\right)\right] \tag{1.5}$$

then the intensity is given by

$$\begin{aligned} I(x,y) &= |u+v|^2 \\ &= |u(x,y)|^2 + A^2 + 2A|u(x,y)| \cos\left[k_1 x + k_2 y - \phi(x,y)\right] \end{aligned} \tag{1.6}$$

on a recording medium. The amplitude and phase of the signal have been recorded as amplitude and phase modulation with a spatial carrier frequency (k_1, k_2). Both amplitude and phase distributions can be reconstructed from the hologram.

1.2.5 Digital Holography

Instead of holographic films, digital holography uses a CMOS or CCD camera to record holograms and a computer to reconstruct images. A digital camera allows fast acquisition of hologram images, usually tens to hundreds of fps at VGA resolution. A high frame rate captures high-frequency fluctuations. According to Eq (1.6), when a CCD camera is placed on the Fourier domain of an imaging system, a 2D FFT of the hologram image will reveal two conjugate images, at $\left(-\frac{1}{k_1},-\frac{1}{k_2}\right)$ and $\left(\frac{1}{k_1},\frac{1}{k_2}\right)$ in the x-space, respectively.

1.2.6 Dynamic Light Scattering (DLS)

A scattering target that is in motion causes dynamic light scattering. In living tissues, uniform, random or active motions happen persistently, which leads to phase drift and intensity fluctuations in the detection device in an interferometric imaging system.

The light-scattering configuration for dynamic light scattering from a moving particle is shown in Figure 1-2. The incident light has an initial *k*-vector $\mathbf{k_1}$ that is scattered by a small particle into a final *k*-vector $\mathbf{k_2}$. The momentum transfer in the scattering process is $\mathbf{q}=\mathbf{k_2}-\mathbf{k_1}$, where the magnitude of the transferred momentum is

$$\begin{aligned}|\mathbf{q}| &= k\sqrt{2(1-\cos\theta)} \\ &= 2k\sin(\theta/2)\end{aligned} \tag{1.7}$$

at the scattering angle θ. The Doppler frequency shift from the central frequency of the incident photon is given by

$$\Delta\omega_\phi = \mathbf{q}\cdot\mathbf{v} = qv\cos\phi = \omega_D\cos\phi \tag{1.8}$$

where

$$\omega_D = qv \tag{1.9}$$

is the maximum (or co-linear) Doppler angular frequency shift, v is the velocity of the particle, and ϕ is the angle between the particle velocity and the momentum transfer vector. For forward

scattering, $\theta = 0$, and the Doppler frequency shift is identically zero. For backward scattering, the momentum transfer $q = 4\pi n / \lambda_0$ is a maximum, and the Doppler frequency shift depends only on the particle velocity through $\omega_D = qv$.

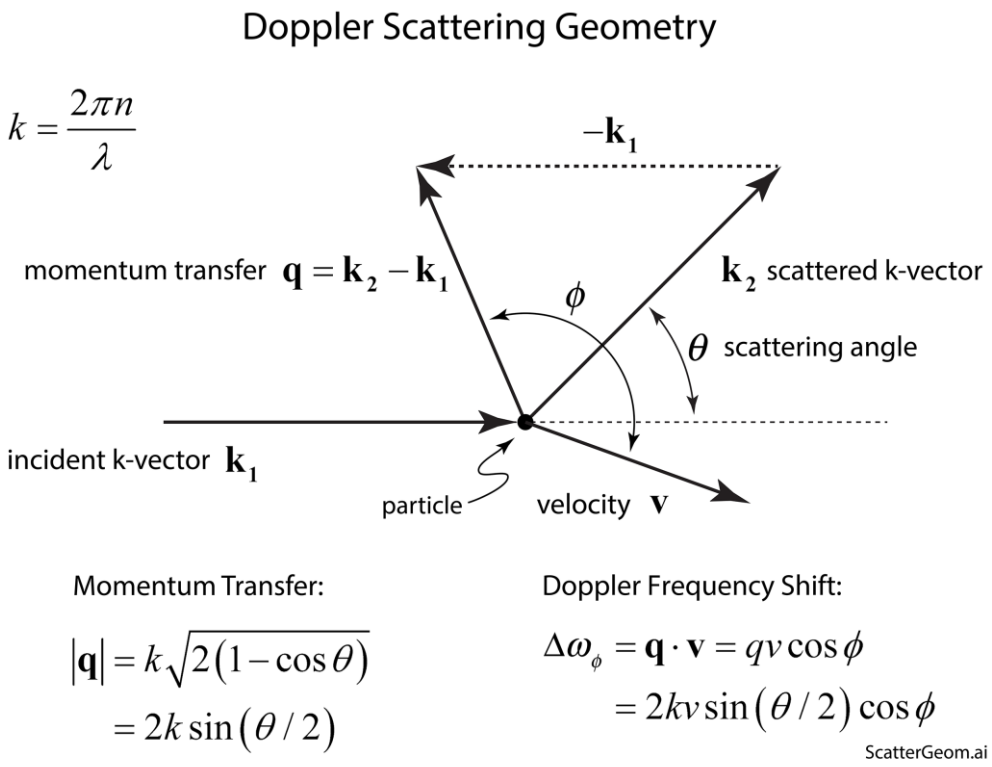

Figure 1-2 Doppler scattering geometry for the incident and scattered *k*-vector, *q*-vector and particle velocity. The scattering angle of the light is θ, and the angle between the *q*-vector and the particle velocity is *v*.

1.3 Living Tissue

1.3.1 Intracellular Transport

Motions inside living cells, and motion of the cells themselves, are ubiquitous signatures of the active processes involved in the maintenance of cellular function and health. Many aspects of cellular function involve active movement driven by energetic processes. Conversely, thermal motions, though participating in subcellular processes such as molecular diffusion and membrane flicker, are physical processes that continue after the death of the cell. Therefore, driven motion is a defining characteristic of living matter. Quantifying the many aspects of active cellular motions

provides a measure of cellular health or a measure of deviation from normal behavior caused by disease or by applied xenobiotics. Cellular dynamics become surrogates that can be used as real-time endogenous reporters in place of nonendogenous fluorophores or end-point measurements [36, 37] when studying how tissues respond to changing environments or to applied therapies.

1.3.2 Size-speed Relation

For cells and subcellular components, a general trend is that the bigger the component is, the slower it moves for most active transport processes (Figure 1-3a). Their corresponding Doppler frequency shifts range from 0.01 Hz to 100 Hz (Figure 1-3b). The rule of thumb is that for wavelength $\lambda = 840$ nm, motion at 1 μm/s corresponds to a Doppler frequency shift of 3 Hz.

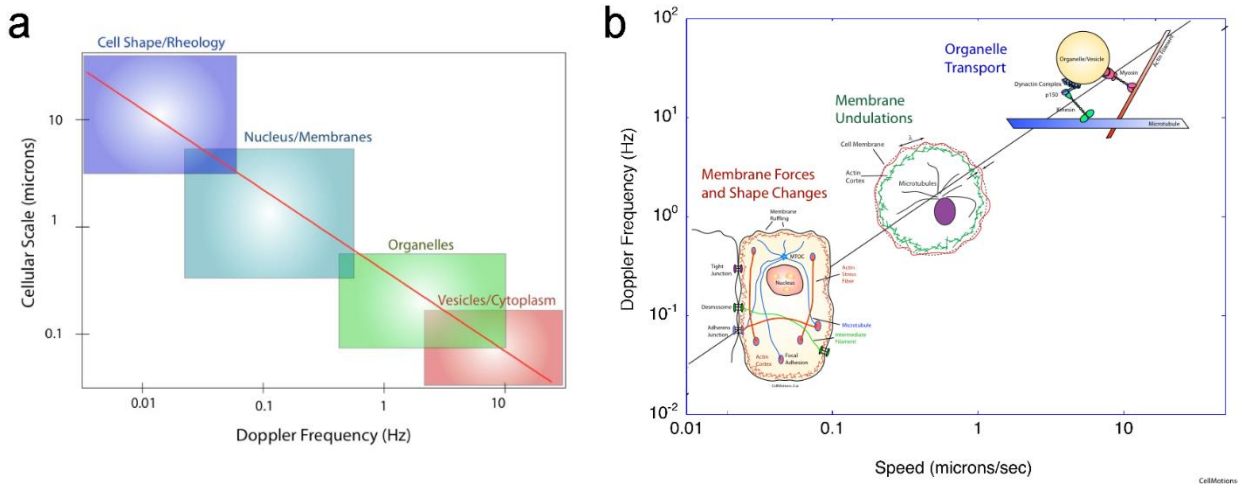

Figure 1-3 a) cellular size – speed relation [38, 39] b) Doppler frequency – cellular speed relation, for wavelength $\lambda = 840$ nm.

1.4 Biodynamic Imaging

1.4.1 Optical Coherence Imaging (OCI)

Biodynamic imaging is capable of measuring objects that have diverse features, from a cell-line tumor spheroid to a USAF test chart and a mouse eye (Figure 1-4).

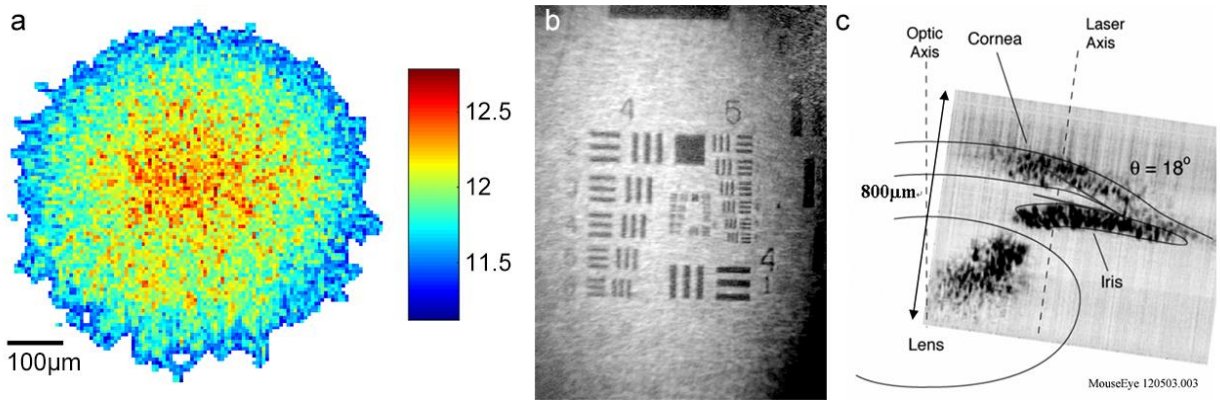

Figure 1-4 a) a DLD-1 tumor spheroid b) USAF test chart c) mouse eye [40]

Biodynamic imaging can do a 3D reconstruction of a sample, and Figure 1-5a) shows the slices of a bone marrow sample every 50 µm, and Figure 1-5b) is a 3D reconstruction of a tumor spheroid.

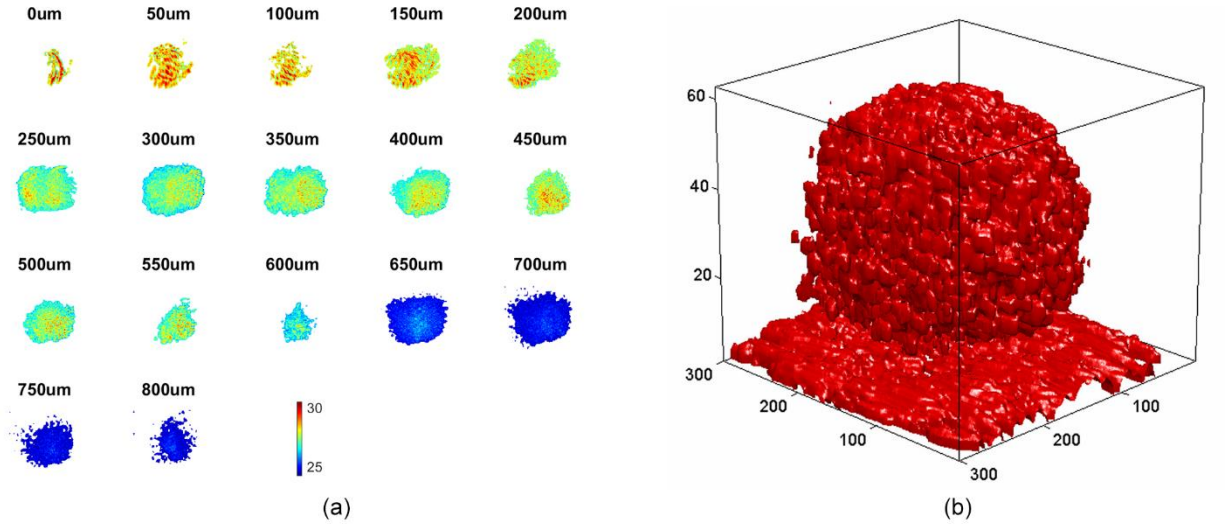

Figure 1-5 a) Slices from the "flythrough" of a bone marrow sample. This sample has a relatively irregular shape and has structures that show up as bright spots in the image. b) 3D reconstruction of a tumor spheroid sample. [40]

1.4.2 Motility Contrast Imaging (MCI)

Motility contrast imaging creates a map of the normalized standard deviation (NSD) for each pixel. NSD is defined as $\frac{\Delta I}{\langle I \rangle}$ for each pixel, where ΔI is the standard deviation and $\langle I \rangle$ is the averaged intensity over time. Figure 1-6 gives an example of how an MCI map of a DLD-1 tumor spheroid changes in response to FCCP, an ionophore that disrupts ATP synthesis [41].

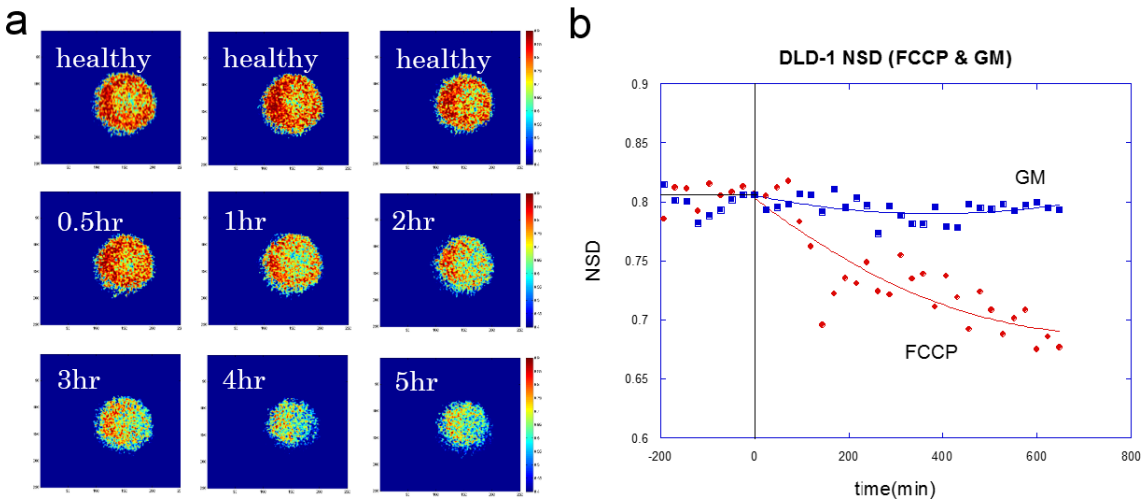

Figure 1-6 a) A change in MCI of a DLD-1 tumor spheroid after FCCP is added. Baseline ("healthy") measurements show an overall NSD > 0.8, and this value gradually decreases over time b) Decrease in overall (i.e. sample averaged) NSD of the DLD-1 tumor spheroid after the FCCP drug, compared with control medium. FCCP, a mitochondrial uncoupling drug that disrupts ATP synthesis, slows down the cellular activity in the DLD-1 spheroid [41].

Heterogeneity in motility is found in some samples and reveals structural information, as shown in Figure 1-7. This also shows the potential of TDSI to be discussed in CHAPTER 6.

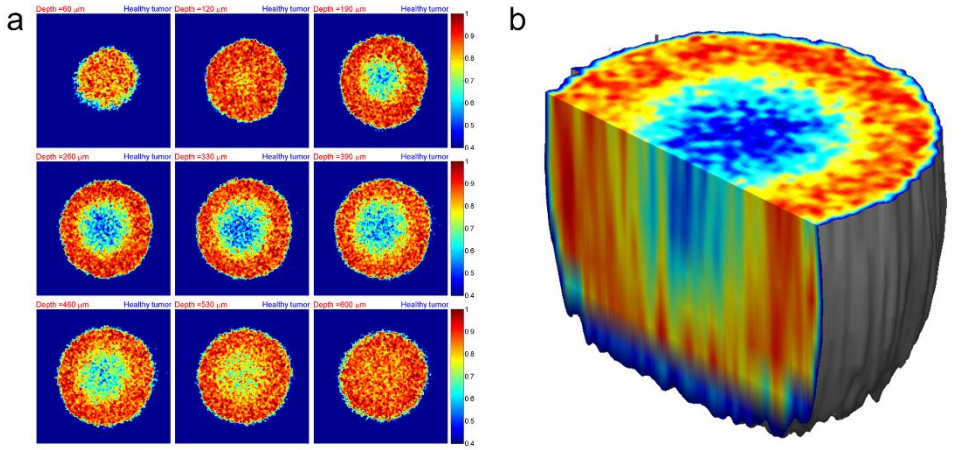

Figure 1-7 MCI maps of a tumor with a 680 μm diameter, with a) 2D slices and b) 3D reconstruction. This sample shows a necrotic core with low activity and a healthy, active shell. [42, 43]

1.4.3 Tissue Dynamics Spectroscopy (TDS)

Frequency-domain decomposition of the light fluctuations using tissue dynamics spectroscopy (TDS) produces broad-band fluctuation spectra that encompass the wide variety of subcellular motions [44, 45]. When pharmaceutical compounds are applied to the tissue, dynamic cellular

processes are perturbed, and these modifications appear as changes in the fluctuation spectra. By applying reference compounds with known mechanisms of action, a library of drug-response spectrograms can be generated against which drug screens may be compared, providing information about the effect of the compound on cellular processes such as necrosis and apoptosis. This type of phenomenological assay is known as a phenotypic profile. Phenotypic profiling has seen a resurgence in recent years as a more systems-based approach to drug discovery and development that captures the complex interplay of cellular processes affected by the drug candidate[46].

The power spectrum of a pixel is calculated as

$$S(x,y;\omega) = \left|\mathrm{FFT}\left(\left|u(x,y;t)\right|^2\right)\right|^2 \tag{1.10}$$

And the power spectrum of an entire sample is the average over all the spectra of the entire sample.

By comparing the power spectrum of a sample after a perturbation relative to the baseline power spectrum of the sample, the time-dependent response of the sample to the perturbation can be determined. A differential spectrogram is defined as

$$\mathrm{d}S(\omega,t) = \log\left[S(\omega,t)\right] - \log\left[S_{\mathrm{base}}(\omega)\right] \tag{1.11}$$

where $S_{\mathrm{base}}(\omega)$ is the baseline spectrum averaged from the last few loops of the baseline measurement. An example of the power spectrum and differential spectrogram is shown in Figure 1-8.

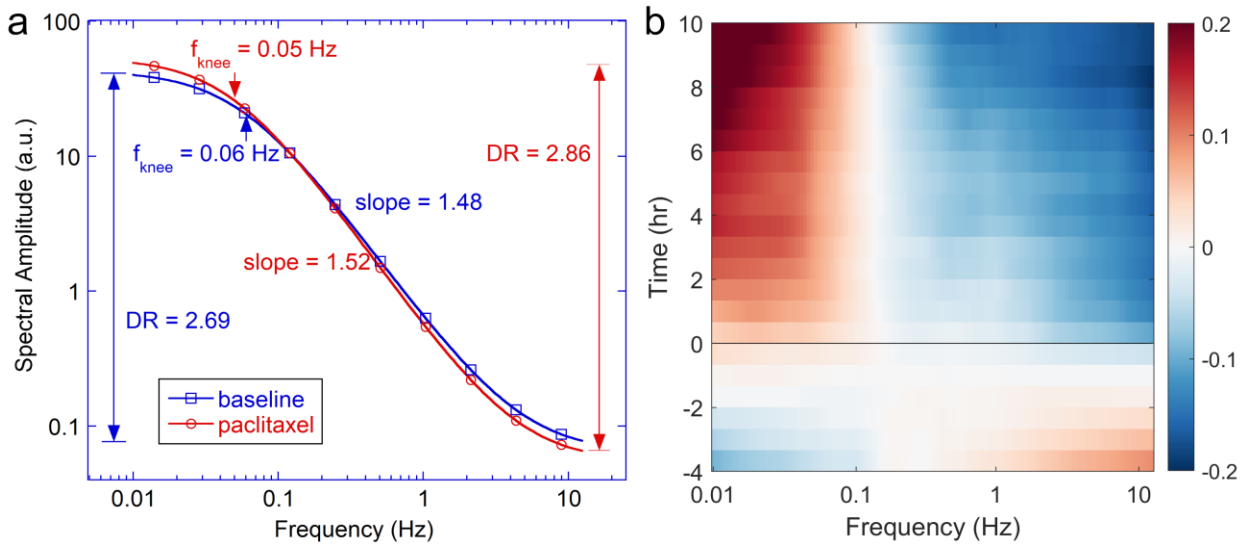

Figure 1-8 Spectra and spectrogram for a DLD-1 tumor spheroid responding to 25μM paclitaxel. a) Spectra of a baseline and drug-treated measurement. The knee of the sample has shifted to a lower frequency. b) Differential spectrogram of the biopsy, showing enhancement in low frequency and suppression in mid-high frequency. Drug was added at *t*=0.

1.4.4 BDI Biomarkers

Biomarkers are created to condense the vast amount of information from OCI, MCI images and TDS spectrograms, and represent them as numerical values. Feature values give characteristic features of sample conditions or responses, and several types of biomarkers are used. The current format contains 40 biomarkers, 4 of which are from OCI, 2 are from MCI, 33 are related to TDS, and one that evaluates data quality. The biomarkers can also be categorized into 4 groups:

- Preconditions, i.e. biomarkers that characterize "basic sample status" in the baseline measurement, including backscatter brightness (BB), overall NSD and knee frequency and Nyquist floor of the spectrum
- Change of precondition biomarkers
- Time-frequency decomposition extracted from spectroscopic response
- Data quality

A vector of 40 numerical biomarker values allows a comprehensive overview of sample conditions and responses. The feature vector is easy and convenient to use when studying sample heterogeneity and drug profiling. A detailed definition of the biomarkers is given in appendix chapter C.1.

References

[1] Z. Yaqoob, J. Fingler, X. Heng, and C. H. Yang, "Homodyne en face optical coherence tomography," Optics Letters **31**, 1815-1817 (2006).

[2] P. Gao, I. Harder, V. Nercissian, K. Mantel, and B. Yao, "Phase-shifting point-diffraction interferometry with common-path and in-line configuration for microscopy," Opt. Lett. **35**, 712-714 (2010).

[3] E. Cuche, F. Bevilacqua, and C. Depeursinge, "Digital holography for quantitative phase-contrast imaging," Optics Letters **24**, 291-293 (1999).

[4] T. Zhang, and I. Yamaguchi, "Three-dimensional microscopy with phase-shifting digital holography," Opt. Lett. **23**, 1221-1223 (1998).

[5] A. Wax, C. H. Yang, R. R. Dasari, and M. S. Feld, "Path-length-resolved dynamic light scattering: modeling the transition from single to diffusive scattering," Applied Optics **40**, 4222-4227 (2001).

[6] K. K. Bizheva, A. M. Siegel, and D. A. Boas, "Path-length-resolved dynamic light scattering in highly scattering random media: The transition to diffusing wave spectroscopy," Physical Review E **58**, 7664-7667 (1998).

[7] J. Evans, W. Gratzer, N. Mohandas, K. Parker, and J. Sleep, "Fluctuations of the red blood cell membrane: Relation to mechanical properties and lack of ATP dependence," Biophys. J **94**, 4134-4144 (2008).

[8] H. Strey, and M. Peterson, "Measurement of Erythrocyte-Membrane Elasticity by Flicker Eigenmode Decomposition," Biophys. J **69**, 478-488 (1995).

[9] K. Tamura, T. Mizutani, H. Haga, and K. Kawabata, "Active fluctuation in the cortical cytoskeleton observed by high-speed live-cell scanning probe microscopy," Acta Biomaterialia **7**, 3766-3772 (2011).

[10] T. Betz, M. Lenz, J.-F. Joanny, and C. Sykes, "ATP-dependent mechanics of red blood cells," Proceedings of the National Academy of Sciences of the United States of America **106**, 15320-15325 (2009).

[11] X. L. Nan, P. A. Sims, and X. S. Xie, "Organelle tracking in a living cell with microsecond time resolution and nanometer spatial precision," Chemphyschem **9**, 707-712 (2008).

[12] V. Racine, M. Sachse, J. Salamero, V. Fraisier, A. Trubuil, and J. B. Sibarita, "Visualization and quantification of vesicle trafficking on a three-dimensional cytoskeleton network in living cells," Journal Of Microscopy-Oxford **225**, 214-228 (2007).

[13] N. A. Brazhe, A. R. Brazhe, A. N. Pavlov, L. A. Erokhova, A. I. Yusipovich, G. V. Maksimov, E. Mosekilde, and O. V. Sosnovtseva, "Unraveling cell processes: Interference imaging interwoven with data analysis," Journal of Biological Physics **32**, 191-208 (2006).

[14] B. Trinczek, A. Ebneth, and E. Mandelkow, "Tau regulates the attachment/detachment but not the speed of motors in microtubule-dependent transport of single vesicles and organelles," Journal of Cell Science **112**, 2355-2367 (1999).

[15] N. Ji, D. E. Milkie, and E. Betzig, "Adaptive optics via pupil segmentation for high-resolution imaging in biological tissues," Nature Methods **7**, 141 (2009).

[16] B. Das, N. S. Bisht, R. V. Vinu, and R. K. Singh, "Lensless complex amplitude image retrieval through a visually opaque scattering medium," Appl Opt **56**, 4591-4597 (2017).

[17] J. Bertolotti, E. G. van Putten, C. Blum, A. Lagendijk, W. L. Vos, and A. P. Mosk, "Non-invasive imaging through opaque scattering layers," Nature **491**, 232-234 (2012).

[18] O. Katz, P. Heidmann, M. Fink, and S. Gigan, "Non-invasive single-shot imaging through scattering layers and around corners via speckle correlations," Nature Photonics **8**, 784-790 (2014).
[19] E. Edrei, and G. Scarcelli, "Optical imaging through dynamic turbid media using the Fourier-domain shower-curtain effect," Optica **3**, 71-74 (2016).
[20] A. S. Somkuwar, B. Das, R. V. Vinu, Y. Park, and R. K. Singh, "Holographic imaging through a scattering layer using speckle interferometry," J Opt Soc Am A Opt Image Sci Vis **34**, 1392-1399 (2017).
[21] K. T. Takasaki, and J. W. Fleischer, "Phase-space measurement for depth-resolved memory-effect imaging," Opt Express **22**, 31426-31433 (2014).
[22] H. Y. Liu, E. Jonas, L. Tian, J. Zhong, B. Recht, and L. Waller, "3D imaging in volumetric scattering media using phase-space measurements," Opt Express **23**, 14461-14471 (2015).
[23] E. M. Buckley, A. B. Parthasarathy, P. E. Grant, A. G. Yodh, and M. A. Franceschini, "Diffuse correlation spectroscopy for measurement of cerebral blood flow: future prospects," Neurophotonics **1** (2014).
[24] B. Yu, A. Shah, V. K. Nagarajan, and D. G. Ferris, "Diffuse reflectance spectroscopy of epithelial tissue with a smart fiber-optic probe," Biomed. Opt. Express **5**, 675-689 (2014).
[25] A. H. Hielscher, A. Y. Bluestone, G. S. Abdoulaev, A. D. Klose, J. Lasker, M. Stewart, U. Netz, and J. Beuthan, "Near-Infrared Diffuse Optical Tomography," Disease Markers **18** (2002).
[26] A. F. Fercher, W. Drexler, C. K. Hitzenberger, and T. Lasser, "Optical coherence tomography - principles and applications," Rep. Prog. Phys **66**, 239 (2003).
[27] J. F. de Boer, C. K. Hitzenberger, and Y. Yasuno, "Polarization sensitive optical coherence tomography - a review [Invited]," Biomed Opt Express **8**, 1838-1873 (2017).
[28] M. Pircher, C. K. Hitzenberger, and U. Schmidt-Erfurth, "Polarization sensitive optical coherence tomography in the human eye," Progress in Retinal and Eye Research **30**, 431-451 (2011).
[29] R. A. Leitgeb, R. M. Werkmeister, C. Blatter, and L. Schmetterer, "Doppler optical coherence tomography," Prog Retin Eye Res **41**, 26-43 (2014).
[30] A. Dubois, and A. C. Boccara, "Full-Field Optical Coherence Tomography," in *Optical Coherence Tomography: Technology and Applications*, W. Drexler, and J. G. Fujimoto, eds. (Springer Berlin Heidelberg, 2008), pp. 565-591.
[31] Y. Zhao, K. K. Chu, W. J. Eldridge, E. T. Jelly, M. Crose, and A. Wax, "Real-time speckle reduction in optical coherence tomography using the dual window method," Biomed. Opt. Express **9**, 616 (2018).
[32] M. Szkulmowski, I. Gorczynska, D. Szlag, M. Sylwestrzak, A. Kowalczyk, and M. Wojtkowski, "Efficient reduction of speckle noise in Optical Coherence Tomography," Opt. Express **20**, 1337-1359 (2012).
[33] E. Götzinger, M. Pircher, B. Baumann, T. Schmoll, H. Sattmann, R. A. Leitgeb, and C. K. Hitzenberger, "Speckle noise reduction in high speed polarization sensitive spectral domain optical coherence tomography," Opt. Express **19**, 14568-14584 (2011).
[34] J. W. Goodman, *Speckle Phenomena in Optics* (2006).
[35] J. W. Goodman, *Introduction to Fourier Optics* (MaGraw-Hill, 1996).
[36] D. Merrill, R. An, H. Sun, B. Yakubov, D. Matei, J. Turek, and D. Nolte, "Intracellular Doppler Signatures of Platinum Sensitivity Captured by Biodynamic Profiling in Ovarian Xenografts," Sci Rep **6**, 18821 (2016).

[37] M. R. Custead, R. An, J. J. Turek, G. E. Moore, D. D. Nolte, and M. O. Childress, "Predictive value of ex vivo biodynamic imaging in determining response to chemotherapy in dogs with spontaneous non-Hodgkin's lymphomas: a preliminary study," Converg. Sci. Phys. Oncol **1**, 015003 (2015).
[38] A. Leal-Egaña, G. Letort, J.-L. Martiel, A. Christ, T. Vignaud, C. Roelants, O. Filhol, and M. Théry, "The size-speed-force relationship governs migratory cell response to tumorigenic factors," Molecular Biology of the Cell **28**, 1612-1621 (2017).
[39] U. H. Lodish, H. Lodish, A. Berk, J. E. Darnell, C. A. Kaiser, C. Kaiser, U. C. A. Kaiser, M. Krieger, M. P. Scott, and A. Bretscher, *Molecular Cell Biology* (W. H. Freeman, 2008).
[40] K. Jeong, "Holographic Optical Coherence Imaging of Living Tissue," (Purdue University, 2007).
[41] H. Sun, "Dynamic Holography in Semiconductors and Biomedical Optics," (Purdue University, 2016).
[42] K. Jeong, J. J. Turek, and D. D. Nolte, "Fourier-domain digital holographic optical coherence imaging of living tissue," Appl. Opt. **46**, 4999-5008 (2007).
[43] K. Jeong, J. J. Turek, and D. D. Nolte, "Volumetric motility-contrast imaging of tissue response to cytoskeletal anti-cancer drugs," Opt. Express **15**, 14057-14064 (2007).
[44] D. D. Nolte, R. An, J. Turek, and K. Jeong, "Tissue dynamics spectroscopy for phenotypic profiling of drug effects in three-dimensional culture," Biomed. Opt. Express **3**, 2825-2841 (2012).
[45] K. Jeong, J. J. Turek, and D. D. Nolte, "Speckle fluctuation spectroscopy of intracellular motion in living tissue using coherence-domain digital holography," J. Biomed. Opt **15**, 030514 (2010).
[46] J. A. Lee, and E. L. Berg, "Neoclassic drug discovery: the case for lead generation using phenotypic and functional approaches," J Biomol Screen **18**, 1143-1155 (2013).

CHAPTER 2. DOPPLER FLUCTUATION SPECTROSCOPY OF INTRACELLULAR DYNAMICS IN LIVING TISSUE

Intracellular dynamics in living tissue are dominated by active transport driven by bioenergetic processes far from thermal equilibrium. This chapter discusses the "persistent walk" model of intracellular constituents, and analytically derives the dynamic light scattering from transport in the ballistic, diffusive or the cross-over regimes. The theory is validated through Monte Carlo simulations. Experimental evidence for the Doppler edge in 3D living tissue is obtained using BDI.[1]

2.1 Introduction

Motions in two-dimensional cell culture are easily observed under a microscope as physical displacements. Adaptive optics combined with light sheet microscopy and lattice light sheet microscopy can achieve 3D *in vivo* aberration-free imaging of subcellular processes [1, 2]. However, dynamic light scattering (DLS) and Doppler fluctuation spectroscopy are better suited for ensemble measurements of a broad range of intracellular motions across a wide field of view. These ensemble techniques are sensitive to motion changes and can be used to monitor cellular health, disease progression and drug response. Spatial localization in DLS in tissue can be achieved with low coherence [3-5], including dynamic signals observed in OCT and OCI.

This chapter focuses on lifetime-broadened Doppler scattering from persistent walks. We present evidence that shows Doppler fluctuation spectra from midsections of 3D cultured tissues as the sum of active intracellular processes with long persistence distances, i.e. in the ballistic regime, which is consistent with findings from motion tracking within 2D tissues. The model is based on random walks with a simple exponential distribution of free path lengths, where a particle walks at a constant velocity along a mean-free path. This "piecewise continuous random walk" model leads to a temporal cross-over from ballistic transport at short time scales to diffusive transport at long time scales. The approach is fully statistical, without resolving individual scattering objects, by restricting the analysis to ensembles of actively transporting subcellular constituents. The

[1] Content from this chapter has been published in Z Li, H Sun, J Turek, S Jalal, M Childress, and DD Nolte, Doppler fluctuation spectroscopy of intracellular dynamics in living tissue, J. Opt. Soc. Am. A 36, 665 (2019).

theory of light scattering from random walks is developed for field-based heterodyne detection. Transport in the ballistic, diffusive and cross-over regime is described analytically, including the derivation of autocorrelation functions in the two limits and an effective driven damped harmonic oscillator model for persistent walks in the cross-over regime. The theory is validated by Monte Carlo simulations. Experimental measurements of Doppler fluctuation spectra, obtained using tissue dynamics spectroscopy on living tissue culture and living cancer biopsies are presented, followed by a general discussion of the potential applicability of Doppler fluctuation spectroscopy for drug screening.

2.2 Models

2.2.1 Persistent Walk

Many biological applications proceed via active persistent walks that have persistent motions of relatively uniform speed v_0 travelling a mean-free length (also known as the persistence length) L_p in a mean-free time t_p (also known as the persistence time) before changing direction or speed. Persistent walks have two opposite limiting behaviors. When the persistence time is much longer than an observation time, then the transport can be viewed as an ensemble of ballistically transported objects. This is the ballistic limit. When the persistence time is much shorter than an observation time, then the transport approaches a Wiener process. The Wiener process has a path that is nowhere differentiable [6]. This is the diffusion limit, although, in the case of active media, it is active diffusion that significantly exceeds thermal Brownian motion. The ballistic limit and the diffusion limit have well-recognized properties in terms of dynamic light scattering. However, many biological transport processes occur in the cross-over regime between these extremes.

The key parameters characterizing the walks are the mean-squared speed during the free runs and the mean-free time between changes in speed or direction. A model that describes this process of free runs with mean persistence times is called the Ornstein-Uhlenbeck process [6] given by

$$dv = -\gamma v dt + \Gamma dW_t \tag{2.1}$$

for one-dimensional transport, where $1/\gamma = t_p$ is the persistence time, Γ is the amplitude of the fluctuations, and dW_t is a Wiener process of unit variance. Setting $x(0) = 0$, the associated position process is described by

$$x(t) = \frac{v_0}{\gamma}\left[1 - \exp(-\gamma t)\right] + \Gamma \int_0^t \mathrm{d}t' \exp(-\gamma t') \int_0^{t'} \mathrm{d}W_{t''} \exp(\gamma t'') \tag{2.2}$$

The mean-squared displacement (MSD) for quasi-ballistic transport in 1D is

$$\left\langle x^2(t) \right\rangle = \frac{\Gamma^2}{\gamma^2} t + \frac{v_0^2}{\gamma^2}\left[1 - \exp(-\gamma t)\right]^2 - \frac{\Gamma^2}{2\gamma^3}\left[3 - 4\exp(-\gamma t) + \exp(-2\gamma t)\right] \tag{2.3}$$

where v_0 is the molecular motor speed. In the long-time limit, this is

$$\left\langle x^2(t) \right\rangle = \frac{\Gamma^2}{\gamma^2} t = 2v_0^2 t_p t = 2Dt \tag{2.4}$$

where the effective diffusion coefficient is $D = v_0^2 t_p$ related to the speed and the persistence time, but unrelated to temperature or thermal processes. The relationship in Eq. (2.4) establishes the fluctuation-dissipation theorem for active transport

$$\Gamma^2 t_p = 2v_0^2 \tag{2.5}$$

that relates the persistence time and speed to the magnitude of the fluctuations. Based on this relation, the MSD in Eq. (2.3) is expressed in terms of the mean-free path length $L_p = v_0 t_p$ as

$$\left\langle x^2(t) \right\rangle = 2L_p^2 \frac{t}{t_p} - 2L_p^2 \left[1 - \exp\left(-\frac{t}{t_p}\right)\right] \tag{2.6}$$

The MSD is plotted in Figure 2-1 for several values of mean-free path. At short times, the MSD grows as the square of time, which is representative of ballistic transport, while for time $t > 2t_p$ the MSD grows linearly in time, which is representative of diffusive transport. Therefore, the MSD displays a temporal transition from ballistic to diffusive transport depending on the observation time relative to persistence time.

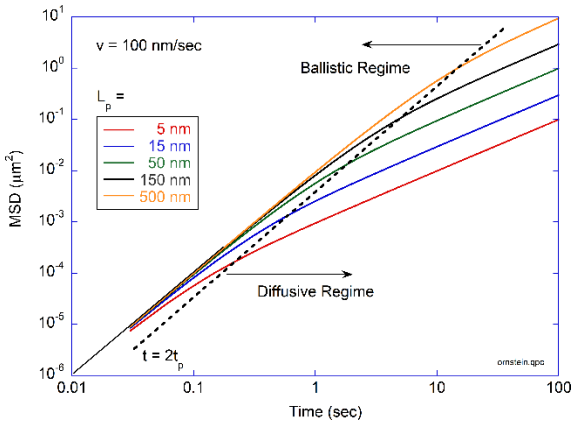

Figure 2-1 Average mean-squared displacement as a function of time for an Ornstein-Uhlenbeck process for a family of L_p values with a fixed speed of 100 nanometers per second. The transition from the ballistic to the diffusion regime occurs at $t = 2t_p$ along the dashed line.

2.2.2 Doppler Number

The co-linear Doppler frequency shift ω_D and the persistence time t_p (and equivalently the momentum transfer q and the mean free path L_p) from dynamic light scattering (1.2.6) set a dimensionless scaling parameter that divides the ballistic transport regime from the diffusive regime. The dimensionless parameter is called the Doppler number, or N_D, given by

$$N_D = \omega_D t_p = qL_p \tag{2.7}$$

The characteristic scale is set when

$$N_D = \frac{L_p}{\lambda_{\text{red}}} = 1 \tag{2.8}$$

which is defined in terms of the reduced wavelength as

$$\lambda_{\text{red}} = \frac{\lambda_0}{4\pi n} \approx 50 \text{ nm} \tag{2.9}$$

for a refractive index $n \approx 1.35$ and a free-space wavelength $\lambda_0 = 840$ nm. Therefore, the dividing line between diffusive transport and ballistic transport occurs when the mean-free path is greater than approximately 50 nm. The conditions on the N_D for the different regimes are

$$N_D > 3 \quad \text{Doppler Regime}$$
$$N_D < \frac{1}{3} \quad \text{Diffusion Regime} \tag{2.10}$$

although the division is not sharp. Doppler effects dominate when $N_D > 3$, and diffusion effects dominate when $N_D < 0.3$. Most active transport processes in cells have mean-free paths larger than the reduced wavelength, placing most active subcellular processes in the Doppler regime (see next section).

2.2.3 Processive Motion in Biological Processes

Active intracellular transport is processive, meaning that motion persists for multiple cycles of ATP or GTP hydrolysis [7]. For molecular motors, the step length is fixed at δ_{ATP} per hydrolysis (e.g. for kinesin $\delta_{\text{ATP}} = 8$ nm [8]), with a mean value of n steps before the motor detaches. The mean-free path for the persistent motion is then $\Delta = n\delta_{\text{ATP}}$. Likewise, for cytoskeletal restructuring, periods of protrusion are interspersed with periods of retraction, with characteristic mean-free lengths. Examples of intracellular dynamics, speeds and lengths are given in Table 2-1 for a variety of motions under a variety of conditions [8-19]. For these processes, the Doppler frequency depends on the observation wavelength and observation direction. The Doppler frequencies in Table 2-1 are calculated for a backscattering configuration using a free-space wavelength of $\lambda_0 = 840$ nm. Speeds range from several microns per second (organelles or vesicles carried by molecular motors) to several nanometers per second (cell membranes driven by cytoskeletal processes). The corresponding Doppler frequencies (maximum frequencies in a backscatter configuration) are tens of Hz to tens of mHz. The mean Doppler frequency (averaged over many cellular volumes in living tissue) is zero because transport is isotropically averaged over all directions. For processive motions associated with kinesin, dynein, myosin V, cytoskeleton restructuring, and filopodia and lamellipodia, the Doppler numbers in Table 2-1 are greater than unity and can range into the hundreds. Therefore, processive motors and cytoskeletal restructuring are in the Doppler regime. An interesting case is for kinesin/dynein complexes, which are engaged in a tug-of-war transporting vesicles in alternating directions on the microtubules. The N_D is smallest for this case in Table 2-1 and is in the cross-over regime.

Table 2-1 Speeds, Doppler Frequencies and Mean Free Path Lengths

Motor or polymerization	Speed	Doppler Frequency Shift	Distance or Time	$\omega_D t_p$ or qL_p	Ref
Kinesin	2 μm/sec	6 Hz			[9]
Kinesin	1 μm/s	3 Hz		15	[8]
Kinesin	800 nm/s	2.7 Hz			[10, 11]
Kinesin	1 μm/s	3 Hz	10 sec	200	[12]
Kinesin			1 micron	20	[13]
Kinesin	1 μm/s	3 Hz	600 nm	10	[14]
Kinesin/Dynein	800 nm/s	2.7 Hz	100 nm - 300 nm	2 - 6	[15]
Dynein/Dynactin	700 nm/sec	2.1 Hz	1	20	[20]
Myosin V	300 nm/s	1 Hz	1.6 microns	30	[16]
ParA/ParB	100 nm/s	0.3 Hz	2 microns	40	[17]
Actin network polymerization	5 nm/s	0.02 Hz			[18]
Tubulin polymerization	20 nm/s – 300 nm/s	0.07 – 1 Hz	300 sec	15-100	[19]
Filopodia extending	40 nm/s	0.12 Hz	130 sec	100	[21]
Filopodia retracting	10 nm/s	0.03 Hz	100 sec	20	[21]

2.2.4 Light Scattering from Persistent Walks

The transport of vesicles and organelles provide the simplest example of dynamic light scattering from persistent walks. Vesicles and most organelles are much smaller than a wavelength of light and hence represent point scattering objects in motion. In addition, the transport of vesicles and organelles is driven actively. In this section, we describe two ideal models of organelle transport. The first model is constrained and consists of organelles moving on one-dimensional filaments or microtubules. The orientation of these one-dimensional tracks is distributed uniformly in three dimensions. The second model assumes a persistent walk in 3D that is unconstrained. An interesting result of these two models is their non-equivalence: isotropic 3D walks produce different Doppler fluctuation spectra than isotropically distributed 1D walks. These two models can be evaluated in both the extreme limit of very short persistence time (diffusion limit) and the

limit of very long persistence time (ballistic limit). The intermediate regime can be approximated by a distribution of lifetime-broadened Doppler spectra to be discussed in the following section.

In dynamic light scattering, coherent speckle is a superposition of the individual partial waves from the individual scattering sources that are in motion. The statistical fluctuations in the speckle intensity are captured by a field autocorrelation function that is obtained as a stochastic sum evaluated using an integral over a probability distribution [22]

$$\begin{aligned} A_E(\tau) &= \left\langle E^*(0)E(\tau)\right\rangle \\ &= E_0^2 + NI_s\int_{-\infty}^{\infty} P(\Delta x)\exp(-\mathrm{i}\mathbf{q}\cdot\boldsymbol{\Delta}\mathbf{x})\mathrm{d}\Delta x \end{aligned} \tag{2.11}$$

where E_0 is the reference field magnitude, and the field autocorrelation is proportional to the Fourier transform of the probability functional [23]. Eq. (2.11) is the field-based autocorrelation that would be equivalent to phase-sensitive detection in a dynamic light scattering experiment. There is also an intensity-based autocorrelation function given by

$$\begin{aligned} A_I(t) &= \left\langle I^*(0)I(t)\right\rangle \\ &= N^2I_s^2 + N^2I_s^2\left|\int P(\Delta x)\exp(-\mathrm{i}\mathbf{q}\cdot\boldsymbol{\Delta}\mathbf{x})\mathrm{d}\Delta x\right|^2 \end{aligned} \tag{2.12}$$

Field-based autocorrelation is linear in multiple underlying dynamical processes that contribute to the field fluctuations, making interpretations of underlying processes simpler compared with intensity-based autocorrelation. However, the most stable form of fluctuation spectroscopy performed experimentally is with intensity-based detection, because it is less sensitive to mechanical disturbance than the field-based detection (phase-sensitive detection). In the discussion below, field-based descriptions will be used when treating multiple dynamical processes. Intensity-based descriptions will be used for experimental studies and for pure theoretical cases with simple limiting behavior when persistent walks along isotropically-oriented filaments or microtubules are driven by molecular motors that run at approximately constant speeds but with a distribution of persistence times. There are three limiting cases: (1) diffusive motion in 1D, (2) diffusive motion in 3D, and (3) ballistic motion. In all three cases, the motion is averaged isotropically over all angles.

1D Isotropically-averaged Diffusion Limit

One-dimensional isotropic transport is a model for which particles are confined in one direction, with both positive and negative excursions along a line, while the direction is distributed isotropically in 3D. The distribution function for one-dimensional motion is [6]

$$P(\Delta x) = \frac{1}{\sqrt{4\pi Dt}} \exp(-\Delta x^2 / 4Dt) \tag{2.13}$$

The isotropic intensity autocorrelation function can be written as

$$\begin{aligned} A_I(t) &= N^2 I_s^2 + N^2 I_s^2 \left(\frac{1}{4\pi} \iint P(\Delta x) \exp(-\mathrm{i} q \Delta x \cos\theta) \mathrm{d}\Delta x \mathrm{d}\Omega \right)^2 \\ &= N^2 I_s^2 + N^2 I_s^2 \left(\frac{1}{2} \int \exp(-q^2 Dt \cos^2\theta) \sin\theta \mathrm{d}\theta \right)^2 \\ &= N^2 I_s^2 + N^2 I_s^2 \frac{\pi}{4q^2 Dt} \mathrm{erf}^2 \left(\sqrt{q^2 Dt} \right) \end{aligned} \tag{2.14}$$

The autocorrelation function behaves as the error function with the characteristic time $1/q^2D$.

3D Diffusion Limit

Three-dimensional isotropic transport is the model for which particles are free in 3 dimensions. The distribution function of the three-dimensional isotropic motion is

$$P(\Delta r) = \left(\frac{1}{\sqrt{4\pi Dt}} \right)^3 \exp(-\Delta x^2 / 4Dt) \exp(-\Delta y^2 / 4Dt) \exp(-\Delta z^2 / 4Dt) \tag{2.15}$$

The intensity autocorrelation function is

$$\begin{aligned} A_I(t) &= N^2 I_s^2 + N^2 I_s^2 \left(\iiint_{\Delta r} P(\Delta x) \mathrm{d}\Delta x P(\Delta y) \mathrm{d}\Delta y P(\Delta z) \exp(-\mathrm{i} q \Delta z) \mathrm{d}\Delta z \right)^2 \\ &= N^2 I_s^2 + N^2 I_s^2 \exp(-2q^2 Dt) \end{aligned} \tag{2.16}$$

The autocorrelation function is an exponential equation, and the characteristic time is $1/q^2D$ that is the same as for the one-dimensional isotropic model. The spectral density, calculated using the Wiener-Khinchin theorem, is

$$S(\omega) = FT\left[A_I(t)\right](\omega) = \sqrt{2\pi}N^2 I_s^2\left[\delta(\omega) + \frac{1}{\pi}\frac{2q^2D}{\left(2q^2D\right)^2 + \omega^2}\right] \tag{2.17}$$

The second term in the spectral density is a typical Lorentzian function. In the low- and high-frequency limits, these are

$$S(\omega) = \begin{cases} \dfrac{\sqrt{\dfrac{2}{\pi}}N^2 I_s^2}{2q^2D} = \text{const}, & \omega \ll 2q^2D \\ \dfrac{2\sqrt{\dfrac{2}{\pi}}N^2 I_s^2 q^2 D}{\omega^2} \propto \omega^{-2}, & \omega \gg 2q^2D \end{cases} \tag{2.18}$$

1D and 3D Isotropic Ballistic Limit

In the ballistic limit of long persistence time, the three-dimensional ballistic transport model is identical to isotropically distributed 1D transport, so they share the same limit. The displacement is $\Delta r = vt$, and the distribution function for this type of motion is

$$P(\Delta r) = \delta(\Delta r - vt) \tag{2.19}$$

The intensity autocorrelation function is

$$\begin{aligned} A_I(t) &= N^2 I_s^2 + N^2 I_s^2 \sum_{i\neq j}\sum_j \exp(-\mathrm{i}qvt\cos\theta_i)\exp(\mathrm{i}qvt\cos\theta_j) \\ &= N^2 I_s^2 + N^2 I_s^2\left(\frac{1}{4\pi}\int \exp(-\mathrm{i}qvt\cos\theta)\mathrm{d}\Omega\right)^2 \\ &= N^2 I_s^2 + N^2 I_s^2 \mathrm{sinc}^2(qvt) \end{aligned} \tag{2.20}$$

where the oscillatory sinc function arises from the ballistic Doppler frequency. The spectral density is

$$S(\omega) = FT\left[A_I(t)\right](\omega) = \sqrt{2\pi}N^2 I_s^2\left[\delta(\omega) + \frac{1}{2qv}\mathrm{tri}\left(\frac{\omega}{2qv}\right)\right] \tag{2.21}$$

where $\mathrm{tri}(x)$ is the triangular function.

Information contained within the autocorrelation function is contained equivalently within the spectral power density, but when there are many subensembles contributing to the dynamic light scattering, and the characteristic time scales are widely separated across several orders of magnitude, the fluctuation spectrum is a more "natural" representation than the autocorrelation by separating processes according to their respective characteristic frequencies. For instance, when the subcellular transport is quasi-ballistic, the fluctuation frequencies of the fluctuation spectra are closely related to the Doppler frequencies of the moving scatterers. Doppler fluctuation power spectra, even in the homogeneous case, have no spectral peak, but are fluctuation spectra with zero mean frequency and characteristic "edge" or "knee" frequencies, as shown in Figure 2-2(a) for the three limiting cases: ballistic, 3D diffusion, and isotropic 1D diffusion. On a logarithmic frequency scale, the diffusive fluctuation spectra show a characteristic "roll-off" of a Lorentzian lineshape of zero mean frequency, while the ballistic spectrum displays a "Doppler edge" above which the fluctuation spectral power density drops rapidly.

Intermediate Cross-Over Regime

Between the diffusive and the ballistic limits is the cross-over regime when $N_D \approx 1$, with the mean free path L_p in the range of 50 nm for a wavelength at 840 nm in the infrared using a backscattering optical configuration. The cross-over regime, with significant deviations from the ideal limits, is relatively wide, with the mean free path spanning from approximately 20 nanometers to a fifth of a micrometer.

An ensemble of N particles executing persistent walks with an exponential distribution of persistence time t_p, inclined at angle ϕ, and with no discontinuous phase jumps between walk segments, produce a characteristic damped-harmonic oscillator power spectrum with a lineshape given by

$$S_E(\omega,\phi) = 2N\pi^2 \frac{\omega_\phi^2 \gamma}{\left(\omega^2 - \omega_\phi^2\right)^2 + \omega^2\gamma^2} \tag{2.22}$$

where the damping factor is inversely related to the mean persistence time t_p through $\gamma t_p = 1$. In an isotropic tissue, the colinearity angles are distributed as

$$P(\phi)\,\mathrm{d}\phi = \sin\phi \mathrm{d}\phi \tag{2.23}$$

For a distribution of Doppler frequencies ω_ϕ caused by the distribution of angles, the increment to the fluctuation power spectrum is

$$\begin{aligned} \mathrm{d}S_E(\omega) &= L(\omega,\phi)\,P(\phi)\,\mathrm{d}\phi \\ &= \frac{\gamma N}{\pi}\left[\frac{\omega_D^2\cos^2\phi}{\left(\omega_D^2\cos^2\phi-\omega^2\right)^2+\omega^2\gamma^2}\right]\sin\phi\mathrm{d}\phi \end{aligned} \tag{2.24}$$

For the frequency distribution from an isotropic tissue, the total power spectrum is integrated over all Doppler frequencies as

$$\begin{aligned} S_E(\omega) &= \frac{\gamma\omega_D^2 N}{\pi}\int_0^\pi\left[\frac{\cos^2\phi}{\left(\omega_D^2\cos^2\phi-\omega^2\right)^2+\omega^2\gamma^2}\right]\sin\phi\mathrm{d}\phi \\ &= \frac{\gamma N}{\pi\omega_D}\int_{-\omega_D}^{\omega_D}\left[\frac{y^2}{\left(y^2-\omega^2\right)^2+\omega^2\gamma^2}\right]\mathrm{d}y \\ &= \frac{\gamma N}{\pi\omega_D}\frac{1}{\sqrt{2\left(\sqrt{\omega^4+\omega^2\gamma^2}-\omega^2\right)}}\left[\arctan\frac{\omega_D-\frac{\sqrt{\omega^4+\omega^2\gamma^2}}{\omega_D}}{\sqrt{2\left(\sqrt{\omega^4+\omega^2\gamma^2}-\omega^2\right)}}+\frac{\pi}{2}\right] \\ &\quad+\frac{1}{2\sqrt{2\left(\sqrt{\omega^4+\omega^2\gamma^2}+\omega^2\right)}}\ln\frac{\omega_D+\frac{\sqrt{\omega^4+\omega^2\gamma^2}}{\omega_D}-\sqrt{2\left(\sqrt{\omega^4+\omega^2\gamma^2}+\omega^2\right)}}{\omega_D+\frac{\sqrt{\omega^4+\omega^2\gamma^2}}{\omega_D}+\sqrt{2\left(\sqrt{\omega^4+\omega^2\gamma^2}+\omega^2\right)}} \end{aligned} \tag{2.25}$$

Examples of isotropically-averaged 1D motion are shown in Figure 2-2(b) for Doppler numbers N_D = 0.1, 1, and 10. The dashed curves are for unidirectional 1D motion, showing a clear Doppler peak at $f_D = 1\,\mathrm{Hz}$ for $\omega_D t_p = 10$. In the $\omega_D t_p = 0.1$ case, there is a diffusion knee at $f_d = q^2 v_0^2 \tau / 2\pi \approx 0.1\,\mathrm{Hz}$. The cross-over regime is captured when $\omega_D t_p = 1$. The isotropic averaging produces a fluctuation spectrum that has no peak at the Doppler frequency, even in the case of large N_D, although there is a distinct edge at the Doppler frequency for this case. When the Doppler number is small, a diffusive knee structure emerges at lower frequencies.

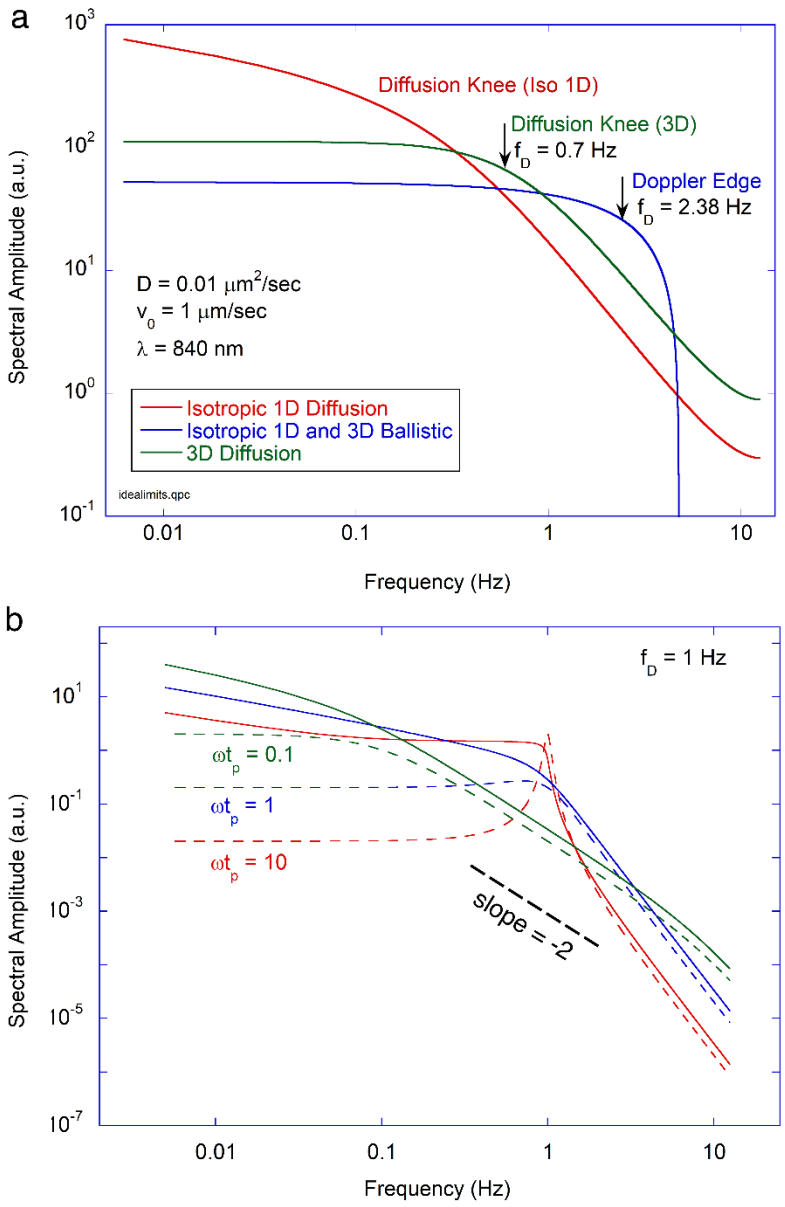

Figure 2-2 (a) Fluctuation spectra for three limiting cases: Isotropic 1D diffusion, 3D diffusion and the ballistic case averaged isotropically over all angles. A diffusion coefficient is used for the first two cases, and a uniform velocity is applied to the last case. (b) Comparison of unidirectional (dashed) versus isotropically averaged 1D (solid) power spectra when the N_D = 0.1, 1, and 10.

The cross-over behavior from the Doppler regime to the diffusion regime is described in terms of a knee frequency, which is a function of diffusion and ballistic frequencies and persistence time

$$\omega_{\text{knee}} = \frac{\omega_D^2}{\sqrt{1/t_p^2 + \omega_D^2}} = \frac{\omega_{\text{diffusion}}}{\sqrt{1+\omega_D^2 t_p^2}} \tag{2.26}$$

For long persistence times t_p, the knee frequency is a Doppler edge that is associated with a slope < -2, while for short persistence times, the knee frequency is the diffusive roll-off frequency $\omega_{\text{diffusion}} = q^2 D$. The knee frequency is shown in Figure 2-3 as a function of the mean intracellular speed for a range of persistence times, assuming no correlation between mean speed and mean persistence time. However, most biological processes display correlations between speeds and persistence times. The simplest scaling for such a correlation is $vt_p = L_p$, as discussed in section 2.2.2.

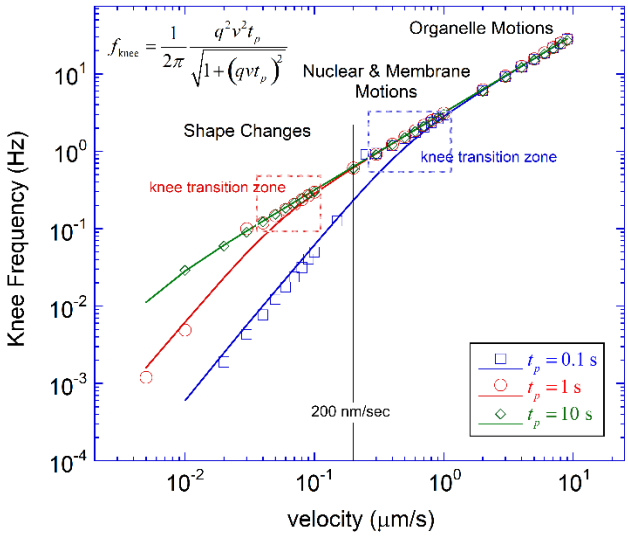

Figure 2-3 Knee frequency versus the mean intracellular speed for persistence times ranging from 0.1 seconds to 10 seconds. The markers are knee frequencies extracted from zero points of $d^3(\log S)/d(\log f)^3$ which are related to change in curvature, and lines are plots of Eqn. (2.27). The values of S are numerical calculations from Eqn. (2.25). The region labeled "knee transition zone" is when more than one knee appears in the 0.01 to 12.5 Hz range. The knee frequencies of living tissue range from 0.01 Hz to 1 Hz, corresponding to speeds from 3 nm/sec (cellular shape changes) to 300 nm/sec (nuclear and membrane motions).

2.2.5 Dynamic Spectroscopy of Living Tissue

Fluctuation frequencies relate to Doppler frequency shifts caused by light scattering from the subcellular constituents that are in motion, creating beats among all the multiple partial waves. The speeds of intracellular dynamics range across three orders of magnitude from tens of nanometers per second (cell membrane) [24-27] to tens of microns per second (organelles, vesicles) [28-31]. For near-infrared backscattering geometry, these speeds correspond to Doppler frequencies from 0.01 Hz to 10 Hz. Because of the wide variety of intracellular processes and the

wide range of speeds, the fluctuation spectra obtained from dynamic light scattering of living tissue contain a continuous distribution of Doppler-broadened spectra. The experimentally-measured field-based fluctuation spectrum is

$$S'_E(\omega) = \int_0^\infty \rho(\omega_D) S_E(\omega, \omega_D)\, d\omega_D \tag{2.28}$$

where $S_E(\omega, \omega_D)$ is the fluctuation spectrum of each individual process and $\rho(\omega_D)$ is a normalized distribution function that captures the range of intracellular Doppler processes. The combined power spectral density of Eq. (2.28) produces an envelope that contains the individual Doppler spectra of the underlying processes. For this reason, the power spectral density from most living tissue samples has a broad frequency dependence without a distinct Doppler edge. However, it is sometimes possible to observe from experiments either sharpening or broadening of an underlying Doppler edge.

2.3 Monte Carlo Simulation of Transport and Light Scattering

The theoretical predictions were compared to Monte Carlo DLS simulations to validate the theoretical model for isotropically-averaged one-dimensional transport processes. A calibration simulation was performed first on transport in the diffusion limit to test the three-dimensional diffusion case in contrast to the isotropically-averaged one-dimensional diffusion case. The Monte Carlo simulations were performed with 5000 particle walkers that contribute coherent scattered waves to the far field where the net complex field is sampled at a chosen sampling rate and transformed to the frequency domain through a fast Fourier transform. The resulting complex-valued fluctuation spectrum is taken modulus-squared and averaged over an ensemble of 50 simulations. The fluctuation spectral power density, in this case, is in the "heterodyne" mode to be compared with theoretical calculations. The walkers were simulated with a diffusion coefficient of $0.002\ \mu m^2/s$ using a probe wavelength of $0.84\ \mu m$. The sampling frame rate was 25 frame/s, and the capture is assumed to be instantaneous (infinitesimal exposure time). The total capture time is either 100 sec or 200 sec.

Figure 2-4 (a) shows the theoretical calculation and simulation of the Wiener process in one-dimensional isotropic and three-dimensional isotropic transport. Numerical calculations are

derived from the autocorrelation function via the Wiener-Khinchin theorem from Eq. (2.14) and Eq.(2.17), respectively. Figure 2-4(b) shows three cases: the two limits with persistence times $t_p \to 0$, $t_p \to \infty$, and for a moderate persistence time $t_p = 0.5$ s in the cross-over regime, with persistence times distributed according to an exponential probability.

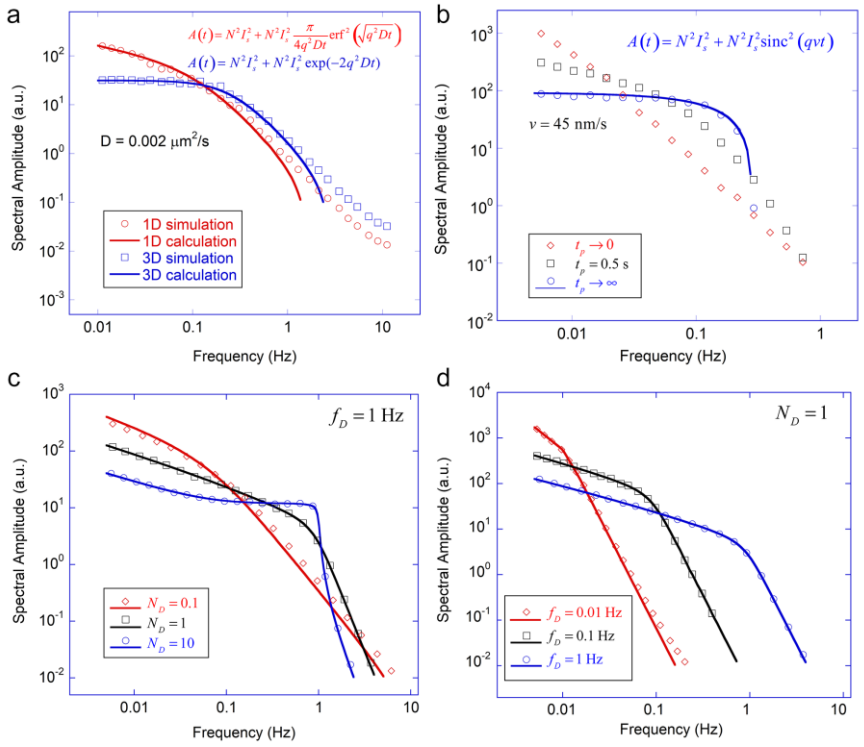

Figure 2-4 (a) Theoretical calculations (solid curves) and Monte Carlo simulations (markers) of three-dimensional isotropic transport versus one-dimensional isotropically-averaged transport. The theoretical calculation is from the Fourier transform of the autocorrelation function. The three-dimensional isotropic transport has a higher knee (0.8 Hz) than the one-dimensional isotropic transport (0.05 Hz). The autocorrelation functions are an exponential and an error function, respectively. In the 3D case, the low-frequency limit is flat and the high frequency has a -2 slope, which agrees with limits in Eq. (2.18). The high-frequency discrepancy in the calculated curve is a numerical artifact originating from the finite sampling of the autocorrelation function. (b) Monte Carlo simulation of 1D isotropic persistent walk in three regimes and theoretical results in the ballistic regime from the autocorrelation function. (c) – (d) Monte Carlo simulation and numerical calculation of persistent walks in the intermediate regime: (c) with fixed Doppler frequency f_D. (d) with fixed Doppler number N_D=1.

Similar Monte Carlo simulations in the cross-over regime were carried out that match closely with the analytical result from Eq. (2.25)[Figure 2-4 (c)-(d)], although the high-frequency side of the spectrum has a Nyquist floor. The simulations were done for conditions similar to experimental measurements (discussed in the next section), and the finite-time sampling means that walk events that are long compared to the persistence time may end outside the observation timeframe, being

recorded as an event with a shorter time. As a result, the spectrum starts to flatten above the frequency around $1/t_p = 2\pi f_D / N_D$, and the effect is more visible in processes with a longer mean persistence time (lower f_D or larger N_D), because of the exponential distribution of persistence times.

2.4 Experimental Setup and Sample Preparation

Spectroscopic responses of several types of biological samples were measured and analyzed using the "Alpha Prime" system shown in the appendix chapter A.1. A Q-Imaging EMC2 camera captures 500 frames at 25 fps and 50 frames at 0.5 fps, and a stitching algorithm is used to construct a continuous spectrum ranging from 0.01 Hz to 12.5 Hz [32].

Two types of tumor tissue were examined experimentally and analyzed for Doppler features in this chapter: tumor spheroids and tumor biopsies. Multicellular tumor spheroids (MCTS) are small clusters of cancer cells grown *in vitro*. The three-dimensional growth of the spheroids captures many of the microenvironmental features of naturally occurring tumor tissues, including extracellular matrix and cell-to-cell contacts [33]. Tumor biopsies are even more biologically and physiologically relevant than 3D tissue culture and are obtained from living patients (animal or human with approved IRB) either through surgical resection or by needle core biopsies.

For the tumor spheroids, cell lines were obtained from American Type Culture Collection (ATCC), Manassas, Virginia, and cultured at 37°C in a humidified CO_2 incubator. HT-29 cells were cultured in McCoy's 5a Medium and the MIA-PACA2 were cultured in Dulbecco's Modified Eagle's Medium. All media contained 10% fetal calf serum (Atlanta Biologicals), penicillin (100 IU), and streptomycin (100 μg/mL). Tumor spheroids were created by seeding a 50 mL rotating bioreactor and growing the cells for 7-14 days until 400-600 μM diameter spheroids were formed. Spheroids were immobilized in a thin layer of 1% low gel temperature agarose (Sigma-Aldrich Chemical Co) made up with the basal medium in 96-well tissue culture plates. DLD-1 samples were grown as 3D tumor spheroids using Corning U-bottom spheroid plates. Cells are incubated in a 96-well plate and immobilized with low gel-temperature agarose. Esophageal tumor biopsies were collected and transported in chilled RPMI-1640 medium supplemented with HEPES (Gibco). Within 2 hours of collection, small pieces 1 mm or less were cut from the biopsy and immobilized in low gel

temperature agarose in basal medium similar to the tumor spheroids. Canine B-cell lymphoma biopsies were handled with the same procedures [34].

2.5 Experiment

Figure 2-5 shows examples of tumor spheroid spectra and their spectral responses to drugs measured with the BDI system. Most spectra have a Lorentzian-like shape, with a knee at low frequency, a power-law roll-off in the mid frequency and a floor near the Nyquist frequency. Figure 2-5(a) compares the spectrum of a PaCa2-derived spheroid to an HT29-derived spheroid, showing a higher Doppler knee frequency in the case of the more loosely aggregated PaCa2 spheroid. In Figure 2-5(b) paclitaxel is applied to a DLD-1 spheroid. The cytoskeletal drug stabilizes polymerization of tubulin, lowers the rates of microtubule dynamic instability in human tumor cells [35] and causes cell death [36, 37]. The Doppler knee shifts to lower frequency caused by the increased stiffness of the cell. This represents a "red shift" in frequency content. In Figure 2-5 (c) valinomycin, a mitochondrial ionophore, facilitates K^+ charge movement and triggers loss of mitochondrial membrane potential, DNA fragmentation and death [38, 39]. The spectrogram pattern observed in this case is correlated with apoptosis [40]. In Figure 2-5(d) the relative change in spectral content for valinomycin is displayed as a relative spectrogram with frequency along the horizontal axis and time along the vertical axis. The spectral change is relative to the average baseline spectrum (average of spectra prior to the application of the drug at $t = 0$) . The spectrogram displays a suppression of the Doppler edge while enhancing high-frequency and low-frequency content.

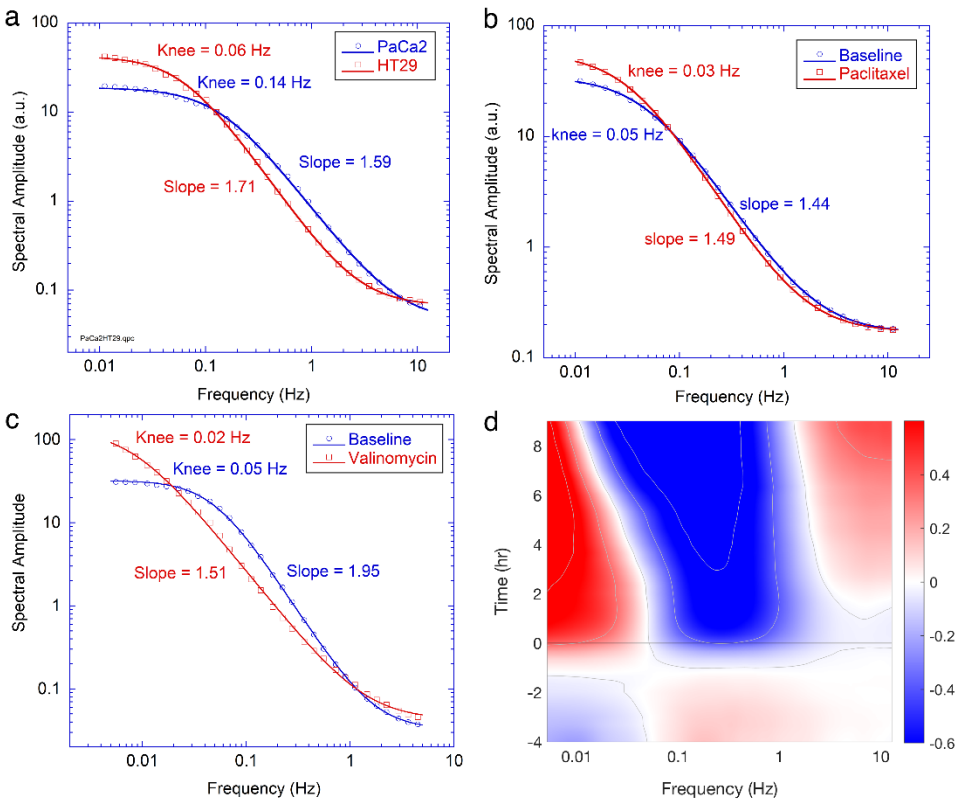

Figure 2-5 Examples of fluctuation power spectra. Markers are experimental data and solid curves are guiding lines. Knee and slope values are approximate numbers from curve fitting. (a) PaCa2-derived spheroids form a loose aggregate of cells and display a higher Doppler knee frequency than HT29-derived spheroids that form compact spheroids with tight and dense cellular adhesions. (b) DLD-1 spheroid responding to 50 μM paclitaxel. (c) The effect of valinomycin, a mitochondrial drug, on a DLD-1 spheroid. The baseline (pre-drug) spectrum shows a strong Doppler knee that is suppressed under the application of 50 μM valinomycin. (d) The relative change in spectral content in a spectrogram (time-frequency) format for the case of valinomycin. The drug is applied at $t = 0$, suppressing the Doppler knee.

Compared with cell-line spheroids, tumor biopsies show more heterogeneity among samples and more diverse responses to treatment. The biopsy samples obtained from resected tissue or needle cores were carefully dissected by hand to avoid connective tissues or fat, which have relatively low activity. Biopsies display spatial heterogeneity in the dynamics, including motility, spectrum and spectral responses. In a study on a standard-of-care chemotherapy treatment (cyclophosphamide, doxorubicin, prednisolone and vincristine) of dogs with B cell lymphoma, lymph node biopsies were treated with the combination treatment as well as by the single-agent compounds. The averaged spectral response of canine biopsy tissue resistant to vincristine is shown in Figure 2-6 (a) and (b) [34]. Vincristine is a *vinca* alkaloid that prevents polymerization of tubulin and induces depolymerization of microtubules, blocking mitosis during metaphase by

arresting the cell cycle, and causing cell death by apoptosis. The spectrogram displays an enhanced mid-frequency in response to the drug which may be a marker for drug resistance. The spectra in Figure 2-6 (c) are biopsies from two different esophageal cancer patients. Patient-1 has low activity with no discernible Doppler edge. However, the biopsy from Patient-2 displays a distinct Doppler edge near 0.2 Hz that becomes sharper after the addition of carboplatin, a DNA drug that leads to apoptosis. The power spectrum has an almost flat power density at low frequencies, with a distinct Doppler edge and a large negative slope of s = -2.4. The associated spectrogram for Patient-2 is shown in Figure 2-6(d). The sharpening of the Doppler edge appears as a dark red strip in the mid-frequency range. These data are consistent with the existence of a Doppler edge in these patient samples. As pointed out in Eq. (2.28), an experimental spectrum is an envelope of Doppler broadened spectra of processes with different N_D's and f_D's. As a result, sharp Doppler edges or knees of individual processes are washed out, and there is not a well-defined single N_D or f_D value for an experimental spectrum. However, a spectrum with a Doppler edge and a steep slope is strongly indicative of processes with high N_D and f_D values and highly ballistic motions.

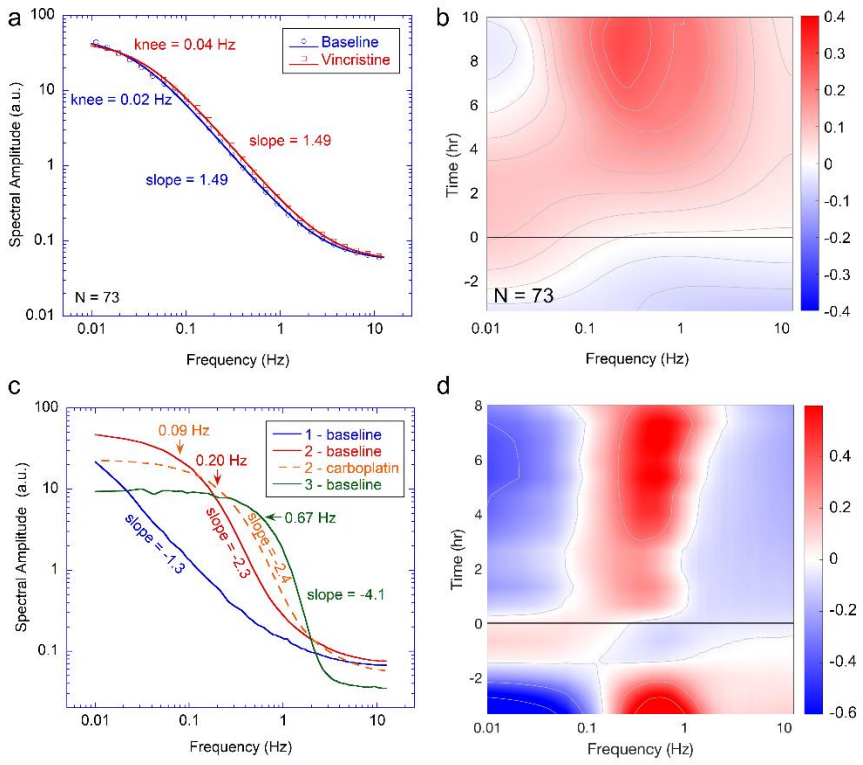

Figure 2-6 Examples of spectral responses for living biopsy samples treated with anti-cancer drugs. (a) Canine B-cell lymphoma biopsies responding to 60 nM vincristine from dogs that are resistant to chemotherapy. The final spectrum is 10 hours after application of the drug compared against baseline. (b) A time-frequency spectrogram response associated with (a) shows enhancement in mid frequency. The spectrogram displays the net effect compared against the control medium DMSO. (c) Effect of 25 μM carboplatin drug on two *ex vivo* biopsy samples for esophageal cancer from different patients, plus the baseline spectrum of a third sample. The spectral shape for sample-1 is almost linear at low-mid frequency, while sample-2 and -3 have a spectrum with a sharp Doppler edge. (d) Time-frequency spectrogram of sample-2 from (c) showing the emergence of a sharper Doppler edge.

2.6 Discussion

Fluctuation power spectra from living tissue display characteristic spectral shapes that are reminiscent of the common diffusive power spectra obtained from dynamic light scattering measurements of diffusing particles. This has led to conventional interpretations that consider intracellular transport to be primarily in the diffusive regime without a strong ballistic character. However, this tentative conclusion from dynamic light scattering contradicts a vast literature from two-dimensional cell culture that directly tracks motions with long persistence lengths that places most active intracellular processes in the ballistic regime. The resolution of this contradiction is simply the superposition of many ballistic processes in living tissue with a wide range of characteristic frequencies.

This chapter investigated the fluctuation spectra of transport modeled by persistent walks in the dynamic light scattering setting. The Doppler number defined as $N_D = qvt_p$ is a dimensionless scaling parameter that determines the regime of the motion and the spectrum shape. Many intracellular motions, including the processes associated with kinesin, dynein, and filopodia, have a long persistence length, leading to Doppler numbers greater than 1, placing the motions in the Doppler regime. In the intermediate regime, the power spectrum of a damped harmonic oscillator averaged over all angles yields the Doppler spectrum while in the ballistic and diffusive regimes, the power spectra are obtained through Fourier transforms of autocorrelation functions of intensities.

The model builds a framework for interpreting fluctuation spectra. A sample spectrum can be understood as a sum of processes with different Doppler frequency shifts (or velocities) and Doppler numbers (or persistence lengths). The slopes of spectra at high frequency for the ballistic and diffusion limits are $-\infty$ and -2, respectively, indicating that a slope steeper than -2 is characteristic of persistent walks. In spheroid and biopsy spectra, the greater the (absolute) slope, the further the motions deviate from diffusive behavior, with walks having longer persistence lengths. It is interesting to note that many metabolically-active tumor spheroids and biopsies show a typical spectral slope parameter of s = -1.7. If the typical Doppler number for active processes is assumed to be $N_D > 3$ (with a sharp Doppler edge), then the probability density function needed to yield a slope parameter of -1.7 would have $(1/f)^k$ character with approximately $k \approx 0.6$. Therefore, the spectral contributions to the fluctuation spectra increase at lower frequencies, consistent with stronger light scattering from membranes and cell-scale optical heterogeneities.

Experimental evidence for the Doppler edge is obtained using biodynamic imaging (BDI). BDI is a coherent imaging technique that records the field information from backscattering and generates Doppler fluctuation spectra. For a given sample, the spectrum change caused by the addition of an anti-cancer drug can be understood as the speed up or slow-down of certain processes. A 10-hour time-lapse measurement of drug response captures the change of the velocities over time. These shifts may eventually be correlated to specific drug mechanisms, providing insights for treatment and drug development.

Active transport processes in cells often are described by variations on the random walk. For instance, a Lévy flight is a random walk where the lengths of individual jumps are distributed with

a probability density function $P(x) \propto |x|^{-\alpha-1}$ when x is large [41]. Levy and Cauchy flights produce anomalous diffusion because they have "heavy tail" distributions with no finite variance [42]. Conversely, in the continuous-time random walk (CTRW) model [43] a particle waits between jumps for times set by a distribution function that also may have heavy tails, producing anomalous subdiffusion. Combining waiting-time with jump-length models produces anomalous diffusion tunable continuously from subdiffusive to superdiffusive behavior. Future work will investigate this anomalous regime.

While the samples used in this paper are tumor biopsies and spheroids, the light scattering analysis can be extended to other forms of life. Swimming bacteria have transport known as "run and tumble". Given that the velocity of a bacterium is 2 μm/sec to 200 μm/sec [44], the motion is firmly in the Doppler regime, and a sharp edge is expected in the spectrum, which would be suppressed if the bacteria slow down. In addition, cell divisions in gametocytes and zygotes may be slow processes that take place over a few hours, but they are firmly in the Doppler regime, because of long persistence lengths. Furthermore, fluctuation spectra of biased random walks, Levy walks, Cauchy walks, etc. can be studied, producing characteristic shapes and features that can help understand experimental observations. Therefore, biodynamic imaging and intracellular Doppler spectroscopy are poised to provide new insight into tissue dynamics and potentially important new screens of drug mechanisms.

References

[1] C. Bourgenot, C. D. Saunter, J. M. Taylor, J. M. Girkin, and G. D. Love, "3D adaptive optics in a light sheet microscope," Opt. Express **20**, 13252-13261 (2012).

[2] T.-L. Liu, S. Upadhyayula, D. E. Milkie, V. Singh, K. Wang, I. A. Swinburne, K. R. Mosaliganti, Z. M. Collins, T. W. Hiscock, J. Shea, A. Q. Kohrman, T. N. Medwig, D. Dambournet, R. Forster, B. Cunniff, Y. Ruan, H. Yashiro, S. Scholpp, E. M. Meyerowitz, D. Hockemeyer, D. G. Drubin, B. L. Martin, D. Q. Matus, M. Koyama, S. G. Megason, T. Kirchhausen, and E. Betzig, "Observing the cell in its native state: Imaging subcellular dynamics in multicellular organisms," Science **360** (2018).

[3] J. Lee, W. C. Wu, J. Y. Jiang, B. Zhu, and D. A. Boas, "Dynamic light scattering optical coherence tomography," Opt. Express **20**, 22262-22277 (2012).

[4] A. Wax, C. H. Yang, R. R. Dasari, and M. S. Feld, "Path-length-resolved dynamic light scattering: modeling the transition from single to diffusive scattering," Applied Optics **40**, 4222-4227 (2001).

[5] G. Popescu, and A. Dogariu, "Dynamic light scattering in localized coherence volumes," Optics Letters **26**, 551-553 (2001).
[6] W. Paul, and J. Baschnagel, *Stochastic Processes: From Physics to Finance* (Springer International Publishing, 2013).
[7] J. M. Berg, L. Stryer, J. L. Tymoczko, and G. J. Gatto, *Biochemistry* (W.H. Freeman, 2015).
[8] M. J. Schnitzer, and S. M. Block, "Kinesin hydrolyses one ATP per 8-nm step," Nature **388**, 386-390 (1997).
[9] C. Kural, H. Kim, S. Syed, G. Goshima, V. I. Gelfand, and P. R. Selvin, "Kinesin and dynein move a peroxisome in vivo: A tug-of-war or coordinated movement?," Science **308**, 1469-1472 (2005).
[10] K. Visscher, M. J. Schnitzer, and S. M. Block, "Single kinesin molecules studied with a molecular force clamp," Nature **400**, 184-189 (1999).
[11] M. J. Schnitzer, K. Visscher, and S. M. Block, "Force production by single kinesin motors," Nature Cell Biology **2**, 718-723 (2000).
[12] J. R. Lee, H. Shin, J. W. Ko, J. Choi, H. Lee, and E. Kim, "Characterization of the movement of the kinesin motor KIF1A in living cultured neurons," Journal of Biological Chemistry **278**, 2624-2629 (2003).
[13] A. R. Thompson, G. J. Hoeprich, and C. L. Berger, "Single-Molecule Motility: Statistical Analysis and the Effects of Track Length on Quantification of Processive Motion," Biophysical Journal **104**, 2651-2661 (2013).
[14] W. J. Walter, V. Beranek, E. Fischermeier, and S. Diez, "Tubulin Acetylation Alone Does Not Affect Kinesin-1 Velocity and Run Length In Vitro," Plos One **7** (2012).
[15] A. G. Hendricks, E. Perlson, J. L. Ross, H. W. Schroeder, M. Tokito, and E. L. F. Holzbaur, "Motor Coordination via a Tug-of-War Mechanism Drives Bidirectional Vesicle Transport," Current Biology **20**, 697-702 (2010).
[16] A. D. Mehta, R. S. Rock, M. Rief, J. A. Spudich, M. S. Mooseker, and R. E. Cheney, "Myosin-V is a processive actin-based motor," Nature **400**, 590-593 (1999).
[17] L. H. Hu, A. G. Vecchiarelli, K. Mizuuchi, K. C. Neuman, and J. Liu, "Directed and persistent movement arises from mechanochemistry of the ParA/ParB system," Proceedings of the National Academy of Sciences of the United States of America **112**, E7055-E7064 (2015).
[18] S. H. Parekh, O. Chaudhuri, J. A. Theriot, and D. A. Fletcher, "Loading history determines the velocity of actin-network growth," Nature Cell Biology **7**, 1219-1223 (2005).
[19] M. Dogterom, and B. Yurke, "Measurement of the force-velocity relation for growing microtubules," Science **278**, 856-860 (1997).
[20] S. J. King, and T. A. Schroer, "Dynactin increases the processivity of the cytoplasmic dynein motor," Nat. Cell. Biol **2**, 20 (1999).
[21] C. Schafer, U. Faust, N. Kirchgessner, R. Merkel, and B. Hoffmann, "The filopodium A stable structure with highly regulated repetitive cycles of elongation and persistence depending on the actin cross-linker fascin," Cell Adhesion & Migration **5**, 431-438 (2011).
[22] B. J. Berne, and R. Pecora, *Dynamic Light Scattering: With Applications to Chemistry, Biology, and Physics* (Dover Publications, 2000).
[23] D. D. Nolte, "Optical Interferometry for Biology and Medicine," (Springer, 2011).
[24] J. Evans, W. Gratzer, N. Mohandas, K. Parker, and J. Sleep, "Fluctuations of the red blood cell membrane: Relation to mechanical properties and lack of ATP dependence," Biophys. J **94**, 4134-4144 (2008).

[25] H. Strey, and M. Peterson, "Measurement of Erythrocyte-Membrane Elasticity by Flicker Eigenmode Decomposition," Biophys. J **69**, 478-488 (1995).
[26] K. Tamura, T. Mizutani, H. Haga, and K. Kawabata, "Active fluctuation in the cortical cytoskeleton observed by high-speed live-cell scanning probe microscopy," Acta Biomaterialia **7**, 3766-3772 (2011).
[27] T. Betz, M. Lenz, J.-F. Joanny, and C. Sykes, "ATP-dependent mechanics of red blood cells," Proceedings of the National Academy of Sciences of the United States of America **106**, 15320-15325 (2009).
[28] X. L. Nan, P. A. Sims, and X. S. Xie, "Organelle tracking in a living cell with microsecond time resolution and nanometer spatial precision," Chemphyschem **9**, 707-712 (2008).
[29] V. Racine, M. Sachse, J. Salamero, V. Fraisier, A. Trubuil, and J. B. Sibarita, "Visualization and quantification of vesicle trafficking on a three-dimensional cytoskeleton network in living cells," Journal Of Microscopy-Oxford **225**, 214-228 (2007).
[30] N. A. Brazhe, A. R. Brazhe, A. N. Pavlov, L. A. Erokhova, A. I. Yusipovich, G. V. Maksimov, E. Mosekilde, and O. V. Sosnovtseva, "Unraveling cell processes: Interference imaging interwoven with data analysis," Journal of Biological Physics **32**, 191-208 (2006).
[31] B. Trinczek, A. Ebneth, and E. Mandelkow, "Tau regulates the attachment/detachment but not the speed of motors in microtubule-dependent transport of single vesicles and organelles," Journal of Cell Science **112**, 2355-2367 (1999).
[32] S. Hao, "Dynamic Holography in Semiconductors and Biomedical Optics," (Purdue University, 2016).
[33] G. Lazzari, P. Couvreur, and S. Mura, "Multicellular tumor spheroids: a relevant 3D model for the in vitro preclinical investigation of polymer nanomedicines," Polym. Chem **8**, 4947-4969 (2017).
[34] H. Choi, Z. Li, H. Sun, D. Merrill, J. Turek, M. Childress, and D. Nolte, "Biodynamic digital holography of chemoresistance in a pre-clinical trial of canine B-cell lymphoma," Biomed Opt Express **9**, 2214-2228 (2018).
[35] A.-M. C. Yvon, P. Wadsworth, and M. A. Jordan, "Taxol Suppresses Dynamics of Individual Microtubules in Living Human Tumor Cells," Molecular Biology of the Cell **10**, 947-959 (1999).
[36] B. A. Weaver, "How Taxol/paclitaxel kills cancer cells," Mol Biol Cell **25**, 2677-2681 (2014).
[37] M. A. Jordan, and L. Wilson, "Microtubules as a target for anticancer drugs," Nat. Rev. Cancer **4**, 253 (2004).
[38] D. L. Nelson, A. L. Lehninger, and M. M. Cox, *Lehninger Principles of Biochemistry* (W. H. Freeman, 2008).
[39] Y. Inai, M. Yabuki, T. Kanno, J. Akiyama, T. Yasuda, and K. Utsumi, "Valinomycin Induces Apoptosis of Ascites Hepatoma Cells (AH-130) in Relation to Mitochondrial Membrane Potential," Cell Structure and Function **22**, 555-563 (1997).
[40] G. Farhat, G. J. Czarnota, M. C. Kolios, V. X. D. Yang, and A. Mariampillai, "Detecting apoptosis using dynamic light scattering with optical coherence tomography," J. Biomed. Opt. **16**, 070505 (2011).
[41] A. V. Chechkin, R. Metzler, J. Klafter, and V. Y. Gonchar, "Introduction to the Theory of Lévy Flights," in *Anomalous Transport*(Wiley-VCH Verlag GmbH & Co. KGaA, 2008), pp. 129-162.
[42] R. Metzler, and J. Klafter, "The random walk's guide to anomalous diffusion: a fractional dynamics approach," Phys. Rep **339**, 1-77 (2000).

[43] H. Felix, and F. Thomas, "Anomalous transport in the crowded world of biological cells," Rep. Prog. Phys **76**, 046602 (2013).
[44] R. H. Luchsinger, B. Bergersen, and J. G. Mitchell, "Bacterial Swimming Strategies and Turbulence," Biophys. J **77**, 2377-2386 (1999).

CHAPTER 3. DESIGN OF COMMON-PATH IMAGING SYSTEMS

Biodynamic imaging has traditionally used a Mach-Zehnder configuration with a signal arm and a reference arm that travels through OPL-controlled paths (such as both the "Alpha Prime" and BDM systems in APPENDIX A). However, the digital holograms recorded by such systems are susceptible to mechanical vibrations and disturbances. By adopting a common-path configuration, the two arms travel through the same optical path, and the hologram can remain stable under environmental disturbances and is useful for many applications [1-4]. This report explores new common-path optical system designs for biodynamic imaging, using off-axis Fresnel- or Fourier-domain BDI system designs.

3.1 System Designs and Experimental Results

Three common-path system designs are considered here: 1) Image-domain system with specularly reflected reference; 2) Fresnel-domain system with specularly reflected reference; and 3) Fourier-domain system with a reference star. The hologram is recorded using off-axis holography. The off-axis reference is generated either through specular reflection from the sample plate, or by a localized reflector adjacent to the sample.

3.1.1 Analysis of Coherent Optical System with Operator Notation

In Fourier Optics, the field distribution on a plane can be analytically obtained by applying Fourier analysis and scalar diffraction theory. Under the assumption of a paraxial condition and monochromatic illumination, operator notations can be used to analyze complex systems that involve many lenses [5]. Basic operators include:

Multiplication by a quadratic-phase exponential:

$$\mathcal{Q}[c]\{U(x)\} = e^{j\frac{1}{2}kcx^2}U(x) \tag{3.1}$$

where $k = \frac{2\pi}{\lambda}$.

Scaling by a constant:

$$\mathcal{V}[b]\{U(x)\} = |b|^{\frac{1}{2}} U(bx) \tag{3.2}$$

Fourier transformation:

$$\mathcal{F}\{U(x)\} = \int_{-\infty}^{\infty} U(x) e^{-j2\pi fx} dx \tag{3.3}$$

And free-space propagation:

$$\mathcal{R}[d]\{U(x_1)\} = \frac{1}{\sqrt{j\lambda d}} \int_{-\infty}^{\infty} U(x_1) e^{j\frac{k}{2d}(x_2 - x_1)^2} dx_1 \tag{3.4}$$

These four operators are sufficient for analyzing many optical systems. Complicated chains of operators can be reduced/simplified based on only a few relations or properties. As an example, in an optical system with two lenses separated by their focal lengths f , the output field is

$$U_f(u) = \frac{1}{\sqrt{\lambda f}} \int_{-\infty}^{\infty} U_0(x) e^{-j\frac{k}{f}xu} dx \tag{3.5}$$

from Fourier optics, which is equivalent to the notation

$$\mathcal{S} = \mathcal{V}\left[\frac{1}{\lambda f}\right]\mathcal{F} \tag{3.6}$$

The phase transformation of a lens is

$$t_l(x, y) = \exp\left[-j\frac{k}{2f}\left(x^2 + y^2\right)\right] \tag{3.7}$$

Therefore, its operator notation is $\mathcal{Q}\left[-\frac{1}{f}\right]$. This operator notation approach will be used in the analyses of responses recorded at the camera in the following sections.

3.1.2 Image-domain System with Specularly Reflected Reference

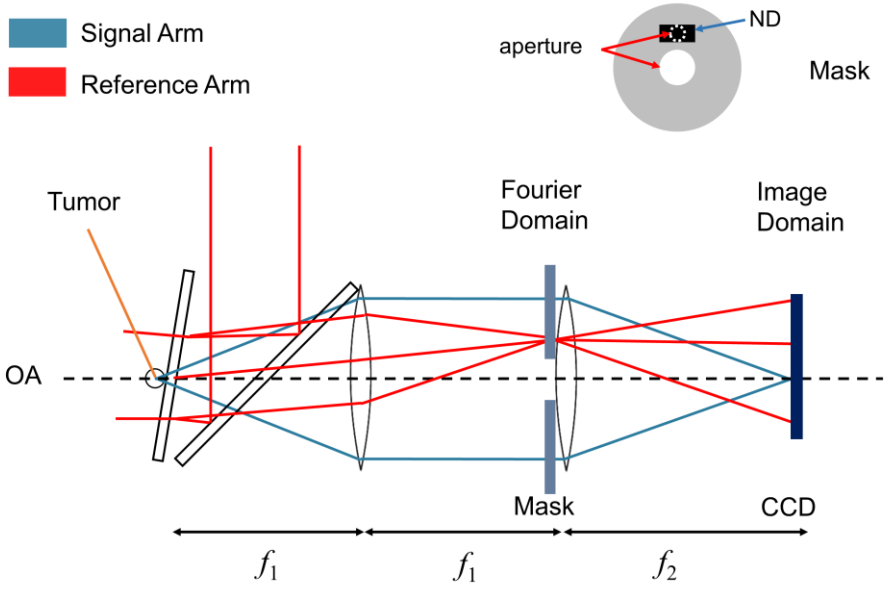

Figure 3-1 Design of the image-domain common-path system. The configuration contains one beamsplitter and two lenses, separated by their focal lengths. A mask containing two apertures is in front of the second lens. The upper aperture has a 500 μm diameter, is covered with an ND with 2.5OD, and is used to reduce the intensity of the reference arm, while the lower one has a diameter of about 1mm and is used in the signal arm to control speckle size.

The image domain configuration is shown in Figure 3-1. Responses at the CCD can be written as the product of a series of operators

$$\mathcal{S} = \mathcal{R}[f_2]\mathcal{Q}\left[\frac{1}{f_2}\right]\mathcal{R}[f_1]\mathcal{Q}\left[\frac{1}{f_1}\right]\mathcal{R}[f_1] \tag{3.8}$$

which can be simplified as

$$\mathcal{S} = \mathcal{Q}\left[\frac{1}{f_2}\right]\mathcal{V}\left[-\frac{f_2}{f_1}\right] \tag{3.9}$$

Therefore, the CCD captures an inverted and magnified image of the object with an additional quadratic phase. The quadratic phase introduces a spherical wavefront on the hologram, but in the hologram, the additional phase is canceled out by the same phase in the reference arm.

In digital holography, an empirical rule for good reconstruction resolution is the "rule-of-9 principle", which means that in the hologram, there should be three pixels per fringe, and three fringes per speckle. With $f_1 = 5\text{cm}$, $f_2 = 20\text{cm}$, the field of view of this system is given by

$$\text{FV} = \frac{D_c}{\frac{f_2}{f_1}} = \frac{f_1}{f_2} D_c = 1.85 \text{ mm} \tag{3.10}$$

and the resolution is

$$\frac{\text{FV}}{\frac{D_c}{a_{sp}}} = 16.6 \text{ μm} \tag{3.11}$$

where the speckle size a_{sp} is determined by the rule-of-9 principle

$$a_{sp} = \frac{f_2 \lambda}{a_{ap}} = 9 a_{pix} = 66.6 \text{ μm} \tag{3.12}$$

where $D_c = 7.4 \text{ mm}$ is the size of the chip of the camera, a_{ap} is aperture size, $\lambda = 650 \text{ nm}$, and $a_{pix} = 7.4 \text{ μm}$ is the pixel size of the camera. The aperture size is then $a_{ap} = \frac{f_2 \lambda}{9 a_{pix}} = 1.95 \text{ mm}$.

A DLD spheroid sample was used as the target object, placed in a well of a 96-well plate, measured at room temperature. A 650 nm wavelength semiconductor laser was used as the light source. In this case, the bottom of the well gives specular reflection that serves as the reference. The results are shown in Figure 3-2 with basic BDI maps.

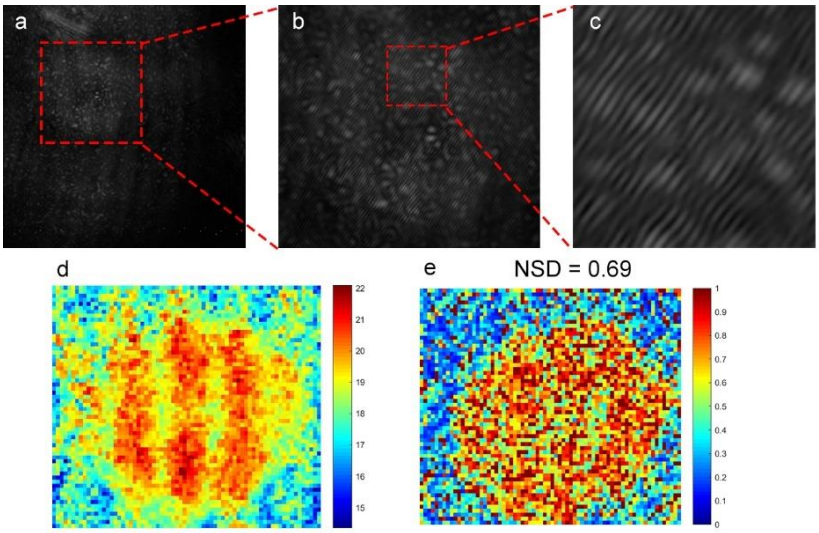

Figure 3-2 DLD images from the image-domain common-path system. a) raw hologram, b) sample, c) fringes, d) OCI; the stripes are caused by self-interference of the long coherence source, e) MCI.

A DLD-1 tumor spheroid was treated with 10 μm nocodazole under room temperature with this image-domain common-path system. The spectrogram shows a red-blue-red pattern, which agrees with Figure 5-1, with differences in the zero-crossing frequency, probably caused by the fact that the sample was not maintained at the physiological temperature during this experiment.

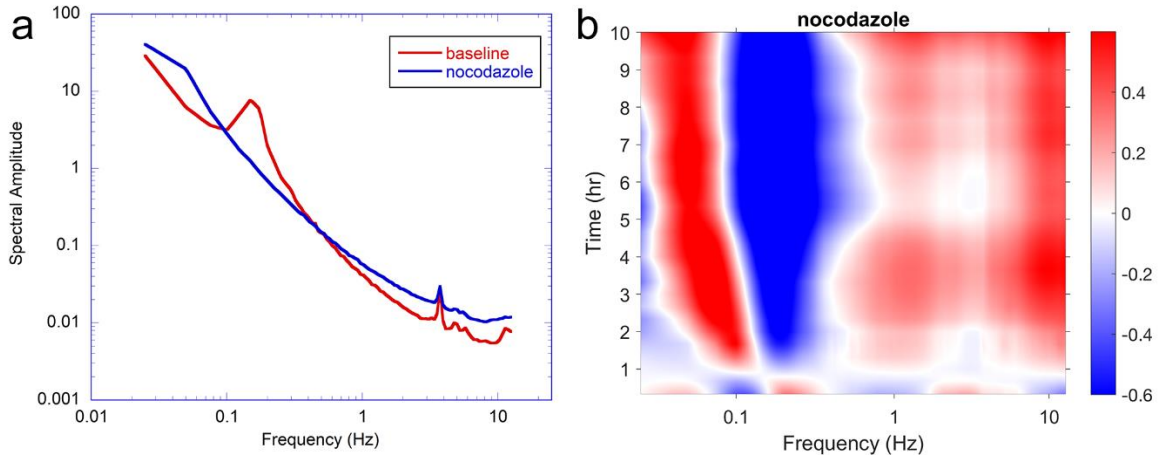

Figure 3-3 Spectroscopic response to 10 μM nocodazole of a DLD-1 tumor spheroid. a) Spectra of baseline and response, b) Differential spectrogram with the response of control medium DMSO subtracted

To test the stability of the system, a small piece of white paper was used as the target, and the optical table on which the system was built was hit by hand repeatedly at about 0.5 fps. 100 holograms were taken continuously at about 6 fps. Hologram washout is small enough to be

imperceptible by the human eye. By taking the intensities of along a line (Figure 3-4a) across all frames, the average relative fluctuations were only about 5% (Figure 3-4b and c).

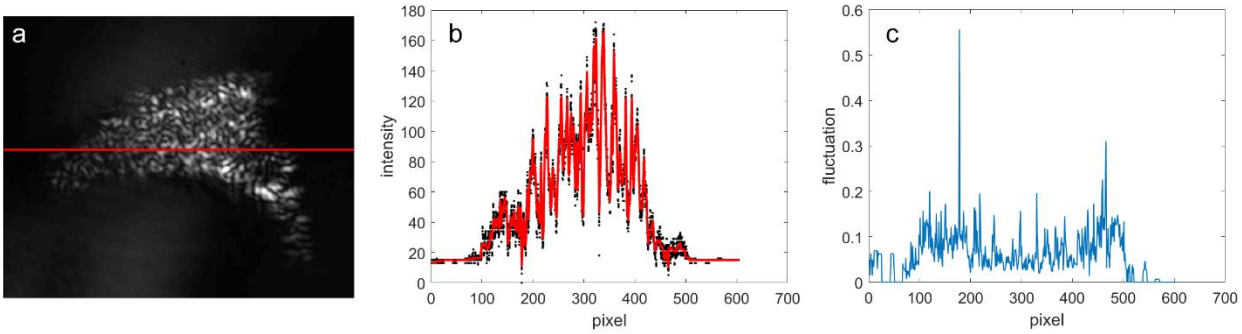

Figure 3-4 a) Raw hologram and the line where the intensities were taken b) Scatter plot of all intensities along the line across 100 frames. c) Relative fluctuations of these pixels, defined as $\frac{\Delta I}{\langle I \rangle}$ for each pixel.

3.1.3 Fresnel-domain System with Specular Reflection as Reference

The image domain system requires an extra step for reconstruction, and the photon efficiency is low (discussed in section 3.2). A system that is more similar to the current "alpha" systems is desired. The design of the Fresnel-domain system is shown in Figure 3-5. With a sample mounted on a glass slide, the scattering from the sample serves as the signal while the specular reflection from the slide serves as the reference arm. The beamsplitter reflects the incoming beam, determining the angle of the specular reflection. The crossing angle between the reference beam and the signal beam can be changed by tuning the orientation of the beamsplitter and the plate. A mask is placed in front of the second lens (same as in Figure 3-1) to control the speckle size of the signal arm and reduce the intensity of the reference. The CCD is placed on the focal plane of the third lens.

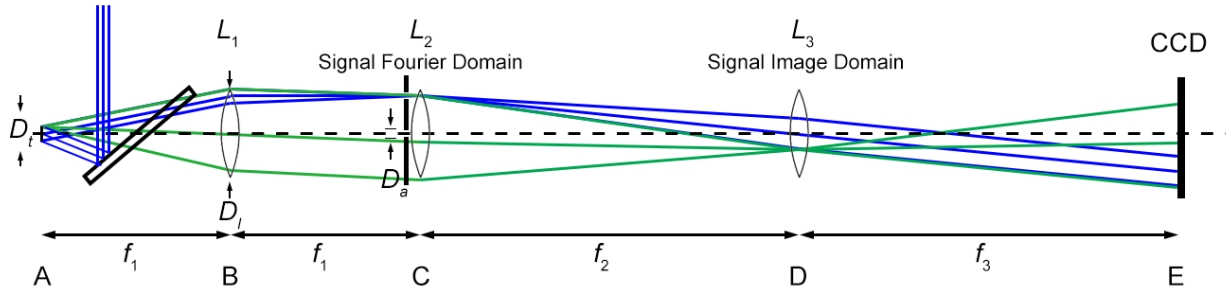

Figure 3-5 Design of the Fresnel-domain common-path configuration using specular reflection from the bottom of the plate as the reference. The system consists of one beamsplitter and three lenses that are spaced by their focal lengths.

The field at the camera of this coherent optical system is analyzed using the operator approach. In Figure 3-5, from left to right, the wave propagates through (1) a free space of distance $f_1 = 5$ cm, (2) a positive lens with focal length f_1, (3) a free space of distance f_1, (4) a positive lens with focal length $f_2 = 15$ cm, (5) a free space of distance f_2, (6) a positive lens with focal length $f_3 = 15$ cm, and (7) free space of distance f_3. The response at the camera can be written as

$$\mathcal{S} = \mathcal{R}[f_3]\mathcal{Q}\left[\frac{1}{f_3}\right]\mathcal{R}[f_2]\mathcal{Q}\left[\frac{1}{f_2}\right]\mathcal{R}[f_1]\mathcal{Q}\left[\frac{1}{f_1}\right]\mathcal{R}[f_1] \tag{3.13}$$

which is simplified as

$$\mathcal{S} = \mathcal{R}[f_3]\mathcal{Q}\left[\frac{1}{f_2}-\frac{1}{f_3}\right]\mathcal{V}\left[-\frac{f_2}{f_1}\right] \tag{3.14}$$

When $f_2 = f_3$, then $\mathcal{S} = \mathcal{R}[f_2]\mathcal{V}\left[-\frac{f_2}{f_1}\right]$, and the signal on the camera is the free-space propagation over distance f_2 of an inverted, magnified object. In this configuration, on the CCD the signal is in neither image domain nor Fourier domain, but instead is in a Fresnel regime. Reconstruction of an image by using an FFT does not produce a faithful image but does produce speckle fields that are useful for biodynamic imaging.

The field of view (FOV) is given by the minimum of either the object size a or aperture size a_{ap}. To satisfy the rule-of-9 principle of digital holography, the focal length of the third lens, the size

of the lower aperture and the distance between the centers of the two apertures of the mask should be chosen so that

$$a_{sp} = \frac{f_3 \lambda}{FV} = 9 a_{pix} \tag{3.15}$$

$$\Lambda = \frac{\lambda}{\sin\theta} = \frac{\lambda}{d / f_2} = 3 a_{sp} \tag{3.16}$$

where a_{sp} is the speckle size on the camera plane, $a_{pix} = 7.2\ \mu\text{m}$ is the pixel size of the camera, and d is the distance between the centers of the apertures. Similar to Eq. (3.11), the resolution is

$$\frac{\text{FV}}{\frac{D_c}{a_{sp}}} = 22.2\ \mu\text{m} \tag{3.17}$$

and the Fresnel number of this system is

$$F = \frac{a^2}{L\lambda} = 1.64 \sim 1 \tag{3.18}$$

where $a = a_{\text{sample}} = 400\ \mu\text{m}$, $L = f_3 = 15\ \text{cm}$ and $\lambda = 650\ \text{nm}$. Therefore, the diffraction is in the Fresnel regime.

Numerical simulation was used to illustrate the system performance of the Fresnel system. A simulation of the signal arm at different positions is shown in Figure 3-6, in which the capital letter "A" is used as the object. Position C is the Fourier transform of the object, and position D shows an inverted image, which agrees with the coherent optical system analysis. Figure 3-6 (f) shows that an FFT operation does not give a clear reconstruction of the object, although some features of the object can still be identified. The letter "A" here is ambiguous and other components appear in the hologram, which decreases the quality of the reconstruction.

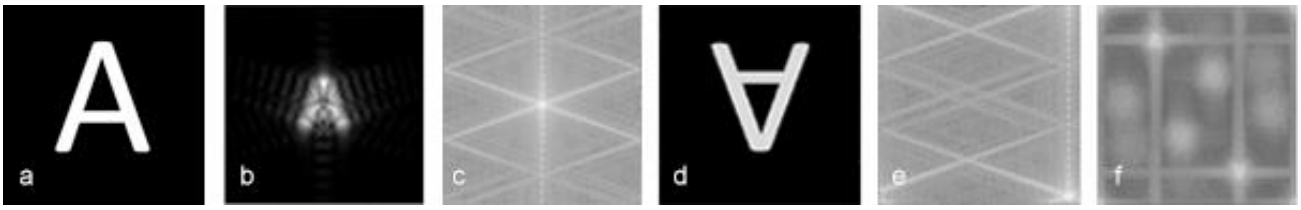

Figure 3-6 Numerical simulation of the system. a-e: signal arm at positions A-E of Figure 3-5 when a capital letter "A" is used as the object. b and d are zoomed-in images. F: FFT Reconstruction of the signal on the "camera" (position E).

In an experimental study, a small triangular clip of paper was used as the target object, a 650 nm semiconductor laser was used as the light source, and the hologram and reconstruction are shown in Figure 3-7. There are first-order images in the reconstruction from the signal of the target, but they do not display the actual shape of the target. Because the camera is in the Fresnel domain, precise optical alignment and more complicated numerical reconstruction are required if an aberration-free object image is desired.

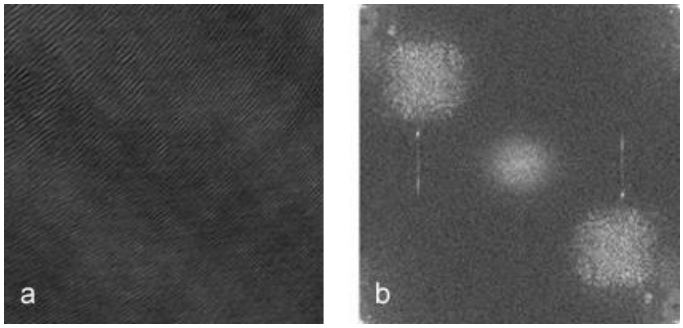

Figure 3-7 Experimental results of the Fresnel design. a. Part of a hologram of captured in the Fourier Domain System, with a triangle paper clip as the object b. Reconstruction of (a) using FFT

3.1.4 Fourier-domain System with a "Reference Star"[2]

One of the critical problems in the design of a common-path imaging system is to properly introduce the reference arm beam. Considerations include:

1) To allow a simple reconstruction process and avoid complicated engineering including precise alignment, it is preferred that the reference is a plane wave at the CCD

[2] Presented at 2017 SPIE Photonics West: Zhe Li, John Turek, David D. Nolte, "Common-path biodynamic imaging for dynamic fluctuation spectroscopy of 3D living tissue," Proc. SPIE 10063, Dynamics and Fluctuations in Biomedical Photonics XIV, 100631G (3 March 2017)

2) The intensity of the reference arm at the CCD should be comparable to that of the signal arm, in order to create maximum fringe contrast
3) The angle between the signal arm and the reference arm at the CCD can be adjusted to the desired value (rule-of-9)
4) Ability to modify the OPL of the reference arm is needed for coherence gating

Therefore, to introduce the reference before the lens in a Fourier domain system and satisfy (1), a point source is required. A metal pinhead can be a good candidate, because of its small size, spherical shape and moderate reflectivity, which helps to achieve (1) and (2). Moving the pinhead transversely satisfies (3) to happen, while by moving it axially parallel to the OA the OPL can be changed, meeting the requirement (4). The pinhead is the "reference star" in the system.

The design of this Fourier-domain common-path system is shown in Figure 3-8. The CCD is located at the Fourier plane while the pinhead adjacent to the sample serves as a point source. The spherical wave from the pinhead becomes rays of equal inclination after the lens, thereby providing a plane-wave reference for the holographic recording. The fringe spacing is determined by the inclination of the plane wave, which is related to the distance between the pinhead and optical axis by

$$\Lambda = \frac{\lambda}{\sin\theta} = \frac{\lambda}{d / f} \tag{3.19}$$

where f is the focal length of the lens and d is the distance between the pin and the optical axis.

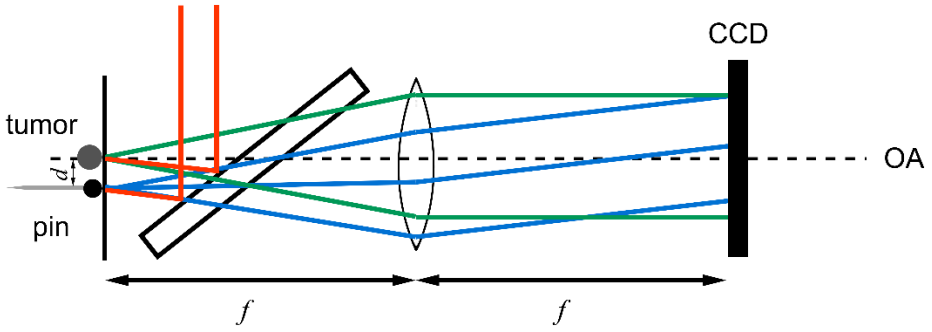

Figure 3-8. Design of a Fourier-domain common-path configuration using the pinhead as a reference star. $f = 150$ mm.

Because the CCD is on the Fourier plane of the system, the field distribution at the CCD is simply

$$\mathcal{S} = \mathcal{F} \tag{3.20}$$

Numerical simulation for this design used the letter "A" as the target, as in Figure 3-6(a), while a two-dimensional delta function $\delta(x-x_0, y-y_0)$ simulates the pinhead, where (x_0, y_0) is the position of the pinhead. The numerical simulation performs the numerical implementation of the Fourier Transform (3.20) [6, 7]. The fringes in the hologram are very clear and the reconstruction gives a reasonable result (Figure 3-9). The parameters used for the simulation are given in Table 3-1.

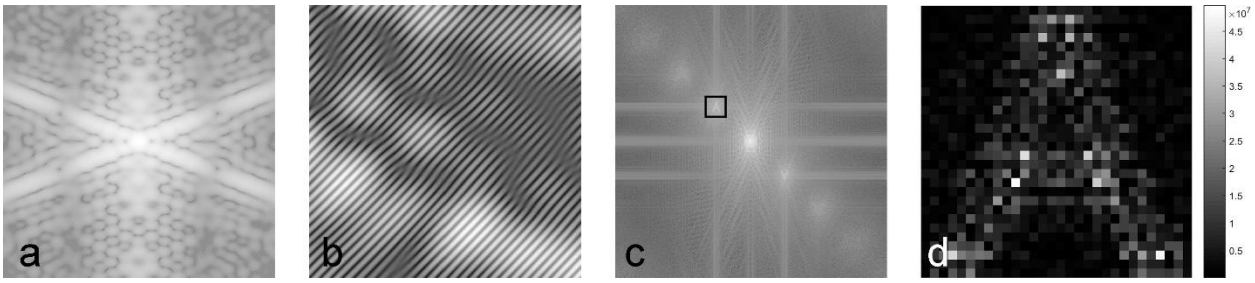

Figure 3-9. Numerical simulation of the reference star design. a) recorded hologram b) Fringes in a section of the hologram c) Reconstruction of the hologram d) zoomed-in image of the box in (c).

Table 3-1 Parameters for the simple pinhead simulation (shown in Figure 3-9).

Sampling interval	**Light wavelength**	**Target size**	**Pinhead position from the optical axis**	**Focal length of the lens**
8 μm	840 nm	640 μm	3 mm	5 cm

This design is called a "reference star method" because the function of the pinhead is similar to a reference star in astronomy. However, a pinhead comes with certain dimensions, which means that it is not an ideal point source. Some modifications to the simulation were used to illustrate the case. Instead of a delta function, the pinhead is simulated by a small matrix of complex values of norm 1 and random phases uniformly distributed from 0 to 2π . The size of the matrix is dependent on the size of the pinhead while the random phases come from the variations in the optical path length caused by the small curvature of the pinhead. The results are given in Figure 3-10 and the parameters are listed in Table 3-2. The quality of the reconstruction is degraded, but a triangular outline of "A" can still be vaguely recognized.

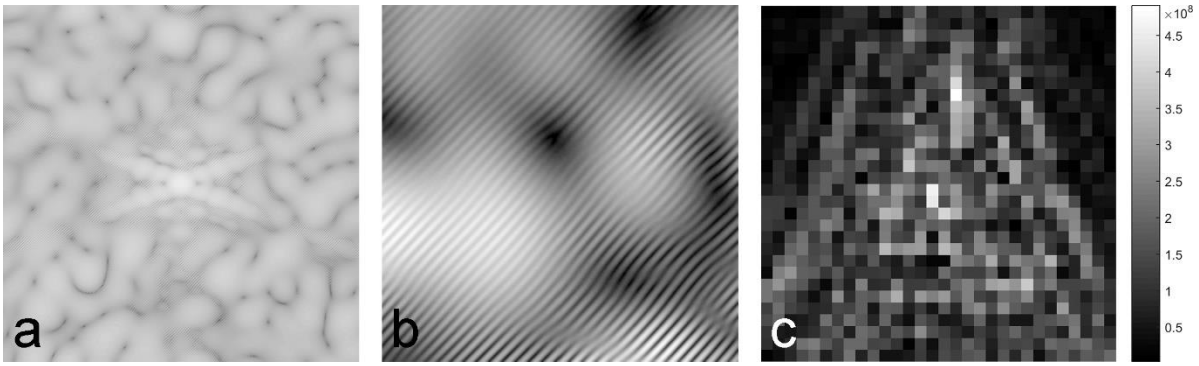

Figure 3-10 Numerical simulation with a non-ideal pinhead. a) recorded hologram, b) fringes of the hologram, c) first-order reconstruction image

Table 3-2 Parameters for the nonideal pinhead simulation shown in Figure 3-10

Sampling interval	Light wavelength	Target size	Pinhead size	Pinhead position from the optical axis	Focal length of the lens
8 μm	840 nm	640 μm	320 μm	3 mm	5 cm

A simple and quick test was used to quantify the quality of the reconstructed images (Figure 3-9d and Figure 3-10c): a linear correlation between an image of target "A" (Figure 3-11) and the reconstruction is calculated. The correlation is 0.41 for the ideal case and 0.25 for the nonideal case. This shows that the nonideal reconstruction result is worse than the ideal case in terms of similarity to the original target.

Figure 3-11 80 px × 80 px image of target "A"

A DLD spheroid was used as the target object and the hologram and reconstruction are shown in Figure 3-12. The pinhead introduced fringes to the hologram, as discussed above, and the reconstruction did reveal a nearly circular object.

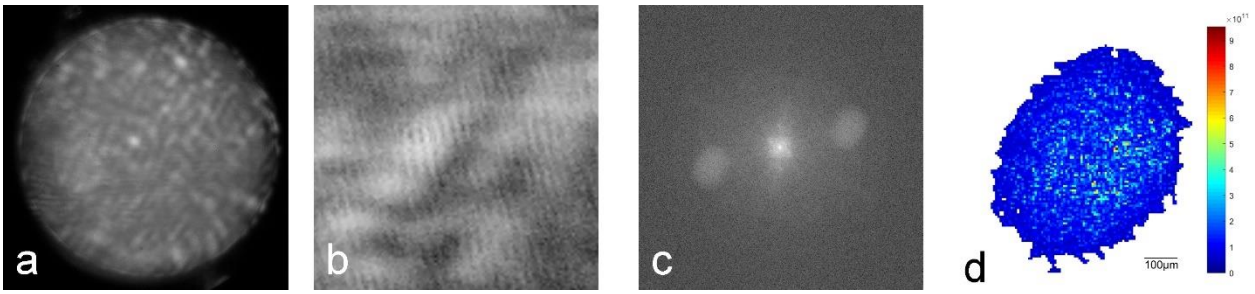

Figure 3-12. Experimental results of the reference star design with a DLD spheroid as the target. a) recorded hologram b) zoomed-in image of the fringes c) reconstruction d) zoomed-in image of the spheroid in (c)

Biological properties of the spheroid were analyzed and the drug response to 10 μM nocodazole at room temperature was studied. The MCI is shown in Figure 3-13(a). Nocodazole was added at time t=0 and the response can be understood by looking at the spectrum [Figure 3-13(b)] and spectrogram [Figure 3-13(c)]. The spectrum has a dynamic range as high as 3 orders of magnitude and it can be seen that after 6 hours, there are noticeable increases in the low and high frequencies and decreases in the mid frequency, which echoes Figure 5-1b and Figure 3-3.

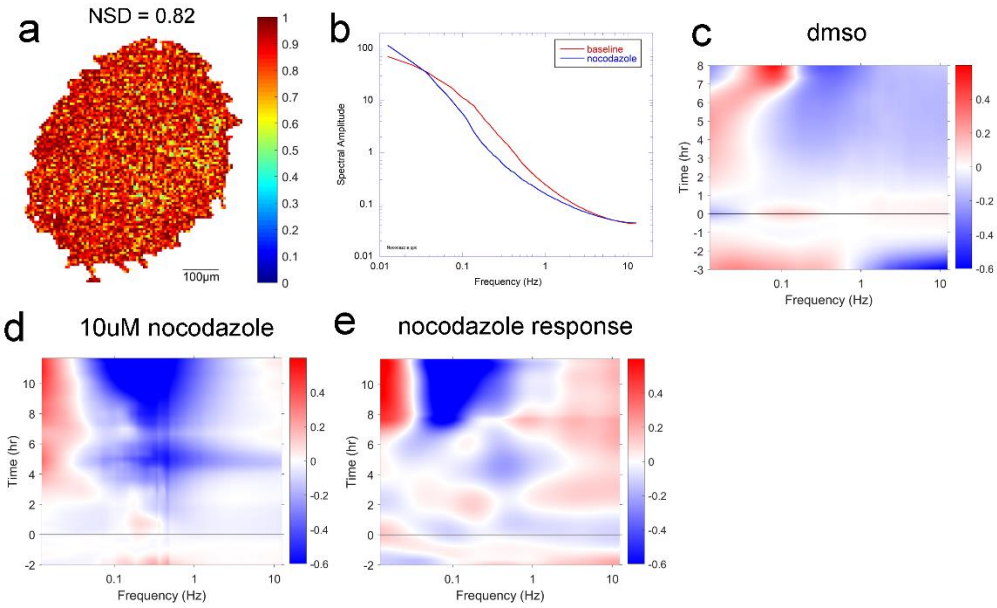

Figure 3-13. Biological information of the DLD spheroid and drug response to nocodazole. a) MCI map of the spheroid b) spectra of the spheroid before and 10 hours after adding nocodazole. c) spectrogram of the control medium DMSO d) spectrogram of the spheroid treated with nocodazole e) c) subtracted by d) i.e. the "net" response of nocodazole

The spectrograms in Figure 3-13 are not as "clean" as in Figure 5-1, with spikes and other features. The main reason is mechanical disturbance. The DLD-1 tumor spheroid was usually immobilized

with agarose, but the gel was not as effective with the introduction of the "reference star" pinhead, and in some cases, the sample does move during the experiment. The motion of the pinhead itself may also be an issue, but since the pinhead was mechanically fixed, it was relatively reliable.

Fringe contrast is evaluated by calculating the ratio of the sum of the intensity of zero-order and first-order components, as in Figure 3-14. The zero-order components contain information from photons that are not coherence gated, which may be from other parts of the sample or noise. The fringe contrast is 0.09, compared with 0.08 from the "Alpha Prime" system image shown in Appendix Figure 2, and 0.39 from the image-domain system in Figure 3-2. Therefore, the fringe contrast is comparable to that of the "Alpha Prime" system. However, the fringe contrast is heavily dependent on the position of the pinhead. When the pinhead is close to the center of the light source, more light is reflected, increasing the intensity of the reference arm, therefore reducing the fringe contrast.

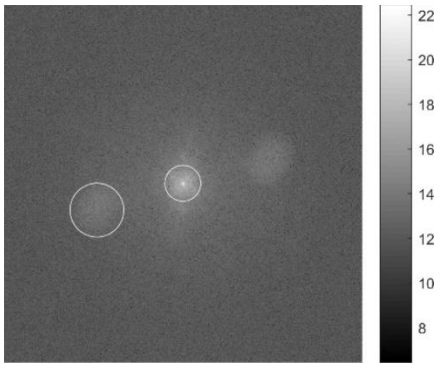

Figure 3-14 Zero-order components (center) and first-order image (left, and its conjugate image on the right) in the image domain after the Fourier transform.

A Signal/background spectrum comparison, which evaluates the signal-to-noise ratio (SNR) of the image, is shown in Figure 3-15. The signal, i.e. the sample, has a smooth spectrum with a dynamic range of about 3 orders of magnitude, while the spectrum of the background has a noisy tail and a dynamic range of only 1 order of magnitude. Since the sample spectrum has a large dynamic range and is at least 2 orders of magnitude greater than the noise spectrum at high frequencies, this imaging method gives a satisfactory SNR.

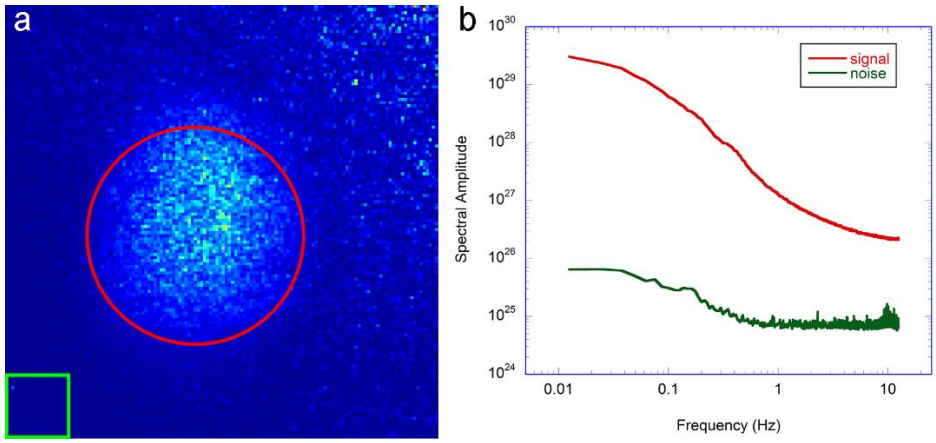

Figure 3-15 Signal-to-background spectrum test. a) Illustration of "signal" area vs "background"/ "noise" area. b) Spectra of signal and background signal, without normalization.

3.2 Comparison of Photon Efficiency of Systems

Tumor spheroids have a relatively small μ_s' of around 140 mm^{-1} [8, 9]. Therefore, to improve SNR and capture intracellular dynamics with the best sensitivity, an optical imaging system should strive to achieve the maximum photon efficiency. In experimental systems, several factors lead to a loss in the utilization of photons, including reflection and limited aperture of optical components like lenses, apertures/windows and unused reflected light at a beamsplitter, etc. This section discusses the factors that determine the photon efficiency of a general Fourier-domain imaging system and a general image-domain imaging system.

Assume that reflection from the sample has ideal Lambertian reflectance, in which the radiant intensity is described by Lambert's cosine law

$$I_0 = \frac{I\, d\Omega dA}{d\Omega_0\, dA_0} \tag{3.21}$$

where $d\Omega_0 dA_0$ is the total solid angle.

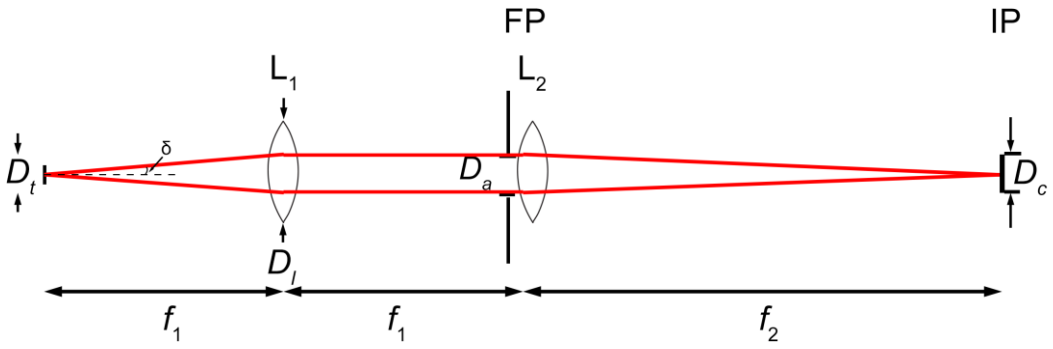

Figure 3-16: A generalized image-domain imaging system. FP: Fourier plane, IP: image plane, D_t : size of the target, D_l : diameter of the lens, D_c : size of the CCD/CMOS chip, or the shorter of length and width if the chip is rectangular

In an image-domain system (Figure 3-16), the rule-of-9 principle is given by

$$\frac{f_2\lambda}{D_a} = 9a_{pix} \tag{3.22}$$

where a_{pix} is the pixel size of the camera. Light is restricted by the size of the aperture, where δ satisfies

$$\tan\delta = \frac{\frac{D_a}{2}}{f_1} \tag{3.23}$$

Photon efficiency is given by

$$\eta_1 = \frac{\int_0^{\delta} d\theta \sin\theta \int_0^{2\pi} d\phi I_{\max} \cos\theta}{\int_0^{\frac{\pi}{2}} d\theta \sin\theta \int_0^{2\pi} d\phi I_{\max} \cos\theta} = \delta^2 = \frac{D_a^2}{4f_1^2} \tag{3.24}$$

For comparison, a general Fourier domain system (Figure 3-17) is

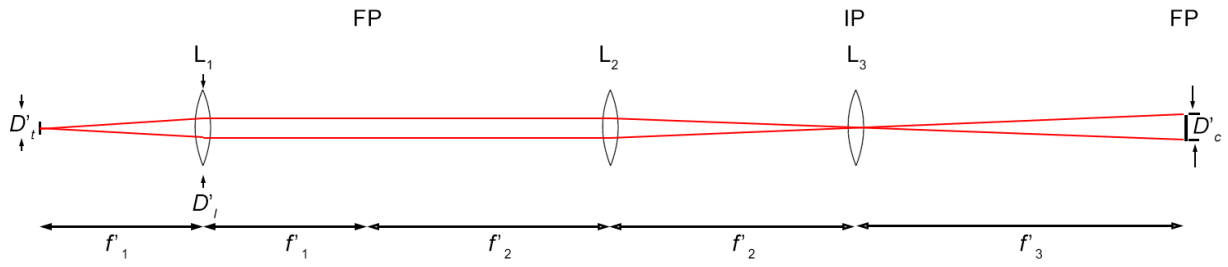

Figure 3-17: A generalized Fourier domain imaging system.

The light is restricted by the size of the chip D_c', and

$$\tan\delta' = \frac{\frac{f_2'}{f_3'}\frac{D_c'}{2}}{f_1'} \tag{3.25}$$

Therefore, photon efficiency is given by

$$\eta_2 = \frac{\int_0^{\delta'} d\theta \sin\theta \int_0^{2\pi} d\phi I_{\max}\cos\theta}{\int_0^{\frac{\pi}{2}} d\theta \sin\theta \int_0^{2\pi} d\phi I_{\max}\cos\theta} = \delta'^2 = \frac{f_2'^2 D_c'^2}{4 f_1'^2 f_3'^2} \tag{3.26}$$

The ratio of photon efficiencies is given by

$$\eta_1 = \eta_2 \Rightarrow \frac{f_2}{f_1} = \frac{f_2'}{f_1'}\frac{D_c'}{D_t} \tag{3.27}$$

In the "Alpha Prime" system used in routine tumor spheroid and biopsy sample experiments, $f_1' = f_2' = 15\text{cm}$, $f_3' = 5\text{cm}$, $D_c' \sim 8$ mm, and $D_t' \sim 500$ μm .

The photon efficiency of the Fourier domain system is greater than the image domain system by a factor of 16. Therefore, for the image-domain common path system to achieve the same efficiency as the "Alpha Prime", the $\frac{f_2}{f_1}$ ratio which is also the magnification in the image-domain system should be 16. However, this is difficult to manage, because:

1) For a tumor spheroid with a 600 μm diameter, a magnification of 16 will lead to loss in field of view because the chip size of the CCD is about 8 mm;

2) A large $\frac{f_2}{f_1}$ leads to a large f_2 value, which is not practical in an optical system. In an actual setup, where there are additional optical components like beamsplitters and where physical dimensions of the lenses, posts, holders and pedestals need to be taken into consideration, f_1 usually needs to be at least 50 mm, resulting in a 800 mm f_2, which will lead to additional difficulties with alignment and other engineering issues.

Therefore, for image-domain systems, it is difficult to achieve the same photon efficiency in an actual setup, and compromises have to be made. The magnification needs to be lower, which leads to a loss in photon efficiency.

3.3 Discussion

The image-domain design has a relatively low photon efficiency and requires an extra step in the numerical reconstruction. Therefore, it is not preferred as a common-path system design.

In the Fresnel-domain system using specular reflection, a Fourier transform of the hologram does not give a direct image, because the camera is neither on the Fourier plane nor an image plane. When the hologram is properly reconstructed, i.e. done by using a Fresnel reconstruction, a good image might be obtained, but more precise optical alignment and a more complicated numerical reconstruction algorithm would be needed. On the other hand, if a high-quality image is not desired, the dynamical information from the reconstruction with a Fourier transform, including amplitude, motility and spectra of the first-order image, may yield meaningful information about the target.

The design of the Fourier system with the reference star is very simple, but the control of the position of the sample and the pinhead is critical. The sample needs to be placed in the center of the Gaussian beam to give maximum backscattering signal, while the pinhead must be placed in the periphery of the beam, but not too close to the sample that the reflected light from the pinhead is too strong and saturates the camera, or too far that the reflected light is too weak, or that the fringe spacing, described in (3.19), is too small and violates the rule-of-9 principle

$$\Lambda = 3a_{sp} = 9a_{pix} \tag{3.28}$$

Here $a_{pix} = 8\ \mu\text{m}$, ideally $d = 1\ \text{mm}$, and in the experiments the placement of the pin needs to be accurate on the level of 100 μm.

References

[1] A. B. Vakhtin, D. J. Kane, W. R. Wood, and K. A. Peterson, "Common-path interferometer for frequency-domain optical coherence tomography," Appl. Opt. **42**, 6953-6958 (2003).

[2] R. Kelner, B. Katz, and J. Rosen, "Common path in-line holography using enhanced joint object reference digital interferometers," Opt. Express **22**, 4995-5009 (2014).

[3] V. Mico, Z. Zalevsky, and J. García, "Common-path phase-shifting digital holographic microscopy: A way to quantitative phase imaging and superresolution," Opt. Commun. **281**, 4273-4281 (2008).

[4] N. T. Shaked, L. L. Satterwhite, M. J. Telen, G. A. Truskey, and A. Wax, "Quantitative microscopy and nanoscopy of sickle red blood cells performed by wide field digital interferometry," J. Biomed. Opt. **16**, 030506-030506-030503 (2011).

[5] J. W. Goodman, *Introduction to Fourier Optics* (W. H. Freeman, 2005).

[6] D. Voelz, *Computational Fourier Optics: A MATLAB Tutorial* (2010).

[7] J. D. Schmidt, *Numerical Simulation Of Optical Wave Propagation With Examples In MATLAB* (2010).

[8] P. Hargrave, P. W. Nicholson, D. T. Delpy, and M. Firbank, "Optical properties of multicellular tumour spheroids," Physics in Medicine & Biology **41**, 1067 (1996).

[9] S. L. Jacques, "Optical properties of biological tissues: a review," Physics in medicine and biology **58**, R37-61 (2013).

CHAPTER 4. BIODYNAMIC IMAGING IN REPRODUCTIVE CELLS

4.1 Introduction

Reproductive health is an important topic in health care, and infertility is a concern for many families. In the US, 6.1% of married women aged 15-44 are infertile, and *in vitro* fertilization (IVF) technology is growing about 5% per year in terms of IVF cycles [1]. The IVF birth rate over all ages of women was 30% in 2015 [2]. *In vitro* fertilization (IVF) success rates are connected to the viability of the blastocyst, and it has been shown that blastocyst quality is related to implantation and pregnancy [3]. Clinics have been transferring two or three embryos at the same time to increase the birth rate. However, this can lead to multi-pregnancy and can increase the risk of adverse health conditions in both the mother and the offspring. The best practice is to transfer only the best embryo at a time.

Morphological grading, using different grading systems, is used to evaluate sample quality, but it is a subjective process [4]. Other non-invasive methods include analysis of spent culture media, metabolomics, and most recently, time-lapse monitoring of embryo development [5]. However, currently there is no solid evidence from randomized controlled trials (RCT) that show these non-invasive techniques are effective in improving the birth rate [6, 7]. Invasive methods usually involve biopsy and manipulation of blastocysts [8] and may be detrimental to later development of samples [9].

Therefore, there is an urgent need for a technology that can serve as the standard of embryo selection. This project aims to create a set of biodynamic imaging biomarkers that is representative of embryo viability and eventually to use it to select good embryos to transfer. This chapter includes several approaches to connect BDI measurements (or their surrogates) with embryo developmental potential and describes experiments related to the development of reproductive cells[3].

[3] Content from this chapter has been published in Z Li, N Ehmke, IM Lorenzo, Z Machaty, DD Nolte, Biodynamic optical assay for embryo viability, J. Biomed. Opt. 24, 1 (2019).

4.2 Methods

4.2.1 Porcine Developmental Biology

In female meiosis, oogenesis consists of three parts: oocytogenesis and ootidogenesis. Oocytogenesis starts the process of developing primary oocytes and is completed before or shortly after birth. Ootidogenesis follows oocytogenesis when a primary oocyte develops into an ootid by meiosis, which leads to 3 polar bodies and 1 ootid. Folliculogenesis occurs at the same time as ootidogenesis, as it refers to the cellular development of the follicle containing an oocyte. This cellular development of the follicle is critical for creating a network with the oocyte to induce and encourage the maturation brought on by ootidogenesis.

In males, spermatocytogenesis is defined as the first and second meiotic division of the male germ cell into primary spermatocytes which form four spermatids. After a series of morphological changes known as spermiogenesis, these round spermatids become spermatozoa.

Fertilization is a series of processes, including spermatozoa penetrating corona radiata, spermatozoa attaching and penetrating zona pellucida and binding and gamete fusion. When the process of fertilization completes, the fertilized egg is called a zygote. Cleavage is the next stage of the embryo. For the first two days, the embryo develops at approximately one cleavage division per blastomere (embryo cell) per day. The embryo is called a morula when it consists of around 16 cells. The zygote then grows into a blastocyst after a phase called compaction, when it consists of two types of cells, trophoblast and inner cell mass. Six to eight days after fertilization in porcine and primate species, the embryo implants into the wall of the uterus.

IVF is the process when fertilization occurs *in vitro*. It also includes co-incubation of the sperm and the egg, and embryo culture, during which embryo selection can be performed. This process takes place during the blastocyst stage of embryonic development in this project.

4.2.2 Sample Preparation

Ovaries were collected from slaughtered pigs, and follicular contents were aspirated from individual follicles in the lab using a hypodermic needle attached to a 10-mL syringe. The oocytes with attached cumulus cells (COCs) were collected from the follicular fluid by means of a stereomicroscope, washed in TL-Hepes medium, and good-quality oocytes were selected for *in*

vitro maturation in the appropriate medium. Matured COCs were placed in 0.1% hyaluronidase, vortexed until denuded and washed in TL-Hepes medium.

Denuded oocytes either undergo parthenogenetic development, or they are incubated with sperm to become IVF embryos. To develop parthenogenetic embryos, oocytes were placed in electroporation medium in a chamber containing two stainless steel electrodes 0.5 mm apart. Parthenogenetic development was induced via electroporation with two direct-current pulses one second apart of 1.2 kV/cm, 60 µs each via a CF-150/B Cell Fusion Instrument. After electric stimulation, prospective embryos were rinsed in TL-Hepes medium and placed into 20 µL droplets of PZM-3 medium. In a negative control group, the medium contained the metabolic inhibitor sodium azide (NaN_3). Each droplet contained 10 embryos, the droplets were covered with light mineral oil to prevent evaporation, and culture dishes containing the droplets were placed in a CO_2 incubator. Both groups were allowed to culture in their prospective medium up to 96 hours, at 39 °C, under 5% CO_2 in air. For *in vitro* fertilization, semen was collected from a boar and diluted with an extender that facilitates prolonged chilled storage. Before fertilization of the oocytes, 600 µL of this extended semen was added to a medium and the sperm cells were washed by centrifugation. The sperm pellet was then resuspended in the fertilization medium. The matured oocytes were agitated in the presence of hyaluronidase to remove the surrounding cumulus cells. The denuded oocytes were co-incubated with sperm at a 10^6/mL concentration in fertilization medium for 5 hours. Fertilized oocytes were then removed from the fertilization medium, washed, and placed in the culture medium the same as before.

After the culture period, the embryos that had reached the early morula stage were selected for assessment. For BDI measurements, each sample was washed in each of the dishes and plated in 50 µL PVA-free TL-Hepes droplet and covered with mineral oil. The plate was heated with the temperature maintained at a physiological 39 °C. A complete BDI dataset for a sample contains 100 background frames and 2500 holograms, captured at 25 fps with an exposure time of 20 ms. The coherence gate was placed approximately at the middle of the sample at a depth of about 100 µm from the embryo surface. The BDI measurement finishes in a short time (1-2 minutes of sample preparation and 2 minutes of data acquisition), putting samples within a safe light exposure range and a non-CO_2 controlled environment.

As mentioned above, when placing samples in culture dishes, they are usually put in groups of 10 in a droplet to achieve better development [10-12]. However, doing so loses the ability to label each sample, which is required in experiments where the correlation between a sample's development and its BDI signatures is studied. A solution is this problem is to use the "well-in-well" method, i.e. using needles to drill small wells in the petri dishes, label them, and place the samples in these wells. This allows samples to share the same droplet environment while maintaining sample identification. This method is illustrated in Figure 4-1. Potential issues with the method include access to oxygen, the lack of which can lead to sample deaths.

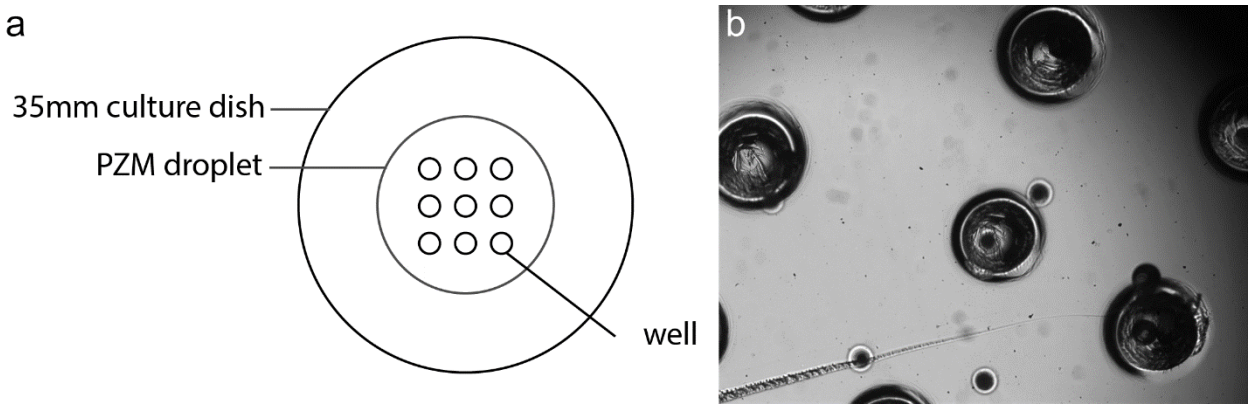

Figure 4-1 Illustration of the "well-in-well" method. a) layout of the smaller wells (sizes are exaggerated). b) microscopy image of the smaller wells.

4.2.3 Morphological Grading

For day 6/7 blastocysts, the Gardner grading system [13] is applied. It scores a blastocyst using three categories: the blastocyst developmental stage, the inner cell mass quality, and the trophectoderm quality. The developmental stage is scored from 1 to 4, with 1 being given to a blastocyst with a small blastocoelic cavity and a 4 being given to a fully expanded and hatched blastocyst. Inner cell mass quality is scored from A to C, with A being given to an embryo with many cells in the inner cell mass that are tightly compacted, and a C being given to an embryo with few cells in the inner cell mass that are loosely packed. Trophectoderm quality was assessed in a manner similar to inner cell mass quality, scored from A to C. A was given to samples with many cells in a cohesive trophectoderm layer, whereas C is given to embryos with large and few cells in the trophectoderm layer. The alphanumeric scores are converted to scores ranging from 3-

18 using the conversion in Table 4-1. The numerical score is the sum of the scores from three categories. As an example, a sample with grading "3AB" would have a score of 15.

Table 4-1 Conversion from blastocyst morphological grading to numerical values.

Categories	Developmental stage				Inner cell mass quality			Trophectoderm quality		
Grading	4	3	2	1	A	B	C	A	B	C
Score	6	5	2	1	6	4	1	6	4	1

Four-day parthenotes and *in vitro* fertilized embryos are graded on a scale of 1 to 5. Examples are given in Table 4-2.

Table 4-2 Grading of 16-cell embryos, examples and descriptions.

Grade	Image	Description
1	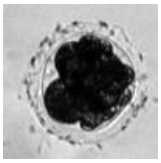	Non-spherical overall structure, fragmentation, unequal size of blastomeres
2	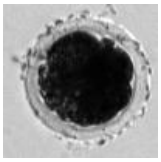	Unsynchronized cellular division and unequal size of blastomeres
3	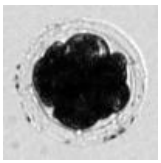	Unequal size of blastomeres
4	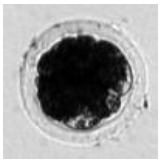	16-cell stage, unequal size of blastomeres
5	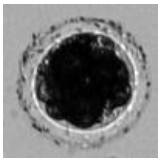	Synchronized cellular division, 16-cell stage and equal size of blastomeres

4.2.4 BDI Measurement and Processing

The microscope images and BDI measurements in this study were taken on the biodynamic microscope (BDM; ADI, Indianapolis, IN), which is a dual-mode imaging system modified from an Olympus IX-73 microscope. The microscope is capable of switching between a conventional transillumination microscope and a BDI system. The BDI mode operates in a similar way to the "Alpha Prime" system, and details of the microscope are given in appendix chapter A.2.

Samples were assessed using the BDM by evaluating speckle fluctuation properties. A BDI dataset includes 100 background and 2500 hologram frames of the sample, captured at 25 fps, with an exposure time of 20 ms. Each sample was characterized by OCI as shown in Figure 4-2(b), MCI

as shown in Figure 4-2(c) and the Doppler power spectrum as shown in Figure 4-2(d) and (e). Sample spectra span a range of 0.01 – 2 Hz and are fit with a "stretched" Lorentzian lineshape

$$S(\omega) = \frac{A}{\omega_0^s + \omega^s} + N_y \tag{4.1}$$

where ω_0 is the knee frequency (the "roll-over" frequency of the spectrum, i.e. where the curvature is at its maximum), s is the slope in the mid-frequency range, and N_y is the Nyquist floor. These parameters are potential biomarkers of embryo viability. Typically, an azide–treated spectrum displays a lower knee frequency, which is correlated with slower intracellular activities. Azide-treated spectra also have a greater dynamic range and a steeper mid-frequency slope on a log-log power spectrum graph. In addition, the spectrum is characterized by slope and R^2 values from linear fittings on the log scale (i.e. a power-law fitting model $S(\omega) = a\omega^{-b}$), both "globally" on the entire spectrum and "locally" in 3 frequency ranges: 0.01 – 0.08 Hz, 0.08 – 0.4 Hz and 0.4 – 2Hz. Values of b and R^2 are used to describe the spectrum shape (values for the three ranges use the notations b_1, b_2, b_3, r_1, r_2 and r_3). Typical values for these parameters across a range of parthenotes are listed in Table 4-3.

Table 4-3 Typical values for biodynamic biomarkers

Quantity	A	ω_0	s	N_y	r	b_1	r_1	b_2	r_2	b_3	r_3
Value	0.04	0.012 Hz	1.86	1.01	0.97	0.97	0.93	1.54	0.98	1.09	0.97

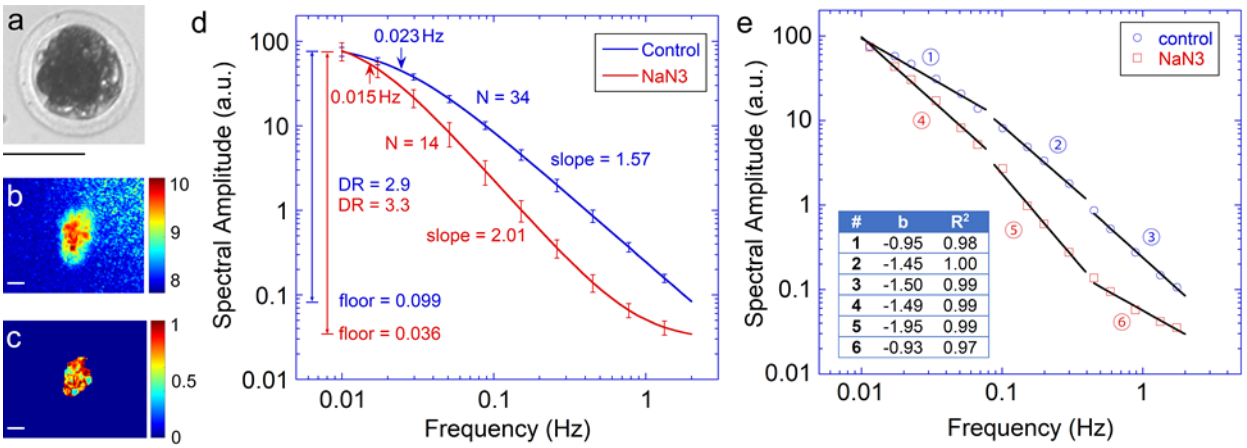

Figure 4-2 (a) Microscope image of a parthenote sample captured in transillumination. (b) OCI of the sample. The color map is on the log scale. (c) MCI of the same sample. The value of each pixel is NSD (scale bar = 100 µm in a,b and c) (d) Averaged fluctuation spectra (smoothed) of control samples and NaN_3-treated samples plated in PVA-free TL-Hepes droplets, with different knee frequencies, slopes, Nyquist floors and dynamic ranges ("DR") on the log-log scale. Standard errors are used as values of error bars. (e) An example of 3-segment linear fitting for spectra. (Markers are a subset of data points with even intervals)

4.2.5 TUNEL Assay

Blastocysts were fixed in a dish containing 3.7% paraformaldehyde. They were then washed in phosphate-buffered saline (PBS) and permeabilized in 0.2% Triton X-100. The sample was again washed in PBS, and then stained for apoptosis using the Promega Tunel Apoptotic Detection Kit. The blastocyst was covered in reaction stain mix and incubated for 60 mins at 37°C, after which the reaction was halted using the stop solution of the kit. The blastocyst was then washed in PBS and stained with Hoechst 33342 to determine the number of nuclei. Finally, the sample was rinsed at room temperature, mounted on a microscope slide and examined using a fluorescence microscope.

4.2.6 ATP Measurement

ATP measurements were performed using Molecular Probes™ ATP Determination Kit on a Spark™ 10M multimode microplate reader. A standard curve was obtained based on bioluminescence from the reactions of standard solutions with known ATP amount. Bioluminescence of each sample was measured and compared against the standard curve and converted to the respective ATP amount of substance.

4.2.7 Timeline

The timeline for the experiments in this project is shown in Figure 4-3.

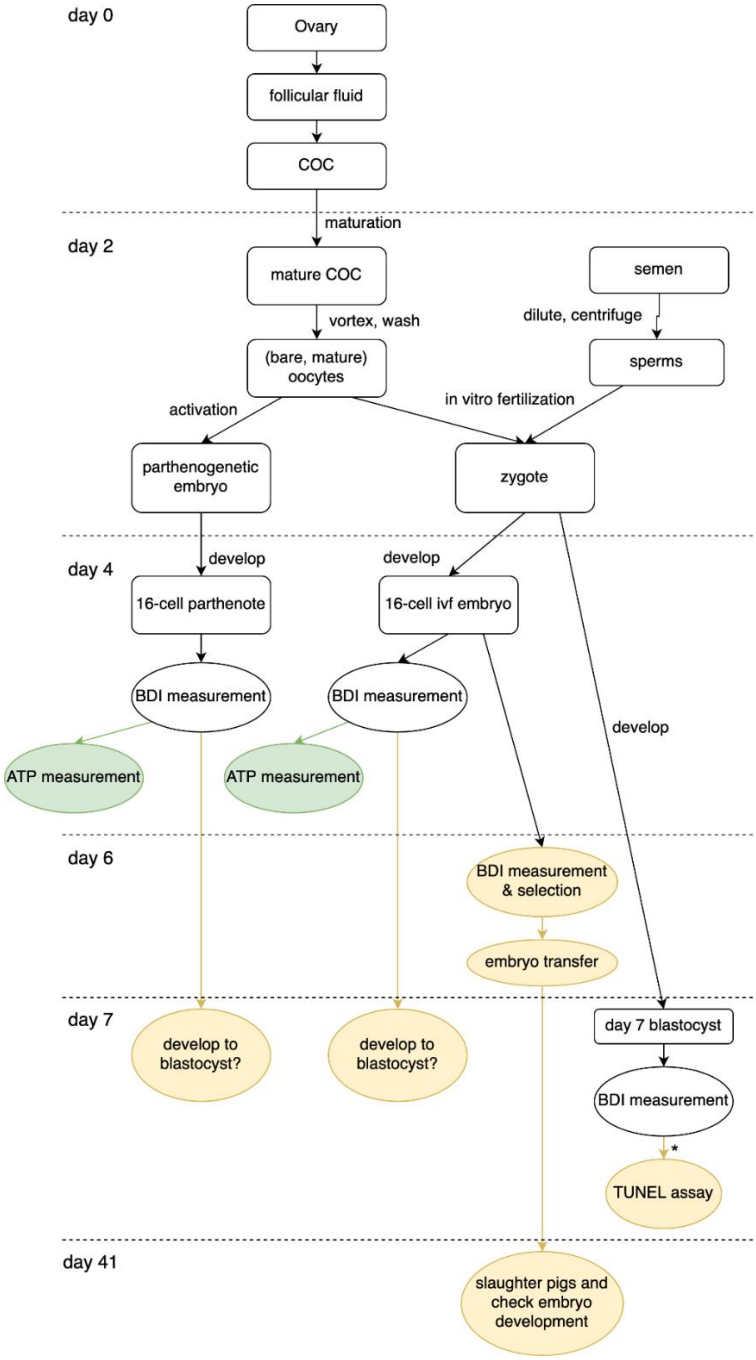

Figure 4-3 Timeline for developmental stages of reproductive cells and their related measurements and tests. Squares denote sample type and circles denote measurements and tests. Green circles are successful experiments, while yellow circles are experiments that are not finished or did not lead to conclusive results.

4.3 Embryo Viability Evaluations

4.3.1 Blastocyst Development

Whether an embryo develops to blastocyst stage, and eventually develop to term *in vivo*, is the "ground truth" for embryo viability by definition. This section discusses the correlation between BDI signatures and blastocyst development. A basic experiment is to evaluate the biodynamic signature of embryos at an early stage (e.g. parthenotes or IVF embryos developed to 16 cells), and check whether they develop to full blastocyst at day 6/7. However, the labeling of each sample is an important technical issue, and a "well-in-well" method would be used for sample labeling. This approach has yet to lead to a conclusion due to low sample numbers related to sample development issues.

4.3.2 Morphology

While morphology is a subjective metric, it is fast and has proven to be successful in predicting embryo viability [3], and has been used as a biological proxy for sample development potential when selecting embryos in clinical settings. A straightforward test is to record the morphological grading of samples, run BDI measurement and analysis, and correlate the results from the two studies.

Morphology is not found to be highly related to BDI metrics. Among 16-cell IVF embryos shown in Figure 4-4 (N=64), samples with higher grading do not have a statistically significant difference in the mean of NSD in two-sample t-tests, except grade 1 and grade 5 samples (p=0.02). In the scatter plot, there is also no evident separation among samples with different grades.

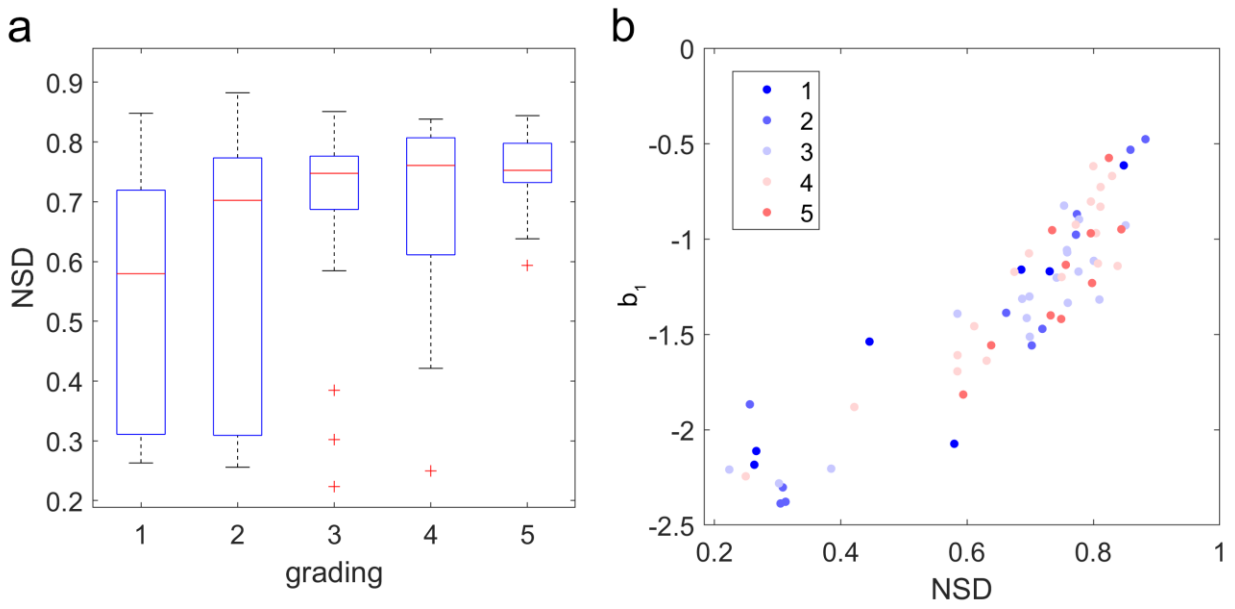

Figure 4-4 a) boxplot of sample NSD, grouped by their grades. b) Scatter plot of sample "b_1" and "NSD" biomarkers, grouped by their grades.

4.3.3 Apoptosis and TUNEL Assay

Embryo quality is related to apoptotic cells in the developing embryo [10]. Apoptosis is believed to be a mechanism that helps to remove cells with chromosomal abnormalities or inappropriate developmental potentials, but it may also be an indication of the embryo responding to adverse developmental environment [11]. If apoptosis surpasses a certain threshold, embryonic development is compromised and may cause embryo death. In this study, results from TUNEL assay, a staining method of cell apoptosis, is used as a surrogate for embryo quality. The study was not successful mainly due to sample immobilization issues (discussed in appendix chapter D.3). There is a low correlation between TUNEL apoptosis number and morphological grading, as shown in Figure 4-5.

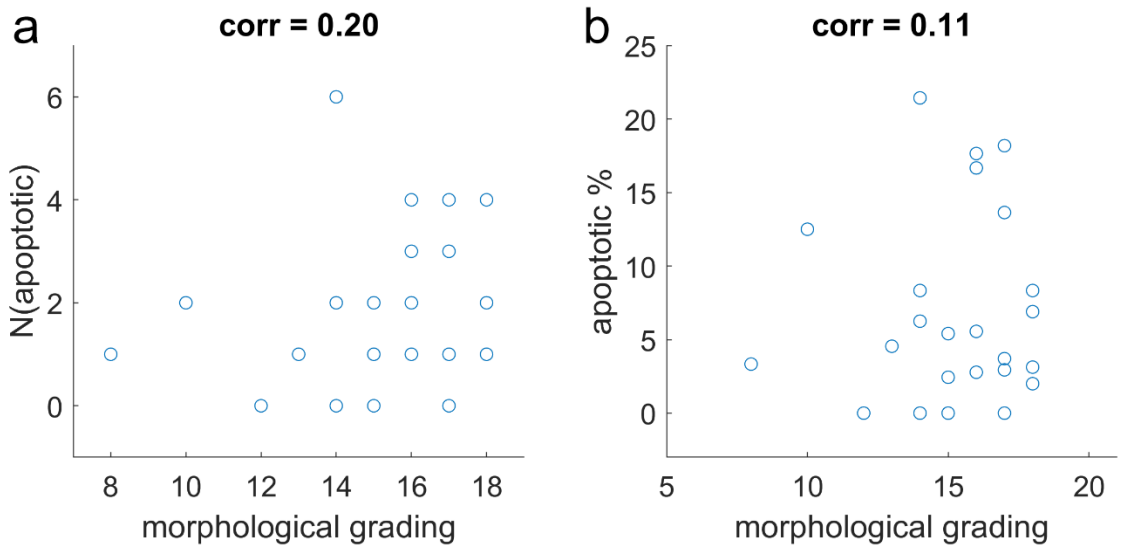

Figure 4-5 Scatter plot of morphological grading vs the number of apoptotic cells from TUNEL assay, and grading vs apoptotic cell percentage.

4.3.4 ATP

Mitochondrial ATP production of the embryo is related to its ability to develop into a healthy blastocyst[14, 15]. In this study, ATP measurements of parthenogenetic embryos are correlated with their BDI feature values, and a machine learning algorithm is used to construct a classifier.

There are two phases in this study. The first phase investigates whether parthenotes incubated with sodium azide (NaN_3) can be separated from normally-developed samples with BDI signatures. The second phase imitates the actual embryo transfer, removes the external stressor (NaN_3) and determines if samples can be separated into a high viability group and a low viability group.

In the first phase, a total of 133 embryo samples measured on 12 separate days were used in the analysis, consisting of 85 control samples and 48 NaN_3-treated samples. The BDI data for the samples with different immobilization methods are normalized and combined in the analysis. When an embryo is cultured with dilute NaN_3 at the 1-cell stage, the azide ion (N_3^-) inhibits the electron transport in the mitochondrial membrane and decreases oxidative phosphorylation. Mitochondrial ATP production of the embryo is thus inhibited, and its ability to develop into a healthy blastocyst is significantly reduced.

Analysis of the sample ATP content shows that the control-group parthenotes have significantly more ATP than NaN_3-treated samples (shown in Figure 4-6(a) with a p-value $p < 10^{-3}$) which signifies that the control-group of parthenotes are metabolically more active. Therefore, a test was run to determine if sample treatment is predictive of sample ATP content with the control-group labeled as condition positive, and ATP content is used as the score. ATP content greater than a threshold value was predicted positive, and ATP content less than that value was predicted negative. A true positive rate (TPR) and a false positive rate (FPR) are calculated for each threshold, and a ROC curve with the threshold as the varying parameter is shown in Figure 4-6(b). This classifier achieves an 89.7% accuracy at an ATP threshold of 5 nmol.

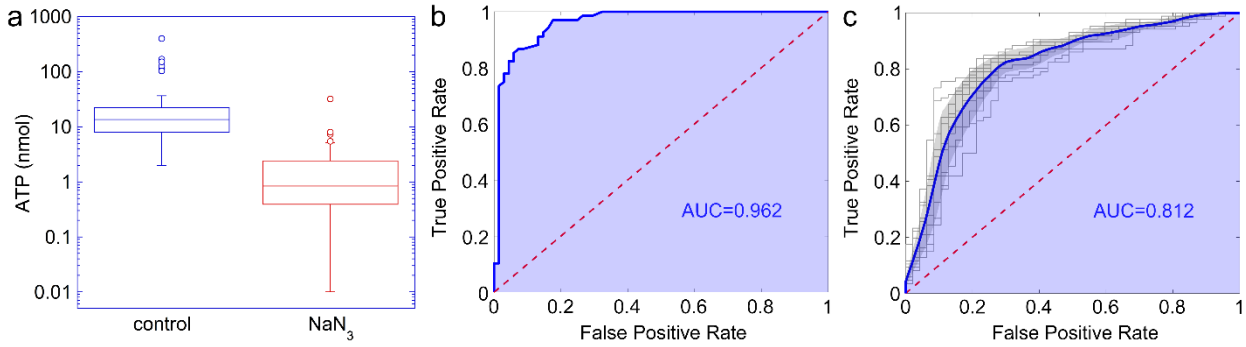

Figure 4-6 (a) Box plot of ATP content in "natural" parthenotes and NaN_3-treated parthenotes. (b) ROC curve of the sample ATP biochemical assay (c) ROC curves and averages from 10 runs of the 5-fold cross-validated SVM classifier on the biodynamic feature vector. The blue curve is the average of true positive rates for each false positive rate, while the grey area is the ±1 standard deviation of the true positive rates.

In this correlative study, biomarkers were used to build sample classifications and estimate the predictive ability of the BDM assay to select embryos with high metabolic activity. A feature vector contains the key biodynamic biomarkers that represent sample properties with 13 elements (BB, NSD, knee, mid-frequency slope, R^2 value of spectrum, floor, DR, and b and R^2 values from 3 frequency ranges). Principal component analysis (PCA) was used for dimensionality reduction, and 9 principal components accounted for 95% of variances, after which a quadratic-kernel support vector machine (SVM) was used to predict the sample group (using MATLAB® Statistics and Machine Learning Toolbox™). In this analysis, the "control" group was defined as condition positive, while the NaN_3–treated samples were defined as condition negative. A 5-fold cross-validation was used to characterize the performance of the SVM classifier, where a classification score, indicating a signed distance from the observation to the decision boundary, was assigned to each sample. Choosing a 5-fold cross-validation ensures that the test groups are large enough (with

n ~ 26 in each group) and that the bias is low. The 5-fold cross-validation was run 10 times, and in each run TPR and FPR values were calculated with varying score thresholds, creating the ROC curves plotted in Figure 4-6. The SVM classifier performed with an AUC of 0.812 and an accuracy of 79.3%, as shown in Figure 4-6c).

The second phase of the study is to create a binary classifier to predict "natural" samples (i.e. not disturbed by external stressor) as high-viability or low-viability. Samples with higher (than median) ATP consistently have higher Nyquist floor and b_1 values (Figure 4-7), but the separation from the lower ATP samples is not good enough to achieve high accuracy with classifiers. This can be attributed to a number of factors, including the accuracy of ATP measurement, sample handling and variability in sample condition.

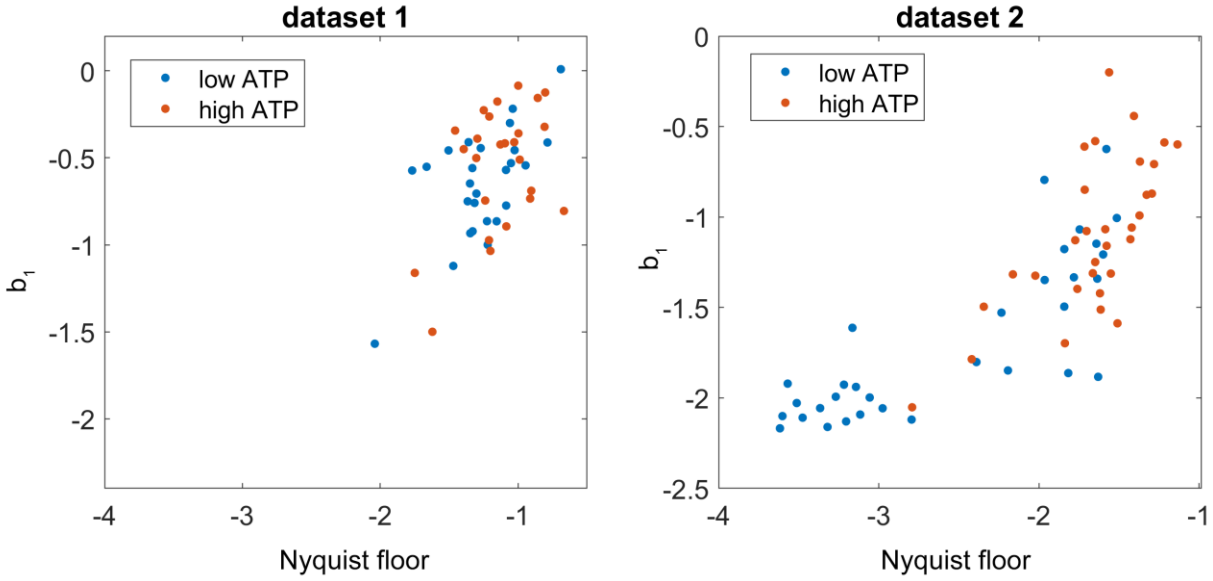

Figure 4-7 Nyquist floor – b_1 slope scatter plot for two datasets. Most of the higher ATP samples appear in the upper right corner. Dataset 1 includes data from naturally developed parthenotes measured in 2018 that were immobilized with Cell-Tak, and dataset 2 includes data from naturally developed parthenotes measured in 2019 that were immobilized with PVA-free TL-Hepes.

The current strategy for embryo transfer is to select embryos with relative high Nyquist floor and b_1 values, as shown in Figure 4-8. While these untreated samples span a large area, most of the samples that have the highest ATP samples are in the solid red circle on the upper right corner. Embryo selection will use samples that are roughly located in the region denoted by the dashed line.

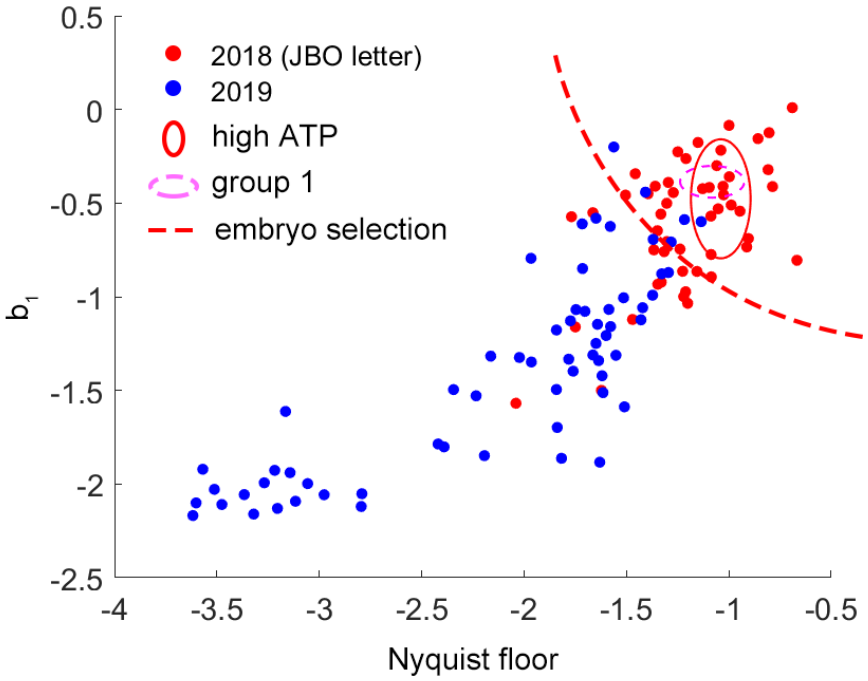

Figure 4-8 Existing sample marked by their Nyquist floor and b_1 values, and the proposed criteria for embryo selection. The ellipse of "high ATP" is one standard deviation from the average of the Nyquist floor and b_1 value of samples with the highest ATP content.

In conclusion, biodynamic imaging of intracellular activity has been demonstrated on early-stage parthenotes as biologically-relevant models of natural embryos. The biodynamic assay performs as a surrogate for destructive ATP assays and can distinguish parthenotes that have high metabolic activity from parthenotes that have compromised metabolism. This assay is non-invasive and can be performed longitudinally to track embryo health while preserving embryo viability. This optical technique has the potential to improve IVF success rates. The next step is a prospective preclinical trial during which porcine embryos will be evaluated with BDI and then transferred *in utero* in sows to establish pregnancy rates for BDI-selected transfer relative to conventional selection.

References

[1] "2011 assisted reproductive technology fertility clinic success rates report," (US Dept. of Health and Human Services, 2013).

[2] D. o. R. H. National Center for Chronic Disease Prevention and Health Promotion, "2015 Assisted Reproductive Technology National Summary Report," (Centers for Disease Control and Prevention, 2017).
[3] B. Balaban, B. Urman, A. Sertac, C. Alatas, S. Aksoy, and R. Mercan, "Blastocyst quality affects the success of blastocyst-stage embryo transfer," Fertil Steril **74**, 282-287 (2000).
[4] P. W. Farin, J. H. Britt, D. W. Shaw, and B. D. Slenning, "Agreement among evaluators of bovine embryos produced in vivo or in vitro," Theriogenology **44**, 339-349 (1995).
[5] P. Kovacs, "Embryo selection: the role of time-lapse monitoring," Reproductive Biology and Endocrinology **12**, 124 (2014).
[6] C. Racowsky, P. Kovacs, and W. P. Martins, "A critical appraisal of time-lapse imaging for embryo selection: where are we and where do we need to go?," Journal of assisted reproduction and genetics **32**, 1025-1030 (2015).
[7] Y. G. Wu, E. Lazzaroni-Tealdi, Q. Wang, L. Zhang, D. H. Barad, V. A. Kushnir, S. K. Darmon, D. F. Albertini, and N. Gleicher, "Different effectiveness of closed embryo culture system with time-lapse imaging (EmbryoScope(TM)) in comparison to standard manual embryology in good and poor prognosis patients: a prospectively randomized pilot study," Reproductive biology and endocrinology : RB&E **14**, 49 (2016).
[8] G. Kakourou, S. Jaroudi, P. Tulay, C. Heath, P. Serhal, J. C. Harper, and S. B. SenGupta, "Investigation of gene expression profiles before and after embryonic genome activation and assessment of functional pathways at the human metaphase II oocyte and blastocyst stage," Fertil Steril **99**, 803-814.e823 (2013).
[9] K. Kirkegaard, J. Juhl Hindkjaer, and H. J. Ingerslev, "Human embryonic development after blastomere removal: a time-lapse analysis," Hum. Reprod. **27**, 97-105 (2012).
[10] Y. Nagao, R. Iijima, and K. Saeki, "Interaction between embryos and culture conditions during in vitro development of bovine early embryos," Zygote **16**, 127-133 (2008).
[11] M. C. Abraham, H. Gustafsson, A. Ruete, and Y. C. B. Brandt, "Breed influences on in vitro development of abattoir-derived bovine oocytes," Acta Veterinaria Scandinavica **54**, 36 (2012).
[12] S. J. Dai, C. L. Xu, J. Wang, Y. P. Sun, and R. C. Chian, "Effect of culture medium volume and embryo density on early mouse embryonic development: tracking the development of the individual embryo," Journal of assisted reproduction and genetics **29**, 617-623 (2012).
[13] R. Jansen, and D. Mortimer, *Towards Reproductive Certainty: Fertility and Genetics Beyond 1999: The Plenary Proceedings of the 11th World Congress* (Taylor & Francis, 1999).
[14] J. Thompson, C. McNaughton, B. Gasparrini, L. McGowan, and H. Tervit, "Effect of inhibitors and uncouplers of oxidative phosphorylation during compaction and blastulation of bovine embryos cultured in vitro," Journal of Reproduction and Fertility **118**, 47-55 (2000).
[15] Z. Macháty, J. G. Thompson, L. R. Abeydeera, B. N. Day, and R. S. Prather, "Inhibitors of mitochondrial ATP production at the time of compaction improve development of in vitro produced porcine embryos," Molecular Reproduction and Development **58**, 39-44 (2001).

CHAPTER 5. INTRACELLULAR DYNAMICS FOR CYTOSKELETAL DRUGS

5.1 Introduction

Anti-cancer drug development has high expenses and low yield. The overall clinical success for oncology products in clinical development is 10%, costing over one billion dollars to bring a new drug to market [1]. To reduce the cost, especially to minimize failure in clinical trials, it is important to dismiss compounds that are ineffective or too toxic as early as possible in the drug development pipeline by using physiologically-relevant cell culture. In cancer drug development, 3D tissue cultures are replacing conventional 2D cultures. Although 2D cell models have been used widely for compound selection, they do not mimic *in vivo* conditions. For instance, 2D cells adhere to a substrate as a monolayer and are only in contact with peripheral cells. Many cellular microenvironmental features are missing, including oxygen and nutrient gradients and cell polarity [2]. Gene expression and growth characteristics are altered due to deficiency in cell-cell and cell-matrix interactions [3]. Therefore, 2D cell culture does not model the organization and architecture of an *in vivo* physiological environment, and preclinical studies based on conventional 2D cell lines often fail to predict drug efficacy in human trials, illustrating the limitation of 2D cell culture [4].

In 3D tissues, on the other hand, cells have physiological cell-cell and cell-matrix interactions that enable complex transport dynamics for nutrients and cells. 3D tissues are closer to the real microenvironment compared to 2D layers in many aspects, including viability, morphology, adhesion, migration, gene expression, drug metabolism and response to stimuli [2, 5]. *In vitro* 3D cultures are believed to fill the gap between 2D in *vitro* testing and animal models and are recommended in drug screening programs[2, 6-8]. Multicellular tumor spheroids (MCTS) are one of the 3D tumor models [9, 10]. The growth of spheroids mimics the growth of naturally occurring *in vivo* tumors and mirror their 3D cellular context. Four common approaches to spheroid culture are: ultra-low attachment plates, hanging drop, bioreactor and micropatterned surface [7]. The advantages of the three-dimensional cell culture for drug screening is partially negated by the difficulty of imaging into deep tissue using conventional microscopy. However, coherence-based laser ranging approaches similar to optical coherence tomography (OCT) can penetrate up to 1

mm inside tissues. Of particular relevance for deep three-dimensional drug screening is a modification of OCT known as biodynamic imaging (BDI).

Biodynamic imaging is sensitive to intracellular transport and has been successfully used to profile drug effects in 3-D cell culture. BDI has been used to classify drugs based on UMR-106 cell responses [11], to separate core and shell responses with apoptotic index [11] and to match resistant/sensitive responses to platinum of tumor xenografts with clinical results using a logistic predictor [12]. BDI is a label-free and non-invasive technology that is a potential tool in early anti-cancer drug screening. It has been used previously to study the effects of cytoskeletal drugs on intracellular dynamics [13, 14].

The cytoskeleton is a system of filaments that is important in many cell functions, including giving the cell shape and making it robust. It also has dynamic functions such as rearranging internal components, cellular shape changing, and migration [15, 16]. Most animal cells have three types of cytoskeletal elements: intermediate filaments, microtubules, and actin filaments. Cytoskeletal filaments are dynamic and adaptable. For instance, intermediate filaments form a protective cage for DNA and provide protection for organs against metabolic, oxidative, and chemical stresses. Actin filaments provide strength and shape to the thin lipid bilayer of animal cells and form many types of cell-surface projections. Their functions also include muscle contraction, cell movement and intracellular transport. Microtubules rearrange themselves to form a bipolar mitotic spindle during cell division, form cilia and flagella on the surface of the cell, and work as tracks for the transport of materials in intracellular transport.

Microtubules and the actin cytoskeleton of cancer cells are successful targets for anticancer therapy [17, 18]. Microtubule-targeting drugs can suppress microtubule dynamics without changing microtubule mass, which leads to mitotic block and apoptosis [18]. Actin drugs such as latrunculins and the cytochalasins inhibit actin polymerization and disrupt the function of the actin cytoskeleton [19], whereas jasplakinolide stabilizes actin filaments *in vitro* while it disrupts actin filaments in *vivo* and induces polymerization of monomeric actin into amorphous masses [20].

In this chapter, biodynamic imaging is used to provide phenotypic profiles of several cytoskeletal drugs that have a wide range of mechanisms of action (MoA). These profiles serve as “fingerprints” of the drug MoA and can be stored in a library of fingerprints that can be queried by machine-learning clustering algorithms when classifying the activity of new or unknown

compounds. In this study, seven cytoskeletal drugs are used, listed in Table 5-1 with their mechanism of action. The cytochalasin and latrunculin inhibit the polymerization of actin, while jasplakinolide enhances actin polymerization. The drugs colchicine and nocodazole inhibit microtubule polymerization, while the taxanes stabilize microtubules. In contrast, blebbistatin is a molecular motor inhibitor that inhibits ATPase activity. These 7 drugs represent 5 different molecular mechanisms of action. All are anti-mitotic drugs, inhibiting cell division by perturbing cytoskeletal functions. Because biodynamic imaging is sensitive to subtle changes in intracellular motion, drugs that affect the cytoskeleton are particularly strong inducers of biodynamic fingerprints.

5.2 Methods

5.2.1 Drugs

A list of drugs used in the study, their MOA, and the concentrations in the paper are listed in Table 5-1.

Table 5-1 Cytoskeletal drugs used in the study

Drug	Target cytoskeletal component	Mechanism of action (MoA)	Concentration	Reference
jasplakinolide	actin	enhances polymerization	40-60 nM	[20]
cytochalasin D		inhibits polymerization, induces depolymerization	160-200 nM	[21]
latrunculin A		prevent polymerization, enhance depolymerization	200 μM	[22]
paclitaxel	microtubule	stabilizes microtubules and therefore prevents mitosis	10 μM	[23]
colchicine		prevents polymerization	4 μM	[24]
nocodazole			10 μM	[25]
blebbistatin	molecular motor	inhibits myosin ATPase activity	60 μM	[26]

DLD-1 samples were grown as 3D tumor spheroids using Corning U-bottom spheroid plates. Cells are divided and incubated in a 96-well plate immobilized with low gel-temperature agarose. Wells are filled with growth medium RPMI.

5.2.2 Experiment Setup

The "Alpha Prime" system described in appendix chapter A.1 was used for the experiments. Each experiment consists of measurements of 16 tumor spheroids placed in a 96-well plate. In each plate, there are 4 control wells treated with DMSO and 12 experimental wells treated with 3 different concentrations of a cytoskeletal drug.

There were two segments in each experiment, 4 hours of baseline measurement and 10 hours of drug response measurement. In each loop, spheroids in the 16 wells were imaged in sequence, and each measurement contained 500 frames of a sample at 25 fps and 50 frames at 0.5 fps, and a continuous spectrum ranging from 0.01 Hz to 12.5 Hz is constructed by stitching the spectra in the two frequency ranges [27].

5.2.3 Drug Response Space

BDI evaluates the dynamics of a biological sample with sample averaged NSD [13] and the fluctuation power spectrum. Cytoskeletal drugs added to the sample perturb the motions of intracellular components and lead to changes in speckle fluctuations. Such changes are correlated with the targeted components and the drug mechanism and can be used as signatures for the drug. For instance, NSD evaluates dynamics for the entire sample, as motions at all frequencies contribute, while the power spectrum provides more detailed information that is related to motions at certain speeds. Features like the knee frequency and the dynamic range can be extracted for each spectrum by curve fitting. Changes in the knee shape and frequency, according to the Doppler light scattering theory, are directly related to the change in persistence length of the random walk. The time-lapse evolution of spectra amplitude produces a differential spectrogram [28, 29] which can be mapped to linear masks (defined in appendix chapter C.1.2) to generate values that characterize certain features of the spectrogram, creating a series of linear biomarkers. Therefore, the result from a 10-hour experiment can be represented as a vector in a high dimensional space, where spectrogram-related values form a subspace with an inner product. With proper averaging, the

effect of a drug at a given concentration is a point in this high-dimensional "drug response" space. Amplitudes and signs reveal information about drug mechanism.

5.3 Results

5.3.1 Spectrograms

The time-lapse differential spectrograms of the 7 drugs explored in this study are shown in Figure 5-1. Jasplakinolide shows a rapid binary response, with suppression in the 0.01 – 0.6 Hz band and enhancement in the 0.6 – 12.5 Hz band. Jasplakinolide augments the rate of actin filament nucleation [30], which can be correlated with the enhancement in the activities with Doppler frequency shift > 10 Hz in the spectrogram. Cytochalasin D inhibits actin polymerization, prevents filaments from growing, leads to disassembly of actin fibers and may cause apoptosis, resulting in a weak mid-frequency enhancement in the spectrogram. It has a very long response time, and the enhancement does not saturate until near the end of our observation (~8 hours after the drug is applied) [28]. Latrunculin A also inhibits polymerization but binds to actin monomer, prevents it from incorporating into polymer, and shows a different pattern from cytochalasin. Its spectrogram drift is the weakest among the seven drugs with a slight enhancement in the low-frequency bands and suppression in the high-frequency bands.

Cytoskeletal drugs that target microtubules consistently show an increase in the low-frequency band between 0.01 Hz to 0.08 Hz. Paclitaxel stabilizes microtubules, and the spectrogram has a typical "redshift" pattern that is the opposite of jasplakinolide, indicating a shift to slower average speeds. The response time is relatively long, and the high-frequency band saturates after about 6 hours. Nocodazole and colchicine have much stronger responses than the other drugs and similar response patterns, with a slight difference in response time (6 hours to saturation vs 7 hours) and response strength.

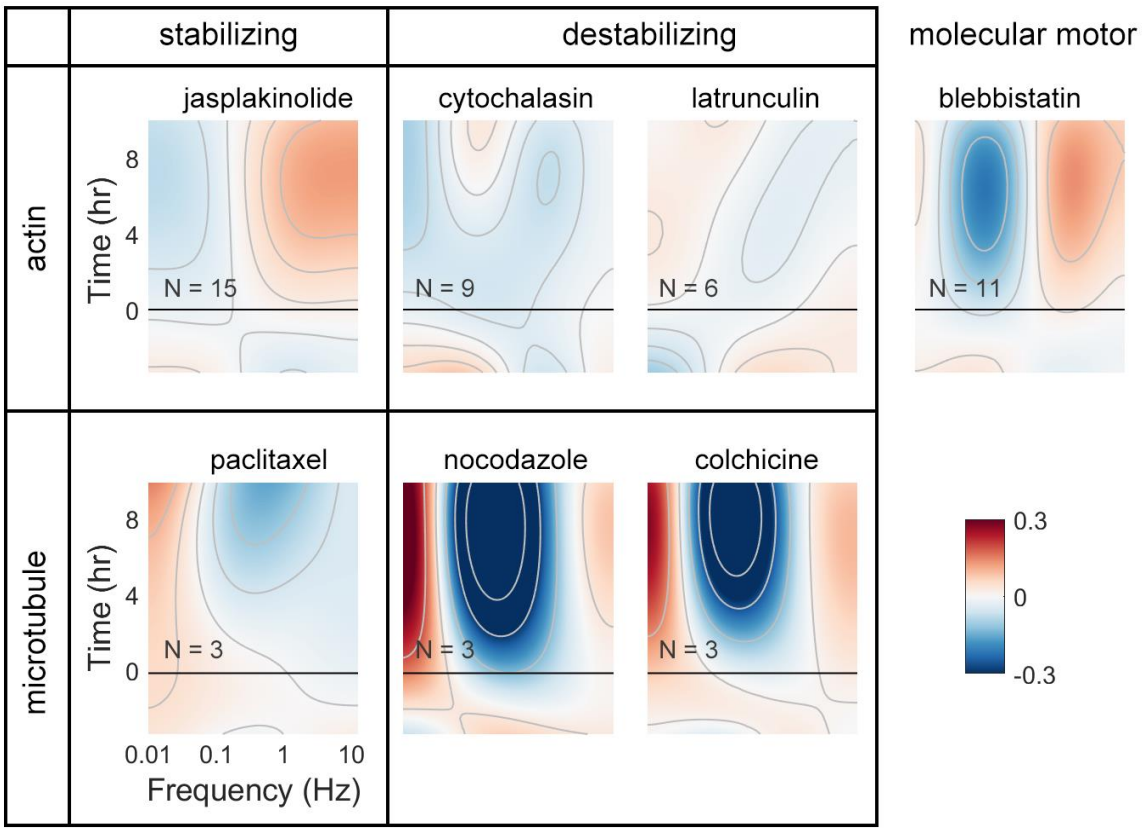

Figure 5-1 Spectrograms of DLD-1 samples treated with the seven drugs listed. Spectrograms are smoothed by interpolation (for visualization only).

Blebbistatin targets myosin II, and its response has a broad enhancement in the high-frequency band. The critical frequency is around 0.017 Hz and 0.56 Hz, corresponding to a decorrelation time of 60 and 2 seconds respectively, which is consistent with a previous report [31] where activity in the 1 – 2 Hz range increases and activity in the 0.1 – 0.3 Hz decreases.

5.3.2 Drugs in Biomarker Space

According to Figure 5-1, the DLDs generally have a monotonic response after drugs are applied at t=0. Therefore, the basic "vector" version of the spectral feature masks is applied to averaged differential spectra from the last 2 hours of measurements. The bases $\{M_1, M_2, M_3\}$ forms a $\mathbb{R}^3$ subspace that can be intuitively visualized in a 3D plot. However, M_1 and M_2 values alone contain mechanistic information, and a 2D plot is presented in Figure 5-2a. Jasplakinolide has a high negative M_1 value and a low M_2 value, which matches the strong blueshift pattern. The late

mid-frequency enhancement shown in cytochalasin agrees with its M_2 value, although the pattern being off-center makes it slightly similar to the blueshift pattern and leads to a -0.26 M_1 value. The weak response of latrunculin A places it close to origin. While paclitaxel has an obvious redshift pattern and has an M_1 value of 0.81, it shows a large M_2 because the low-mid frequency bands match that of the M_2 pattern. Nocodazole and colchicine both have large M_1 values that match their strong responses.

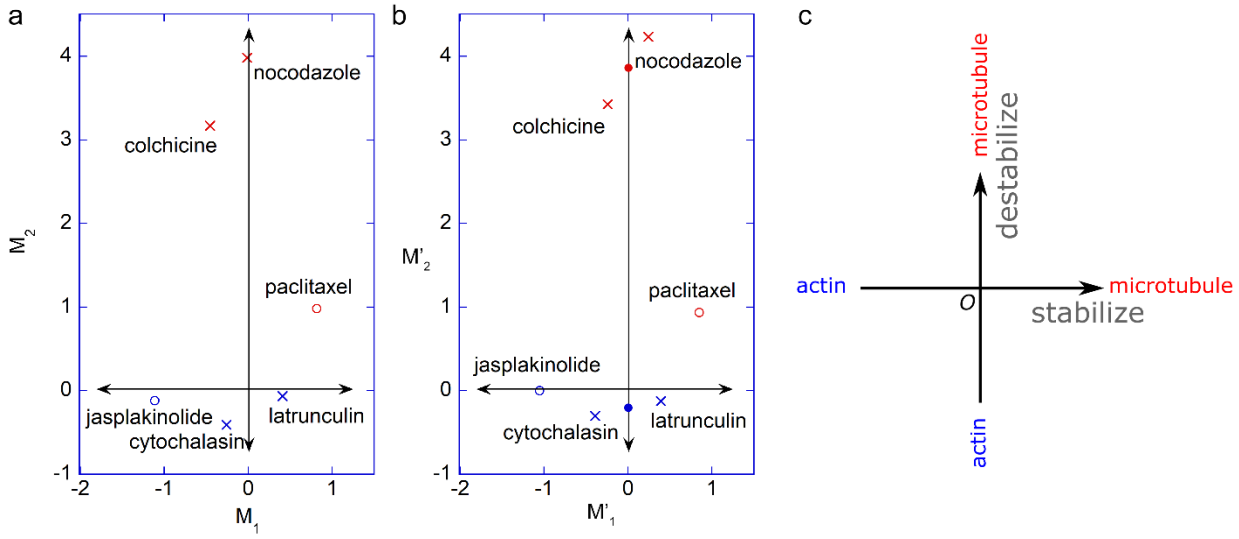

Figure 5-2 a) M_1 and M_2 feature values of the drugs presented in a 2D space (with equal axis unit); b) M_0, M_1 and M_2 subspace projected to a 2D plane. The blue filled circle is the midpoint of cytochalasin and latrunculin, while the red filled circle is the midpoint of colchicine and nocodazole c) illustration of the axes and associated mechanisms and cytoskeletal components in a).

There is an evident mechanism-based separation of drugs, and the coordinates are closely connected to their mechanisms. By including the M_0 feature, we can find a 2D plane in this subspace where the coordinates, i.e. the projection on the plane, best illustrate this idea. The plot is shown in Figure 5-2b. The jasplakinolide is on the negative M_1' axis. The midpoint of cytochalasin and latrunculin (two actin destabilizing drugs) is on the negative M_2' axis, while the midpoint of two microtubule destabilizing drugs is on the other end of this axis. Since this is a linear projection, M_1' and M_2' are still orthogonal to each other. This way, we can directly relate the axes with cytoskeletal drug mechanisms which is shown in Figure 5-2c. The horizontal axis represents stabilizing mechanisms, where the negative value is associated with actin-targeted drugs

while the positive is with microtubule-target drugs. The vertical axis represents the destabilizing mechanism.

Alternative methods also separate actin/microtubule and stabilizing/destabilizing drugs. In Figure 5-3a, positive LOF and negative MID0 biomarkers are related to microtubule drugs, while the opposite is related to actin drugs. In Figure 5-3b which features two non-linear biomarkers, actin drugs lead to much lower NSD changes than microtubule drugs.

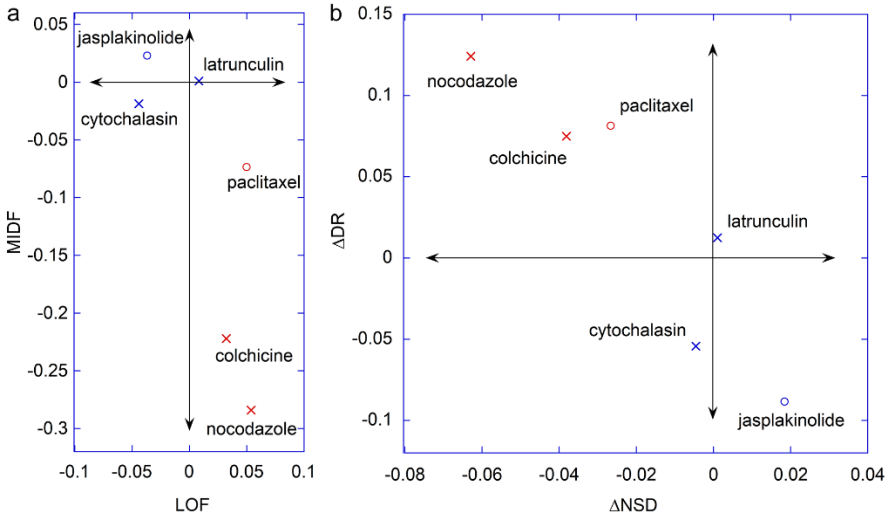

Figure 5-3 drugs represented on two other pairs of biomarkers: a) low frequency ("LOF") vs mid frequency ("MIDF"), and b) change in NSD ("ΔNSD") and change in dynamic range ("ΔDR")

5.4 Discussion

This chapter shows that the complex and diverse drug action of cytoskeletal drugs can be characterized and differentiated by Doppler fluctuation spectroscopy of cell-line tumor spheroids. Feature values obtained from broad-band spectrograms and other dynamic metrics map the drug responses to high-dimensional Euclidean spaces where the dimensions are related to targeting components and mechanisms of drugs. This effectively abstracts each drug as a point that can be located in a coordinate system, with coordinates representing drug strength and drug mechanisms and distances among drugs indicating similarity. This provides a high perspective for understanding cytoskeletal drugs.

A limitation of this method is that the feature values from BDI reflect the cell-line samples' responses to cytoskeletal drugs *in vitro*, but samples may respond to drugs differently *in vivo*. For

example, jasplakinolide, a drug used in this study, stabilizes actin filaments *in vitro* but disrupts actin filaments *in vivo*. The dose-response relationship also can complicate the drug representation in the biomarker space, as the off-target effects, especially at high concentrations, can modify the feature values from a drug's primary mechanism.

In this chapter, 7 drugs in 3 categories are featured, but the dataset can be expanded by measuring drug responses from a variety of other cytoskeletal drugs in the same way. The tissue samples in this study are DLD-1 tumor spheroids grown in flat-bottom cell-culture plates, which can be substituted with other cell lines and other 3D growth methods. One can reasonably expect to see differences in the drug response, but the same methodology could be applied. This builds a library of drug mechanisms that enables intuitive interpretation of the relationship among drugs and will help drug screening in expensive anti-cancer drug research.

References

[1] W. N. Hait, "Anticancer drug development: the grand challenges," Nature Reviews Drug Discovery **9**, 253 (2010).

[2] D. Antoni, H. Burckel, E. Josset, and G. Noel, "Three-dimensional cell culture: a breakthrough in vivo," Int J Mol Sci **16**, 5517-5527 (2015).

[3] S. Khanna, A. N. Bhatt, and B. S. Dwarakanath, "Multicellular Spheroid," 195-210 (2014).

[4] A. M. Edwards, C. H. Arrowsmith, C. Bountra, M. E. Bunnage, M. Feldmann, J. C. Knight, D. D. Patel, P. Prinos, M. D. Taylor, M. Sundstrom, and S. G. C. O. S. T.-D. Partnership, "Preclinical target validation using patient-derived cells," Nat Rev Drug Discov **14**, 149-150 (2015).

[5] F. Pampaloni, E. G. Reynaud, and E. H. K. Stelzer, "The third dimension bridges the gap between cell culture and live tissue," Nature Reviews Molecular Cell Biology **8**, 839 (2007).

[6] S. Breslin, and L. O'Driscoll, "Three-dimensional cell culture: the missing link in drug discovery," Drug Discov Today **18**, 240-249 (2013).

[7] Y. Fang, and R. M. Eglen, "Three-Dimensional Cell Cultures in Drug Discovery and Development," SLAS discovery : advancing life sciences R & D **22**, 456-472 (2017).

[8] R. Edmondson, J. J. Broglie, A. F. Adcock, and L. Yang, "Three-Dimensional Cell Culture Systems and Their Applications in Drug Discovery and Cell-Based Biosensors," ASSAY and Drug Development Technologies **12**, 207-218 (2014).

[9] L. A. Kunz-Schughart, J. P. Freyer, F. Hofstaedter, and R. Ebner, "The use of 3-D cultures for high-throughput screening: The multicellular spheroid model," Journal Of Biomolecular Screening **9**, 273-285 (2004).

[10] R. M. Sutherland, "Cell and environment interactions in tumor microregions - The multicell spheroid model," Science **240**, 177-184 (1988).

[11] R. An, J. Turek, D. E. Matei, and D. Nolte, "Live tissue viability and chemosensitivity assays using digital holographic motility contrast imaging," Applied Optics **52**, A300-A309 (2013).
[12] D. Merrill, R. An, H. Sun, B. Yakubov, D. Matei, J. Turek, and D. Nolte, "Intracellular Doppler Signatures of Platinum Sensitivity Captured by Biodynamic Profiling in Ovarian Xenografts," Sci Rep **6**, 18821 (2016).
[13] K. Jeong, J. J. Turek, and D. D. Nolte, "Imaging Motility Contrast in Digital Holography of Tissue Response to Cytoskeletal Anti-cancer Drugs,," Opt. Express **15**, 14057-14064 (2007).
[14] H. Sun, D. Merrill, R. An, J. Turek, D. Matei, and D. D. Nolte, "Biodynamic imaging for phenotypic profiling of three-dimensional tissue culture," Journal of Biomedical Optics **22** (2017).
[15] D. A. Fletcher, and D. Mullins, "Cell mechanics and the cytoskeleton," Nature **463**, 485-492 (2010).
[16] N. Wang, J. P. Butler, and D. E. Ingber, "Mechanotransduction Across The Cell-Surface And Through The Cytoskeleton," Science **260**, 1124-1127 (1993).
[17] F. Foerster, S. Braig, C. Moser, R. Kubisch, J. Busse, E. Wagner, E. Schmoeckel, D. Mayr, S. Schmitt, S. Huettel, H. Zischka, R. Mueller, and A. M. Vollmar, "Targeting the actin cytoskeleton: selective antitumor action via trapping PKCvarepsilon," Cell death & disease **5**, e1398 (2014).
[18] M. A. Jordan, and L. Wilson, "Microtubules as a target for anticancer drugs," Nat. Rev. Cancer **4**, 253 (2004).
[19] A. Holzinger, and K. Blaas, "Actin-Dynamics in Plant Cells: The Function of Actin-Perturbing Substances: Jasplakinolide, Chondramides, Phalloidin, Cytochalasins, and Latrunculins," Methods in molecular biology **1365**, 243-261 (2016).
[20] M. R. Bubb, I. Spector, B. B. Beyer, and K. M. Fosen, "Effects of Jasplakinolide on the Kinetics of Actin Polymerization: AN EXPLANATION FOR CERTAIN IN VIVO OBSERVATIONS," Journal of Biological Chemistry **275**, 5163-5170 (2000).
[21] J. F. Casella, M. D. Flanagan, and S. Lin, "Cytochalasin D inhibits actin polymerization and induces depolymerization of actin filaments formed during platelet shape change," Nature **293**, 302 (1981).
[22] E. G. Yarmola, T. Somasundaram, T. A. Boring, I. Spector, and M. R. Bubb, "Actin-latrunculin A structure and function. Differential modulation of actin-binding protein function by latrunculin A," The Journal of biological chemistry **275**, 28120-28127 (2000).
[23] B. A. Weaver, "How Taxol/paclitaxel kills cancer cells," Mol Biol Cell **25**, 2677-2681 (2014).
[24] B. N. Cronstein, Y. Molad, J. Reibman, E. Balakhane, R. I. Levin, and G. Weissmann, "Colchicine alters the quantitative and qualitative display of selectins on endothelial cells and neutrophils," J Clin Invest **96**, 994-1002 (1995).
[25] M. A. Jordan, D. Thrower, and L. Wilson, "Effects of vinblastine, podophyllotoxin and nocodazole on mitotic spindles. Implications for the role of microtubule dynamics in mitosis," Journal of Cell Science **102**, 401-416 (1992).
[26] M. Kovács, J. Tóth, C. Hetényi, A. Málnási-Csizmadia, and J. R. Sellers, "Mechanism of Blebbistatin Inhibition of Myosin II," Journal of Biological Chemistry **279**, 35557-35563 (2004).
[27] H. Sun, "Dynamic Holography in Semiconductors and Biomedical Optics," (Purdue University, 2016).

[28] D. D. Nolte, R. An, J. Turek, and K. Jeong, "Tissue dynamics spectroscopy for phenotypic profiling of drug effects in three-dimensional culture," Biomed. Opt. Express **3**, 2825-2841 (2012).
[29] Z. Li, H. Sun, J. Turek, S. Jalal, M. Childress, and D. D. Nolte, "Doppler fluctuation spectroscopy of intracellular dynamics in living tissue," J. Opt. Soc. Am. A **36**, 665-677 (2019).
[30] M. R. Bubb, A. M. Senderowicz, E. A. Sausville, K. L. Duncan, and E. D. Korn, "Jasplakinolide, a cytotoxic natural product, induces actin polymerization and competitively inhibits the binding of phalloidin to F-actin," Journal of Biological Chemistry **269**, 14869-14871 (1994).
[31] C.-E. Leroux, F. Bertillot, O. Thouvenin, and A.-C. Boccara, "Intracellular dynamics measurements with full field optical coherence tomography suggest hindering effect of actomyosin contractility on organelle transport," Biomed. Opt. Express **7**, 4501 (2016).

CHAPTER 6. INVESTIGATION OF HETEROGENEOUS DRUG RESPONSE

Dynamic intracellular motions provide the endogenous image contrast for three-dimensional optical imaging of spatial heterogeneity in tumor biopsies. Biodynamic imaging is a full-field optical coherence imaging approach based on digital holography that captures dynamic contrast through the response of living tissue to applied therapeutics. By performing Doppler spectroscopy on a voxel basis, and extracting biodynamic biomarkers, functional images are obtained of the heterogeneous spatial response of tumor tissue to anticancer drugs. This technique, called tissue dynamics spectroscopic imaging (TDSI) is applied to tumor spheroids grown from cell lines and to *ex vivo* esophageal biopsies. Spatial maps of biodynamic biomarkers are created using a bivariate color merge to represent the spatial distribution of pairs of signed drug-response biomarkers. Spatial variability of the drug response within biopsies is mapped using TDSI to quantify intra-tumor spatial heterogeneity as well as patient-to-patient variability.

6.1 Introduction

Tumor heterogeneity presents a challenge for the successful treatment of cancer using chemotherapeutics[1-5]. For instance, genetic variability in tumors caused by clonal outgrowth of selected genotypes within a tumor may cause subsets of cells with genetic variations to be resistant even while the majority of the tumor responds to treatment. Selective pressure and genetic drift of the cancer cell population during treatment often leads to patient relapse and the emergence of broad chemoresistance and refractory disease [6-8]. In addition to genetic heterogeneity, there is also spatial heterogeneity in tumor tissue arising from varying tissue constituents as well as varying microenvironments, including differences in extracellular matrix and connective tissues. The tumor microenvironment [9, 10] and epigenetic variations [9, 11-13] pose significant challenges to the selection of treatment based on genetic profiles. This has led, as an alternative, to phenotypic profiling [14-16] of cancer tissue that captures the systemic response of cancer tissue to applied therapy. The challenge for phenotypic profiling of cancer tissue is the need to image intact microenvironments deep inside tissue, far from surface damage caused by surgical resection, and

deep inside transport-limited regions that experience hypoxia, nutrient depletion and metabolite build-up.

Optical coherence imaging (OCI) [17, 18] is a deep-tissue coherence-domain imaging approach based on digital holography [19-21] that is a form of full-frame optical coherence tomography (FF-OCT) [22, 23]. Dynamic speckle in OCI images caused by dynamic light scattering from intracellular motions enables biodynamic imaging (BDI) [24] to use intracellular dynamics as a unique form of image contrast. The changes in intracellular motions caused by applied therapeutics have been studied using tissue dynamics spectroscopy (TDS) [25] to separate the effects of drugs across broad spectral bands and to capture specific signatures from different classes of drugs with different mechanisms of action [26]. Preclinical trials of therapy responsivity assessment have been completed using TDS in spontaneous canine B-cell lymphoma and in ovarian xenografts [27, 28]. In a substantially different setting, assisted reproductive technology (ART) correlates the viability of cumulus-oocyte complexes with parameters from sample fluctuation power spectra [29].

The methodology of TDS is usually applied to entire samples that can be as large as 1 mm^3 in volume (e.g. biopsies). However, intra-sample variability in the TDS signatures poses a challenge for the prediction of patient response to therapy. While previous work has identified and characterized the different baseline conditions and drug responses in the "shell" and "core" areas of the samples [26, 29, 30], in that analysis, the boundary between the shell and core was arbitrarily defined. Some samples have a more complicated drug response structure than a simple "shell" and "core" model, as shown in Figure 6-1, where the sample shows variation in both strength and pattern in its drug response in the two areas. To address this problem, we introduce a functional imaging method called tissue dynamics spectroscopic imaging (TDSI) that evaluates sample response on a pixel level. In addition to a full-duration response map, the response can be segmented along the time axis to derive the time-lapse evolution of drug response, which can reveal the different rates at which a drug acts on each area. This methodology offers a quick, intuitive visualization of sample heterogeneity and drug effects. Sample heterogeneity is verified with high-resolution 3D images obtained from inverted selective plane illumination microscopy (iSPIM).

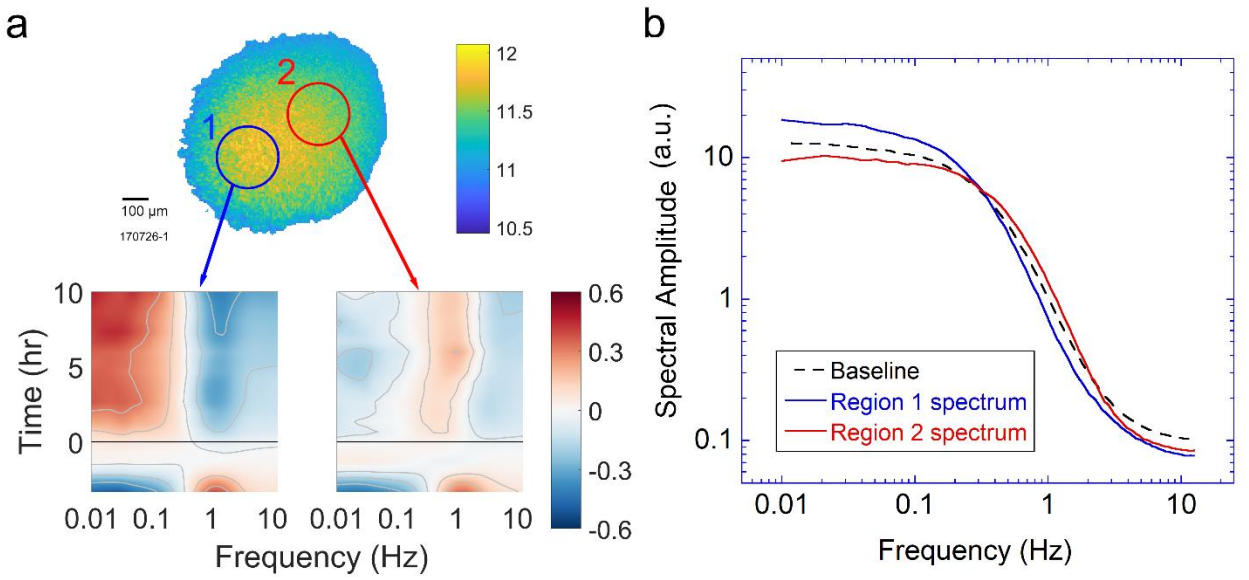

Figure 6-1 a) an OCI image of an esophageal biopsy and differential spectrograms for the two circled areas. At time *t*=0 (black line), the sample was refreshed with nutrients in the DMSO medium. The two regions have significantly different responses: Region 1 shows enhancement in low frequency and suppression in high frequency ("redshift"), while region 2 has a mid-frequency enhancement and low- and high-frequency suppression. b) The terminal spectrum of regions 1 and 2, respectively, compared to the average sample baseline spectrum.

6.2 Materials and Methods

6.2.1 Sample Preparation

Biological samples used in this project include tumor spheroids grown from the DLD-1 intestinal adenocarcinoma cell line (ATTC, Manassas, VA) and human esophageal tumor biopsies. The multicellular DLD-1 spheroids are the same as in chapter 2.4. Tumor biopsies were collected and transported in chilled RPMI-1640 medium with HEPES buffer, and cut into small pieces of 1 mm size or less. Both types of samples were immobilized in 1% low-gel temperature agarose in the RPMI-1640 basal medium. Immobilized samples were overlaid with RPMI-1640 containing 10% heat-inactivated fetal calf serum (Atlanta Biologicals), penicillin (100 IU), and streptomycin (100 µg/mL).

To prepare samples for iSPIM imaging, 10% neutral buffered formalin (NBF) was injected into each well to fix the tissues. After being washed with PBS, the samples were stained with 50 µM DRAQ5 overnight, then 2 mg/mL 80% ethanol-based Eosin Y for 30 minutes. The samples were

then washed with DI water three times and PBS once, and immersed in X-CLARITY mounting solution for 15 minutes. Finally, the samples were fixed in the imaging chamber with silicone glue and immersed in X-CLARITY mounting solution for iSPIM imaging. After imaging, the samples were processed for traditional H&E through the Tulane Medical School Histology Department. Four micrometer-thickness sections were cut and stained until each tissue was exhausted.

6.2.2 Data Processing

Two data acquisition formats are used for data presented in this chapter: A format containing 2048 frames captured at 25 fps, and an (older) format with 500 frames at 25 fps and 50 frames at 0.5 fps that are stitched to a single spectrum. These two formats are proved to be equivalent with a negligible difference with a specially designed experiment. Standard spectrogram calculations are used to evaluate time-lapse changes [Eq. (1.11)]. Condensed data format (CDF) described in appendix chapter C.2.2 is applied to the dataset to generate microspectrograms.

6.2.3 Biodynamic Biomarkers and TDS Visualization

This chapter focuses mainly on the drug response and feature values from spectrograms (Appendix chapter C.1.2).

Despite the differences in drug responses related to sample baseline conditions and drug mechanisms, a BDI drug spectrogram usually has one of a limited number of patterns. Spectroscopic masks (filters) are designed to match the characteristics of the spectrograms, a few of which are shown in Figure 6-2a. (These masks are similar to the ones introduced in appendix chapter C.1.2, and only used in this chapter for legacy reasons.) The top 3 patterns form a set of "orthonormal" masks that are related to the broadband (in the sense of frequency components) pattern of a spectrogram, while the bottom 3 patterns form another set of masks related to local response patterns. These frequency bands can be related to changes in intracellular motions and their associated speeds [27, 31]. For each mask, a feature value is obtained by calculating the inner products of the spectrogram and the mask, i.e. projecting the spectrogram onto the mask [26], and the features of a spectrogram are represented by a vector of feature values.

After CDF files are generated, a (differential) spectrogram for each TDSI pixel (referred to as "microspectrogram") is calculated as

$$\mathrm{d}S_{\sigma(\tilde{i},\tilde{j})}\left(f;\tau\right)=\log S_{\sigma(\tilde{i},\tilde{j}),\mathrm{norm}}\left(f;\tau\right)-\log\frac{1}{N}\sum_{i=1}^{N}S_{\Sigma,\mathrm{norm}}\left(f;\tau=\tau_i\right) \tag{6.1}$$

where the average baseline spectrum of the entire sample is used instead of the TDSI pixel's "own" baseline. For a given mask, a feature value discussed above can be calculated for each pixel, and the feature values of an entire sample produce a 2D image called a TDS image. Two TDS images under the "G1" mask and "G2" mask are shown in Figure 6-2b. For the "G1" TDS image, the area in the blue circle has negative values, indicating the inverse of the "G1" mask (i.e. the "blue-red" pattern spectral response shown in Figure 6-2a), which matches the differential spectrogram of the circled area of the same sample as shown in Figure 6-1a. Similarly, the "blue-red-blue" spectral response in the red circle area agrees with the positive values in the same area in the "G2" TDS image.

As discussed above, this sample has a large variation in drug response in terms of strength and spectral patterns, displayed by the distribution of values in the TDS images (TDSI) of Figure 6-2b. Both "G1" and "G2" images show a change in magnitude and sign from bottom left to top right (corresponding to changes in the strength of drug response, referred to as "intramask heterogeneity"), and the "G1" image has a different pattern than "G2", where "G1" has strong positive values on the top right while "G2" has strong negative values in the bottom left (corresponding to changes in pattern, referred to "intermask heterogeneity"). In order to better visualize the variation, bivariate images are introduced to produce a single visualization that captures drug response distribution over the entire sample, where each "variable" is a feature value of a mask. Feature values from two masks are a convenient way to illustrate drug response heterogeneity within a sample, and the following discussion will focus on bivariate representations of drug response.

Bivariate color maps are used in cartography [32, 33] and medical imaging [34], and many studies have addressed how to choose proper color maps for bivariate data visualization [35-37]. Here the "Teuling3" color map is used for the following visualizations, which is generated by linearly interpolating four colors at the four corners in the sRGB space plus a "whitening" core in the center [35, 38]. This color map has good color saturation, relatively equal visual impact, and a zero value appears as white, which is consistent with the diverging "blue-red" 1D color map used in our spectrograms and univariate TDS maps. (A detailed discussion of 2D color maps is given in

Appendix chapter C.3.2) Figure 6-2c shows a bivariate image of the esophageal sample "merged" from the two univariate TDS images in Figure 6-2b.

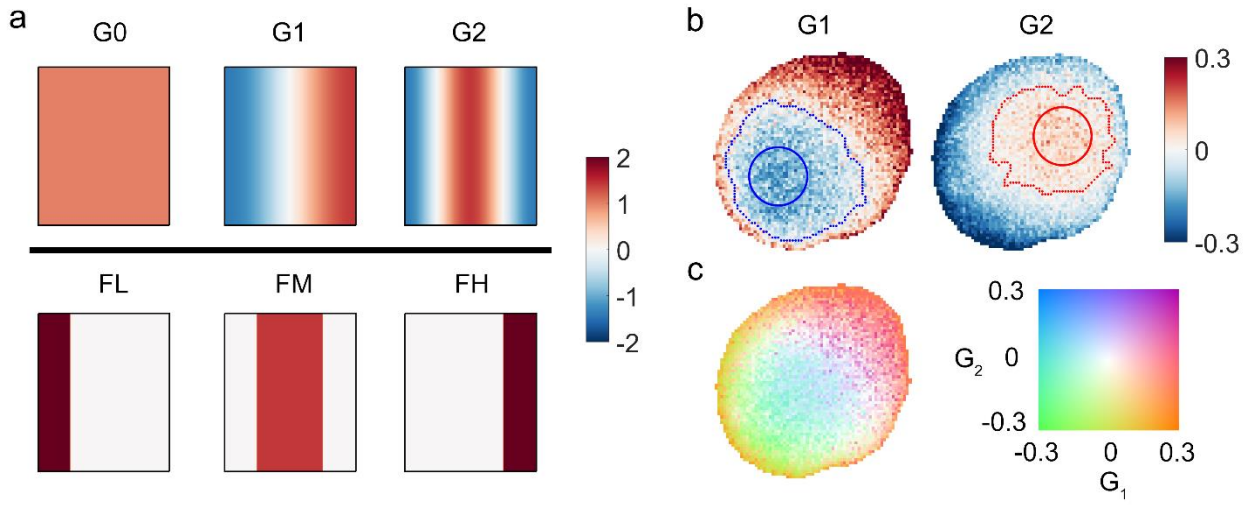

Figure 6-2 a) A subset of the spectrogram masks used in the color merge. b) Two maps of drug response of an esophageal sample "170726-1" (same as in Figure 6-1) under masks G1 and G2. c) A "merged" bivariate image with its 2D color map.

When a full sample has areas with spectrograms that are inverse to each other, they cancel each other out, resulting in a mild spectrogram and near-zero feature values. In this case, the average response belies the strong change in the intracellular dynamics and the fluctuation spectra and can lead to the misinterpretation that the sample does not respond to the drug. To address this problem, two new biomarkers that evaluate sample heterogeneity are added to the "traditional" average spectrogram-based biomarkers. The two biomarkers evaluate the "intramask" and "intermask" heterogeneity respectively. To achieve a high signal-to-noise ratio, TDS images are first (re)generated with an 8 × 8 pixel averaging (instead of the standard 2 × 2 px). The feature values are bounded to a range $\left[-A_{\text{th}}, A_{\text{th}}\right]$ and then assigned "scores" ranging from 0 to 1 for both heterogeneity evaluations, calculated using the following steps:

1. Select a set of *n* masks and create *n* TDS images
2. For each mask *u*, calculate Δa^u and $\Delta\left[\text{sgn}\left(a^u\right)\right]$
3. For each mask pair *u*-*v*, calculate $\left|\rho\left(a^u, a^v\right)\right|$ and $\left|\rho\left[\text{sgn}\left(a^u\right), \text{sgn}\left(a^v\right)\right]\right|$
4. The first biomarker denoting overall intra-mask heterogeneity is calculated as

$$h_1 = \frac{1}{2n}\left(m_1 \sum_{i=1}^{n} \Delta a^u + m_2 \sum_{i=1}^{n} \Delta \operatorname{sgn}\left(a^u\right) \right) \tag{6.2}$$

5. And the second biomarker representing overall inter-mask heterogeneity is calculated as

$$h_2 = 1 - \frac{1}{n(n-1)} \sum_{i-j \text{ pairs}} \left[\left| \rho\left(a^u, a^v\right) \right| + \left| \rho\left(\operatorname{sgn}\left(a^u\right), \operatorname{sgn}\left(a^v\right)\right) \right| \right] \tag{6.3}$$

where $a^u = \left\{ a^u\left(\tilde{i}, \tilde{j}\right) \right\}$ are values of the TDS image of mask *u*, $\operatorname{sgn}\left(a^u\right)$ is a map of signs of a^u, Δa^u is the standard deviation of a^u, $\rho\left(a^u, a^v\right)$ is the correlation coefficient of a^u and a^v, and m_1 and m_2 are normalization factors

$$\begin{cases} m_1 = \dfrac{1}{A_{th}} \\ m_2 = 1 \end{cases} \tag{6.4}$$

based on Popoviciu's inequality on variances [39]. We use $A_{\text{th}} = 0.3$ and $n = 3$, and the masks FL, FM and FL are used for heterogeneity scores.

Based on these definitions, the extreme values are achieved under these cases: h_1=0 when *n* TDS images are completely uniform (totally homogeneity), and h_1=1 when TDS images have only two values of opposite signs in an equal number of pixels. When the TDS images are completely non-linearly correlated to each other, then h_2=0, in the opposite case when all values are completely correlated then h_2=1. Some examples will be provided in the next section to illustrate these two heterogeneity benchmarks.

6.2.4 Time-lapse Drug Response Visualization

After a drug is added to a biopsy sample, the change in its intracellular dynamics is usually not immediate and depends on the drug mechanism of action, especially for drugs targeting DNA. Also, some parts of the sample may respond to a drug faster than the entire sample. TDSI allows us to study the spatial delay and non-uniformity in drug action, which is called time-lapse TDSI. Instead of extracting feature values from full-length spectrograms, time-lapse TDSI uses responses

within a small moving time “window” of the spectrogram. Examples are included in the next section.

6.2.5 Inverted Selective Plane Illumination Microscopy (iSPIM) and Data Processing

The iSPIM system has been described in previous publications [40, 41]. In brief, two orthogonally-placed objectives are mounted above the sample, each at 45° angle from the norm. They alternatively act as illumination and detection for dual-view imaging, but only single-view was adopted for the application in this paper. Volumetric images were obtained by moving the sample with respect to the objectives, with multiple y strips acquired with about 20% overlap between two adjacent strips. After imaging is completed, the images were shifted with custom MATLAB code to recover its 45° angle, multiple y paths were stitched with Fiji plugin [42], and the red and blue channels were remapped to RGB colors. Finally, 3D reconstruction was obtained from the alpha blending mode of the 3D viewer of Vaa3D [43, 44].

6.3 TDSI Results

A large number of esophageal biopsies have shown heterogeneous responses to drugs. In Figure 6-3a, two biopsy samples that have large intra-mask heterogeneity are presented in univariate and bivariate forms. Sample “151208-6” has a weak response in the whole-sample averaged spectrogram (Figure 6-3b “global”), while the local areas (area “1” and “2”) have strong but opposite responses that tend to cancel in the sample average.

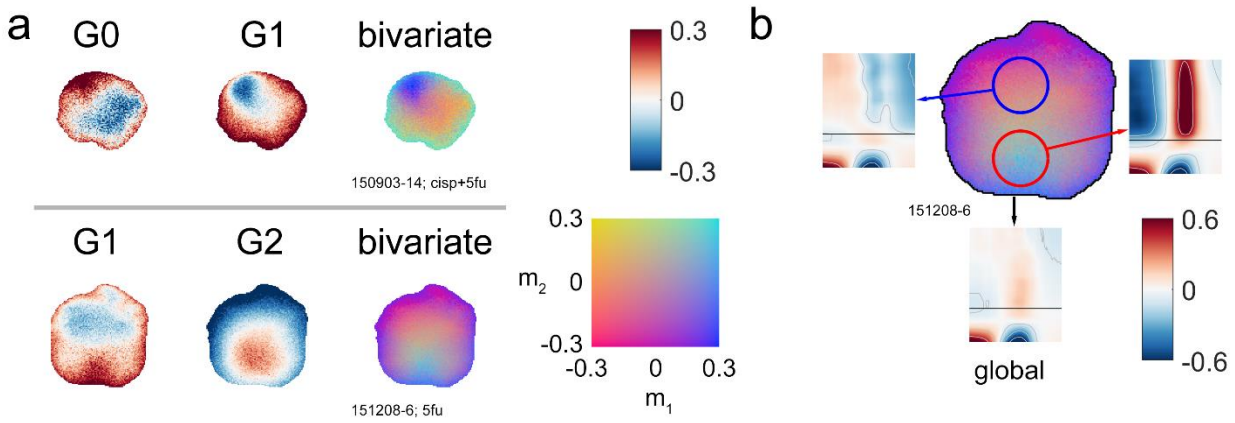

Figure 6-3 a) Bivariate representation of drug responses from 2 samples treated with different drugs, showing two univariate maps and a "merged" bivariate map. The drugs are 5fu (25 μM fluorouracil) and cisp (25 μM cisplatin) where "+" denotes a combination of the two drugs. b) Global and regional spectrograms of sample "151208-6" from a). The global spectrogram has a relatively weak response (max<10%), while the two circled areas have 30%-60% enhancement or suppression. Drugs were added at *t*=0 (black line).

Additional bivariate TDS images are shown in Figure 6-4. Some samples (e.g. 150603-12) have more uniform color in the "merged" map, indicating smaller variation in the biomarker values, while others (e.g. 170620-14) have a rainbow-like smooth transition across the sample, which is related to high heterogeneity in the drug response.

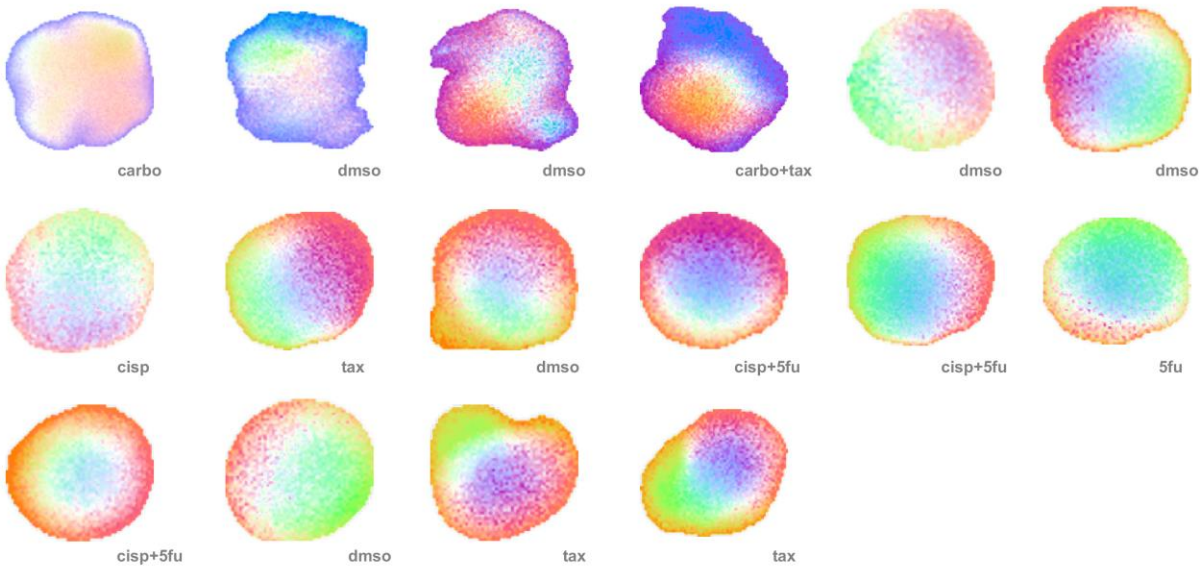

Figure 6-4 More examples of bivariate TDS images showing sample-to-sample variability in drug responses. Mask pairs used in the collage are from G0, G1 and G2. Drug abbreviations are the same as in Figure 6-3

There are roughly three types of heterogeneity, shown in Figure 6-5 along with their h_1 and h_2 scores: (i) Type I are samples that have almost uniform responses under all masks. These featureless biopsies may be connective tissues that do not respond to drugs or are from patients that are resistant to treatment. (ii) Type II samples have spatial variability but show similar patterns across different masks. (iii) Type III samples have TDS images with non-overlapping strongly responding areas. Types I and III are the most common.

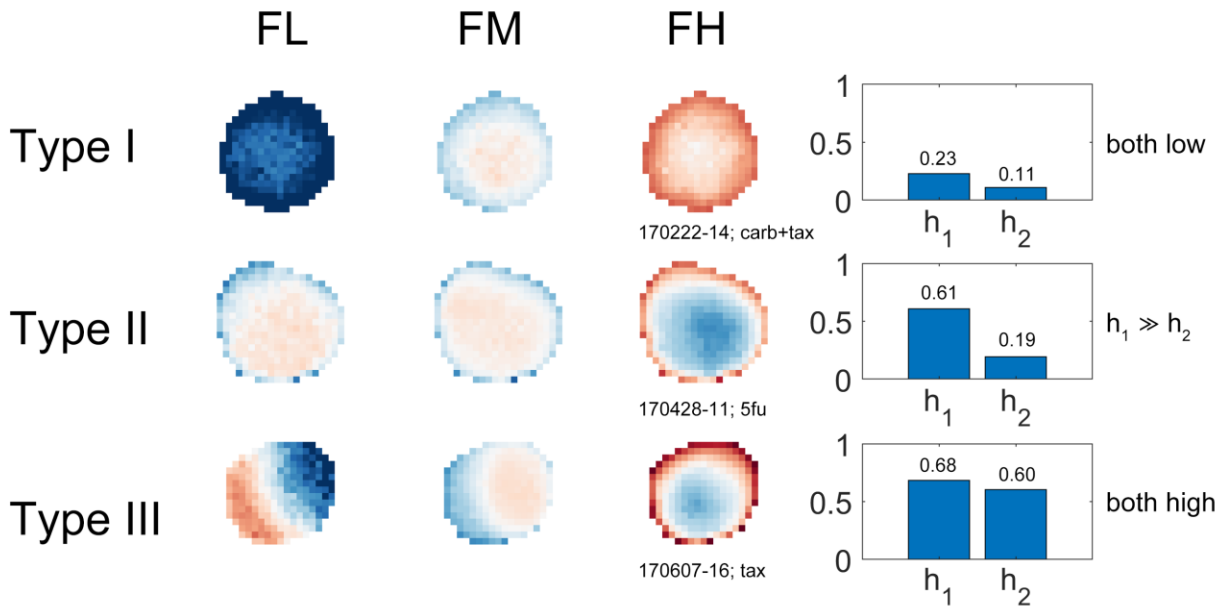

Figure 6-5 Three types of samples that have different levels of same-mask heterogeneity and cross-mask heterogeneity, with scores on the right.

Time-lapse images offer an additional layer of understanding of the spatial evolution of drug effects. In Figure 6-6 for sample "170317-9" treated with nocodazole, the blue response pattern (mid-frequency suppression and low- and high-frequency enhancement) grows stronger over time before saturation, which indicates that nocodazole's suppression of microtubule polymerization begins at the outer periphery and slowly penetrates the core of the sample. As another example, the red area in the TDS image of sample "170606-15" becomes stronger until around 9 hours, when the sample displays an overall suppression across the entire sample, which can be associated with sample apoptosis.

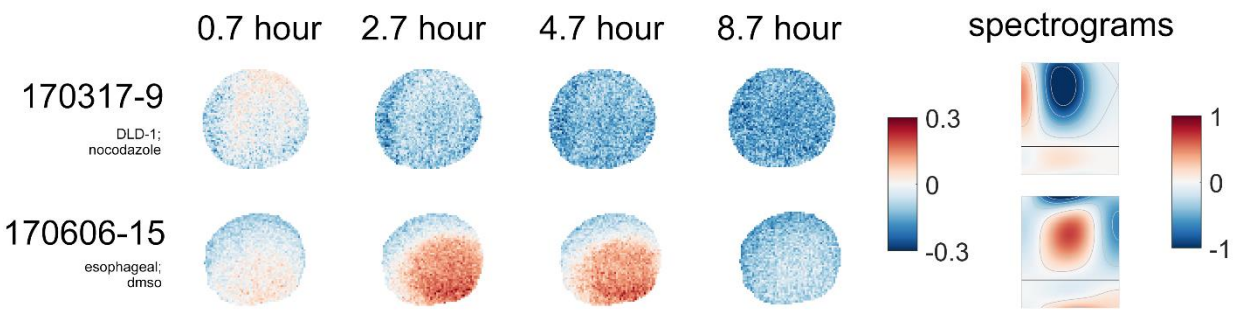

Figure 6-6 Time-lapse TDS image of samples responding to drugs. Sample "170317-9": Response of a DLD spheroid sample treated with 10 μM nocodazole with the G2 mask, showing a silent core shortly after drug was added, which was "invaded" by the drug and later achieved a spatially homogeneous response. Sample "170606-15": Response of an esophageal biopsy sample in the control medium, also under the G2 mask.

6.4 Comparison with Selective-Plane Illumination Microscopy

Given that BDI is a 3D imaging technology that uses low-coherence light, the different drug response phenotypes revealed by TDSI can be related to different types of tissues in a certain area of a sample. A contrasting technique is SPIM that produces microscopic images of 3D slices with high lateral and axial resolutions, which allows us to distinguish features in the images. Therefore, by comparing TDS and SPIM images side by side, we can verify whether the heterogeneity related to drug response variability from TDSI is also present in microscopic images, i.e. link dynamic information from functional imaging with the anatomy of biological tissues.

As an example, TDSI images for sample 190801-15 are compared against its iSPIM images and H&E histology images in Figure 6-7. In the TDSI image, the center shows a strong enhancement while the right side has a pattern of suppression. Meanwhile, the left half of the iSPIM and lower part of the histology image contains a large concentration of DNA, and the right half of the iSPIM image is cytoplasm or unstained tissues, matching the lack of nuclei in the upper part of the histology image, which potentially indicates collagenous connective tissues. Both images demonstrate heterogeneity in the tissue, which is consistent with the spectral signatures found in the TDS image.

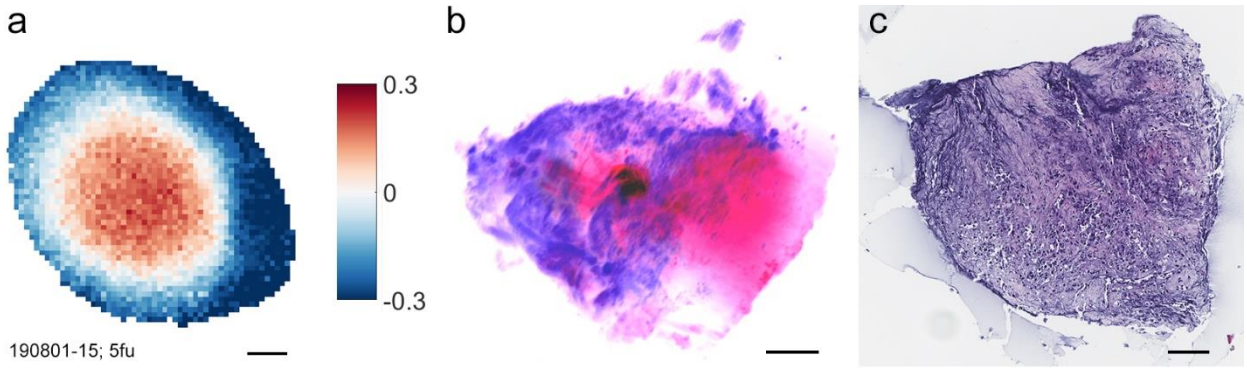

Figure 6-7 TDS image of biomarker G2, iSPIM image and H&E histology image for an esophageal biopsy sample. All scale bars are 100 μm. a) TDS image, b) the iSPIM image with DRAQ 5 (blue) and Eosin (pink) for the same sample in a), and c) Histology image. The orientations of the samples are not registered.

6.5 Discussion

Biodynamic imaging is a tool that is sensitive to intracellular dynamics and has been applied successfully to phenotypic profiling and patient outcome predictions. For instance, sample motility and dynamic biomarkers have been shown to be consistent and reliable indicators of pharmacodynamics effects. However, these biomarkers are usually calculated as whole-sample averages when used in classification and similarity analyses, overlooking intra-sample heterogeneity. The introduction of TDSI provides a solution to this issue by evaluating the responses of subregions of the sample to reveal new information on the complex spatial structures in sample drug response, which is supported by evidence from other imaging techniques like SPIM and histology. Visualization of sample heterogeneity is facilitated with a bivariate color representation and quantitatively characterized by h1 and h2 scores. This imaging method is further extended to generate whole-sample time-lapse TDS images, providing a novel method to monitor drug mechanisms.

In addition to visualizing sample heterogeneity, TDSI maps can provide additional information and improve classification accuracy when evaluating anti-cancer drug effectiveness on a patient level. For samples with regions of opposite responses, the whole-sample average spectrogram and its feature values may demonstrate a mild response to the drug, making the sample and the patient appear to be less sensitive to the treatment. The proposed solution here is to introduce additional biomarkers that characterize regional drug responses. As an example, the sample shown in Fig. 3b can be split into two regions based on the sign of G1 biomarker values (which can be related to

the sample's heterogeneous structure), and the feature values of these two regions can be calculated. The set of feature values that capture both sample average response, as well as regional response, would provide a more comprehensive assessment of drug response.

TDSI can be extended for further imaging and analysis applications. Since BDI is a 3D imaging technique and achieves depth selection with coherence gating, a volumetric TDS image can be generated by scanning different slices of a sample. Also, time-lapse TDS analysis is a quantitative approach to visualize drug action time dependence. Features like delay and distribution can be obtained from time-lapse images to provide insight into processes like dose-response relationships.

Challenges to TDSI include sample immobilization and multiple light scattering. TDSI evaluates drug spectral response on the pixel level and requires that the same part of the sample is imaged throughout the experiment. This requires the sample to maintain the same lateral and axial positions. In addition, multiple light scattering induces aberrations of the image and reduces the signal-to-noise ratio, which makes TDSI most effective at shallower depths.

TDSI is an important extension to the current BDI analysis (OCI, MCI, TDS). MCI maps are simple and intuitive functional images that visualize sample motility and have revealed the contrast between a viable shell and a necrotic core for rat tumor spheroids (Figure 1-7). TDSI, by comparison, generates a set of more detailed functional maps that complement MCI. The critical frequencies in spectral masks used in TDSI are related to specific types of intracellular components and motions that are affected, offering a comprehensive view of changes occurring in the sample. TDSI is a versatile functional imaging method that could provide new information for drug response profiling and has the potential for improving predictions of response to therapy and drug screening.

References

[1] M. Gerlinger, A. J. Rowan, S. Horswell, J. Larkin, D. Endesfelder, E. Gronroos, P. Martinez, N. Matthews, A. Stewart, P. Tarpey, I. Varela, B. Phillimore, S. Begum, N. Q. McDonald, A. Butler, D. Jones, K. Raine, C. Latimer, C. R. Santos, M. Nohadani, A. C. Eklund, B. Spencer-Dene, G. Clark, L. Pickering, G. Stamp, M. Gore, Z. Szallasi, J. Downward, P. A. Futreal, and C. Swanton, "Intratumor Heterogeneity and Branched Evolution Revealed by Multiregion Sequencing," New England Journal of Medicine **366**, 883-892 (2012).

[2] R. A. Burrell, N. McGranahan, J. Bartek, and C. Swanton, "The causes and consequences of genetic heterogeneity in cancer evolution," Nature **501**, 338-345 (2013).
[3] L. L. Campbell, and K. Polyak, "Breast tumor heterogeneity," Cell Cycle **6**, 2332-2338 (2007).
[4] I. Serganova, M. Doubrovin, J. Vider, V. Ponomarev, S. Soghomonyan, T. Beresten, L. Ageyeva, A. Serganov, S. D. Cai, J. Balatoni, R. Blasberg, and J. Gelovani, "Molecular imaging of temporal dynamics and spatial heterogeneity of hypoxia-inducible factor-1 signal transduction activity in tumors in living mice," Cancer Research **64**, 6101-6108 (2004).
[5] J. J. Salk, E. J. Fox, and L. A. Loeb, "Mutational Heterogeneity in Human Cancers: Origin and Consequences," in *Annual Review of Pathology-Mechanisms of Disease*(2010), pp. 51-75.
[6] A. S. Little, P. D. Smith, and S. J. Cook, "Mechanisms of acquired resistance to ERK1/2 pathway inhibitors," Oncogene **32**, 1207-1215 (2013).
[7] D. Barbone, T. M. Yang, J. R. Morgan, G. Gaudino, and V. C. Broaddus, "Mammalian target of rapamycin contributes to the acquired apoptotic resistance of human mesothelioma multicellular spheroids," Journal Of Biological Chemistry **283**, 13021-13030 (2008).
[8] G. A. Cirkel, C. G. Gadellaa-van Hooijdonk, M. J. Koudijs, S. M. Willems, and E. E. Voest, "Tumor heterogeneity and personalized cancer medicine: are we being outnumbered?," Future Oncology **10**, 417-428 (2014).
[9] O. Tredan, C. M. Galmarini, K. Patel, and I. F. Tannock, "Drug resistance and the solid tumor microenvironment," Journal Of The National Cancer Institute **99**, 1441-1454 (2007).
[10] A. Tomida, and T. Tsuruo, "Drug resistance mediated by cellular stress response to the microenvironment of solid tumors," Anti-Cancer Drug Design **14**, 169-177 (1999).
[11] M. Esteller, and J. G. Herman, "Cancer as an epigenetic disease: DNA methylation and chromatin alterations in human tumours," Journal Of Pathology **196**, 1-7 (2002).
[12] P. A. Kenny, and M. J. Bissell, "Tumor reversion: Correction of malignant behavior by microenvironmental cues," International Journal of Cancer **107**, 688-695 (2003).
[13] X. Xu, M. C. Farach-Carson, and X. Q. Jia, "Three-dimensional in vitro tumor models for cancer research and drug evaluation," Biotechnology Advances **32**, 1256-1268 (2014).
[14] P. D. Caie, R. E. Walls, A. Ingleston-Orme, S. Daya, T. Houslay, R. Eagle, M. E. Roberts, and N. O. Carragher, "High-Content Phenotypic Profiling of Drug Response Signatures across Distinct Cancer Cells," Molecular Cancer Therapeutics **9**, 1913-1926 (2010).
[15] H. S. Seol, Y. A. Suh, Y. J. Ryu, H. J. Kim, S. M. Chun, D. C. Na, H. Fukamachi, S. Y. Jeong, E. K. Choi, and S. J. Jang, "A patient-derived xenograft mouse model generated from primary cultured cells recapitulates patient tumors phenotypically and genetically," Journal Of Cancer Research And Clinical Oncology **139**, 1471-1480 (2013).
[16] H. Y. Deng, C. M. Wang, and Y. Fang, "Label-free cell phenotypic assessment of the molecular mechanism of action of epidermal growth factor receptor inhibitors," Rsc Advances **3**, 10370-10378 (2013).
[17] P. Yu, M. Mustata, L. L. Peng, J. J. Turek, M. R. Melloch, P. M. W. French, and D. D. Nolte, "Holographic optical coherence imaging of rat osteogenic sarcoma tumor spheroids," Applied Optics **43**, 4862-4873 (2004).
[18] P. Yu, M. Mustata, J. J. Turek, P. M. W. French, M. R. Melloch, and D. D. Nolte, "Holographic optical coherence imaging of tumor spheroids," Applied Physics Letters **83**, 575-577 (2003).

[19] E. Cuche, F. Bevilacqua, and C. Depeursinge, "Digital holography for quantitative phase-contrast imaging," Optics Letters **24**, 291-293 (1999).
[20] P. Marquet, B. Rappaz, P. J. Magistretti, E. Cuche, Y. Emery, T. Colomb, and C. Depeursinge, "Digital holographic microscopy: a noninvasive contrast imaging technique allowing quantitative visualization of living cells with subwavelength axial accuracy," Optics Letters **30**, 468-470 (2005).
[21] N. T. Shaked, L. L. Satterwhite, N. Bursac, and A. Wax, "Whole-cell-analysis of live cardiomyocytes using wide-field interferometric phase microscopy," Biomedical Optics Express **1**, 706-719 (2010).
[22] E. Beaurepaire, A. C. Boccara, M. Lebec, L. Blanchot, and H. Saint-Jalmes, "Full-field optical coherence microscopy," Opt. Lett. **23**, 244-246 (1998).
[23] Z. Yaqoob, J. Fingler, X. Heng, and C. H. Yang, "Homodyne en face optical coherence tomography," Optics Letters **31**, 1815-1817 (2006).
[24] K. Jeong, J. J. Turek, and D. D. Nolte, "Imaging Motility Contrast in Digital Holography of Tissue Response to Cytoskeletal Anti-cancer Drugs,," Opt. Express **15**, 14057-14064 (2007).
[25] D. D. Nolte, R. An, J. Turek, and K. Jeong, "Holographic tissue dynamics spectroscopy," Journal of Biomedical Optics **16**, 087004-087013 (2011).
[26] D. D. Nolte, R. An, J. Turek, and K. Jeong, "Tissue dynamics spectroscopy for phenotypic profiling of drug effects in three-dimensional culture," Biomedical Optics Express **3**, 2825-2841 (2012).
[27] D. Merrill, H. Sun, J. Turek, D. Nolte, B. Yakubov, D. Matei, and R. An, "Intracellular Doppler Signatures of Platinum Sensitivity Captured by Biodynamic Profiling in Ovarian Xenografts," Nature Scientific Reports **6**, 18821 (2016).
[28] M. R. Custead, R. An, J. J. Turek, G. E. Moore, D. D. Nolte, and M. O. Childress, "Predictive value of ex vivo biodynamic imaging in determining response to chemotherapy in dogs with spontaneous non-Hodgkin's lymphomas: a preliminary study," Converg. Sci. Phys. Oncol **1**, 015003 (2015).
[29] R. An, C. Wang, J. Turek, Z. Machaty, and D. D. Nolte, "Biodynamic imaging of live porcine oocytes, zygotes and blastocysts for viability assessment in assisted reproductive technologies," Biomed. Opt. Express **6**, 963-976 (2015).
[30] D. D. Nolte, R. An, J. Turek, and K. Jeong, "Holographic tissue dynamics spectroscopy," J. Biomed. Opt. **16**, 087004-087004-087013 (2011).
[31] Z. Li, H. Sun, J. Turek, S. Jalal, M. Childress, and D. D. Nolte, "Doppler fluctuation spectroscopy of intracellular dynamics in living tissue," J. Opt. Soc. Am. A **36**, 665-677 (2019).
[32] M. Harrower, and C. A. Brewer, "ColorBrewer.org: An Online Tool for Selecting Colour Schemes for Maps," The Cartographic Journal **40**, 27-37 (2003).
[33] A. J. Teuling, R. Stöckli, and S. I. Seneviratne, "Bivariate colour maps for visualizing climate data," International Journal of Climatology **31**, 1408-1412 (2011).
[34] K. G. Baum, M. Helguera, J. P. Hornak, J. P. Kerekes, E. D. Montag, M. Z. Unlu, D. H. Feiglin, and A. Krol, "Techniques for Fusion of Multimodal Images: Application to Breast Imaging," in *2006 International Conference on Image Processing*(2006), pp. 2521-2524.
[35] J. Bernard, M. Steiger, S. Mittelstädt, S. Thum, D. Keim, and J. Kohlhammer, "A survey and task-based quality assessment of static 2D colormaps," SPIE/IS&T Electronic Imaging **9397** (2015).

[36] S. Bremm, T. von Landesberger, J. Bernard, and T. Schreck, "Assisted Descriptor Selection Based on Visual Comparative Data Analysis," Computer Graphics Forum **30**, 891-900 (2011).
[37] M. Steiger, J. Bernard, S. Thum, S. Mittelstädt, M. Hutter, D. Keim, and J. Kohlhammer, "Explorative Analysis of 2D Color Maps," (2015).
[38] M. Steiger, J. Bernard, S. Mittelstädt, H. Lücke-Tieke, D. Keim, T. May, and J. Kohlhammer, "Visual Analysis of Time-Series Similarities for Anomaly Detection in Sensor Networks," Computer Graphics Forum **33**, 401-410 (2014).
[39] R. Bhatia, and C. Davis, "A Better Bound on the Variance," The American Mathematical Monthly **107**, 353-357 (2000).
[40] B. Hu, G. Li, and J. Q. Brown, "Enhanced resolution 3D digital cytology and pathology with dual-view inverted selective plane illumination microscopy," Biomed Opt Express **10**, 3833-3846 (2019).
[41] B. Hu, D. Bolus, and J. Q. Brown, "Improved contrast in inverted selective plane illumination microscopy of thick tissues using confocal detection and structured illumination," Biomed Opt Express **8**, 5546-5559 (2017).
[42] S. Preibisch, S. Saalfeld, and P. Tomancak, "Globally optimal stitching of tiled 3D microscopic image acquisitions," Bioinformatics **25**, 1463-1465 (2009).
[43] H. Peng, Z. Ruan, F. Long, J. H. Simpson, and E. W. Myers, "V3D enables real-time 3D visualization and quantitative analysis of large-scale biological image data sets," Nat Biotechnol **28**, 348-353 (2010).
[44] H. Peng, A. Bria, Z. Zhou, G. Iannello, and F. Long, "Extensible visualization and analysis for multidimensional images using Vaa3D," Nature protocols **9**, 193-208 (2014).

APPENDIX A. BDI SYSTEM CHARACTERIZATION

A.1 Alpha Prime system

A.1.1 Overview

The optical layout of the "Alpha Prime" system is shown in Appendix Figure 1. A Superlum S840-B-I-20 superluminescent diode (SLD), with a center wavelength at 836.2 nm and full power output of 22.9 mW, was used as the light source. The SLD has a short coherence length of approximately 10 microns, enabling the formation of low-coherence holograms in a Mach-Zehnder interferometric configuration with a CCD camera as the detector at the Fourier plane.

Holograms are written by scattered photons that share the same optical path length (OPL) as the reference arm. By adjusting the delay stage, light scattered from different depths inside the sample can be selected, setting the "coherence gate" for the detection. The coherence gate is typically set at about 200 to 500 microns inside the sample. The transport length of light in many types of tissue samples is approximately 100 microns. Therefore, the light selected by the coherence gate in our experiments is multiply scattered with between 4 to 10 high-angle scattering events. Multiple scattering compounds the Doppler shifts and broadens the fluctuation spectra. The digital holograms are reconstructed numerically using a 2D FFT to generate optical sections approximately 400 microns inside the tissue. A reconstructed image and its conjugate are shown in Appendix Figure 2(c) with a close-up in Appendix Figure 2(d).

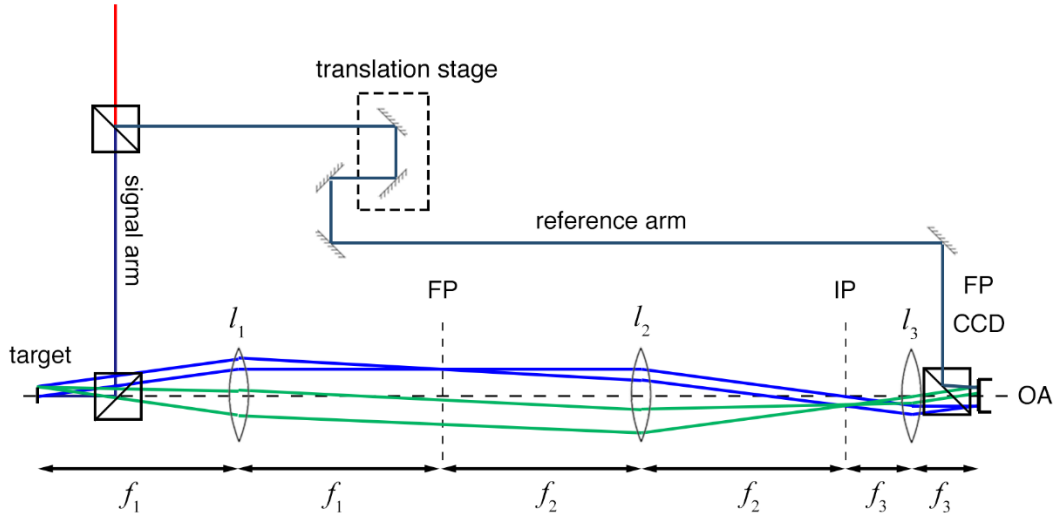

Appendix Figure 1 Biodynamic imaging system in a Mach-Zehnder configuration. The camera is located on the Fourier domain of the sample. A translation stage is used to select the coherence gate and to form images at different depths inside the sample. $f_1 = f_2 = 15$ cm, $f_3 = 5$ cm

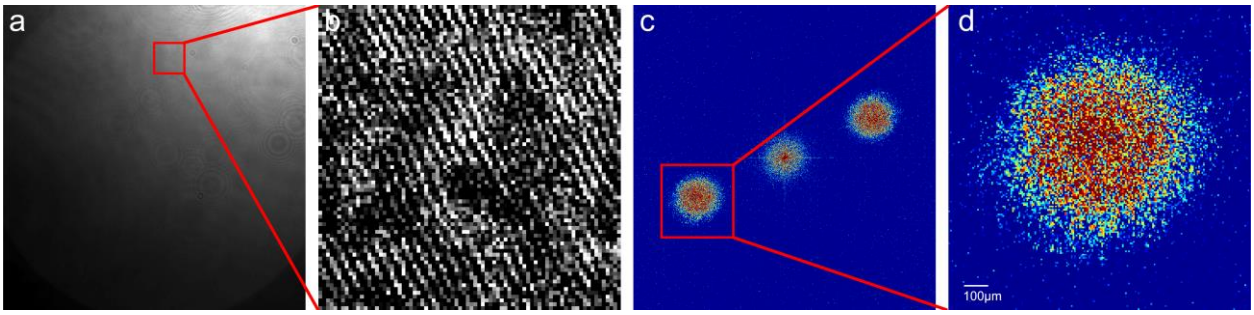

Appendix Figure 2 An example of reconstruction of holograms captured by the BDI system. (a) Raw hologram image, (b) fringes, (c) FFT of the hologram and (d) sample image in the first order

A.1.2 Marginal Ray

The marginal ray of the system is determined by the size of the chip, or the actual detection area if it is smaller, as illustrated in Appendix Figure 3 and Appendix Figure 4.

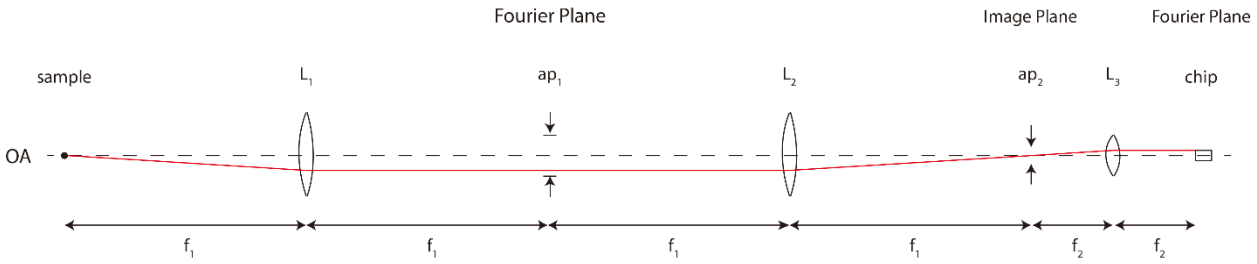

Appendix Figure 3 Ray tracing for marginal ray in the "alpha prime" system. The marginal ray is limited by the size of the chip.

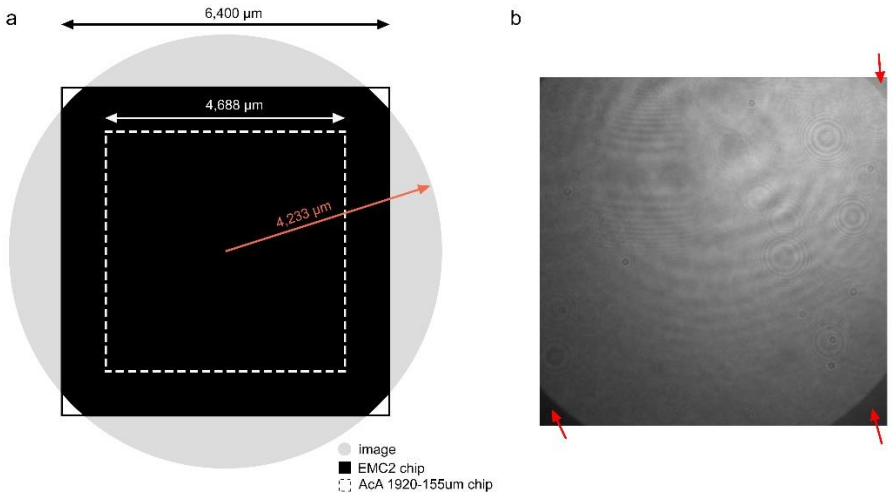

Appendix Figure 4 a) Illustration of the size comparison of image and the camera detection area (when the system is perfectly aligned). Both QImaging EMC2 and Basler AcA 1920-155um cameras are drawn. b) an actual image captured by the EMC2, and the dark part in the corners are equivalent to the corners shown in a).

The beam that illuminates the sample has a Gaussian intensity profile with a full width at half maximum (FWHM) of 460 µm.

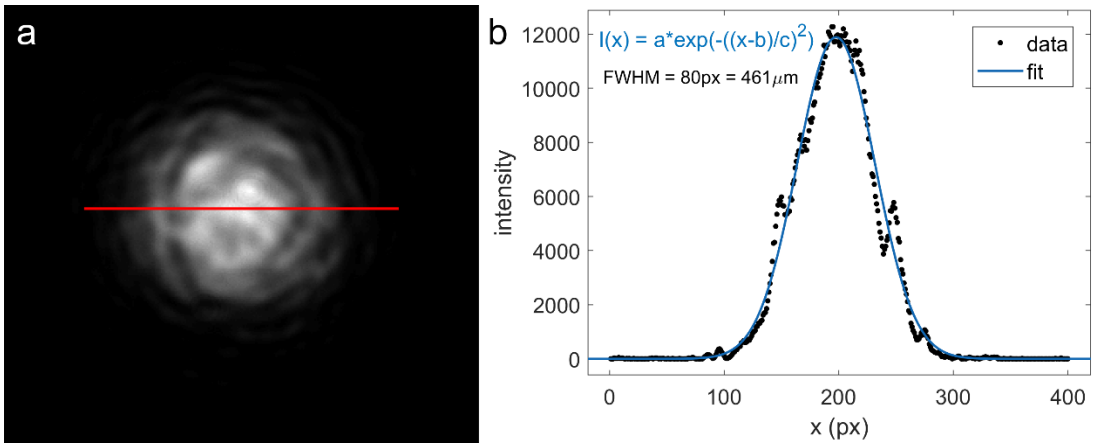

Appendix Figure 5 Beam profile before the sample in the Alpha Prime system.

A.1.3 Sample Flythrough

A “flythrough”, i.e. depth step scan of an entire sample, is done on the Alpha Prime system and shown in Appendix Figure 6.

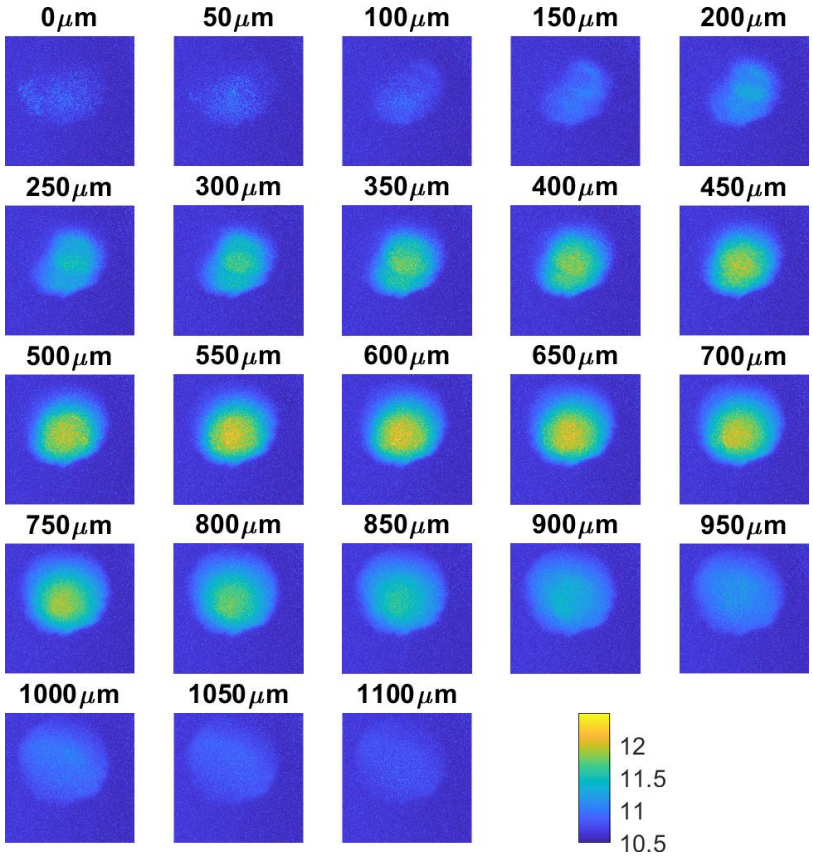

Appendix Figure 6 The flythrough of a DLD sample without background removal (i.e. “masking”).

During the flythrough, the sample averaged BSB increases and then decreases, while the NSD values follow the reverse trend (Appendix Figure 7a). Under the standard "onekey" normalization (i.e. divide the power spectrum by the sum of all components in the spectrum), the dynamic range increases with depth before it decreases after a certain point. Also, as the depth increases, low-frequency bands get enhanced, the mid-frequency slope increases (in its absolute value), and the Nyquist floor decreases at first, and then these trends are reversed (Appendix Figure 7b). Spectra appear at different positions under different normalization methods, but the general trend is consistent. In Appendix Figure 7c, the "raw" spectra do not intersect with each other, although the change of spectral amplitude large follows the trend of low frequency in Appendix Figure 7b). When using the alternative normalization method where the spectrum is divided by the square of BSB (Appendix Figure 7d), the trend is similar to that in the standard normalization.

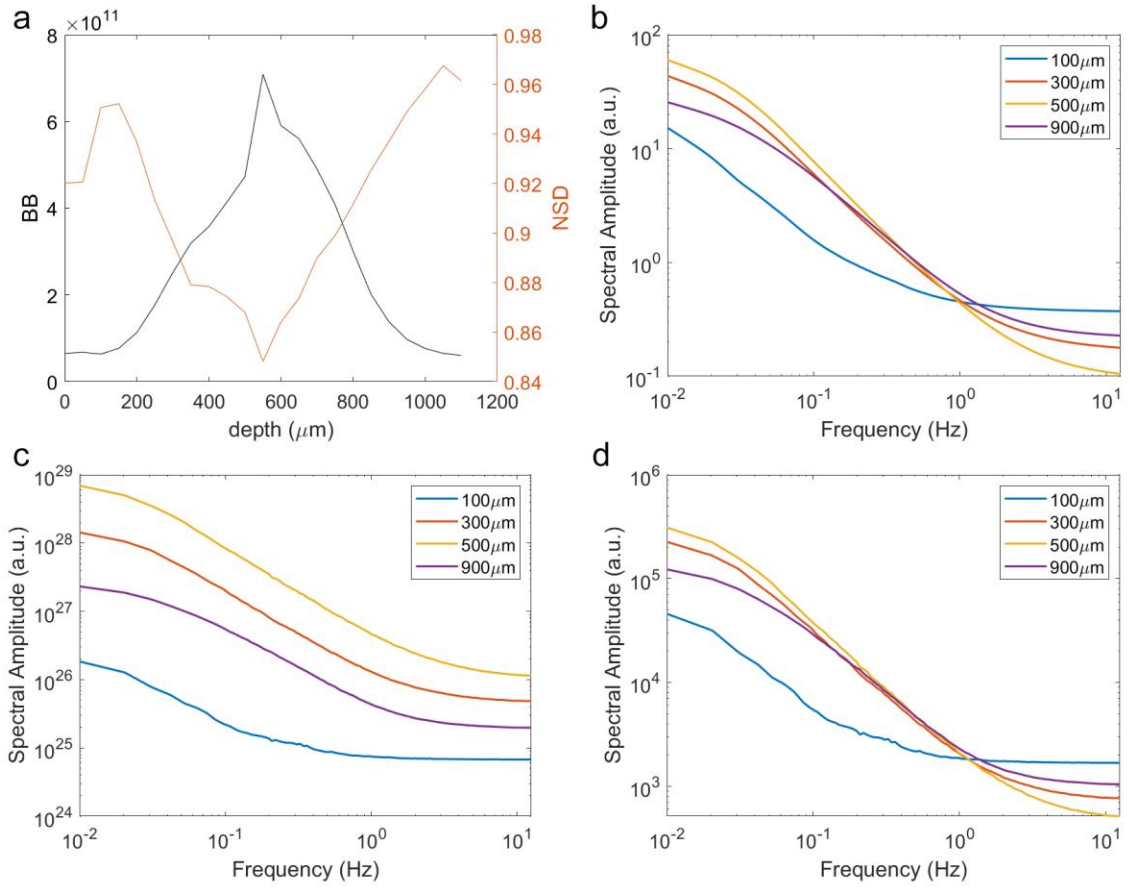

Appendix Figure 7 a) BB and NSD values across the sample b) power spectra at 4 different depths using standard onekey normalization c) "raw" power spectra without normalization d) power spectra divided by the square of BB

A.2 Biodynamic Microscope (BDM)

The biodynamic microscope is a stand-alone module manufactured by Animated Dynamics, Inc. that inserts into a conventional Olympus IX-73 inverted microscope, allowing a user to switch between conventional transillumination microscopy and a BDI mode (Appendix Figure 8a-b). The BDM interferometry system is a Mach-Zehnder configuration (Appendix Figure 8c). A Superlum superluminescent diode centered at 841.2 nm with a 28.9 nm bandwidth and 20.9 mW output power is used as the light source that is incident on the sample at a 45° angle relative to the optic axis of the collection objective lens (Appendix Figure 8c-d). The translation stage controls the coherence gate based on optical path length (OPL). In conventional backscatter coherence-gated holography, the optical section plane is perpendicular to the optic axis. However, the 45° illumination, combined with three-dimensional volumetric scattering, creates a coherence plane that is tilted at 22.5° (half of the illumination angle), and the sample "flythrough" occurs at this oblique angle when translating the reference mirrors. The advantages of this novel BDM design are the reduction of specular background reflections, and the elimination of the conventional beamsplitter normally used in the backscatter configuration to improve optical brightness of dim translucent samples. The oblique coherence plane needs minor additional digital post-processing after holographic reconstruction to regain a balanced aspect ratio of the volumetric target. The transilluminational microscopy mode of the BDM uses an Olympus UPLFLN 4x objective lens with 0.13 numerical aperture, 17 mm working distance and 45 mm parfocal distance. The BDI mode has a 0.05 numerical aperture, up to 1 mm field of view (determined by the illumination beam size) and a pixel size of 8 μm. The BDM is placed on a vibration isolation platform to minimize mechanical disturbance.

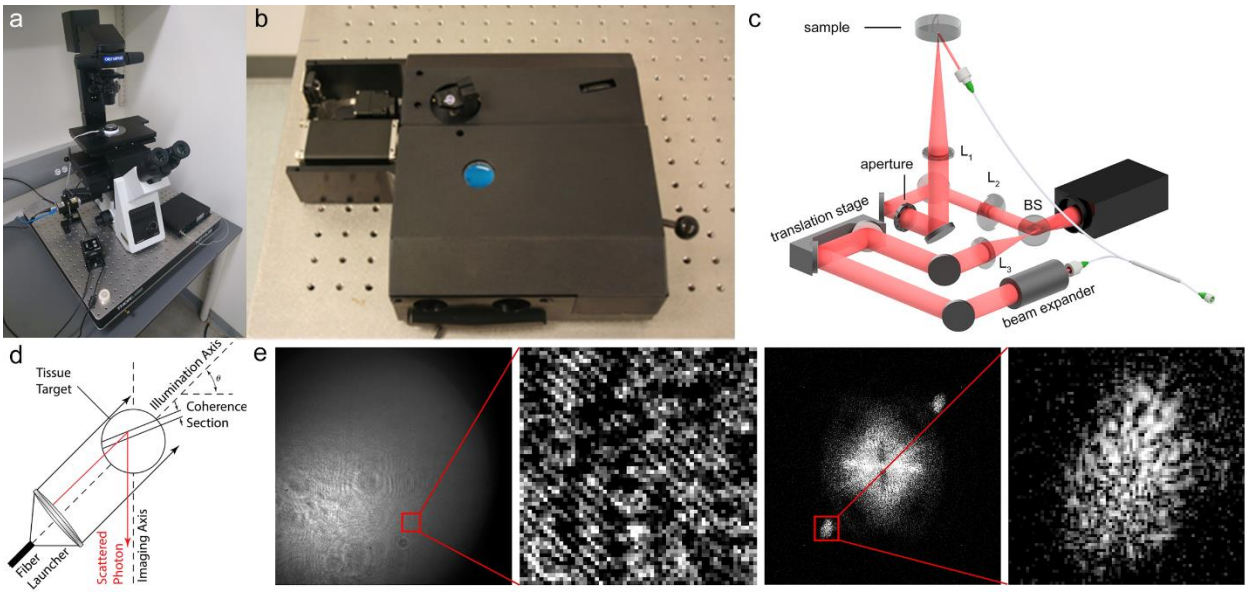

Appendix Figure 8 System setup of the BDM. a) picture of the entire BDM. b) the BDI module inserted into the BDM. c) 3D layout of the optical design of the BDI system. L_1: Fourier transform lens, L_2: imaging lens, and L_3: phase compensation lens d) illustration of the 45-degree illumination e) hologram, fringe, Fourier transform and the cropped image for a COC sample

The marginal ray of the system is determined by the chip size, or actual detection area if only part of the chip is used for detection, as shown in Appendix Figure 9.

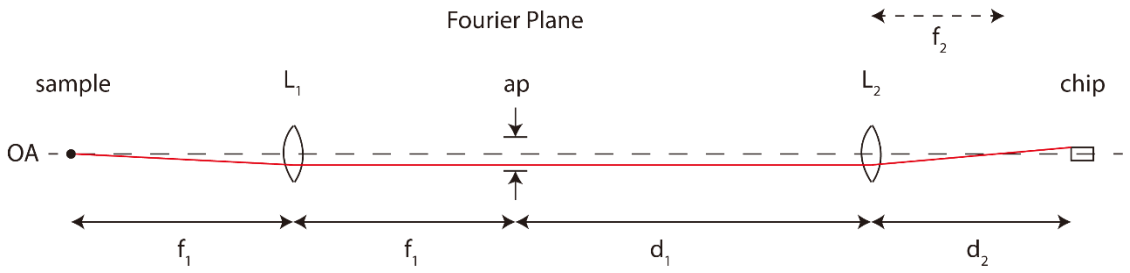

Appendix Figure 9 ray tracing for the marginal ray in the BDI module of the BDM. The marginal ray is also determined by the chip size.

A “flythrough” of a DLD-1 sample on the BDM is shown in Appendix Figure 10.

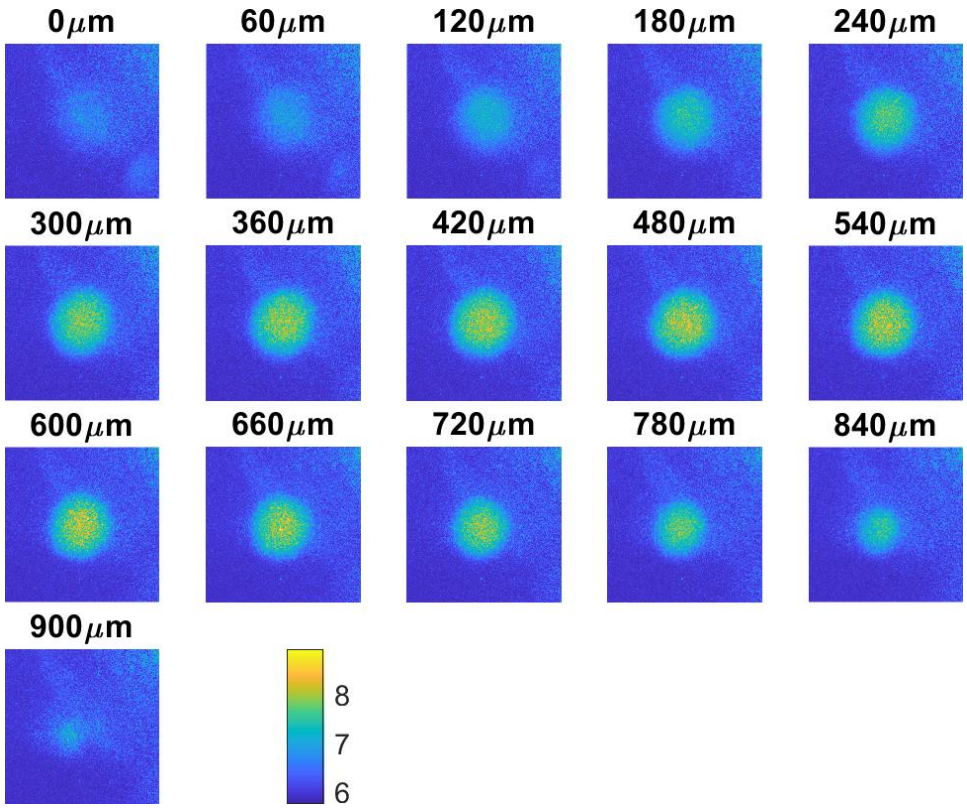

Appendix Figure 10 flythrough of a DLD-1 sample on the BDM.

The performance of the BDM is shown in Appendix Figure 11 with the power spectra of several types of biological samples. Many biological samples have near three orders of magnitude in spectral amplitude. Healthy DLD spheroid and parthenotes span 10^{2} – 10^{-1} Hz, while NaN_3 treated parthenogenetic embryos that have low viability have a lower Nyquist floor and a lower knee frequency than normally developed samples. When parthenote samples are crosslinked with glutaraldehyde, there is an overall suppression over all frequencies, meaning that intracellular activities are shut down in the sample. A paper and a tape are also measured with the BDI, showing a spectrum with much lower activity over all frequencies than biological samples, with a flat Nyquist floor > 1 Hz, indicating the true Nyquist floor of the system.

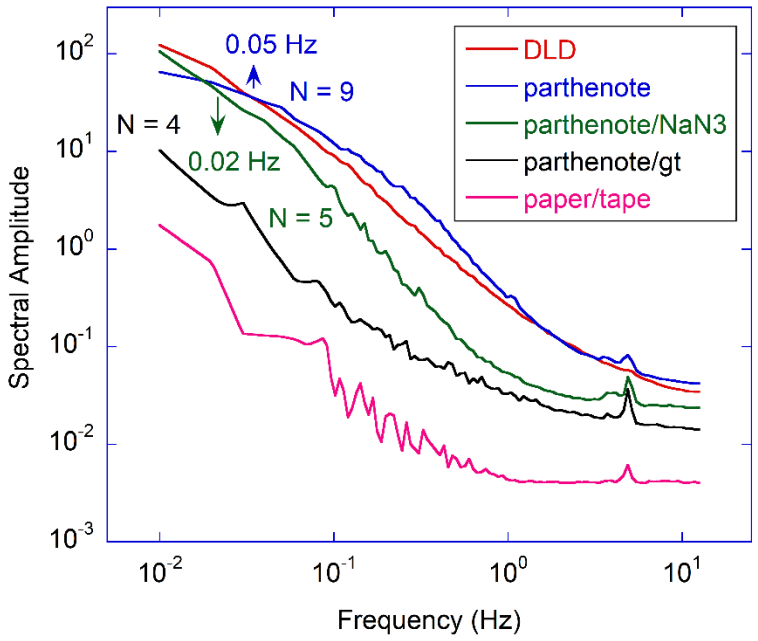

Appendix Figure 11 Several types of biological samples imaged from the BDI module of the BDM. "NaN3": samples incubated with culture medium containing NaN_3 (see chapter 4.2.6). "gt": samples cross-linked with glutaraldehyde.

A.3 Specifications

Some parameters of the BDI systems are shown in Appendix Table 1. Camera speckle size and image pixel size are obtained from theoretical calculations, while speckle sizes are from autocorrelation of images.

Appendix Table 1 Specification of the BDI systems

	BDM **Basler piA 1600-35gm**	**Alpha Prime**	
		Rolera EMC2	**Basler AcA 1920-155um**
Wavelength λ	841.2 nm	836.2 nm	
lens focal length f	100 mm, 60 mm	150 mm, 50 mm	
Distance d	100 mm, 100 mm, 160 mm, 95.4 mm	150 mm, 150 mm, 150 mm, 150 mm, 50 mm, 50 mm	
Camera chip type	CCD	EMCCD	CMOS
pixel size (camera) $a_{\text{pix-cam}}$	7.4 μm	8 μm	5.76 μm
speckle size (camera) a_{sp}	125 μm	105 μm (400 μm aperture)	
pixel size (image) $a_{\text{pix-img}}$	8.44 μm	6.56 μm	
fringe spacing Λ	2.25px	variable	
crossing angle θ	2.89°		
speckle size (px; exp) a_{sp}	1.53, 1.45	1.67, 1.58	
aperture size a_{ap}	0.6 in = 15.2 mm	variable	
speckle size (reconstruction image)	12.66 μm	10.5 μm	

APPENDIX B. DEVELOPMENT OF BIODYNAMIC DATA ACQUISITION SOFTWARE

B.1 Introduction

A majority of biodynamic data acquisition programs written before the year of 2016 are based on LabVIEW, which employs labels and textboxes in the “front panel” as the user interface and blocks and wires in the block diagram as the logic. An example is given in Appendix Figure 12. While these programs are capable of controlling motion controllers and taking data, they are not written with the best software development principles. This appendix chapter discusses the issues with the existing software and improvements.

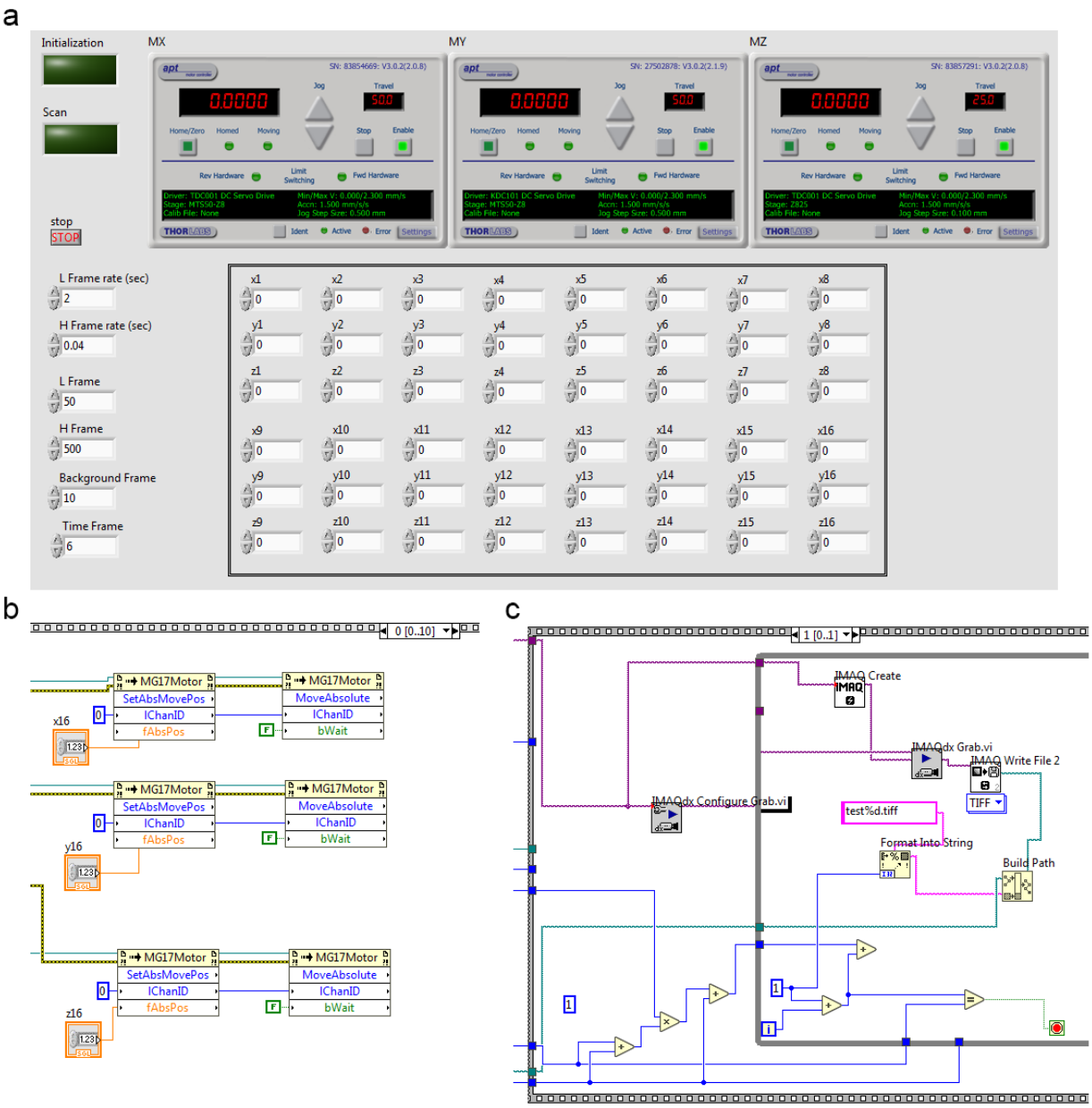

Appendix Figure 12 Example of LabVIEW programs. a) the "front panel" of a program for standard 16-sample preclinical trial experiments b) the "block", or the logic for motion controller movement c) another program for data acquisition with a Basler GigE camera

B.2 Issues

B.2.1 Lack of Real-time Sample Image Previewing

The first part of a multiplexed BDI experiment is to locate the x, y coordinates and coherence gate (i.e. depth) of each sample. Finding the coherence gate finding has been based on the identification of fringes in hologram images. However, this method is not reliable, as fringes can be very dim and difficult to observe (Appendix Figure 13), especially for embryos where the sample is mostly transparent. Also, sometimes fringes may come from specular reflections rather than a biological sample, but they cannot be distinguished from fringes alone.

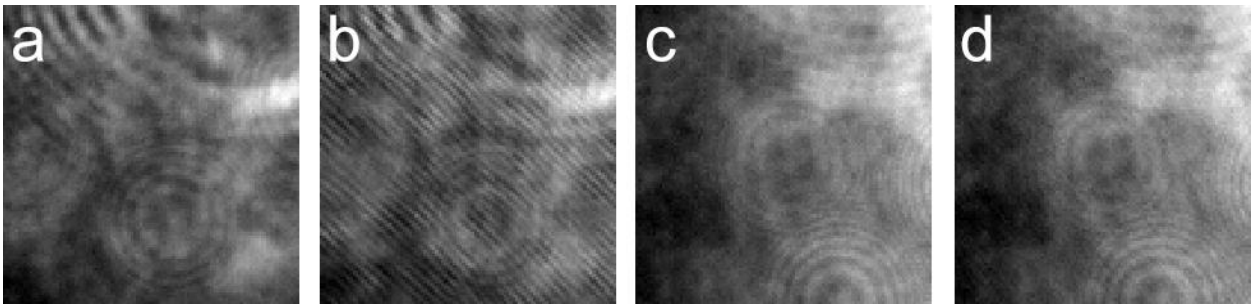

Appendix Figure 13 a) a background frame for an esophageal biopsy sample when the coherence gate is out of the sample b) a hologram frame with high fringe contrast for the same sample in a) c) a background frame for a different biopsy sample d) a hologram where fringes are barely visible

B.2.2 Lack of Error Handling

The LABVIEW programs are "barebone" tools that accomplish the basic job of controlling instruments and taking data, which are good for fast, *ad hoc* exploratory work, but too simple for long time experiments with well-established protocols like biopsy samples enrolled in pre-clinical trials. Over the years, various problems have happened during experiments, including solid-state drive (SSD) performance issues causing frame drops, SSD running out of storage, motion controller getting stuck, cable connection issues, and unreachable coordinates being given to motion controllers. These errors either lead to complete termination of data collection or corruption of part of the dataset, which can go unnoticed until the second day of the experiment or not even until data analysis. This often means time and resources are wasted. However, such issues can be detected by computer programs before an experiment starts, or can be reported as "exceptions" by the programs and handled appropriately. If the experiment operator can be notified in time of any

issues, there is a good chance that underlying software/hardware issues can be quickly resolved so that the experiment can resume without major damage to the data quality.

B.2.3 Lack of Automatic Logging

Lab notes are important parts of research, and they can play an important role in understanding results (especially erratic results). The same idea applies to the automatic data acquisition process. Information like camera exposure time, time of motion controller movement, can provide additional information for troubleshooting when there is an irregularity in the data collected.

B.2.4 Difficulty in Adaptation and Migration

The current programs are difficult to be modified for different measurement routines or require a lot of re-programming for new systems or new instruments. Take the LabVIEW program in Appendix Figure 12 as an example: The program is capable of measuring 16 wells, and it requires a lot of front end and back end change if the experiment uses 8 or 20 wells instead, which involves a lot of manual and repetitive work (like adding numerical textboxes and wiring them to the correct controllers). If the same experiment needs to be run on a different system, because of the different cameras and different motion controllers used, a large part of the program also needs to be rewritten.

B.2.5 LabVIEW Program Limitations

LabVIEW is good for fast prototyping of lab experiments, as it provides an easy way to connect GUI components with data and logic and supports a large number of scientific instruments ranging from GPIB devices, oscilloscopes to cameras from many different vendors. However, as measurement tasks get larger and more complicated, the drawbacks of LabVIEW programming quickly surface, which includes

1) Lack of real-time analysis capabilities. LabVIEW is mainly used for instrument controlling and data recording, but real-time analysis can be very helpful and LabVIEW is very limited in terms of data analysis.

2) As a visual programming language, the logic of LabVIEW, i.e. block diagrams, can be difficult to understand and make. Wires are often unorganized, icons look similar to each other and are confusing, and finding the correct ports and connecting wires to them are often time-consuming and unintuitive.
3) Poor version control. LabVIEW programs are saved as binary files, rather than text-based source codes, making it difficult to use popular version control software like Git to track changes.
4) Generic tasks in programming, including string manipulation, type converting, and basic arithmetic, are almost all done with blocks and wires, which appears very complicated and is time-consuming to do with mice.

In other words, the "visual programming" method can be quickly out of control in complex programs. Therefore, an alternative solution to data acquisition is desired.

B.3 Solutions

B.3.1 Transition to a Different Programming Language

The solution to a number of the aforementioned issues starts with substituting LabVIEW with a text-based and more generic programming language. The replacement to LabVIEW should have good support for instrument control and data analysis, and good for basic programming tasks. MATLAB and Python stand out in these aspects.

MATLAB is a numerical computing software and programming language widely used in scientific research and engineering. Combined with its many toolboxes, the software suite provides very powerful capabilities in signal processing, image processing, instrument control and many other areas. It also has relatively good support for daily tasks like string manipulation. Python, on the other hand, is a well-designed generic programming language widely used for open-source projects and has seen a lot of popularity in the scientific research community in recent years. Companies like Basler AG are providing first-party Python support for their instruments. With NumPy, matplotlib and a few other modules, python programs can practically achieve data acquisition and analysis tasks equally well as MATLAB.

For GUI programming, MATLAB introduced an “App Designer” in version R2016a, and has become a relatively complete GUI toolkit that supports common controls and has most 2D and 3D plotting capabilities. In Python, PyQt or PySide, which are “bindings” of C++ version of Qt, is a popular solution for GUI programming. It provides full GUI functionality and is well documented.

MATLAB and Python are both particularly good for instrument control programming, as the interactive mode allows the developer to easily interact with hardware, like sending commands and receiving responses. This allows a user to easily debug instrument-related programs.

Compared with MATLAB and Python, the C++ language is a low-level language, has more complex syntax, and is a compiled language, which leads to a lower developing efficiency. Therefore, it is not very suitable for lab experiment software.

B.3.2 Abstraction and Object-oriented Programming

The LabVIEW program in Appendix Figure 12, which moves three motion controllers to given coordinates and uses the camera to take a certain number of images, would look like Appendix Figure 14 if translated to Python code

```
# omitting import statements for simplicity

# moving Thorlabs motion controllers

MOTION_CONTROLLER_X_SN = '83854669'
MOTION_CONTROLLER_Y_SN = '27502878'
CAMERA_SN = '23060909'

DeviceManagerCLI.BuildDeviceList()
motion_controller_x = TCubeDCServo.CreateTCubeDCServo(MOTION_CONTROLLER_X_SN)
motion_controller_x.Connect(MOTION_CONTROLLER_X_SN)

if not motion_controller_x.IsSettingsInitialized():
    motion_controller_x.WaitForSettingsInitialized(2000)

motion_controller_x.StartPolling(250)
time.sleep(0.1)
motion_controller_x.EnableDevice()
time.sleep(0.1)

motion_controller_x.LoadMotorConfiguration(MOTION_CONTROLLER_X_SN)

motion_controller_x.MoveTo(Decimal(15), 0)

motion_controller_y = TCubeDCServo.CreateTCubeDCServo(MOTION_CONTROLLER_Y_SN)
motion_controller_y.Connect(MOTION_CONTROLLER_Y_SN)

if not motion_controller_y.IsSettingsInitialized():
    motion_controller_y.WaitForSettingsInitialized(2000)

motion_controller_y.StartPolling(250)
time.sleep(0.1)
motion_controller_y.EnableDevice()
time.sleep(0.1)

motion_controller_y.LoadMotorConfiguration(MOTION_CONTROLLER_Y_SN)

motion_controller.MoveTo(Decimal(9), 0)

# capture a frame and save it to file 'D:\1.tiff'

camera_info = pylon.CDeviceInfo()
camera_info.SetSerialNumber(CAMERA_SN)
camera = pylon.InstantCamera(pylon.TlFactory.GetInstance().CreateFirstDevice(cam-
era_info))
camera.Open()

grab_result = camera.GrabOne(2000)

image = pylon.PylonImage()
image.AttachGrabResultBuffer(grab_result)
image.Save(pylon.ImageFileFormat_Tiff, r'D:\1.tiff')

image.Release()
grab_result.Release()

motion_controller_x.Disconnect()
motion_controller_y.Disconnect()
camera.Close()
```

Appendix Figure 14 A “low-level” Python code for controlling motion controller and capturing images.

It can be easily seen that there is a lot of repetitions in the code, and involves a lot of device-level details, making the code hard to read and debug. The initializations for the two motion controllers are essentially the same but are repeated. It also lacks logging and error handling. A way to improve the code is to use object-oriented programming (OOP) principles, abstract the instruments, and make them objects. Use a specific camera, Basler AcA 1920-155um as an example. The basic functionality of the camera is to acquire images. It should be able to set the exposure time, gain, acquisition framerate among many other functionalities. Therefore, the camera can be abstracted as an object, with functions like `grab_one()`, `set_exposure_time(exposure_time)` etc. Motion controllers can be abstracted similarly and given functions like `move_absolute(position)`. This way, Appendix Figure 14 can be simplified below

```
from basler_camera import BaslerAcA1920155um
from thorlabs.kinesis import TCubeDCServo, KCubeDCServo

MOTION_CONTROLLER_X_SN = '83854669'
MOTION_CONTROLLER_Y_SN = '27502878'
CAMERA_SN = '23060909'

motion_controller_x = TCubeDCServo(MOTION_CONTROLLER_X_SN)
motion_controller_y = KCubeDCServo(MOTION_CONTROLLER_Y_SN)
camera = BaslerAcA1920155um(CAMERA_SN)

motion_controller_x.connect()
motion_controller_y.connect()
camera.connect()

motion_controller_x.move_absolute(15)
motion_controller_y.move_absolute(9)
image = camera.grab_one_save(r'D:\1.tiff')

motion_controller_x.disconnect()
motion_controller_y.disconnect()
camera.disconnect()
```

Appendix Figure 15 An equivalent code snippet for Appendix Figure 14, after using OOP and writing classes for instruments.

This is much simpler and easier to read and is very close to plain English.

The code can be abstracted even further. This particular model Basler camera is also a Basler camera, meaning some functions like `set_exposure_time()` could be "shared" with other models of Basler cameras. The Basler cameras are essentially cameras, and all cameras should be able to take pictures. (This uses the "inheritance" concept in OOP.) On the other hand, cameras are also scientific instruments, which all need to be connected before being used and disconnected after an experiment finishes, which is the same for motion controllers. And this behavior is the same in all

experiments. Therefore, connecting and disconnecting of instruments, plus many other functionalities of instruments, can be automatically handled in an "experiment". With the factory method pattern, the previous code snippet can be simplified to Appendix Figure 16.

```
from model import ExperimentModel

class BasicExperiment(ExperimentModel):

    instruments = {'motion_controller_x': ('Thorlabs T-Cube', '83854669'),
                   'motion_controller_y': ('Thorlabs K-Cube', '27502878'),
                   'camera': ('Basler AcA 1920-155um', '23060909')
    }

    job = [('motion_controller_x', 'move_absolute', {'position': 15}),
           ('motion_controller_y', 'move_absolute', {'position': 9}),
           ('camera', 'grab_one_save', {'filename': r'D:\1.tiff'}),
    ]


if __name__ == '__main__':
    experiment = BasicExperiment()
    experiment.run()
```

Appendix Figure 16 An equivalent code snippet for Appendix Figure 15, after another level of abstraction.

This is the highest level of abstraction. The code is very concise and only contains essential information. It allows very easy modification of instruments and the tasks in the experiment. The "BDI experiment framework" aims to be able to allow all measurement programs to be written in such a way.

B.3.3 Real-time Analysis

A basic but important improvement is to include real-time previews of sample images, which allows the experiment operator to see the real-time reconstruction and determine if the correct coherence gate is achieved by evaluating the shape and intensity of the image and the depth of the coherence gate. This real-time reconstruction reads image data directly from the camera, runs FFT and displays the reconstructed image, all of which takes place in the memory only (without the file I/O exchange) to achieve the maximum framerate.

B.3.4 Testing and Validation

Software testing is an important procedure in professional software development. Testing helps discover bugs in the code and ensures that the software is good for use. In the lab setting, testing also helps detect instrument errors before an actual experiment is run.

Instrument-related tests that can be run before the experiment include: verifying if a motion controller can move to a given position, verifying if a camera can capture images at the desired framerate, and confirming the light source is "ON" after switching power. For other experiment-related environment, validations include whether there is enough disk space and whether the expected number of frames are saved to hard disk. If an issue is found, it can be reported on the screen or notified via email, and the issue may be resolved as early as possible.

B.3.5 Logging, Error Handling and Error Reporting

In Python, logging can be done with the built-in `logging` module, which offers a lot of customization options enough for daily tasks.

Errors thrown by instruments should be properly handled, which includes logging and email notification.

B.4 Result

The current BDM experiments use a measurement program that uses many of these improvements. The system is capable of switching the power of the light source, switching between conventional microscopy mode and BDI mode, capturing images, running real-time BDI reconstruction, controlling motion controller, running experiment sequence, notifying user, and using MATLAB to run onekey analysis immediately after data acquisition is finished, all in the same program.

The user interface for the program is shown in Appendix Figure 17. This program uses Python, with PyQt5 for the graphical user interface (GUI) and multithreading, PySerial for controlling Superlum light source power, official Basler pylon package adapted for Python for camera image acquisition, official Thorlabs control for motion controller movement, Scipy and NumPy for data analysis including hologram image reconstruction, and matplotlib for displaying images.

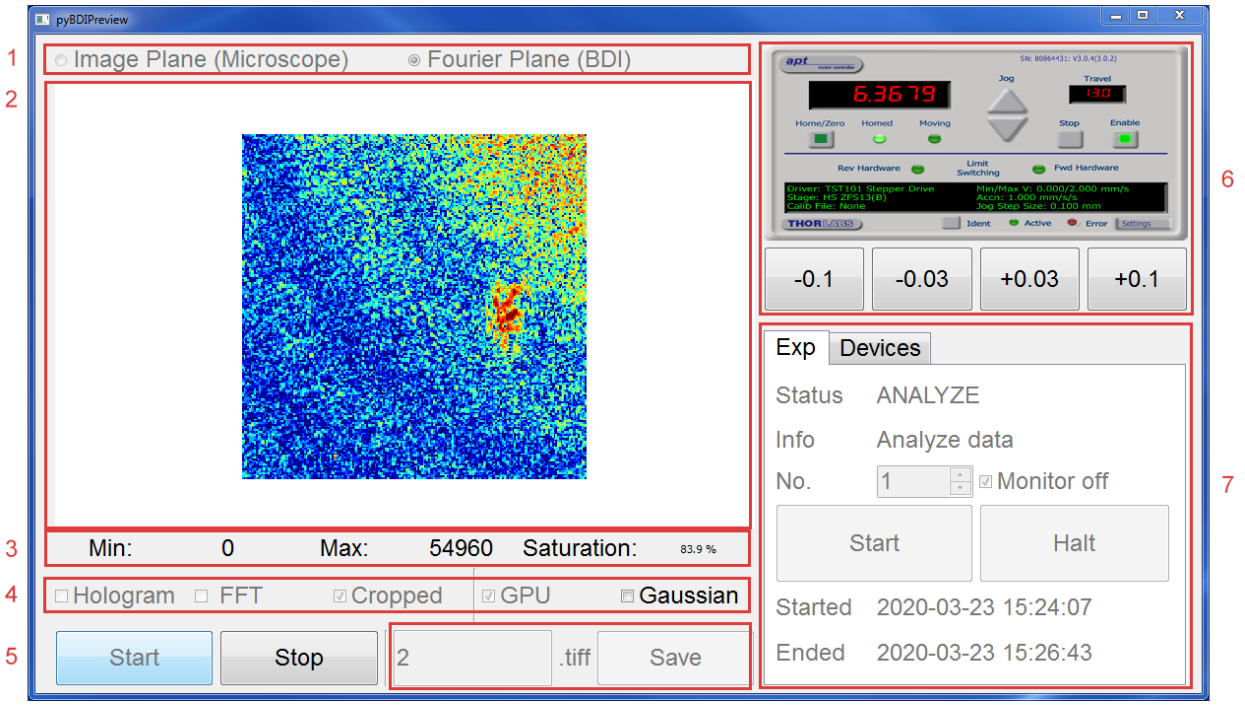

Appendix Figure 17 The all-in-one measurement program for the BDM. 1) mode switch, 2) microscopy/OCI preview area, 3) image statistics, 4) preview options 5) image saving area 6) motion controller 7) experiment sequence execution and instrument power switches

The program greatly reduces the time and hassle in switching between different programs and manually running analyses. This workflow measures a sample and returns BDI analysis results within 4 minutes (from mounting a sample to seeing results) and allows the experiment to proceed in quick succession. The real-time preview helps evaluate sample imaging quality and immobilization quality, the fast turnaround time reduces samples' exposure to non-CO_2 controlled environment and preserves samples' quality, and the immediate feedback allows predictive IVF experiments to be done.

APPENDIX C. FORMALIZING BIODYNAMIC DATA PROCESSING

C.1 BDI Biomarkers

C.1.1 Precondition Biomarkers and Changes

Precondition biomarkers indicate the sample condition before any perturbation is applied. Such biomarkers include intensity biomarker backscatter brightness ("BSB"), general motility biomarker normalized standard deviation ("NSD"), image pixel count ("NCNT"), and spectroscopy biomarkers like knee frequency ("KNEE"), dynamic range ("DR"), Nyquist floor ("NY"), mid-frequency slope ("S") and half-width at half maximum ("HW").

On a pixel basis, BSB is the average intensity over 500 frames, and NSD is defined as $\Delta I / \langle I \rangle$, i.e. the standard deviation for the pixel divided by the average intensity or BSB. These biomarkers are usually averaged over an entire sample to denote the general brightness and motility of the sample.

A Doppler fluctuation spectrum is shown in Appendix Figure 18a. Spectrum-related precondition biomarkers like knee frequency, mid-frequency slope and dynamic range are from curve fitting of a Lorentzian function.

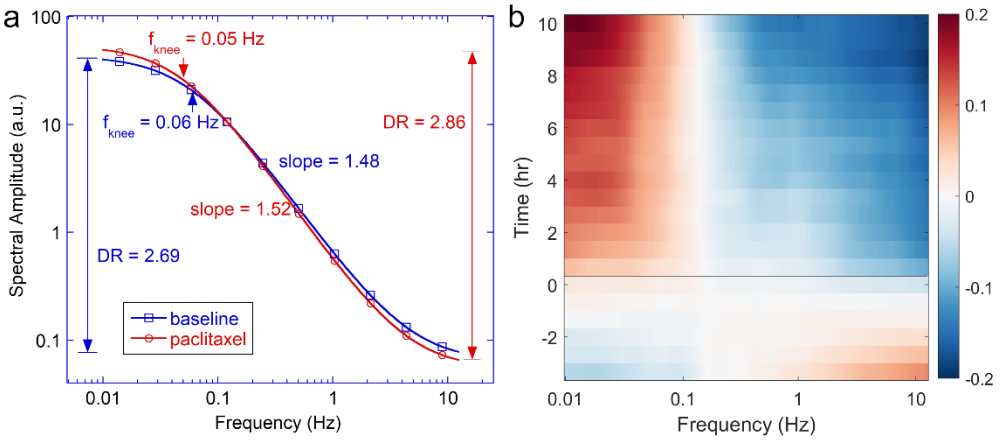

Appendix Figure 18 An example of sample baseline and terminal spectra, and the differential spectrogram. a) baseline spectrum and final spectrum after the sample is treated with 10 μM paclitaxel. b) time-lapse differential spectrogram.

The changes in these precondition values form another set of biomarkers, and they are related to variation in Doppler frequency shift and persistence time caused by drug effects, and their interpretations are given in CHAPTER 2.

C.1.2 Time-frequency Spectroscopic Biomarkers

Time-lapse differential spectrograms usually fall into a few of the following patterns: overall suppression, low-frequency suppression and high-frequency enhancement (blueshift), low-frequency enhancement and high-frequency suppression (redshift, as in Appendix Figure 18b), and mid-frequency enhancement and suppression at other frequencies. The critical frequencies, i.e. zeros of the spectrograms, also vary across different drugs.

To quantitatively characterize features in the drug spectrograms, these time-lapse spectral responses are first processed as $N_t \times N_f$ matrices (N_t being the number of measurement loops, and N_f being the number of sampling frequencies). Fluctuation spectra usually have a dynamic range of 3 orders of magnitude, and they span the frequency range of 0.01 Hz – 12.5 Hz which also covers 3 orders of magnitude. While the original frequency axis of the spectra is on the linear scale (or as an arithmetic sequence), according to the Fourier transform it is resampled to N_f frequencies on the logarithmic scale (or as a geometric sequence) based on a binning method (see appendix chapter C.2.2).

Drug response spectrograms can be projected to spectrogram masks defined below. A set of "global" masks that describe general spectrogram pattern is constructed with univariate time-domain and frequency-domain vectors shown as below

$$\mathbf{T}^k = \begin{cases} \sqrt{\frac{1}{N_t}}(1,1,\cdots,1) & k = 0 \\ \sqrt{\frac{2}{N_t}}\left(\cos kt_1, \cos kt_2, \cdots, \cos kt_{N_t}\right) & k > 0 \end{cases} \tag{C.1}$$

$$\mathbf{F}^l = \begin{cases} \sqrt{\dfrac{1}{N_f}}\left(1,1,\cdots,1\right) & l = 0 \\ \sqrt{\dfrac{2}{N_f}}\left(\cos lf_1, \cos lf_2, \cdots, \cos lf_{N_f}\right) & l > 0 \end{cases} \tag{C.2}$$

where $t_p = \dfrac{\pi}{2N_f} + \dfrac{\pi}{N_f}\left(p-1\right)$ and $f_q = \dfrac{\pi}{2N_f} + \dfrac{\pi}{N_f}\left(q-1\right)$. It can be shown that

$$\left\langle \mathbf{T}^k, \mathbf{T}^{k'} \right\rangle = \delta_{kk'}, \quad \left\langle \mathbf{F}^l, \mathbf{F}^{l'} \right\rangle = \delta_{ll'} \tag{C.3}$$

where δ_{kl} is the Kronecker delta. The "global" spectrogram masks are outer products of the two vectors, i.e.

$$\mathbf{M}^{kl} = \mathbf{T}^k \otimes \mathbf{F}^l \tag{C.4}$$

A drug spectrogram $\mathbf{R}$, represented as a matrix of size $N_t \times N_f$, can be mapped to spectrogram masks by calculating their Frobenius inner products, i.e.

$$\begin{aligned} v_{k+1,l+1} = \left\langle \mathbf{R}, \mathbf{M}^{kl} \right\rangle_{\mathrm{F}} &= R_{11}M_{11}^{kl} + R_{12}M_{12}^{kl} + \ldots + R_{1N_f}M_{1N_f}^{kl} \\ &+ R_{21}M_{21}^{kl} + R_{22}M_{22}^{kl} + \ldots + R_{2N_f}M_{2N_f}^{kl} \\ &\vdots \\ &+ R_{N_t1}M_{N_t1}^{kl} + R_{N_t2}M_{N_t2}^{kl} + \ldots + R_{N_tN_f}M_{N_tN_f}^{kl} \end{aligned} \tag{C.5}$$

i.e. v_{kl} is the $\left(k-1,l-1\right)$-th order feature value for the drug spectrogram $\mathbf{R}$, and they can form a "feature value matrix" $\mathbf{V} = \left(v_{kl}\right)$. (Matrix element subscripts starts from 1, which corresponds to the 0^{th} order.)

It can be shown that the spectrogram masks are orthonormal to each other, i.e. $\left\langle \mathbf{M}^{kl}, \mathbf{M}^{k'l'} \right\rangle = \delta_{kk'}\delta_{ll'}$ under the Frobenius inner product, and they form a set of orthonormal and complete bases for the spectrogram of size $\left(N_t, N_f\right)$, and thus form a $N_t \cdot N_f$ dimensional space. While $\left(k,l\right)$ can be arbitrarily large in this generalized theory, the spectrograms observed in 10-hour post-drug measurements are selected to have up to the 2rd order in frequency and time, due to the broadband nature of the BDI.

Alternatively, a set of "local" biomarkers that filter the low/mid/high-frequency responses can be constructed. Similar to "global" masks, they are orthogonal in the response space, and the time-dependent matrices are also orthogonal. (But the global masks are not orthogonal to the local ones.)

The first few "global" and "local" spectral feature masks are shown in Appendix Figure 19.

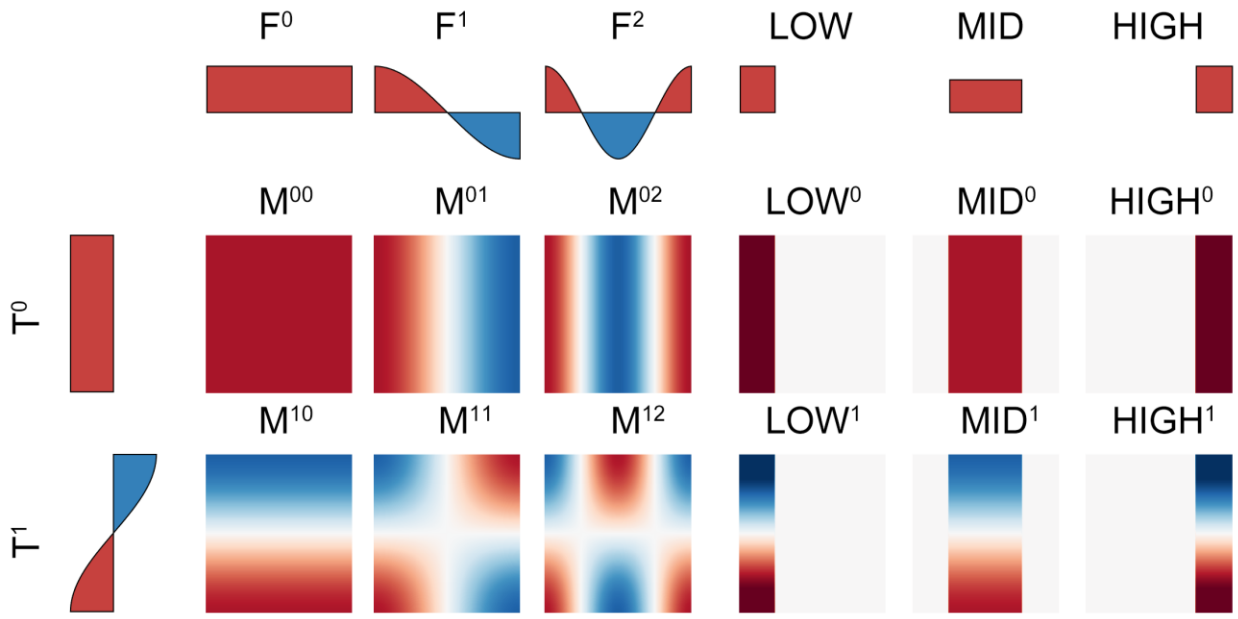

Appendix Figure 19 The spectral masks with 0^{th} and 1^{st} orders in time and 0^{th}, 1^{st} and 2^{nd} orders in frequency, plus "local" biomarkers with 0^{th} and 1^{st} order in time.

While the previous discussion on orthonormal masks has a strong mathematical basis and offers an intuitive interpretation of feature values, it can be restrictive in actual BDI analysis. The orthonormality only works well for spectrograms of the same size, but the research group has used various measurement formats in experiments, including 9 baseline loops, 27 baseline loops with each loop of 24 minutes (denoted as "9+27/24"), 15+6/48 and 15+6/40. As a result, spectrogram feature values from experiments with different data formats cannot be directly compared, which means that old but important data are unusable. A simple example is that when a spectrogram matrix $\mathbf{R} = J_{N_f,N_t}$ is mapped to mask $\mathbf{M}^{00} = \sqrt{\frac{1}{N_f N_t}} J_{N_f,N_t}$ ($J_{m,n}$ denotes an all-ones matrix of size $m \times n$), the feature value is $\left\langle \mathbf{R}, \mathbf{M}^{00} \right\rangle = \sqrt{N_f N_t}$ which is dependent on the format, although the drug response itself is not directly related to how many loops or how many frequency components are used. There are two ways to solve this problem.

When the time-lapse drift in the spectrogram is negligible, a "basic" version of the feature values can be obtained by mapping time-averaged differential spectrogram $\mathbf{R}$ to a frequency-domain vector $\mathbf{F}$ that are masks compressed along the time axis

$$v = \left\langle \mathbf{R}, \mathbf{F} \right\rangle \tag{C.6}$$

which forms a feature vector $\mathbf{V} = \left(v_l \right)$. Since the frequency format is consistent (130 components in the current analysis), it is irrelevant. This method gives up temporal information but works for a majority of responses observed.

The second method is to revise the calculation used in (C.5) by adding a coefficient $\sqrt{\frac{1}{N_t N_f}}$, i.e.

$$\begin{aligned} v_{k+1,l+1} &= \sqrt{\frac{1}{N_t N_f}} \left\langle \mathbf{R}, \mathbf{M}^{kl} \right\rangle_{\mathrm{F}} \\ &= \sqrt{\frac{1}{N_t N_f}} \begin{pmatrix} R_{11} M_{11}^{kl} + R_{12} M_{12}^{kl} + \ldots + R_{1N_f} M_{1N_f}^{kl} \\ + R_{21} M_{21}^{kl} + R_{22} M_{22}^{kl} + \ldots + R_{2N_f} M_{2N_f}^{kl} \\ \vdots \\ + R_{N_t 1} M_{N_t 1}^{kl} + R_{N_t 2} M_{N_t 2}^{kl} + \ldots + R_{N_t N_f} M_{N_t N_f}^{kl} \end{pmatrix} \end{aligned} \tag{C.7}$$

This is the current normalization method used in programs like "dbread", but different from a previous publication [1]. The sum and multiplication properties remain under this linear scaling, and mathematically this is the optimal solution to dealing with different formats of data.

C.1.3 Relation between spectrogram masks and DFT

The "global" part of the feature vector defined in Eq. (C.6) is closely related to DFT (or FFT), as

$$
\begin{aligned}
v_l &= \sqrt{\frac{2}{N_f}} \sum_{q=1}^{N_f} r_q \cos\left[(l-1) f_q \right] \\
&= \sqrt{\frac{2}{N_f}} \sum_{q=1}^{N_f} r_q \cos\left[(l-1)\left(-\frac{\pi}{2N_f} + \frac{\pi}{N_f} q \right) \right] \\
&= \sqrt{\frac{2}{N_f}} \sum_{q=1}^{N_f} r_q \operatorname{Re}\left[\mathrm{e}^{\mathrm{i}(l-1)\left(-\frac{\pi}{2N_f} + \frac{\pi}{N_f} q \right)} \right] \\
&= \sqrt{\frac{2}{N_f}} \sum_{l=1}^{N_f} r_l \operatorname{Re}\left[\mathrm{e}^{\mathrm{i}(l-1)\frac{2\pi}{4N_f}(2q-1)} \right]
\end{aligned}
\tag{C.8}
$$

for $l > 0$ ($l = 0$ case is trivial and can be merged with the $l > 0$ case). This is very similar to the definition of DFT. If one constructs a signal $\left\{ r'_{q'} \right\}$ of length $4N_f$ that consists of 0's interleaved with $\left\{ r_i \right\}$ followed by $2N_f$ of 0's, i.e.

$$
\left\{ r'_i \right\} = \underbrace{0, r_1, 0, r_2, \cdots, 0, r_{N_f}}_{2N_f}, \underbrace{0, 0, \cdots, 0}_{2N_f} \tag{C.9}
$$

Eq. (C.8) becomes

$$
v_l = \sqrt{\frac{2}{N_f}} \sum_{q'=1}^{4N_f} r'_{q'} \operatorname{Re}\left[\mathrm{e}^{\mathrm{i}(l-1)\frac{2\pi}{4N_f}(q'-1)} \right] \tag{C.10}
$$

By comparing this with the definition of DFT $v_l = \sum_{q=1}^{N} x_q \mathrm{e}^{\mathrm{i}\frac{2\pi}{N}(l-1)(q-1)}$ where $\left\{ x_q \right\}$ is a signal, it is obvious that the feature vector is the first N_f components of the real part of the DFT of the signal $\left\{ \tilde{R}'_i \right\} = \mathrm{DFT}\left(\left\{ r'_i \right\} \right)$ with a normalization factor, i.e.

$$
v_{l+1} = \begin{cases} \sqrt{\frac{1}{N_f}} \operatorname{Re}\left(\tilde{R}_l' \right) & l = 0 \\ \sqrt{\frac{2}{N_f}} \operatorname{Re}\left(\tilde{R}'_l \right) & l > 0 \end{cases} \tag{C.11}
$$

The feature matrix from projection onto bases in Eq. (C.5) is also related to the DFT of the response (for $k > 0$, $l > 0$)

$$
\begin{aligned}
v_{kl} &= \sqrt{\frac{4}{N_f N_t}} \sum_{p=1}^{N_t} \sum_{q=1}^{N_f} r_{pq} \cos\left[(k-1)t_p\right] \cos\left[(l-1) f_q\right] \\
&= \sqrt{\frac{4}{N_f N_t}} \sum_{p=1}^{N_t} \sum_{q=1}^{N_f} \frac{1}{2} r_{pq} \left\{ \cos\left[(k-1)t_p + (l-1) f_q\right] + \cos\left[(k-1)t_p - (l-1) f_q\right] \right\} \\
&= \sqrt{\frac{1}{N_f N_t}} \sum_{p=1}^{N_t} \sum_{q=1}^{N_f} r_{pq} \, \mathrm{Re} \left\{ \mathrm{e}^{\mathrm{i}\left[(k-1)\frac{2\pi}{4N_t}(2p-1)+(l-1)\frac{2\pi}{4N_f}(2q-1)\right]} + \mathrm{e}^{\mathrm{i}\left[(k-1)\frac{2\pi}{4N_t}(2p-1)+(l-1)\frac{2\pi}{4N_f}(2q-1)\right]} \right\} \\
&= \sqrt{\frac{1}{N_f N_t}} \sum_{p=1}^{N_t} \sum_{q=1}^{N_f} r_{pq} \, \mathrm{Re} \left\{ \mathrm{e}^{\mathrm{i}\left[(k-1)\frac{2\pi}{4N_t}(2p-1)+(l-1)\frac{2\pi}{4N_f}(2q-1)\right]} + \mathrm{e}^{\mathrm{i}\left[(k-1)\frac{2\pi}{4N_t}(4N_t+2-2p-1)+(l-1)\frac{2\pi}{4N_f}(2q-1)\right]} \right\}
\end{aligned}
$$

Therefore, if two matrices of size $4N_t \times 4N_f$ are prepared, **A** with 0's interleaved and padded, similar in the 1D case, and the other **B** that is similarly constructed but with time axis reversed, i.e

$$\mathbf{A}=\begin{pmatrix}
0 & 0 & 0 & 0 & \cdots & 0 & 0 & 0 & 0 & \cdots & 0\\
0 & R_{11} & 0 & R_{12} & \cdots & 0 & R_{1N_f} & 0 & 0 & \cdots & 0\\
0 & 0 & 0 & 0 & \cdots & 0 & 0 & 0 & 0 & \cdots & 0\\
0 & R_{21} & 0 & R_{22} & \cdots & 0 & R_{2N_f} & 0 & 0 & \cdots & 0\\
\vdots & \vdots & \vdots & \vdots & \ddots & \vdots & \vdots & \vdots & \vdots & \ddots & \vdots\\
0 & 0 & 0 & 0 & \cdots & 0 & 0 & 0 & 0 & \cdots & 0\\
0 & R_{N_t 1} & 0 & R_{N_t 2} & \cdots & 0 & R_{N_t N_f} & 0 & 0 & \cdots & 0\\
0 & 0 & 0 & 0 & \cdots & 0 & 0 & 0 & 0 & \cdots & 0\\
0 & 0 & 0 & 0 & \cdots & 0 & 0 & 0 & 0 & \cdots & 0\\
\vdots & \vdots & \vdots & \vdots & \ddots & \vdots & \vdots & \vdots & \vdots & \ddots & \vdots\\
0 & 0 & 0 & 0 & \cdots & 0 & 0 & 0 & 0 & \cdots & 0
\end{pmatrix}_{4N_t\times 4N_f}$$

$$\mathbf{B}=\begin{pmatrix}
0 & 0 & 0 & 0 & \cdots & 0 & 0 & 0 & 0 & \cdots & 0\\
0 & 0 & 0 & 0 & \cdots & 0 & 0 & 0 & 0 & \cdots & 0\\
\vdots & \vdots & \vdots & \vdots & \ddots & \vdots & \vdots & \vdots & \vdots & \ddots & \vdots\\
0 & 0 & 0 & 0 & \cdots & 0 & 0 & 0 & 0 & \cdots & 0\\
0 & 0 & 0 & 0 & \cdots & 0 & 0 & 0 & 0 & \cdots & 0\\
0 & R_{N_t 1} & 0 & R_{N_t 2} & \cdots & 0 & R_{N_t N_f} & 0 & 0 & \cdots & 0\\
0 & 0 & 0 & 0 & \cdots & 0 & 0 & 0 & 0 & \cdots & 0\\
0 & R_{N_t-1,1} & 0 & R_{N_t-1,1} & \cdots & 0 & R_{N_t-1,N_f} & 0 & 0 & \cdots & 0\\
\cdots & \cdots & \cdots & \cdots & \ddots & \vdots & \vdots & \vdots & \vdots & \ddots & \vdots\\
0 & 0 & 0 & 0 & \cdots & 0 & 0 & 0 & 0 & \cdots & 0\\
0 & R_{11} & 0 & R_{12} & \cdots & 0 & R_{1N_f} & 0 & 0 & \cdots & 0
\end{pmatrix}_{4N_t\times 4N_f}$$

with $\tilde{\mathbf{R}}' = \mathrm{DFT}\left(\mathbf{A}+\mathbf{B}\right)$, we will have

$$v_{k+1,l+1}=\begin{cases}
\sqrt{\dfrac{1}{4N_fN_t}}\,\mathrm{Re}\left(\tilde{\mathbf{R}}'_{k+1,l+1}\right) & k=l=0\\
\sqrt{\dfrac{1}{2N_fN_t}}\,\mathrm{Re}\left(\tilde{\mathbf{R}}'_{k+1,l+1}\right) & k=0,l=1 \text{ or } k=1,l=0\\
\sqrt{\dfrac{1}{N_fN_t}}\,\mathrm{Re}\left(\tilde{\mathbf{R}}'_{k+1,l+1}\right) & k>0,l>0
\end{cases} \qquad \text{(C.12)}$$

Despite the relation, Eqs. (C.11) and (C.12) do not offer computational benefits for calculating the feature values in real situations, as the orders of the spectrogram masks are very low ($k,l \leq 2$).

C.2 Condensed Data Format (CDF)

C.2.1 Overview

In CHAPTER 2 - CHAPTER 5, the Doppler fluctuation spectrograms are calculated based on sample-averaged fluctuation spectra, which is the standard routine of onekey analysis. The onekey program determines the boundary of the sample and removes the background (i.e. "masking") based on a histogram approach, and calculates the dynamics within this region. However, there are some problems with this approach: (1) The mask can be unreliable in certain cases, either choosing a very small region of the sample or including irrelevant content as part of the sample (2) This method ignores the variability within the sample, as discussed in CHAPTER 6. If one wants to analyze the dynamics of a certain region other than the default masked area, one can always do so by reanalyzing raw data, but it is costly to do such a re-analysis in terms of retrieval time and computation time. The situation is similar for phase histograms that use complex field information from sample images. Therefore, the condensed data format (CDF) is introduced as an intermediate data format for quick spectrum and phase histogram reconstruction. This format calculates the fluctuation spectrum and phase transition information (intermediate processing) in 2px × 2px squares (subsampling), allowing reconstruction without losing information.

C.2.2 Power Spectrum Subsampling

The fluctuation power spectrum for one pixel at position (i, j) in the sample is calculated as the square of the FFT of the intensity time series:

$$S(i, j; f) = \left| \mathcal{F}_t \left[I(i, j; t) \right] \right|^2 \tag{C.13}$$

The average spectrum of a region σ is calculated as

$$S_{\sigma,\mathrm{raw}}(f) = \left\langle S(i, j; f) \right\rangle_{i,j} = \frac{\sum_{(i,j)\in\sigma} S(i, j; f)}{\sum_{(i,j)\in\sigma} 1} \tag{C.14}$$

where σ is a spatial mask segmenting the entire sample. The "raw" spectrum is normalized based on Parseval's theorem [2]:

$$S_{\sigma,\mathrm{norm}}(f) = \frac{S_{\sigma,\mathrm{raw}}(f)}{\sum_f S_{\sigma,\mathrm{raw}}(f)} \tag{C.15}$$

Spatial down-sampling enables the analysis of spectral features with low noise at good spatial resolution. The spectrum of a single sample can be too noisy to extract spectral features by methods like curve fitting. Therefore, each sample is divided into 2 × 2 pixel squares (referred to as "TDSI pixels" below) as the basic unit for spectral averaging. Because biodynamic imaging is an interferometric technique using short coherence, each image is reconstructed from backscattered light from a selected depth in the sample. Therefore, each TDSI pixel represents a voxel of the sample. As a nominal choice that balances spatial resolution and spectral resolution, the spectrum of each TDSI pixel is the average over the 4 pixels,

$$S_{\mathrm{raw}}(\tilde{i}, \tilde{j}; f) = \frac{1}{4} \sum_{(i,j)\in\sigma(\tilde{i},\tilde{j})} S_{\mathrm{raw}}(i, j; f) \tag{C.16}$$

where $\sigma(\tilde{i}, \tilde{j})$ is the area $\{2\tilde{i}-1, 2\tilde{i}\}\times\{2\tilde{j}-1, 2\tilde{j}\}$ in the original image, and $(\tilde{i}, \tilde{j})$ are the coordinates in the sub-sampled image.

Frequency down-sampling reduces the frequency components stored while still allowing high-precision reconstruction. Our data acquisition format generates spectra of 1024 frequency components evenly spaced on the linear scale. However, most TDS analysis is based on the spectra on the log-log scale, which have sparse points in the low frequencies and dense points in high frequencies. Our frequency down-sampling method remaps the 1024 components to 130 that are evenly spaced on the log scale. The low-frequency part is up-sampled with interpolation, while the high frequency uses a binning method and preserves the average. The original normalization factor $M(\tilde{i}, \tilde{j}) = \sum_f S_{\mathrm{raw}}(\tilde{i}, \tilde{j}; f)$ [the denominator in Eq. (C.15)] is stored to maintain the same normalization. In our data analysis, the order of averaging is not relevant

$$\sum_f \sum_{(\tilde{i},\tilde{j})\in\sigma} S(\tilde{i}, \tilde{j}; f) = \sum_{(\tilde{i},\tilde{j})\in\sigma} \sum_f S(\tilde{i}, \tilde{j}; f) \tag{C.17}$$

and the normalized spectrum is reconstructed by

$$S_{\sigma,\mathrm{norm}}(f)=\frac{S_{\sigma,\mathrm{raw}}(f)}{\sum_{f}S_{\sigma,\mathrm{raw}}(f)}=\frac{\sum_{(\tilde{i},\tilde{j})\in\sigma}S(\tilde{i},\tilde{j};f)}{\sum_{f}\sum_{(\tilde{i},\tilde{j})\in\sigma}S(\tilde{i},\tilde{j};f)}=\frac{\sum_{(\tilde{i},\tilde{j})\in\sigma}S(\tilde{i},\tilde{j};f)}{\sum_{(\tilde{i},\tilde{j})\in\sigma}\sum_{f}S(\tilde{i},\tilde{j};f)}=\frac{\sum_{(\tilde{i},\tilde{j})\in\sigma}S(\tilde{i},\tilde{j};f)}{\sum_{(\tilde{i},\tilde{j})\in\sigma}M(\tilde{i},\tilde{j})} \quad \text{(C.18)}$$

Eq. (C.18) shows that once the TDSI pixel-wise down-sampled spectra $S(\tilde{i},\tilde{j};f)$ and normalization factors $M(\tilde{i},\tilde{j})$ are obtained, the normalized spectrum of any given region σ can be reconstructed.

On log-log plots, the difference between spectrograms reconstructed from CDF files and those reconstructed from original pixels is negligible. The comparisons are presented in Appendix Figure 20c and d.

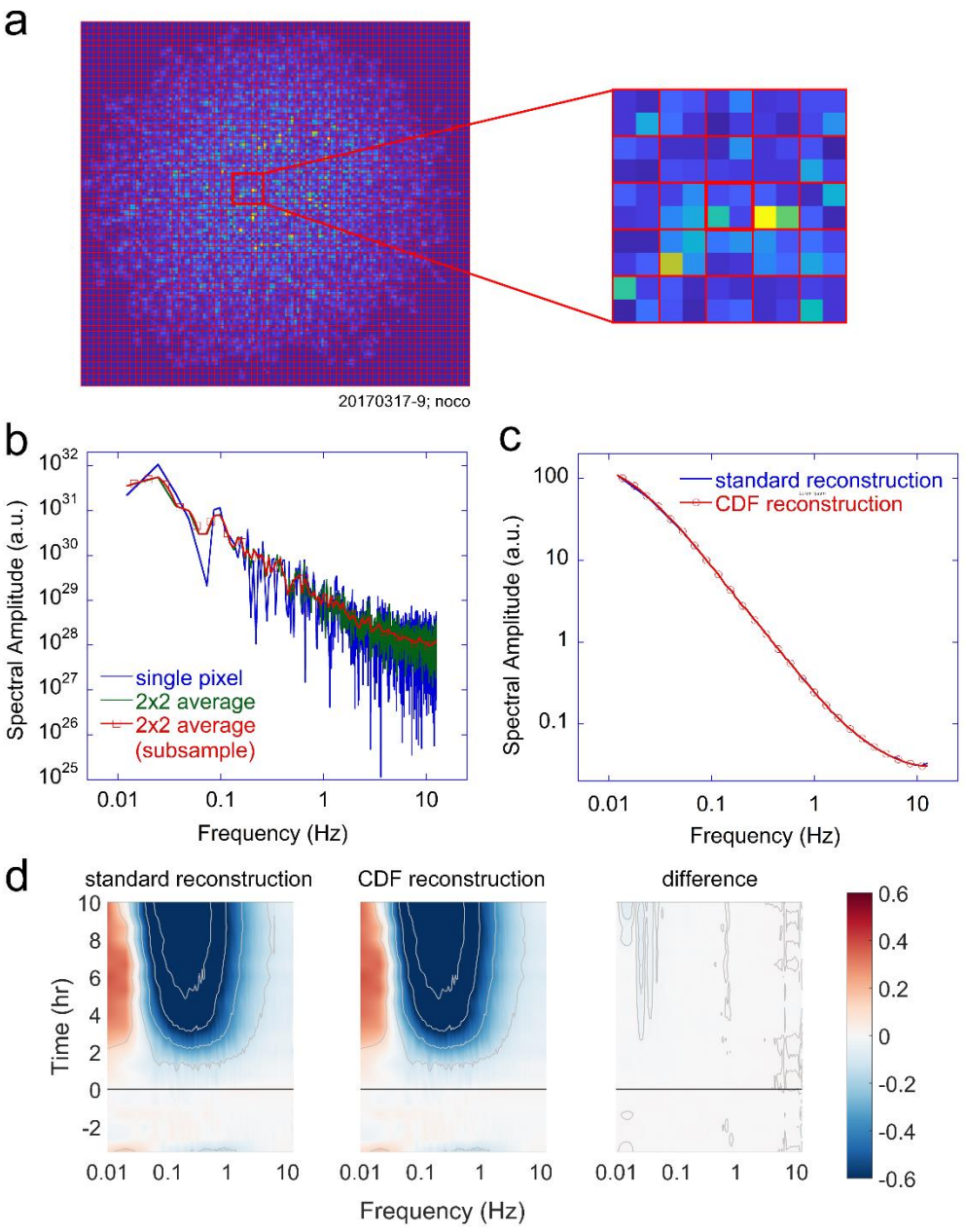

Appendix Figure 20 Demonstration of the condensed data format (CDF). The sample used in this figure is a DLD-1 spheroid treated with 10 μM nocodazole. a) Spatial down-sampling, with a 10 x 10 pixel region enlarged. b) Frequency down-sampling, with the spectrum of a single pixel in the 2 x 2 px area [labeled in a) with heavy border lines], the average spectrum of 4 pixels in the area, and down-sampled spectrum with 130 components evenly spaced on the log frequency axis. c) Comparison of a sample average spectrum reconstructed from raw data and from the CDF. d) Whole sample full-length spectrogram reconstructed from raw data and from a CDF file. The relative difference is <0.5%. Nocodazole was added at t=0.

The data format and disk spaces used in raw images, analyzed data and CDF are shown in Appendix Table 2.

Appendix Table 2 Comparison of three levels of data formats for speckle dynamics fluctuation spectrum reconstruction

Type	Format	Disk Space	Notes
Raw Images	2048 x 800 x 800 x 16bit uint16	2.44 GB	16-bit TIFF files
Analyzed Data	2048 x 256 x 256 x 64bit double	1 GB	All reconstructed frames
Condensed Data format	130 x 128 x 128 x 64bit double + 1 x 128 x 128 x 64bit double	16 MB	Homodyne only, down-sampled spectrum and normalization factor

Both homodyne spectrum (i.e. FFT of the intensity of pixels) and heterodyne spectrum (i.e. FFT of the complex image field) are processed this way. The discussion is based on the "new" 2048 frame format, which requires no stitching in constructing a spectrum. When dealing with legacy 500/50 frame data, CDF can still be defined with slight modifications. In the stitching program, both the low-frequency part (0.5Hz, 50 frames, resulting in 0.01 Hz – 0.25Hz) and the high-frequency part (25Hz, 500 frames, resulting in 0.05 Hz – 12.5 Hz) are resampled to 101 frequencies before being stitched together. Therefore, the legacy-format-specific CDF retains the 25 low-frequency components and resamples the high-frequency part to 101 frequencies, which allows the same stitching method to be used while saving the smallest amount of data.

C.2.3 Phase Histogram Subsampling

In phase-sensitive BDI analysis, for a datacube of N frames of size $N_y \times N_x$ in each loop, N-1 matrices of size $N_y \times N_x$ are calculated as one frame divided by the previous frame. The background is removed and only sample-related pixels are kept. The complex values are converted to four-quadrant inverse tangent (or "2-argument arctangent") ranging between $-\pi$ and π, creating N-1 new matrices. All the elements in these N-1 matrices are put into 630 interval bins [-3.15, 3.14), [-3.14, 3.13), … [3.14, 3.15), creating a "phase histogram". In other words, suppose the measurement starts at t_0, $\Delta t = \frac{1}{\mathrm{FPS}}$ is the capture interval, and $\mathbf{M}\left[t_0 + (k+1)\Delta t\right]$ is the k-th image, we have

$$\mathbf{M}\left[t_0+(k+1)\Delta t\right]=\mathbf{A}(t_0+k\Delta t)e^{i\mathbf{P}(t_0+k\Delta t)}\mathbf{M}\left[t_0+k\Delta t\right] \tag{C.19}$$

where $\mathbf{A}(t_0+k\Delta t)$ is the amplitude transition matrix and $\mathbf{P}(t_0+k\Delta t)$ is the phase transition matrix, and $\mathbf{P}(t_0+k\Delta t)=(p_{kl})\in[-\pi,\pi]$. The phase histogram is the histogram of values in matrices $\{\mathbf{P}(t_0+k\Delta t)\}_{k=0,1,\ldots,N-1}$.

The phase information can be subsampled in a similar way as spectrum subsampling. $\mathbf{P}(t_0+k\Delta t)$ matrices are calculated for each 2 px × 2px areas (instead of an entire image), and all the four-quadrant inverse arctangent values are put into the aforementioned bins. This results in a data matrix of dimension $630\times\frac{N_y}{2}\times\frac{N_x}{2}$. To reconstruct a histogram of an entire sample, simply add all the counts in individual subsampled pixels within the region, as histograms with the same bins can be added to create a new histogram.

C.3 Choosing Color Maps

C.3.1 1D Color Maps

Previous publications from our group have used "jet" color maps in the publications [1, 3, 4], but it is not the optimal choice for visualizing 2D data. The "jet" color map, one type of "rainbow" color maps, while having vibrant colors, is not "perceptually linear" and can introduce false details in the data because of the human eye's non-uniform sensitivity to different colors. A few publications have addressed this issue [5, 6], and an example using the group's own data is given in Appendix Figure 21. The differences in value between areas 1 and 2 are about 0.9, which is roughly the same as between the areas 3 and 4. However, in the spectrogram with "jet" color map, area 1 appears to be yellow and area 2 is red-ish, while areas 3 and 4 both appear as blue with slight differences. One might be led to think that area 2 shows a real feature, while it is not present. Such an artifact does not exist in the spectrograms with other color maps in the figure. These color maps are smoother in the perception.

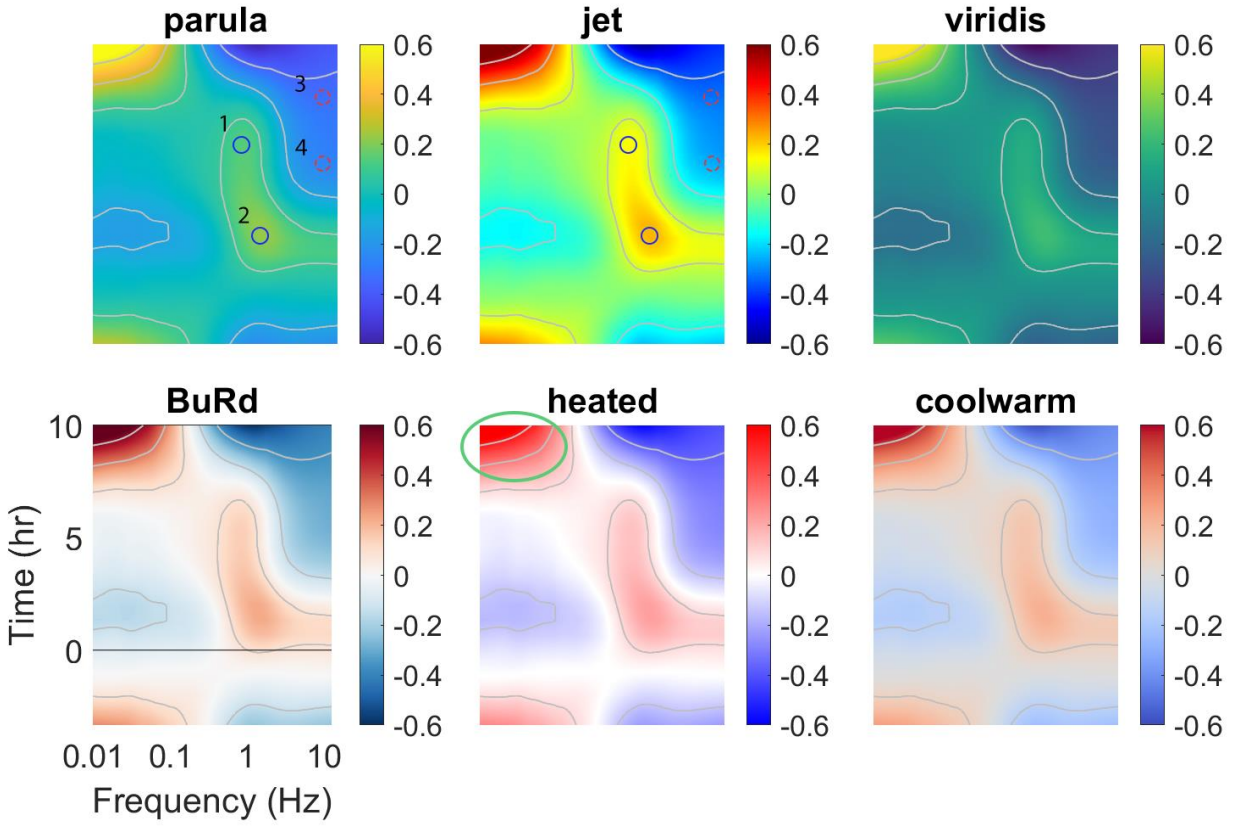

Appendix Figure 21 Comparison of different color maps on a drug spectrogram for a canine lymphoma biopsy treated with CHOP. All the color maps in this section use 256 levels of colors to ensure a smooth presentation.

Appendix Figure 21 shows two types of color maps: the ones in the top row are "sequential color maps", and the ones in the bottom row are "diverging color maps" which is suitable for data that are centered around a certain value. "parula" is the default color map for MATLAB since R2014b version, and the "viridis" is the default color map for the Python plot package matplotlib since version 2.0. Both parula and viridis are more perceptually linear than jet.

The diverging color maps shown in Appendix Figure 21 all use red and blue colors as contrasting colors, although there are many more choices. "BuRd" and "heated" both have a white center, while the "coolwarm" is slightly grey in the middle. The white color can help identify BDI spectrogram features, as zero values indicate zero net responses.

The perceptual uniformness of the color maps can be evaluated by the lightness (L*) of the color in the CIELAB (L*a*b*) color space, which is designed to approximate human vision. The lightness component is very close to the human perception of lightness. The lightness values for

the 6 color maps are shown in Appendix Figure 22. The colors of the lines are the actual colors of the color maps. “viridis” has a perfectly linear lightness vs index, “parula” is not strictly linear but smooth enough to allow good contrast, while the “jet” is very unsmooth, and the slope near the cyan and yellow colors dramatically changes, which partly explains the false details found in images using this color map.

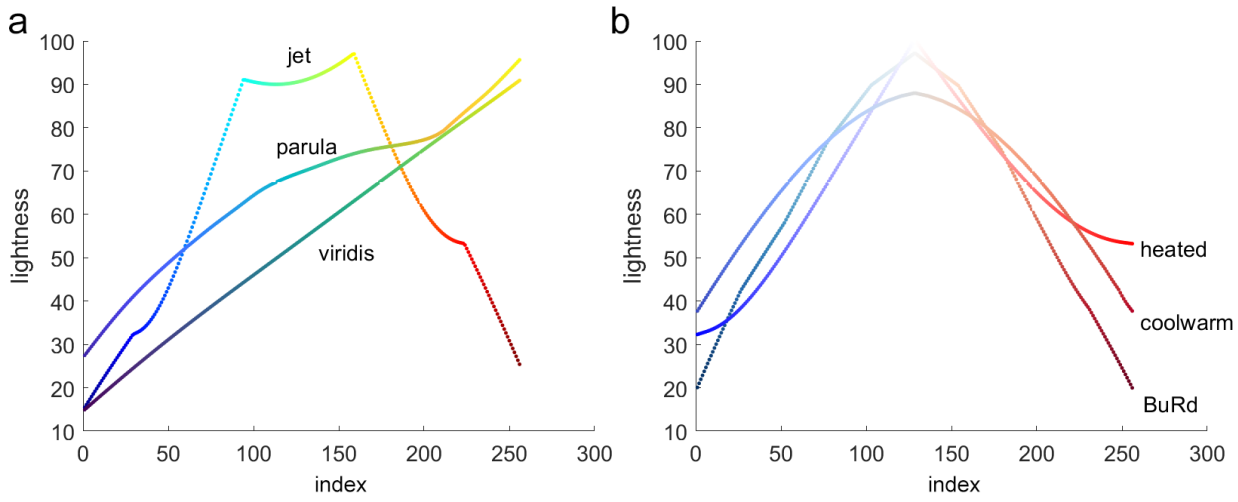

Appendix Figure 22 Color lightness in the CIELAB space vs the color’s index within the color map for sequential and diverging color maps.

For the three diverging color maps used in Appendix Figure 21, the lightness values are all relatively linear. The lightness value curve of the “heated” color map becomes very flat at both the blue and red color ends, which explains why the contrast reduces at the two extremes. This low contrast can be seen in the green circle in Appendix Figure 21, where the late, low-frequency response appears to saturate in the “heated” color map, which is not the case and is better visualized in the other color maps.

Considering perceptual accuracy and visual appeal, the current “onekey” programs use “parula” for sequential color maps used in OCI and MCI images, and “BuRd” for diverging color maps used in spectrograms.

C.3.2 2D Color Maps

Bivariate data visualization has been used in a number of disciplines like cartography and medical imaging. A suitable color map for these visualization tasks is as important as in the 1D case, and the idea of perceptual uniformity also applies. Several studies have been done on the subject [7-

11]. The TDSI work discussed in CHAPTER 6 of this dissertation extensively uses bivariate data visualization to illustrate the variability within biological samples. A few 2D color map candidates are shown in Appendix Figure 23 for esophageal biopsy samples.

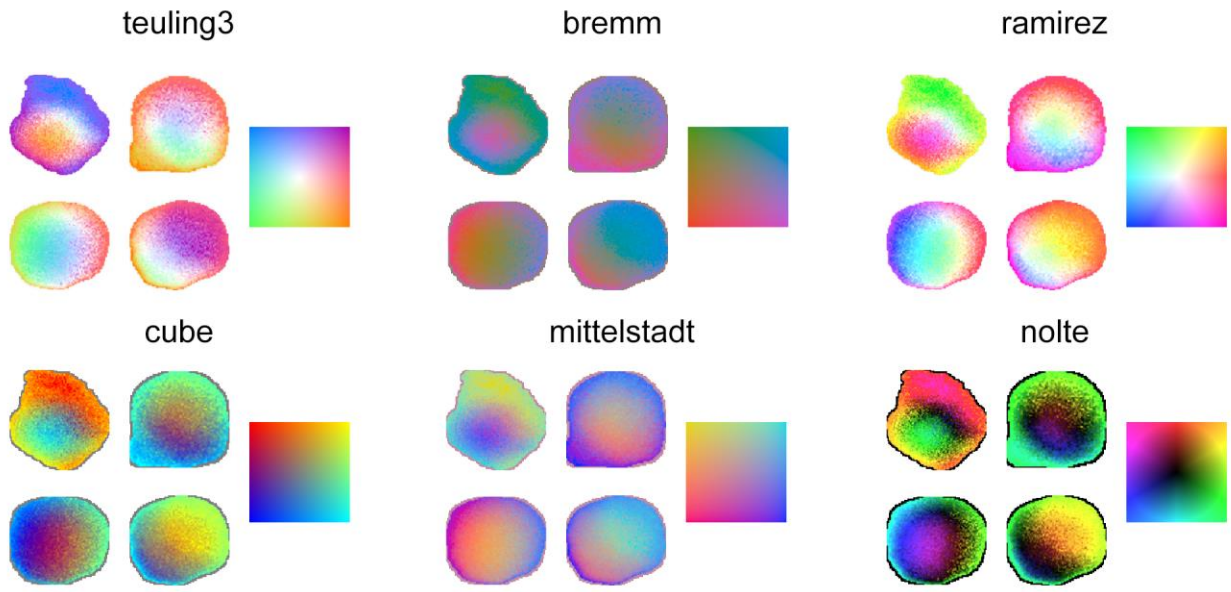

Appendix Figure 23 TDSI images of 4 esophageal biopsy samples using 6 different 2D color maps. [7-11]

The descriptions of these color maps and assessments are given in Appendix Table 3. Some of the assessments come from [7].

Appendix Table 3 A list of the 2D color maps and their assessments.

Name	Description	Color space	Perceptual uniformity	Color
Teuling3	Linear combination of 3 color planes in the sRGB space	sRGB	high	high
Cube	2D interpolation of a square with red, yellow, blue and cyan in the four corners		low	
Bremm	An area in the L*=55 plane in the CIELAB space	CIELAB	high	low
Mittelstadt	2D interpolation of a square with four chosen colors in the corners			
Ramirez	A radial map with the radius as saturation (S) and angle as hue (H). Center is white	HSV	low	high
Nolte	A radial map with the radius as value (V) and angle as hue (H). Center is black			

Considering the assessments and to make the "zero" value point appear as white (for the same reason in the appendix chapter C.3.1), "teuling3" color map is chosen for TDSI visualizations.

References

[1] D. D. Nolte, R. An, J. Turek, and K. Jeong, "Tissue dynamics spectroscopy for phenotypic profiling of drug effects in three-dimensional culture," Biomed. Opt. Express **3**, 2825-2841 (2012).

[2] H. Sun, "Dynamic Holography in Semiconductors and Biomedical Optics," (Purdue University, 2016).

[3] H. Choi, Z. Li, H. Sun, D. Merrill, J. Turek, M. Childress, and D. Nolte, "Biodynamic digital holography of chemoresistance in a pre-clinical trial of canine B-cell lymphoma," Biomed Opt Express **9**, 2214-2228 (2018).

[4] H. Sun, D. Merrill, R. An, J. Turek, D. Matei, and D. D. Nolte, "Biodynamic imaging for phenotypic profiling of three-dimensional tissue culture," J Biomed Opt **22**, 16007 (2017).

[5] S. Eddins, "Rainbow Color Map Critiques: An Overview and Annotated Bibliography," (2014).

[6] K. Moreland, "Diverging Color Maps for Scientific Visualization," (Springer Berlin Heidelberg, Berlin, Heidelberg, 2009), pp. 92-103.

[7] J. Bernard, M. Steiger, S. Mittelstädt, S. Thum, D. Keim, and J. Kohlhammer, "A survey and task-based quality assessment of static 2D colormaps," SPIE/IS&T Electronic Imaging **9397** (2015).
[8] S. Mittelstädt, J. Bernard, T. Schreck, M. Steiger, J. Kohlhammer, and D. A. Keim, "Revisiting Perceptually Optimized Color Mapping for High-Dimensional Data Analysis," (2014).
[9] M. Steiger, J. Bernard, S. Mittelstädt, H. Lücke-Tieke, D. Keim, T. May, and J. Kohlhammer, "Visual Analysis of Time-Series Similarities for Anomaly Detection in Sensor Networks," Computer Graphics Forum **33**, 401-410 (2014).
[10] S. Bremm, T. von Landesberger, J. Bernard, and T. Schreck, "Assisted Descriptor Selection Based on Visual Comparative Data Analysis," Computer Graphics Forum **30**, 891-900 (2011).
[11] A. J. Teuling, R. Stöckli, and S. I. Seneviratne, "Bivariate colour maps for visualizing climate data," International Journal of Climatology **31**, 1408-1412 (2011).

APPENDIX D. NOTES ON SAMPLE IMMOBILIZATION

D.1 Introduction

Sample immobilization is an important, if not the most important, factor of successful BDI measurements. Bad immobilization severely affects both "baseline condition" and "drug response" biomarker values. Among baseline condition biomarkers that may be affected, an obvious example is NSD value. A sample that is vibrating in the dish/well will have a higher NSD value than when it is firmly attached to the bottom. Intracellular dynamics also vary a lot at different layers (as shown in Appendix Figure 7), and the power spectra at different layers can have large differences. A drift in the sample "z" position changes the coherence gating and may lead to a spectrogram with a redshift/blueshift pattern that is not caused by slowdown/speedup of the intracellular dynamics.

D.2 Immobilization of Cell Line and Biopsy Samples

D.2.1 Overview

Cell line and biopsy samples have been immobilized with agar or by being grown and plated in poly-lysine coated plates. Cell line samples have a relatively large amount of variability in immobilization across wells and dishes.

D.2.2 Quantitative Evaluation of Sample Movement

Appendix Figure 24 shows the raw OCI images ("raw" means before background masking) and backscatter brightness ("BSB") of selected samples in the baseline measurement over time. Samples No. 2 and 6 had low relative fluctuations in their OCI images and BSB values, while sample No. 4 shows fluctuations and the BSB of sample No. 7 decreased over time and dropped to 33% of the initial value in the final loop. It is worth noting that (1) the possibility of sample movement introduced by pipetting during drug addition is not present in this case, since this is a baseline measurement (2) there is no evidence that the motion controller is malfunctioning and not moving to given positions, as OCI images are either very consistent or inconsistent. However, pipetting does introduce unwanted perturbation to samples and reduces the sample's adhesion, and

when consecutive samples show significant changes in their OCI images in the same loop, there is a high possibility that the motion controller is not working as expected (which has been recorded in the past) and should be serviced or replaced as soon as possible.

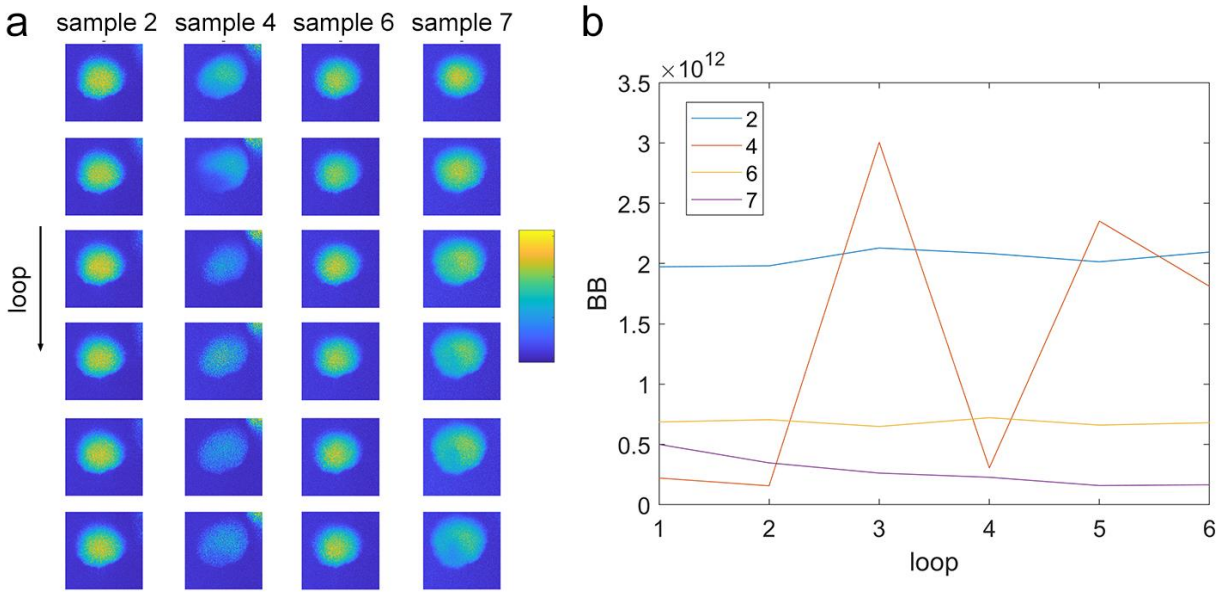

Appendix Figure 24 a) raw OCI images for baseline measurements of DLD-1 samples 2, 4, 6, and 7 in a 96-well plate on 5/4/2017. The color scale is consistent for the same sample across multiple loops (but vary from sample to sample) b) the sample averaged BSB values for these samples

D.2.3 Improvement to Experiment and Analysis

While sample immobilization cannot be changed after a dish is prepared, there are a few ways to minimize the impact and improve the success of overall BDI measurement and analysis. A possible improvement during an experiment is to identify samples that have bad immobilization as early as possible, and (re)allocate the drugs so that there will be at least a few samples under each treatment. This can be done by running a program named “diagnose baseline” just after the baseline measurement finishes. This program generates a figure similar to Appendix Figure 24a), which allows the experiment operator to review the sample raw OCI images and gives the operator a chance to evaluate sample immobilization quality.

During the data analysis, the “data quality” program produces a number that evaluates the quality of a sample dataset based on BDI biomarkers (see Appendix chapter C.1), many of which are based on BSB fluctuations. Therefore, a sample with large BSB fluctuations or a significant decline in

BSB value is likely to be rated as low quality (which also works as a weighting factor) or even vetoed.

D.3 Immobilization of COCs, Oocytes and Zygotes

D.3.1 Overview

Vibration of small samples like oocytes is an important issue. It leads to high NSD values that are not biologically related, which misrepresents the motility and viability of embryos. As NSD is an important biomarker, in classification analysis, the accuracy of a classifier can be significantly reduced when there are many ill-immobilized samples.

The first immobilization attempt was done with Cell-Tak coating. Cell-Tak is a protein solution used as a coating on a substrate to immobilize cells or tissues and is commonly used in *in vitro* cell culture. This method is relatively expensive and has not worked as effectively as expected.

The other less expensive and easier way is to remove the PVA protein in the TL-Hepes medium. This method proves to be very successful in immobilizing samples.

D.3.2 Quantitative Evaluation of Sample Movement

Various methods can help determine the immobilization quality of reproductive cells. Since reproductive cells are measured on the BDM, conventional microscopy images can be captured with a camera, which can be used to monitor sample movement. A basic study is to evaluate how the sample position changes in response to externally (i.e. external to the dish) introduced vibrations. A well- and an ill-immobilized sample are placed in two dishes separately, and the BDM is disturbed by gently tapping the mechanical stage or pounding the table on which the microscope stands. The center (calculated as the center of mass) of the inner cell mass is obtained from microscopy images, and the x component over time is shown in Appendix Figure 25. For a sample with good immobilization, gentle tapping introduces <1 pixel (7.4 μm) of displacement, and pounding on the table only introduces about 2 pixels of vibration in amplitude, while a sample with bad immobilization experiences significant movement under these conditions.

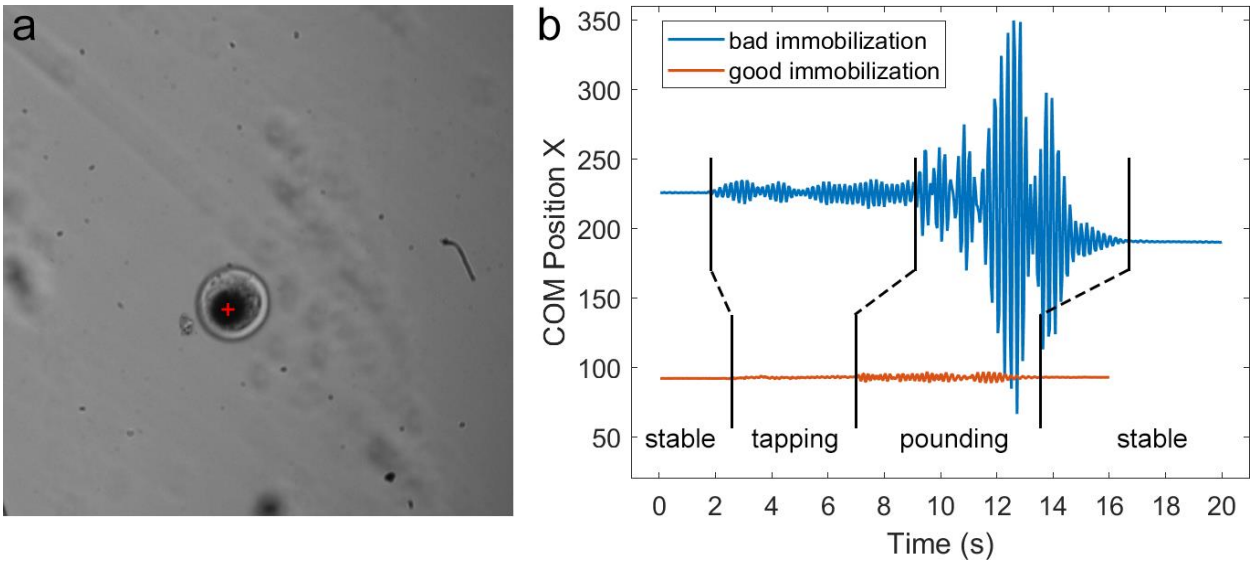

Appendix Figure 25 a) An example of the center of inner cell mass used for tracking sample position b) the x coordinate of the center of two samples under three different vibration conditions. The bad sample is sample #2 and the good sample is #3 in Appendix Figure 26 and Appendix Figure 27.

Sample immobilization quality is also related to a few BDI biomarkers. Replaying sample OCI movies helps determine if a sample has mainly fluctuations or mechanical movements that may appear as either flashing or "wobbling". Line plots of OCI stack images along the x-axis is a way to present sample movement in a static form. In an example shown in Appendix Figure 26, 6 samples are used, where samples #1 and #5 have very good immobilization, sample #2 has moderate immobilization, and samples #3 shows "wobbling", #4 shows highly irregular movements, and #6 drifts from right to left during the measurement. The drift in sample #6 can be seen in Appendix Figure 26b, and samples #3, #4 and #6 all have hologram washouts in the OCI image stacks, as shown in Appendix Figure 26c and Appendix Figure 26d.

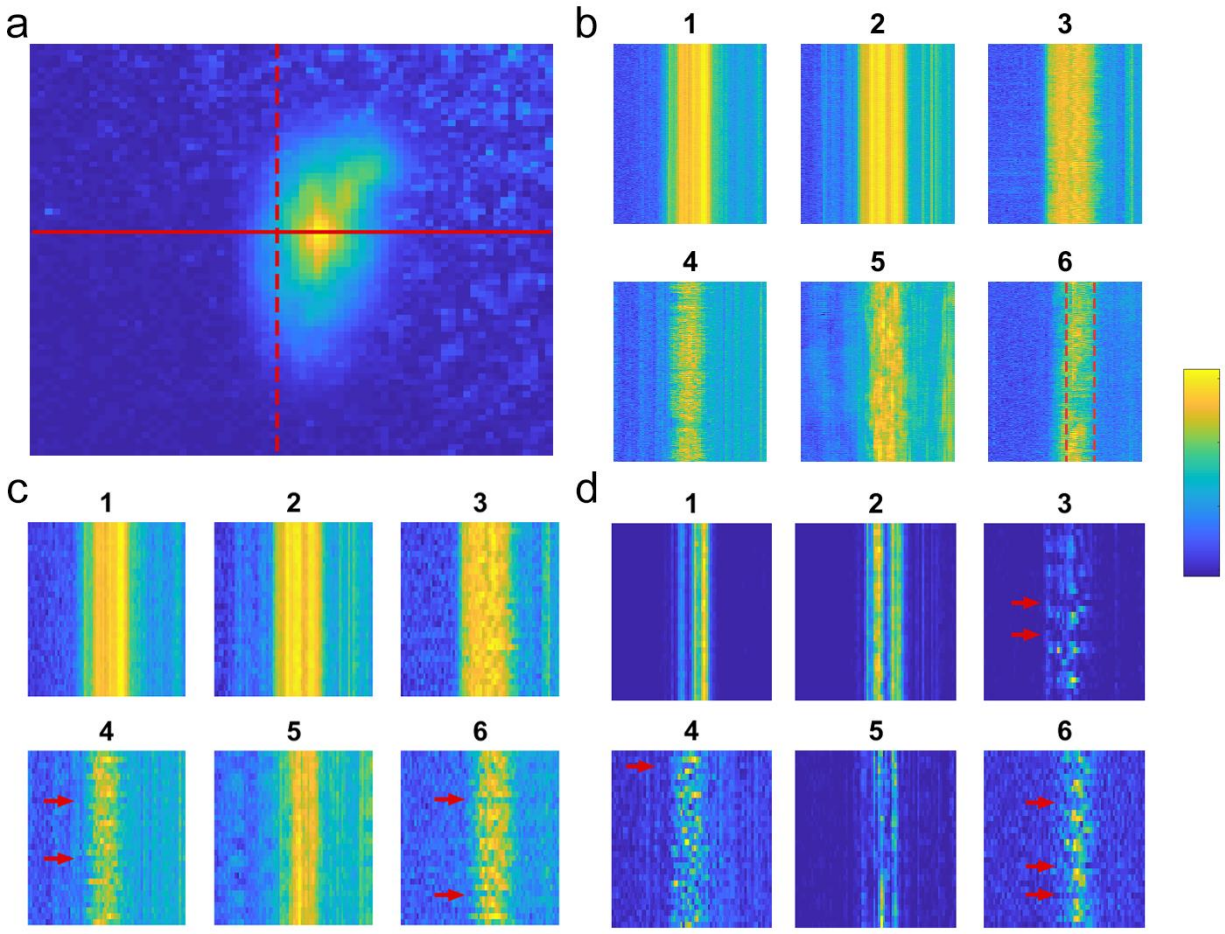

Appendix Figure 26 OCI intensity line plots for 6 samples. a) examples of horizontal and vertical lines used in the following figures. b) maximum value plots, where the x-axis is the x coordinate, while the y-axis is the frame number. Each value is the maximum intensity of a vertical line for a given x value [e.g. dashed line in a)]. Dashed lines are vertical. The plots use 500 frames. c) the same maximum value plots similar to b) but use 30 frames. d) value plots, where the x-axis is the x coordinate, and the y-axis is the frame number. Each value if the intensity of a horizontal line that crosses the center of the samples [e.g. dashed line in a)].

The motion from bad immobilization is consistently correlated with spikes in the sample power spectrum around 5 Hz, as in Appendix Figure 27a), and this method has been used to automatically filter out samples with major immobilization issues in the analysis of BDI data in CHAPTER 4. Sample movement can also be evaluated by the center of mass and BB fluctuations, but these metrics alone are not consistent enough to identify sample immobilization quality.

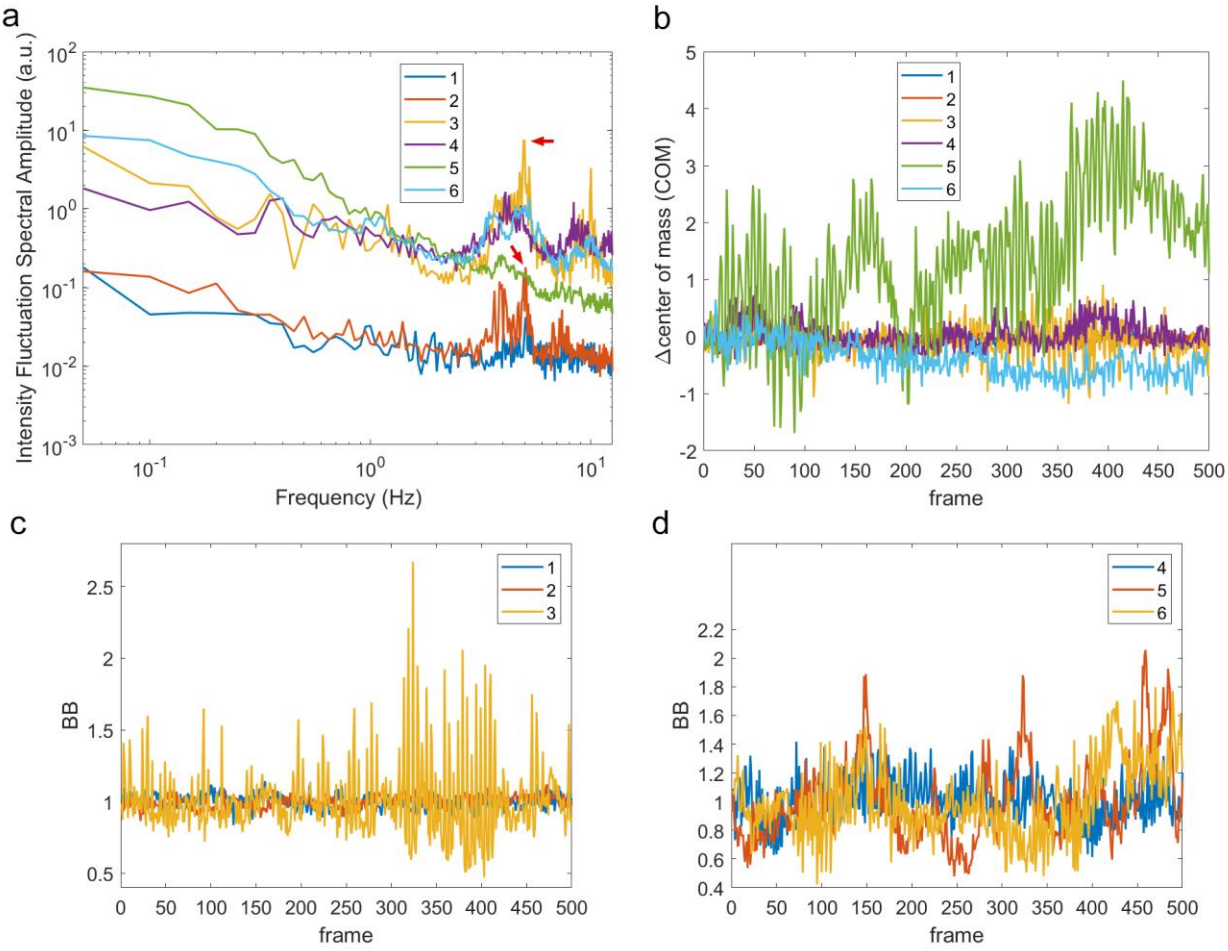

Appendix Figure 27 a) power spectra of 6 samples b) center of mass displacement for 6 samples across 500 frames compared with their initial positions for x component c)-d) average backscatter brightness for 6 samples after masking

A comparison of the effectiveness of both immobilization methods is given in Appendix Figure 28. Samples immobilized with TL-Hepes have much lower high-frequency spike values than Cell-Tak adhesive, and can be part of the reason many experiments using Cell-Tak did not turn out successful.

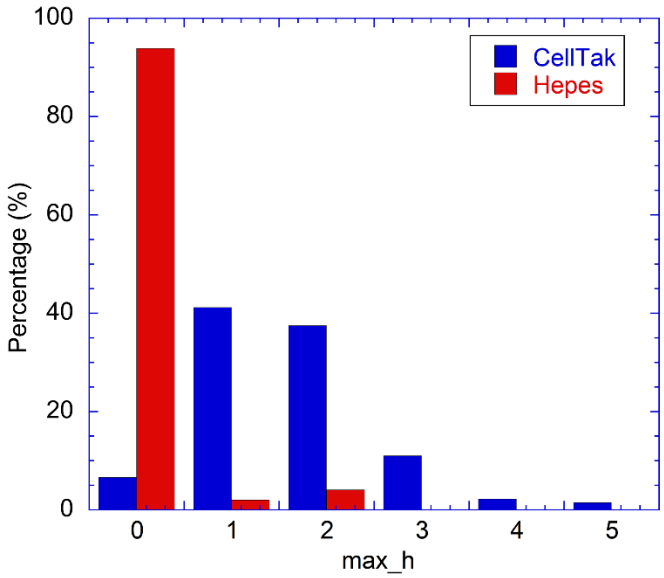

Appendix Figure 28 comparison of the effectiveness of Cell-Tak coating and PVA-removed TL-Hepes methods. “max_h” is the amplitude of spikes found in the 2 Hz -12.5 Hz range of power spectra.

D.3.3 Improvement to Experiment and Analysis

When a sample is prepared in the dish and ready for BDI measurement, the tapping method can be used to quickly determine the quality of immobilization. A low-quality sample should either be re-plated (if possible) or discarded. During the analysis, samples with large vibrations should be discarded, and such samples can be filtered using the high-frequency spike values.

APPENDIX E. OPTICAL DOPPLER PHENOTYPES OF CHEMOSENSITIVITY IN HUMAN EPITHELIAL OVARIAN CANCER

The development of an assay to predict response to chemotherapy has remained an elusive goal in cancer research. Chemoresponse assays have traditionally relied on isolated cancer cells that are cultured and exposed to various treatments *in vitro*, or more recently, as patient-derived xenografts. These techniques destroy the local microenvironment of the complex disease state and have had only marginal success in predicting patient response to therapy. This chapter reports a study using a new chemosensitivity assay based on intact living three-dimensional tumor tissue challenged *ex vivo* with chemotherapy agents. The response of the tissue to chemotherapy treatment *in vitro* was measured using Doppler spectroscopy of infrared light scattered from intracellular motions in the living tissue. Doppler fluctuation spectra were obtained through digital holography and phase-sensitive detection. Frequencies in the range from 10 mHz to 10 Hz were considered to be sensitive to changes in intracellular dynamics caused by applied therapeutics. The study analyzed biospecimens from 20 patients with ovarian cancer. For a small subset of patients, matched primary and metastatic tumor tissue were collected. Shifts in spectral density of the biospecimen following *in vitro* drug treatment were correlated with clinical outcomes to platinum-based chemotherapy regimens. Metastatic tumor samples were more likely to display a phenotype that was resistant to drug treatment in the *in vitro* chemosensitivity assay.

E.1 Introduction

The tumor microenvironment in cancer plays an essential role in the complex biological and molecular communication between cancer cells and the host, determining both tumor progression and response to therapy. The microenvironmental influence on the cancer state is associated with mechano-transduction [1, 2] and paracrine signaling, as well as immune cell infiltration and endocrine signaling. Conventional chemosensitivity assays destroy these influences by disaggregating cells from tumor biopsies and growing them in two-dimensional cell culture or as xenografts implanted in host animals. The growth in the alien environment of the unnatural geometry of the cell culture plate or the animal host changes the cellular phenotype, which may no longer represent the phenotype of the intact tumor. In consequence, chemosensitivity assays

[3, 4] have limited ability to test cancer cells from clinical specimens, they lack predictive power for subsequent clinical applications [5-7] and they rely exclusively on epithelial tumor components.

A Doppler fluctuation spectroscopy approach to chemosensitivity testing, called biodynamic imaging (BDI), is the first imaging technology to use intracellular motion as functional image contrast [8]. The technology uses principles of coherent laser radar with digital holography and represents an innovative and highly sensitive assay that can quantify the dynamic response of tumors to treatment [9]. Cellular motions are unusual but specific biomarkers of cellular health and response to treatment. By penetrating volumetrically into tissue up to 1 mm deep, BDI maps out heterogeneous tissue layers. BDI has previously been applied to drug screening [10-12], phenotypic profiling [12, 13], and preclinical chemosensitivity testing [9, 14, 15]. Light scattering of near-infrared light from living *ex vivo* tissue biopsies displays Doppler frequency shifts caused by intracellular motion [16]. Chemotherapy agents applied to the living biopsies *in vitro* modify the intracellular dynamics and the associated Doppler frequencies. The Doppler frequency shifts and their changes are interpretable through the speeds of intracellular motions affected by anti-cancer drugs. This information can be correlated with a patient's sensitivity to chemotherapy treatment in the clinic. Biodynamic imaging was used in a pilot study of chemosensitivity testing for canine B-cell lymphoma in which patients with long progression-free survival (PFS) displayed a different phenotypic signature of Doppler frequencies than patients with short PFS [9]. In addition, a preclinical trial of biodynamic imaging for human disease studied ovarian xenografts in mice using ovarian cancer cell lines with platinum resistance [17]. The results presented here are the first application of BDI to human patient samples.

E.2 Methods

E.2.1 Patients

Patients eligible for study inclusion were age ≥ 18 years, planning to undergo surgery or biopsy as a standard-of-care treatment for suspected ovarian cancer, with subsequent histologic confirmation of ovarian, fallopian or primary peritoneal cancer. All histological types and stages were eligible for enrollment. The study was approved by the Northwestern University Institutional Review

Board (protocol # STU00202733), and all patients provided written informed consent. Tissue was deidentified before processing. Enrolled patients underwent cytoreductive surgery followed by a platinum-based chemotherapy regimen, as indicated by the treating physician, per standard of care. Patients were followed for up to 18 months for clinical outcomes. Given that most patients underwent surgery with removal of tumor bulk, response to treatment (i.e., platinum sensitivity versus resistance) was determined based on time to progression (i.e., calculated from the platinum-free interval), using standard criteria. Platinum-sensitive tumors were defined as those tumors that did not recur for ≥ 6 months, while platinum-resistant tumors were those that progressed within < 6 months after completion of platinum-based therapy.

Forty-eight patients enrolled in the study between June 2016 and November 2018. Twenty-eight patients were withdrawn, and twenty evaluable patients were included in the final analysis. The most common reason for withdrawal was the inability to collect sufficient tumor tissue for research at the time of surgery. A total of twenty-three biospecimens were collected and used for analysis. Of these, sixteen were primary tumors and seven were metastatic tumors. Three of the metastatic implants were collected from patients who also had primary tumors collected, allowing a direct comparison of the response of primary versus metastatic lesions to chemotherapy treatment in the chemosensitivity assay. A table of enrolled patients is given in Appendix Table 4.

Appendix Table 4 Enrolled patients

Pat. No.	Cancer Type	Pathology	Response	Cell	Tissue	Immob.
1	ovarian	papillary serous carcinoma	S	hov5	ov	agar
2	ovarian	clear cell carcinoma	S	hov7	ov	
3	recurrent platinum-sensitive ovarian	serous carcinoma	R	hov8	ov	
4				hov8b	bowel	
5	ovarian	serous carcinoma	S	hov9	peritoneum	
6	ovarian	serous carcinoma	S	hov10	ov	
7	fallopian tube	serous carcinoma	S	hov11	peritoneum	
8	ovarian	serous adenocarcinoma	S	hov12	met	
9	ovarian	serous carcinoma	S	hov13	ov	poly
10	ovarian	clear cell adenocarcinoma	R	hov14	ov	
11	fallopian tube	serous adenocarcinoma	S	hov15	ov	
12	recurrent platinum-sensitive ovarian	carcinosarcoma	R	hov16	ov	
13	ovarian	serous carcinoma	R	hov17	ov	
14	ovarian	serous carcinoma	S	hov18a	ov	
15				hov18b	met	
16	ovarian	serous carcinoma	S	hov20a	ov	
17				hov20b	met	
18	ovarian	serous carcinoma	S	hov22	ov	
19	ovarian	serous carcinoma	S	hov23	ov	
20	ovarian	endometrioid adenocarcinoma	S	hov25	ov	
21	primary peritoneal	serous adenocarcinoma	S	hov26	met	
22	ovarian	serous carcinoma	S	hov30	ov	
23	ovarian	serous carcinoma	S	hov31	ov	

E.2.2 Sample Preparation

Living biopsy materials from the patients were shipped in cold-packs overnight to the measurement facilities where the samples were dissected into approximately 72 samples of approximately 1 mm^3 volume and immobilized in wells of a 96-well plate. Two different immobilization methods were used to keep the samples fixed during measurements. Samples from 5 patients (hov5, hov7, hov8, hov8b, hov9, and hov10) were placed in a layer of agarose covered with culture medium, while samples of the other 15 patients were immobilized on poly-lysine coated plates. Poly-lysine is more effective than agar at attaching a sample to the bottom of the plate. Each sample received one of the four treatments: carboplatin, paclitaxel, carboplatin+paclitaxel, and the carrier dimethyl sulfoxide (DMSO) as a negative control.

E.2.3 BDI Measurement and Drug Treatment

Sample imaging was carried out on the biodynamic platform (BDP; Animated Dynamics Inc, Indianapolis; not included in the appendix). A schematic of the optical core of the biodynamic imaging system is shown in Appendix Figure 29. The imaging system is placed on a motorized optical platform that moves on the horizontal plane, while the plate is on a fixed mount keeping it stationary during the entire measurement. The BDI system is an interferometer in a Mach-Zehnder configuration. A delay stage is placed in the reference arm to modify the optical path length of the arm to achieve depth-selective coherence gating of the sample. The light source is a low-coherence superluminescent diode that illuminates the sample at an oblique angle. The scattered light is collected through a Fourier imaging system that projects the Fourier transform of the tissue speckle onto the camera plane. Image acquisition and reconstruction procedures are the same as the “alpha prime” system and the BDM introduced in APPENDIX A.

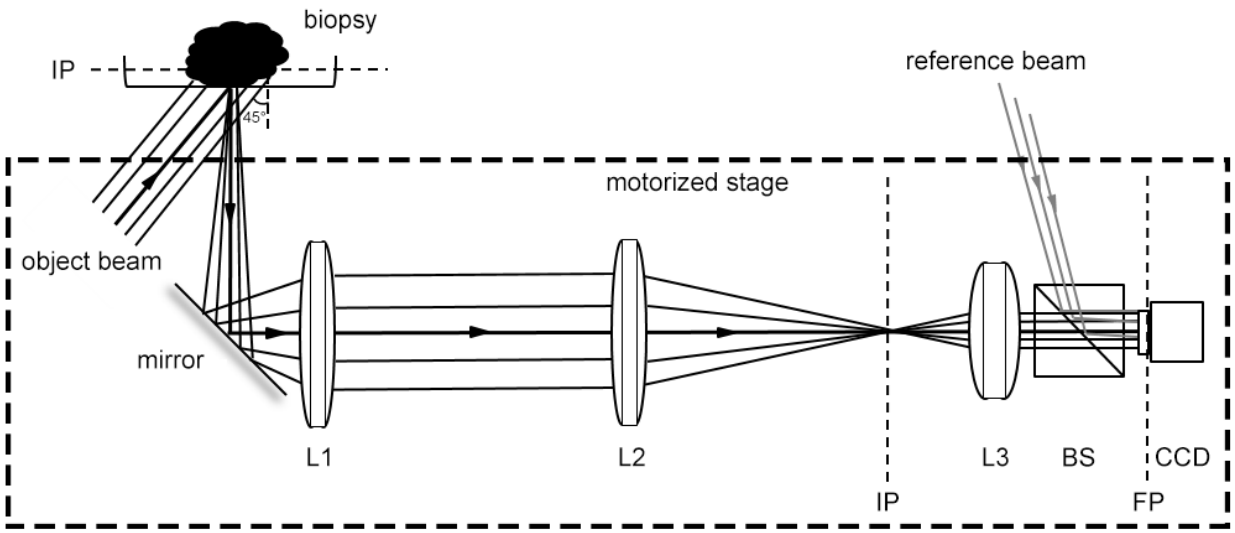

Appendix Figure 29 A schematic of the biodynamic platform (BDP). The imaging system (including the light source, lenses, beam splitters and the CCD in the dashed rectangle) is placed on an optical platform mounted on a motorized stage that can travel freely on the horizontal plane.

Each measurement includes 4 loops of baseline, drug injection, and 9 loops of drug response recording, where each loop is 82 minutes long. BDI measures a sample at 25 fps for 2000 frames in each loop. The baseline is the six-hour period of tissue stabilization prior to the application of the drug. The six-hour stabilization has been established as an effective time for the biopsy to equilibrate, although biopsies never become static. Treatments of carboplatin, paclitaxel or carboplatin+paclitaxel were applied to individual wells and were monitored using the biodynamic imaging system for up to 12 hours. Samples were imaged in two groups of 36 samples for a total of 72 measurements. The replicate numbers were 18 dmso (negative controls), 18 paclitaxel, 18 carboplatin, and 18 carboplatin+paclitaxel. The Taxol dose was 5 μM and the carboplatin dose was 25 μM. Once the drug is applied, intracellular dynamics are altered and are captured in the relative change in the spectral content over a period of 12 hours.

During the data analysis, feature values from samples immobilized with agar were shifted in such a way that their average and standard deviation equal the average and standard deviation of samples immobilized with poly-lysine.

E.3 Results

E.3.1 Biodynamic Spectra Predict Response to Chemotherapy

Examples of average spectrograms are shown in Appendix Figure 30 for samples that were isolated from platinum-resistant and -sensitive patients. Frequency is along the horizontal axis spanning from 10 mHz to 10 Hz. Time is along the vertical axis spanning 18 hours. The baseline is used for reference, and the treatment is applied at the time of the horizontal blue line. The shifts in the spectral content caused by the drug action are captured in color in the figure, blue representing inhibition and red representing enhanced spectral content. The drug response spectrograms for the taxane treatments are similar between samples isolated from platinum- resistant and -sensitive samples. However, there is a notable difference for the single-agent treatments. The differences of the resistant minus the sensitive spectrograms are shown in Appendix Figure 30b. Single-agent treatments show a much more suppressed response in the low-frequency region of sensitive cohort than the resistant cohort. The high-frequency region corresponds to the organelle transport band, indicating that the resistant cohort has activated organelle transport in response to the applied therapy *in vitro*. The low-frequency region is the cell-shape-change band representing slow membrane rearrangement and possible cell motility.

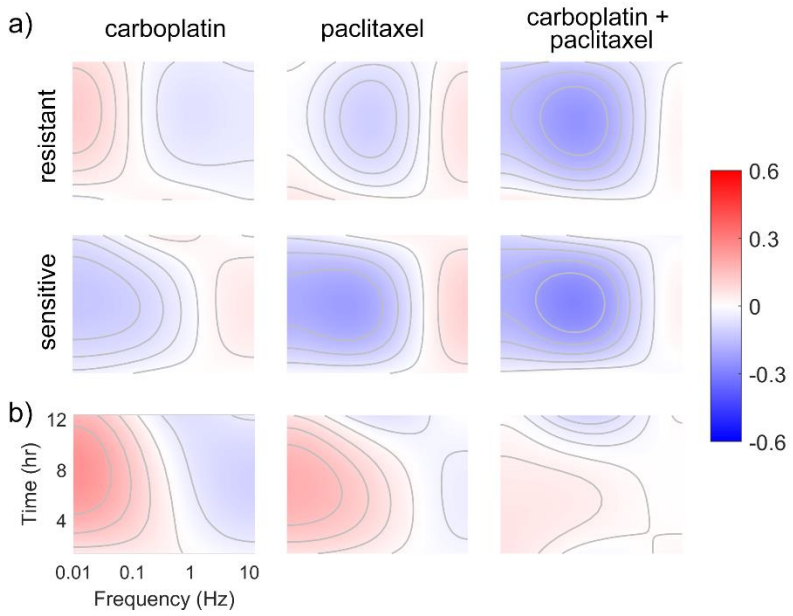

Appendix Figure 30 Drug-response spectrograms for treatment with carboplatin (25 μM), paclitaxel (5 μM) and carboplatin + paclitaxel (25 μM + 5 μM). a) The average spectrograms (dmso-subtracted) for resistant and sensitive phenotypes b) The difference of the resistant spectrograms minus the sensitive. The resistant phenotype is characterized by enhancement of low-frequencies relative to the sensitive phenotype.

The biomarkers used for the study are discussed in Appendix chapter C.1. Two of the spectrogram-based biomarkers having the largest signal-to-noise ratios that differentiate the resistant/sensitive groups are M_{00} ("ALLF") and M_{01} ("SDIP") on samples treated with paclitaxel. The selected feature vectors in Appendix Figure 31a) are the central data structure for all downstream machine learning algorithms. The goal is to identify which patients share similarities with each other, and with the sensitive/resistant phenotypes. For instance, the feature vectors are used to construct the similarity matrix in Appendix Figure 31b). The order of the specimens was preselected according to their clinical outcomes, separated into resistant/primary, metastatic, and sensitive/primary groups. Metastatic specimens are placed in the primary groups to which they are highly correlated despite their clinical outcomes, as the assumption here is that the drug response of metastatic specimens may deviate from the phenotype of their primary counterparts. The similarity matrix distance measure is the vector contrast values. Identical vectors have vector contrast near unity (red), opposite vectors have vector contrast near negative unity (blue), and independent vectors have vector contrast near-zero (white). The similarity matrix has an approximately block-diagonal structure. The resistant block of specimens shares strong similarities with each other, and strong dissimilarity with the sensitive block of patients.

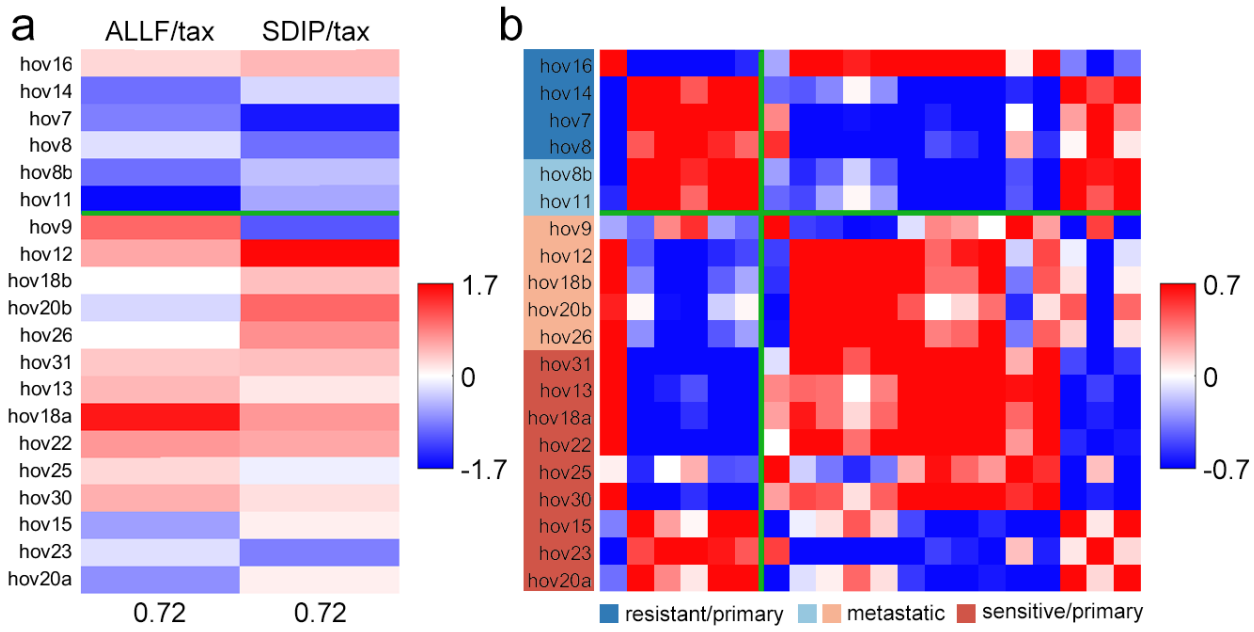

Appendix Figure 31 a) feature values of all specimens, which are divided into resistant/primary, metastatic and sensitive/primary groups b) similarity matrix of the samples constructed through the inner product of the two refined biomarkers.

Linear separability analysis is a primary analysis technique for separating groups into binary classes. By combining the resistant and "resistant-like" metastatic into a "resistant" group, and the "sensitive-like" metastatic and sensitive patients into a "sensitive" group, several linear separability algorithms were applied to classify individual specimens into these groups. Conventional one-hold-out cross-validation was used in all cases to train the algorithm with a training set of all other specimens, and then applying the trained algorithm to classify the held-out specimen. The linear separability algorithms used were a single-neuron perceptron, a high-dimensional vector bisector, log-likelihood and binary network analysis. This ensemble of approaches is combined into an ensemble average that is correlated against clinical outcomes.

As an example of the analysis, network theory provides analysis techniques for identifying relationships among a set of feature vectors. A similarity network for this clinical study is shown in Appendix Figure 32. Links in the network are assigned according to a linkage assignment threshold that yields the strongest clustering coefficient among the two cohorts.

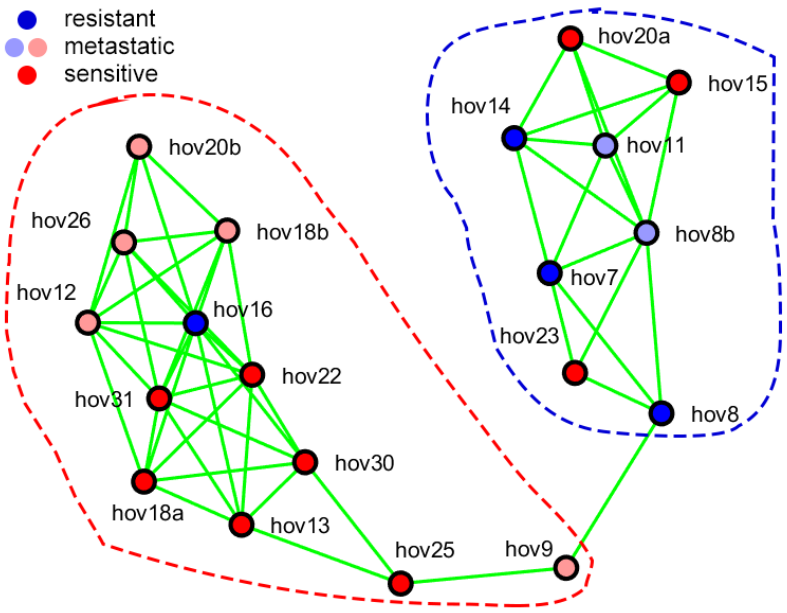

Appendix Figure 32 A similarity network relating patient samples to clinical outcomes and biodynamic signatures. Dark blue dots have resistant clinical outcomes, dark red dots have sensitive clinical outcomes. The colors of metastatic specimens follow the primary groups they belong to like in Appendix Figure 31b). The only metastatic specimen that has a BDI phenotype different from its clinical outcome is hov11 which is sensitive to treatment.

Using primary specimens, 10 out of 14 patients have BDI phenotype consistent with their clinical outcome. (The misclassified patients are hov15, hov16, hov20a and hov23.) And when taking metastatic samples into account, the correspondence is 75% (15 out of 20, with hov11, hov15, hov16, hov20a and hov23 misclassified).

E.4 Discussion

The work presented in this chapter is the first application of biodynamic imaging to human tissue samples. This study included 23 specimens prospectively collected from 20 patients with ovarian cancer. Among the specimens tested here, 5 samples were found to be resistant to carboplatin and paclitaxel chemotherapy and 18 specimens were sensitive. Seven specimens were derived from metastatic tumors and sixteen were from primary tumors. There were three patients from which matched metastatic implant and primary tumor were collected and analyzed. Two strong biodynamic phenotypes emerged from the analysis. The drug-response spectrograms, capturing changes in intracellular motions caused by the applied therapies, are generally able to discriminate between two phenotypes that correlate with patients who were resistant or sensitive to platinum-

based chemotherapy. Our findings support that BDI has the potential to predict chemotherapy outcomes and warrants future testing. In ovarian cancer patients, new predictive biomarkers, such as BDI profiles, could be particularly helpful for selecting second and later lines of treatment. Interestingly, four metastatic specimens displayed a resistant phenotype via BDI technology, even though the patients themselves were clinically sensitive to platinum. It is possible that some metastatic implants may display resistant behavior, but this possibility must be studied with a larger trial size.

References

[1] D. E. Ingber, "Cellular mechanotransduction: putting all the pieces together again," Faseb Journal **20**, 811-827 (2006).

[2] M. A. Wozniak, and C. S. Chen, "Mechanotransduction in development: a growing role for contractility," Nature Reviews Molecular Cell Biology **10**, 34-43 (2009).

[3] P. Kornblith, A. Wells, M. J. Gabrin, J. Piwowar, A. Chattopadhyay, L. D. George, R. L. Ochs, and D. Burholt, "In vitro responses of ovarian cancers to platinums and taxanes," Anticancer Res **23**, 543-548 (2003).

[4] P. E. Andreotti, I. A. Cree, C. M. Kurbacher, D. M. Hartmann, D. Linder, G. Harel, I. Gleiberman, P. A. Caruso, S. H. Ricks, M. Untch, and et al., "Chemosensitivity testing of human tumors using a microplate adenosine triphosphate luminescence assay: clinical correlation for cisplatin resistance of ovarian carcinoma," Cancer Res **55**, 5276-5282 (1995).

[5] I. A. Cree, "Chemosensitivity and chemoresistance testing in ovarian cancer," Curr Opin Obstet Gynecol **21**, 39-43 (2009).

[6] M. Markman, "Counterpoint: chemosensitivity assays for recurrent ovarian cancer," J Natl Compr Canc Netw **9**, 121-124 (2011).

[7] H. Neubauer, M. Stefanova, E. Solomayer, C. Meisner, M. Zwirner, D. Wallwiener, and T. Fehm, "Predicting resistance to platinum-containing chemotherapy with the ATP tumor chemosensitivity assay in primary ovarian cancer," Anticancer Res **28**, 949-955 (2008).

[8] P. Yu, L. Peng, M. Mustata, J. J. Turek, M. R. Melloch, and D. D. Nolte, "Time-Dependent Speckle in Holographic Optical Coherence Imaging and the State of Health of Tumor Tissue," Opt. Lett. **29**, 68-70 (2004).

[9] H. Choi, Z. Li, H. Sun, D. Merrill, J. Turek, M. Childress, and D. Nolte, "Biodynamic digital holography of chemoresistance in a pre-clinical trial of canine B-cell lymphoma," Biomed Opt Express **9**, 2214-2228 (2018).

[10] K. Jeong, J. J. Turek, and D. D. Nolte, "Fourier-domain digital holographic optical coherence imaging of living tissue," Appl. Opt. **46**, 4999-5008 (2007).

[11] D. D. Nolte, R. An, J. Turek, and K. Jeong, "Tissue dynamics spectroscopy for phenotypic profiling of drug effects in three-dimensional culture," Biomed. Opt. Express **3**, 2825-2841 (2012).

[12] R. An, D. Merrill, L. Avramova, J. Sturgis, M. Tsiper, J. P. Robinson, J. Turek, and D. D. Nolte, "Phenotypic Profiling of Raf Inhibitors and Mitochondrial Toxicity in 3D Tissue Using Biodynamic Imaging," Journal Of Biomolecular Screening **19**, 526-537 (2014).
[13] H. Sun, D. Merrill, R. An, J. Turek, D. Matei, and D. D. Nolte, "Biodynamic imaging for phenotypic profiling of three-dimensional tissue culture," J Biomed Opt **22**, 16007 (2017).
[14] D. Merrill, H. Sun, J. Turek, D. Nolte, B. Yakubov, D. Matei, and R. An, "Intracellular Doppler Signatures of Platinum Sensitivity Captured by Biodynamic Profiling in Ovarian Xenografts," Nature Scientific Reports **6**, 18821 (2016).
[15] M. R. Custead, R. An, J. J. Turek, G. E. Moore, D. D. Nolte, and M. O. Childress, "Predictive value of ex vivo biodynamic imaging in determining response to chemotherapy in dogs with spontaneous non-Hodgkin's lymphomas: a preliminary study," Converg. Sci. Phys. Oncol **1**, 015003 (2015).
[16] Z. Li, H. Sun, J. Turek, S. Jalal, M. Childress, and D. D. Nolte, "Doppler fluctuation spectroscopy of intracellular dynamics in living tissue," J. Opt. Soc. Am. A **36**, 665-677 (2019).
[17] D. Merrill, R. An, H. Sun, B. Yakubov, D. Matei, J. Turek, and D. Nolte, "Intracellular Doppler Signatures of Platinum Sensitivity Captured by Biodynamic Profiling in Ovarian Xenografts," Sci Rep **6**, 18821 (2016).

APPENDIX F. MONTE CARLO SIMULATION FOR BIODYNAMIC IMAGING

Monte Carlo model of steady-state light transport in multi-layered tissues (MCML) is a common way to simulate photon transport. A number of tissue models are proposed, and the model has been used for studying forward problems like fluorescence for a given tissue model, or inverse problems like estimating optical properties or distribution of oxygen. MCML is also used to simulate OCT signals and images [1, 2].

An important goal of biodynamic imaging experiments is to understand how external disturbance (e.g. drugs) introduces changes in the intracellular dynamics of samples, and how it can be correlated with NSD, spectrograms and biomarkers. Because the resolution of BDI systems is not high enough to resolve cytoskeletal components, OCI and MCI images do not provide a one-to-one direct comparison of BDI signatures to visualization. Therefore, MCML can provide an approach to understand what contributes to the BDI signals.

F.1 Methods

There are two parts of the simulation, both using the Monte Carlo method. The first part is mostly MCML, i.e. to simulate a light source and tissue and generate backscattered photons. The second part is to simulate intracellular dynamics, interaction with light, and low-coherence digital holography. The photons generated in the first step are a reservoir and can be used in digital holography simulations.

The MCML simulation generates a number of photons that satisfy a number of exit requirements (so that they can be detected on the "camera"). Non-qualifying photons are discarded, and the simulation repeats until a certain number of photons pass the cut ("constant N" mode). Alternatively, when the property of the light source, or the incident condition like incident angle, is the subject of study, a more realistic approach is to run the simulation a fixed number of times, which equals "constant power" of a light source, and keep the photons that qualify ("constant power" mode).

A flow chart of the MCML simulation is shown in Appendix Figure 33.

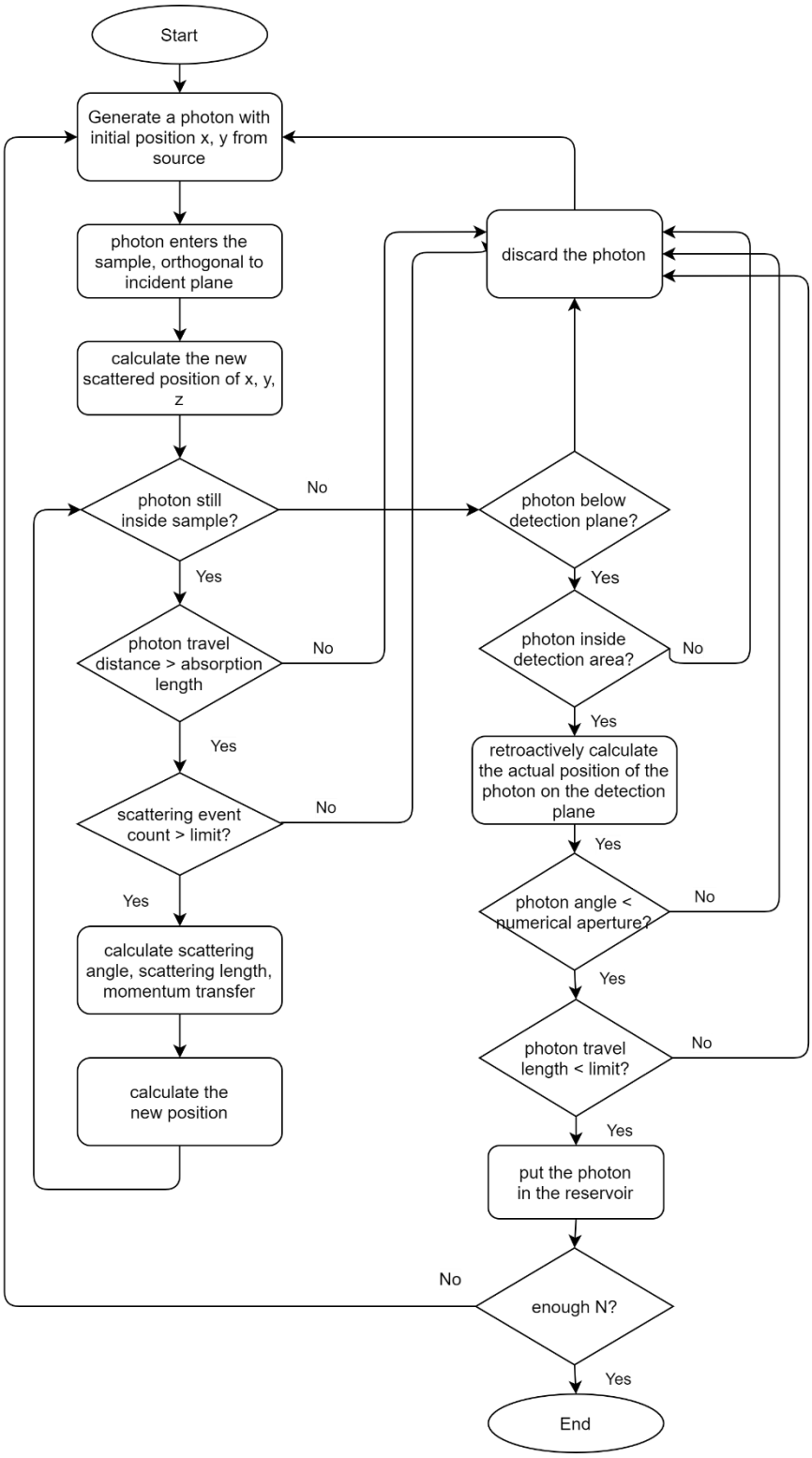

Appendix Figure 33 Flow chart of the photon generation in the “constant N” mode.

The light source can be configured as a circularly uniform distribution, or as a Gaussian source that is similar to typical laser and SLD source in the lab (Appendix chapter A.1.1). The incident beam can be normal to the detection area, or at an angle. The sources are shown in Appendix Figure 34.

In each scattering event, the scattering length follows an exponential law, and the scattering angle is given by a distribution related to a "hard-backscattering" coefficient and Henyey-Greenstein phase function [3]. The azimuthal angle follows the distribution of $P(\alpha)=\frac{1}{\pi}\sin^2\alpha$ which is related to the polarization and angular dependence of light scattering. The new position of the photon is calculated in each iteration, and the program determines if the photon is still inside the sample. If true, the next iteration of scattering starts, otherwise a few checks will be made to determine if the photon qualifies and should be retained.

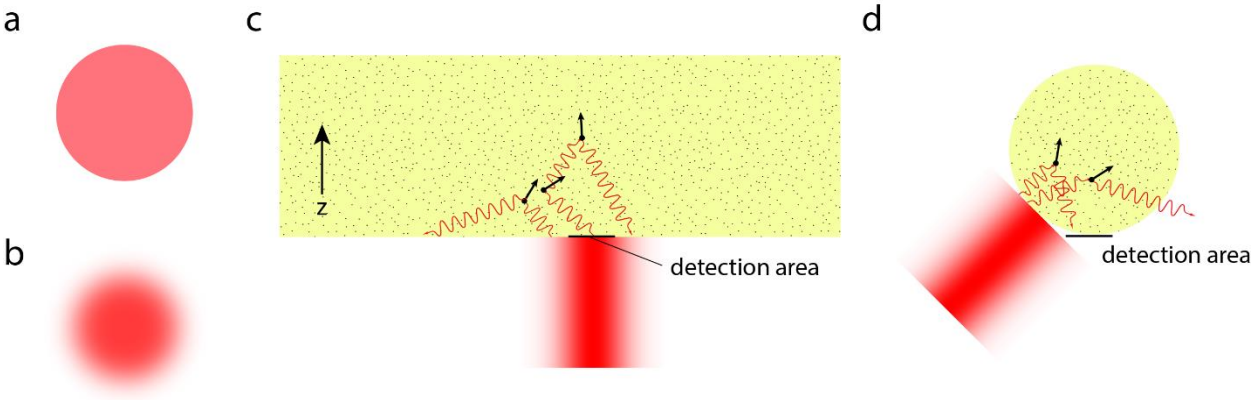

Appendix Figure 34 a) a uniform light source, b) a Gaussian light source, c) the "infinite half-plane slab" model, and d) the spheroid model with an incident angle of 45 degrees.

In the low coherence digital holography simulation, an imaginary interferometer in the Mach-Zehnder configuration is used. The signal arm comes from the phase information from the intracellular dynamics in the tissue based on Fourier optics, and the light fluctuation is from the output of the previous photon simulation. The reference arm is an artificial collimated beam, and the coherence gating is achieved in the signal arm by selecting photons whose OPL is inside a certain range. The detection plane is located on the Fourier plane of the image.

The intracellular dynamics follow the "persistent walk" model discussed in chapter 2.2.1, and the momentum transfer for each Doppler scattering event is calculated. The simulation of the

persistent walk is done with the Monte Carlo method, and the persistence time is distributed according to an exponential function. The point spread function (PSF) calculates the signal arm of the complex light field on the detection plane derived from the scattering events. The detection device ("camera") captures the holograms at a frame rate similar to that in real BDI experiments. These holograms are effectively the same as the images captured in real systems with CCD or CMOS cameras. The standard onekey analysis is run on the images, which calculates the OCI, MCI and power spectrum of the sample. Appendix Figure 35 is an example of an OCI flythrough from the simulation.

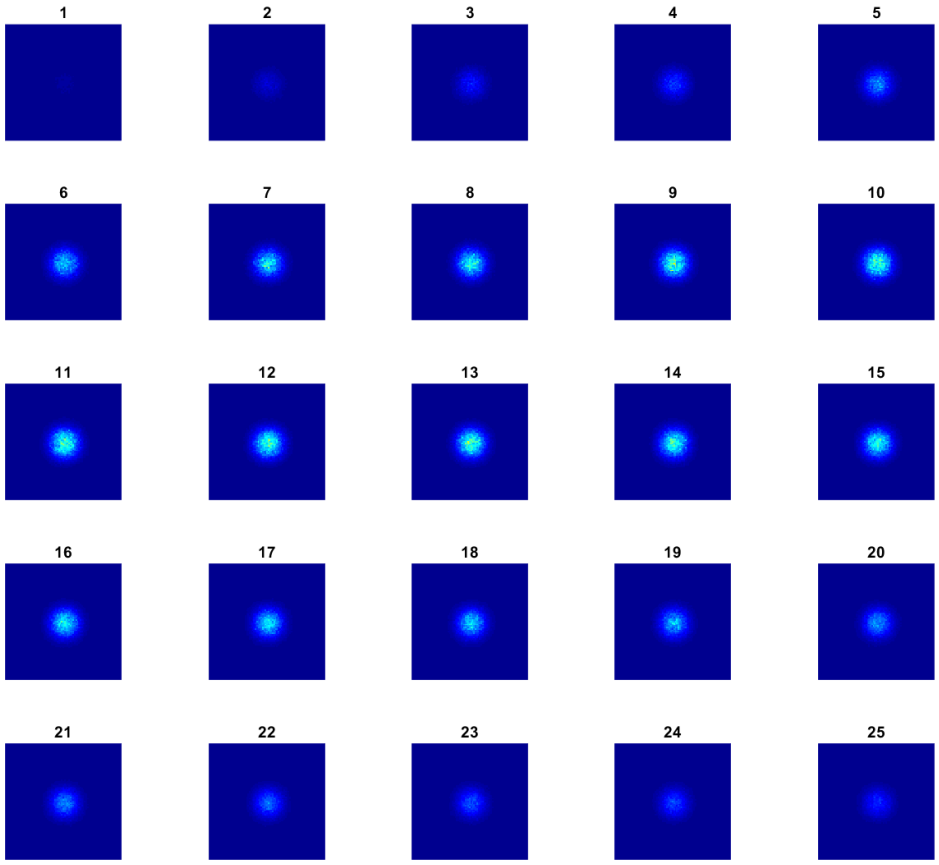

Appendix Figure 35 A "flythrough" of a spheroid model sample, with incident beam normal to the detection plane.

F.2 Tests

F.2.1 Parametric Studies

Velocity, Persistence Time, Coherence Gate and NSD

The first parametric study is a basic study that looks at how backscatter brightness and NSD change with regard to depth (coherence gate) in the simple "slab" model. The parameters are given in Appendix Table 5, and the results are shown in Appendix Figure 36. The BB decreases exponentially with depth but is not related to persistence time (Appendix Figure 36a), while NSD increases linearly with depth (Appendix Figure 36b). The backscatter brightness is likely determined by the number of photons within the coherence gate, since there is a clear linear dependence (Appendix Figure 36c).

Appendix Table 5 Parameters used in the basic flythrough test

Test number	Persistence time (s)	Velocity (mm/s)	Detection interval (s)	frame
1	0.04	0.05	0.04	2000
2	0.08		0.02	1000
3	0.02		0.04	2000
4	0.01		0.04	2000

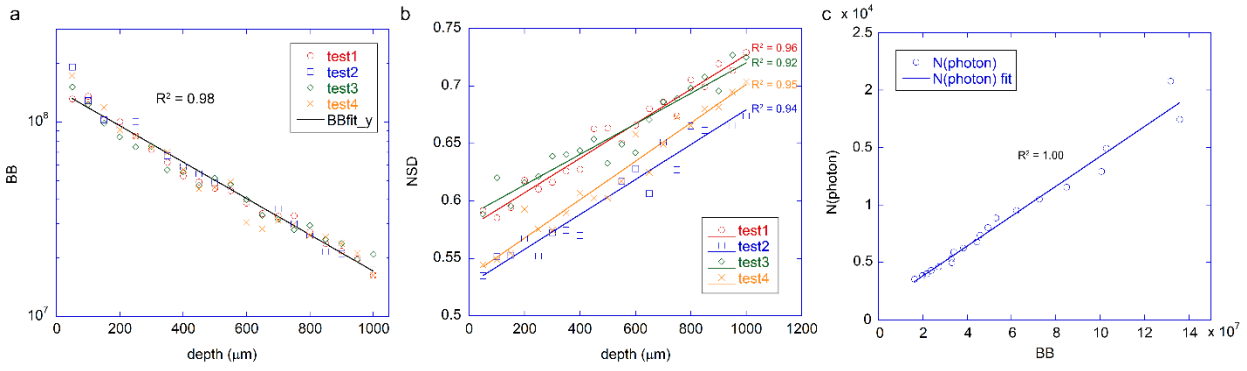

Appendix Figure 36 Result from the basic parametric study. a) BB vs depth. Depth is calculated as half of the OPL. b) NSD vs depth c) number of photons within the coherence gate vs BB

The monotonic trends of BB and NSD do not match those of DLD and tumor biopsies observed in experimental systems (Appendix Figure 7), which shows that this model, where the number of photons decreases monotonically with the increase of depth, is too simplified.

A follow-up study is needed to understand the origin of NSD's linear dependence on the coherence gate. Also, velocity and persistence time could be functions of depth, which mimics "necrotic" regions within a sample, and simulations could study how BDI signatures change in these regions.

Incident Angle and Sample Imaging Plane

This study explores how the incident angle changes the coherence gate plane for a spheroid sample in both 0-degree and 45-degree incident cases. The imaging plane should be parallel to the detection plane for a 0-degree incident angle, or at 22.5 degrees to the detection plane for a 45-degree angle which can be derived from basic geometry (as shown in Appendix Figure 8). This is based on the single scattering assumption, and multiple scattering can change the actual coherence gate. In Appendix Figure 37, the locations of the "deepest" scattering events of 50 random photons are shown as points, along with the assumed coherence gate. ("deepest" is defined as having the largest z coordinate for the 0-degree incident angle case, and having the largest $x+z$ value for the 45-degree case.). For the right-angle incidence, the envelope of the dots roughly matches the assumed coherence gate when the depth is low, while above 600 μm, there is an obvious "gap" between the dots and the dashed line, and there is not a pronounced envelope anymore. This is similar for the 45-degree incident angle situation. Therefore, the 22.5° coherence gate angle is verified with the simulation. The gap and the disappearance of the envelope can be explained by multiple scattering, and a follow-up study defines an "effective depth" and explores how it is related to coherence gating.

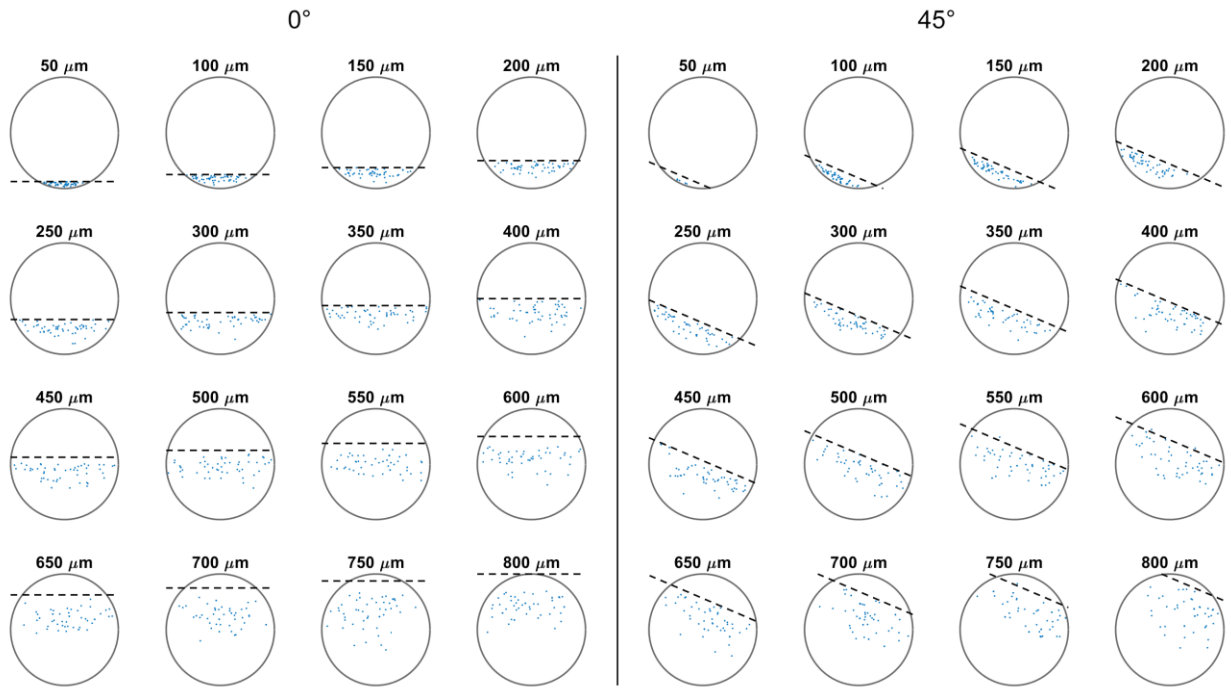

Appendix Figure 37 Visualization of the locations of the "deepest" scattering events in the sample at both right angle and 45-degree incidence. The horizontal line marks the "expected" or "assumed" coherence gate plane. The aspect ratio is 1:1 for the axes.

Hard Backscattering, Anisotropy factor (g), Incident Angle, and Backscatter Brightness

In the MCML simulation, the scattering angle is related to a "hard" backscattering coefficient (i.e. the probability of having a scattering angle of π) and the Henyey-Greenstein phase function. The phase function is dependent on the anisotropy factor *g*, a value that characterizes the degree of forward scattering and is an important parameter in understanding light propagation in tissues. In addition, the angle between the light source and the detection plane changes the intensity distribution, which is particularly important for the BDM and can help understand if the 45-degree incident angle leads to some photon loss (although such a design can also increase photon efficiency by avoiding using a beamsplitter). This study explores how these parameters change the backscatter brightness.

A series of simulations are run with the spheroid model using different values of the aforementioned parameters, the digital holography simulation is run, and the backscatter brightness when the coherence gate is placed in 200 μm – 300 μm is obtained for each MCML simulation.

As shown in Appendix Figure 38, hard backscattering significantly increases the backscatter brightness in the low-angle incidence scenarios, although at higher angles the difference diminished. A simple explanation would be that at high angles, hard-backscattered photons are more likely to be "lost" i.e. not hitting the "camera" or the detection area, and in this regime, most of the photons are not hard-backscattered in both cases.

In the no hard-backscattering scenario, the lower g factor increases the backscatter brightness, which is expected behavior. When g = 0.93, the backscatter brightness begins to steadily decline after about 10 degrees, which does not happen for the g = 0.85 case until after the 30-degree incident angle.

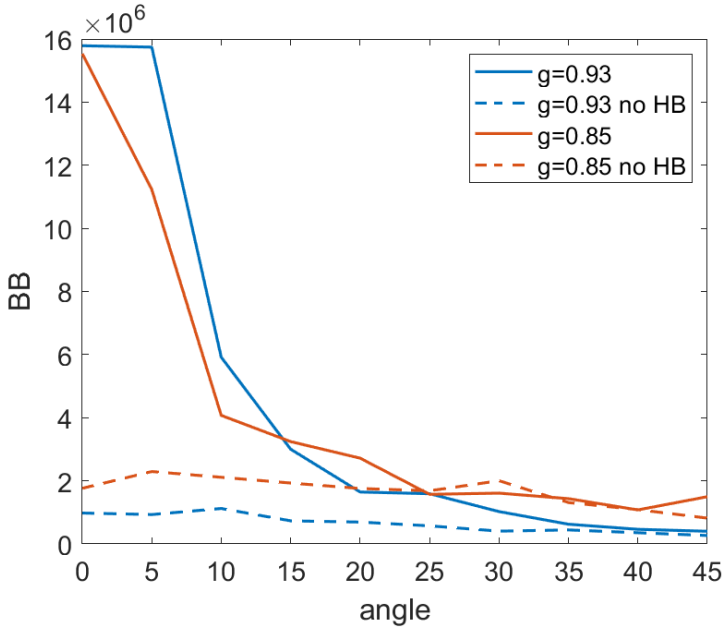

Appendix Figure 38 backscatter brightness—incident angle under different backscattering parameters and models.

This result is again directly related to the number of photons in the coherence gate. Appendix Figure 39 shows how the total number of photons and those in the coherence gate change with the angle for g = 0.93, no hard-backscattering case. While the number of total photons declines monotonically, the gated photon population does not change until the incident angle is around 15 degrees. At 45 degrees, the number of coherence-gated photons is only about a quarter of the photon number in the 90-degree angle incidence case. The trend of the backscatter brightness curve in the Appendix Figure 38 basically follows the "gated photon" curve here.

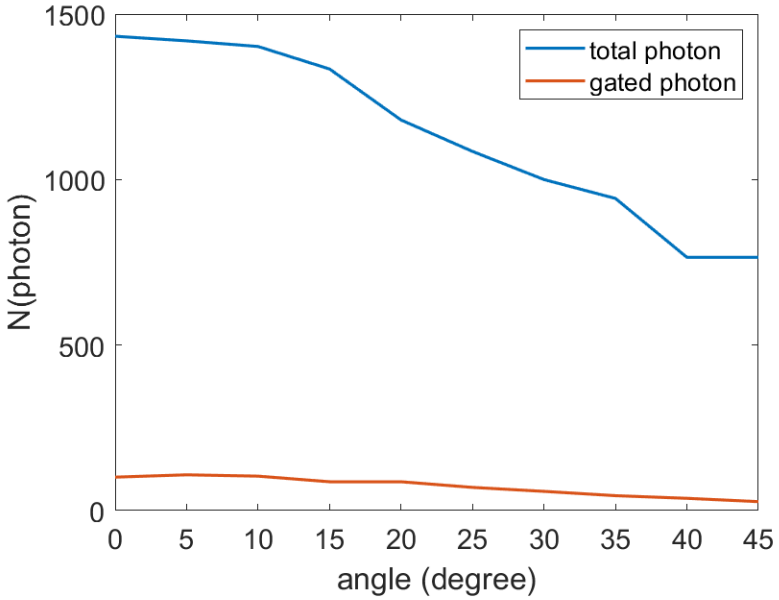

Appendix Figure 39 the relationship between the number of photons and incident angle.

A follow-up study is to fit the curves in Appendix Figure 39 and relate the curves to intensity derived from light scattering theories. [3]

Spheroid Flythrough

A "flythrough" is run on a spheroid sample under the "no hard-backscattering" assumption. The backscatter brightness and NSD vs gate depth is shown in Appendix Figure 40.

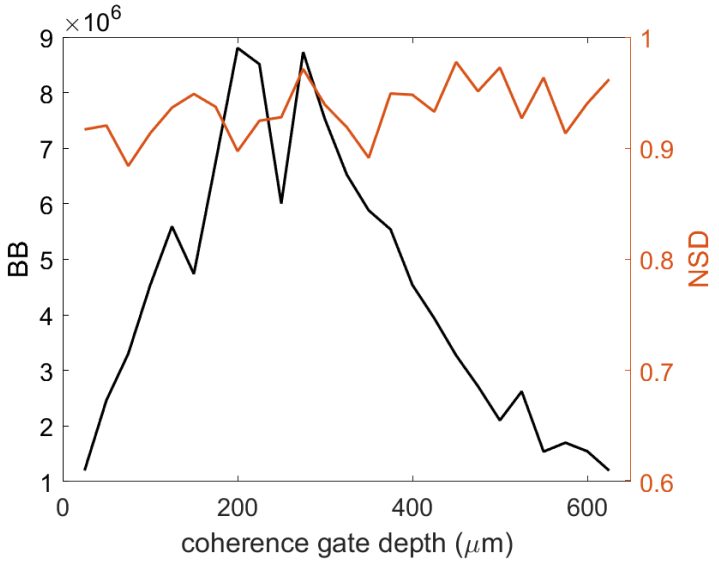

Appendix Figure 40 Backscatter brightness and NSD vs depth for a simulated spheroid sample.

The spheroid model is more accurate than the infinite half-plane slab model, and the "increase-then-decrease" nonmonotonic trend of backscatter brightness found in real samples (e.g. Appendix Figure 7) is captured here. The figure could be further improved by running repetitions of the tests to smooth the curves. The trend of the NSD, which is supposed to be opposite to that of the backscatter brightness, is not yet present in this case. The NSD trend may be related to additional light scattering properties of the samples and sample dynamics not used in the model. Being able to simulate the NSD trend would be very helpful in understanding sample intracellular dynamics and optical properties of biological tissues.

F.2.2 Other studies

"Effective" Depth vs Incident Position

Multiple scattering in biological tissues affects focus, reduces resolution in images, and participates in many advancements in biomedical imaging technologies like confocal microscopy and adaptive optics. This effect is illustrated in the photon Monte Carlo simulations by introducing the "effective" imaging depth and studying how multiple scattering affects this quantity.

Since $q=\sqrt{2-2\cos\theta}$, a simple weighting factor w that is related to hard-backscattering is defined as $w=\sqrt{\frac{1-\cos\theta}{2}}=\frac{q}{2}\in[0,1]$, and the "effective" depth is defined as

$$z=\frac{\sum_i z_i w_i}{\sum_i w_i} \tag{F.1}$$

When a "hard-backscattering" event occurs, as in the first case, the photon carries all the information from depth $z=1$, and the effective depth is 1. However, if there are two scattering events, one at $z=1$ and another at $z=0.5$, with a $\frac{\pi}{3}$ scattering angle, the photon carries information of the blend of the two depths, giving an effective z of 0.83. The more scattering events there are, the smaller the scattering angles, the more "mixed" the signal is. Four such scenarios are shown in Appendix Figure 41.

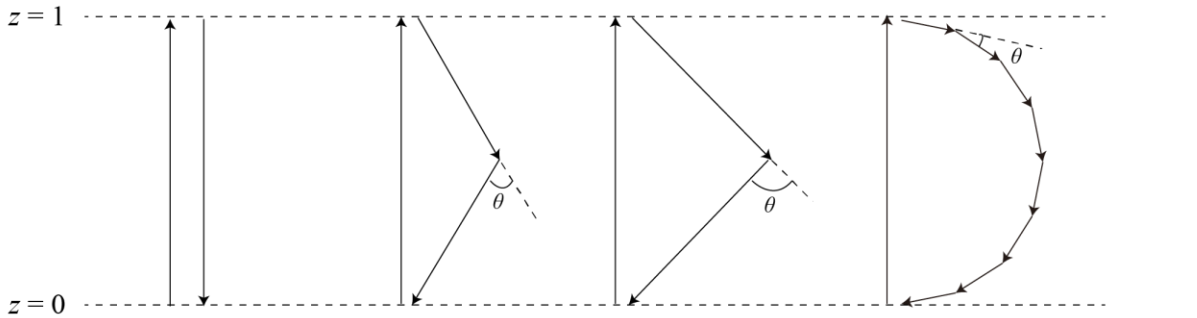

θ		π/3	π/2	π/8
w	1	0.96, 0.5	0.92, 0.7	0.83, 0.19 for each π/8 scattering
effective z	1	0.83	0.78	0.68

Appendix Figure 41 Four scattering scenarios with their scattering angles, w values and effective depths.

The median of the effective depths is studied at different coherence gate depths for photons that have initial incident x coordinates within a certain region. As shown in Appendix Figure 42b), the effective depth first increases quickly with coherence gate depth with a slope close to 1, before quickly slows down and increases with a slope around 0.5.

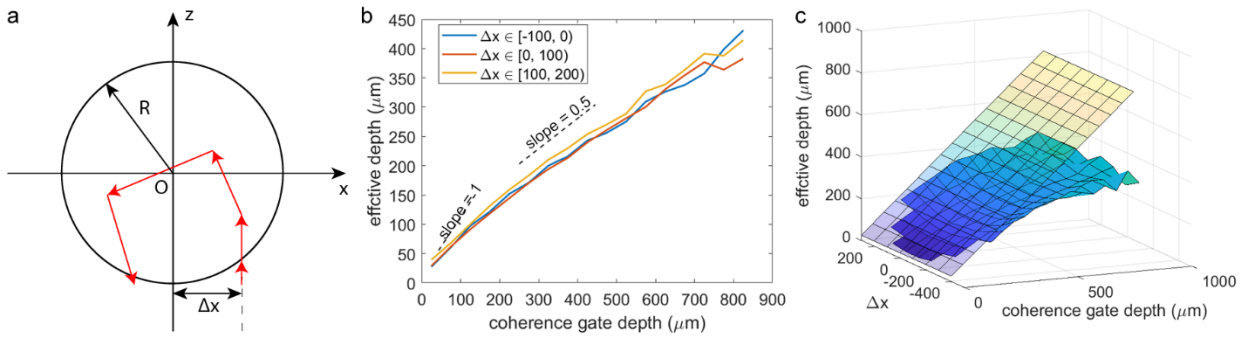

Appendix Figure 42 a) illustration of the Δx incident position b) effective depth vs "coherence gate depth" (i.e. half of the OPL) for three incident ranges of Δx c) a 3D surface of effective depth vs Δx and coherence gate depth. The translucent surface is the "z = coherence gate depth" plane.

The effective depth has a small dependence on the x coordinate of the incident position, as shown in Appendix Figure 42. The effective depth is larger with higher Δx, potentially due to the fact that these photons have a longer free travel distance and have high z values when they hit the target.

The next step is to use the "effective depth" as an intermediate variable and help understand how the BDI signatures, especially power spectra, are related to effective depths.

References

[1] L. Wang, S. L. Jacques, and L. Zheng, "MCML—Monte Carlo modeling of light transport in multi-layered tissues," Comput. Meth. Prog. Bio. **47**, 131-146 (1995).

[2] C. Zhu, and Q. Liu, "Review of Monte Carlo modeling of light transport in tissues," J. Biomed. Opt. **18**, 050902 (2013).

[3] D. D. Nolte, "Optical Interferometry for Biology and Medicine," (Springer, 2011).